Optical Sensors for Planetary Radiant Energy (OSPREy): Calibration and Validation of Current and Next-Generation NASA Missions

Stanford B. Hooker, Germar Bernhard, John H. Morrow, Charles R. Booth, Thomas Comer, Randall N. Lind, and Vi Quang

The NASA STI Program Office … in Profile

Since its founding, NASA has been dedicated to the advancement of aeronautics and space science. The NASA Scientific and Technical Information (STI) Program Office plays a key part in helping NASA maintain this important role.

The NASA STI Program Office is operated by Langley Research Center, the lead center for NASA's scientific and technical information. The NASA STI Program Office provides access to the NASA STI Database, the largest collection of aeronautical and space science STI in the world. The Program Office is also NASA's institutional mechanism for disseminating the results of its research and development activities. These results are published by NASA in the NASA STI Report Series, which includes the following report types:

- TECHNICAL PUBLICATION. Reports of completed research or a major significant phase of research that present the results of NASA programs and include extensive data or theoretical analysis. Includes compilations of significant scientific and technical data and information deemed to be of continuing reference value. NASA's counterpart of peer-reviewed formal professional papers but has less stringent limitations on manuscript length and extent of graphic presentations.

- TECHNICAL MEMORANDUM. Scientific and technical findings that are preliminary or of specialized interest, e.g., quick release reports, working papers, and bibliographies that contain minimal annotation. Does not contain extensive analysis.

- CONTRACTOR REPORT. Scientific and technical findings by NASA-sponsored contractors and grantees.

- CONFERENCE PUBLICATION. Collected papers from scientific and technical conferences, symposia, seminars, or other meetings sponsored or cosponsored by NASA.

- SPECIAL PUBLICATION. Scientific, technical, or historical information from NASA programs, projects, and mission, often concerned with subjects having substantial public interest.

- TECHNICAL TRANSLATION. English-language translations of foreign scientific and technical material pertinent to NASA's mission.

Specialized services that complement the STI Program Office's diverse offerings include creating custom thesauri, building customized databases, organizing and publishing research results . . . even providing videos.

For more information about the NASA STI Program Office, see the following:

- Access the NASA STI Program Home Page at http://www.sti.nasa.gov/STI-homepage.html

- E-mail your question via the Internet to help@sti.nasa.gov

- Fax your question to the NASA Access Help Desk at (443) 757-5803

- Telephone the NASA Access Help Desk at (443) 757-5802

- Write to:
  NASA Access Help Desk
  NASA Center for AeroSpace Information
  7115 Standard Drive
  Hanover, MD 21076
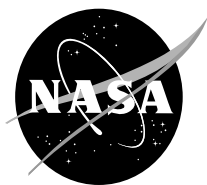
Optical Sensors for Planetary Radiant Energy (OSPREy): Calibration and Validation of Current and Next-Generation NASA Missions

Stanford B. Hooker
NASA Goddard Space Flight Center, Greenbelt, Maryland

Germar Bernhard
Biospherical Instruments Inc., San Diego, California

John H. Morrow
Biospherical Instruments Inc., San Diego, California

Charles R. Booth
Biospherical Instruments Inc., San Diego, California

Thomas Comer
Biospherical Instruments Inc., San Diego, California

Randall N. Lind
Biospherical Instruments Inc., San Diego, California

Vi Quang
Biospherical Instruments Inc., San Diego, California

S.B. Hooker, G. Bernhard, J.H. Morrow, C.R. Booth, T. Comer, R. Lind, and V. Quang

Table of Contents

S.B. Hooker, G. Bernhard, J.H. Morrow, C.R. Booth, T. Comer, R. Lind, and V. Quang

ABSTRACT

A principal objective of the Optical Sensors for Planetary Radiance Energy (OSPREy) activity is to establish an above-water radiometer system mounted on an offshore-platform as a lower-cost alternative to existing in-water buoys for the collection of ground-truth observations. The goal is to be able to make *high-quality* measurements satisfying the accuracy requirements for the vicarious calibration and algorithm validation of current and next-generation ocean color satellites. This means the measurements will have a documented uncertainty satisfying the established performance metrics for producing climate-quality data records (CDRs). The activity is based on enhancing commercial-off-the-shelf (COTS) fixed-wavelength and hyperspectral sensors to create thermally regulated *hybridspectral* instruments with an improved accuracy and spectral resolution, as well as a dynamic range extended into shorter and longer wavelengths. Greater spectral diversity in the ultraviolet (UV) will be exploited to separate the living and nonliving components of marine ecosystems; UV bands will also be used to flag and improve atmospheric correction algorithms in the presence of absorbing aerosols. The short-wave infrared (SWIR) is expected to improve atmospheric correction, because the ocean is radiometrically *blacker* at these wavelengths. The cost savings are derived not only from using existing technologies as a foundation of the instrument designs, most notably recently developed microradiometers, but also from the above-water approach itself. From the oceanographic perspective, above-water radiometry involves the use of offshore platforms, which have several advantages: a) offshore platforms and towers already exist, b) a tower provides a very stable platform and deterministic solar geometry, c) biofouling is a significantly lesser problem compared to an in-water instrument system, d) acquiring high-quality data at longer wavelengths is easier to achieve, and e) the offshore structure offers a great deal of protection for the instruments. In addition to the relevance to NASA Earth Science, the OSPREy approach significantly impacts the state of the art of optical calibration technology, which is in transition. The production of a transfer radiometer and demonstration of its utility should help interrupt the cycle of escalating costs associated with lamp standards, because it encourages the transition toward detector-based standards. The world ocean is immense and it is not possible for one agency or one country to produce global CDRs of a uniform quality without strong partners from other nations. Establishing a high-quality and cost-effective sampling capability that is readily reproduced—*because it can be purchased as a COTS system*—is an important first step towards establishing a global calibration and validation paradigm. This report describes the overall design of OSPREy; the documented uncertainty will be presented in a subsequent report.

Prologue

NASA has a continuing requirement to collect high-quality *in situ* data for the vicarious calibration of ocean color satellite sensors and to validate the algorithms for which the remotely-sensed observations are used as input parameters. Within this context, "high quality" refers to *measurements with a documented uncertainty in keeping with established performance metrics for producing climate-quality data records (CDRs)*. The Optical Sensors for Planetary Radiant Energy (OSPREy) activity establishes a lower-cost alternative to existing practices for such data collection activities while satisfying the necessary accuracy and precision requirements. The lower cost is achieved by enhancing existing, but recently developed, state-of-the-art commercial instruments (with a spectral sampling capability exceeding current and planned satellite requirements), the use of sensors already being used in the field, reduced maintenance costs from the use of above-water sensors (which have no significant biofouling), and deploying the equipment on an offshore structure already maintained by other institutes and agencies.

The enhancements to existing radiometric technology permits the measurement of a suite of atmospheric parameters, so for the first time, self-consistent observations—that is, data from instruments with a common calibration—of the ocean and atmosphere are possible. The benefits of this new sampling capability are expected to be better atmospheric correction of ocean color data, an improved ability to accurately separate the living and nonliving components of seawater, and improved understanding of the interaction between the ocean and atmosphere.

The OSPREy activity is designed as an important initial step in the ability of the ocean color community to support a coupled ocean–atmosphere observing system, i.e., a calibration and validation capability for a combined satellite mission. Such a mission will very likely emphasize coastal as well as open ocean processes, so a capability for making high-quality measurements in the near-shore environment is an inevitable requirement. The work presented here is based on the use of offshore structures as sampling sites, which means this important work can start now with enough time for establishing what will be needed to support the next mission. In addition, as long as the location

of the site is selected carefully to ensure the range in environmental properties are satisfactory for both vicarious calibration and algorithm validation, the opportunity exists to test whether or not the response of a vicariously calibrated system is linear across a much wider dynamic range than has been done before.

In addition to the relevance to NASA Earth Science, the OSPREy activity will significantly impact the state of the art of optical calibration technology, which is in transition. The evolution is occurring, because traditional calibration sources (e.g., a lamp standard of spectral irradiance) are becoming incrementally expensive at an increasing rate. For example, the National Institute of Standards and Technology (NIST) increased primary standard lamp prices from $7,202 in 1997, to $14,945 in 2007, with delivery times as long as eight months. In addition, a reduction in lamp quality, possibly due to the closing of domestic manufacturing facilities, have led to substantially shorter lifetimes for working standards that are derived from the NIST primary standard lamps.

These direct and indirect escalations in costs impact calibration facilities, scientific researchers, and NASA programs. In addition, commercial activities are affected, because the cost of calibrating instruments must be passed on to the customer. As a further complication, increased costs discourages researchers from recalibrating their instruments on a frequent schedule, which can in turn lead to spurious scientific results and degraded CDRs. Development of the OSPREy Transfer Radiometer (OXR) and demonstration of its utility should help interrupt the cycle of escalating costs, because it encourages the transition away from lamp-based standards, which are consumed with use, to detector-based standards, which are not. Another type of calibration that is not consumed with use is a solar calibration, but this requires instruments that function as sun photometers.

The OXR instruments are from a new class of thermally regulated sensors that are based on combining two different, but complementary, commercial off-the-shelf (COTS) detection capabilities—fixed-wavelength microradiometers and a hyperspectral spectrograph—to build a *hybridspectral* instrument called the Enhanced Performance Instrument Class (EPIC) sensor. Unlike legacy sensors, which were built primarily for narrowly specified light sources and sampling targets, EPIC sensors are anticipated to be used with a tracker and can view a multitude of intended sources and targets under varying conditions. For brevity and specificity, an individual radiance (L) and irradiance (E) instrument from this EPIC Multitarget Radiometer (EMR) product line is denoted as EML and EME, respectively. This same naming approach is also used for the radiance and irradiance OXR sensors as the OXL and OXE, respectively.

The use of two different detector technologies coupled with custom-built primary (housing) and secondary (spectrograph) thermal regulation increases the spectral resolution and decreases the uncertainty of OXR and EMR

measurements. The addition of a nine-position filter wheel in front of the spectrograph fiber in an EML (radiance) sensor provides an index (home) position, improved stray-light correction (cut-on filter), dark offset measurements (opaque disk), three-axis polarimetry, solar (bright target) viewing through the use of two neutral density (ND) filters, and an open position (for relatively dim targets, e.g., the Moon, with respect to the Sun). Integration of a video camera into an EML sensor and mounting the sensor on an automated tracker creates a sensor that can target the Sun, sea, sky, and Moon with sufficient accuracy and precision to function as a sun photometer.

When an EML (radiance) sensor is used with an EME (irradiance) sensor having a shadowband accessory, the sensor pair—or *dyad*—produces a wide diversity of oceanic and atmospheric (or atmospheric and terrestrial) data products with a common calibration history. The large number of variables means an OSPREy system can support a commensurately large number of missions. The use of two dyads provides synchronous and asynchronous sampling scenarios plus intra- and inter-sensor comparisons to maximize quality assurance (QA) and quality control (QC) opportunities, while minimizing the likelihood of degrading the CDRs.

Another mechanism for minimizing the likelihood of degraded CDRs is to implement a completely open data policy—*from the very beginning, at the point of acquisition*—whereby researchers can access the data in near-real time. The philosophy espoused in the OSPREy activity is to use the increasing availability of online resources to make the data available on a Web site, so the quality of the work at every step in the process can be evaluated independently. The access of near-real time data to worldwide institutes is also an educational-outreach that Government agencies, such as the National Science Foundation (NSF) and NASA, have found valuable. The OSPREy activity is anticipated to have an online data availability, which should generate similar interest from educational programs in remote sensing.

The increasing interest of foreign agencies in satellite remote sensing, and their attempts at emulation (or at least, appreciation) of NASA calibration and validation activities, brings increased market opportunities to domestic companies, such as Biospherical Instruments Inc. (BSI) the manufacturers of OSPREy systems, in exploiting these markets. Activities like OSPREy contain technologies that could be exported, and when robust calibration and validation programs are exported, worldwide remote sensing programs gain a more common calibration base. The world ocean is immense and it is not possible for one agency or one country to produce global CDRs of a uniform quality without strong partners from other nations. Establishing a high-quality, but nonetheless cost-effective sampling system that is readily reproduced—*because it can be purchased commercially*—is an important first step in providing solutions for the global calibration and validation problem set.

S.B. Hooker, G. Bernhard, J.H. Morrow, C.R. Booth, T. Comer, R. Lind, and V. Quang

The OSPREy approach delivers data with documented quality metrics for both the oceanic and atmospheric science communities (with terrestrial applications, as well). These data form a solid basis for ocean color calibration and validation activities. Continuous monitoring at high sampling rates further provides a wealth of information that can be used to analyze geophysical parameters on time scales from seconds to years. The level of temporal coverage combined with the diversity and number of data products is unprecedented, when compared to existing calibration and validation systems, and will stimulate new research. Where OSPREy deployments overlap with other research programs, there is an opportunity to foster mutual synergistic opportunities. For example, the aerosol optical depth (AOD) measurements from OSPREy can augment the measurements made by the Aerosol Robotic Network (AERONET), which has numerous sun photometers deployed worldwide (Holben et al. 1998). In turn, algorithms developed for AERONET may benefit OSPREy in terms of standardizing aspects of the data product suite.

The NIST irradiance scales implemented by the Spectral Irradiance and Radiance Responsivity Calibrations using Uniform Sources (SIRCUS), which are intended to be used for OSPREy calibrations as maintained by OXR instruments and a library of 21 FEL lamps (plus a reflectance plaque), will be compared to the calibrations from the NIST Facility for Spectroradiometric Calibrations (FASCAL), as well as solar calibrations, which are used for the Ultraviolet Spectral Irradiance Monitoring Network (UVSIMN). The calibrations will be validated against each other to the benefit of all programs. Because the UVSIMN scale is also interlinked with other domestic and international UV monitoring networks through the National Oceanic and Atmospheric Administration (NOAA) Central UV Calibration Facility (CUCF) located in Boulder (Colorado), the detector-based irradiance scale established for OSPREy may also be of sufficient benefit to further those programs.

The connection of OSPREy to other programs is also linked to the legacy sensors still used in those programs and extends into the baseline understanding of calibration uncertainties, particularly in the UV domain. Because the topics of interest span calibration, data acquisition, data processing, and quality monitoring, the OSPREy approach is necessarily complex with many nuances to understand. To aid the reader, frequently asked questions (FAQs) regarding many aspects of EMR and OXR sensors, as well as OSPREy systems, are provided as a separate section (see Table of Contents). A summary of the material presented in each chapter is given below.

1. The OSPREy System Concept

The primary objective of the OSPREy activity is to develop and deploy a new class of commercial radiometers to support existing and next-generation NASA ocean color satellites. An EPIC sensor is a *hybridspectral* device combining measurements of spectral irradiance and radiance from recently developed microradiometers with a commercially available hyperspectral spectrograph plus a pointing system. Over common parts of the spectrum, fixed-wavelength microradiometers and the spectrograph can be continuously intracompared to maintain stability and accuracy of the system. Radiance sensors have a nine-position filter-wheel assembly in line with the spectrograph fiber optics to permit hyperspectral polarimetric measurements (three polarized filters), direct-Sun viewing (neutral density filters), stray-light correction (395 nm cut-on filter), and dark current measurements (opaque disk). Radiance sensors also have an integrated camera for locating the Sun and Moon (in lieu of a quadrant detector), as well as verifying the condition of all targets (cloud-free solar and lunar disks, cloud presence in sky data, and sea surface debris or foam detection). All sensors include thermal stability control to increase filter and detector stability and reduce drift. The field sensor suite includes shadowband accessories to the solar irradiance sensors, which are combined with radiance observations of the Sun, Moon, sea, and sky across a wide spectral range—the UV, through the visible (VIS) and into the short-wave infrared (SWIR); 305–1,640 nm is the full spectral range for radiance, as well as irradiance because of a new cosine collector design. The diversity of targets and measurement types provides an unprecedented number of near-simultaneous atmospheric and oceanic data products. This new sampling capability is expected to improve a) the atmospheric correction of ocean color data; b) the accuracy in satellite data products, particularly in optically complex (coastal) waters; and c) the understanding of the interaction between the ocean and atmosphere. The combination of wide spectral and dynamic ranges with accurate pointing are also anticipated to have application to terrestrial observations.

2. Application of Microradiometers to EMR and OXR Sensors

Microradiometers are small, fast, reliable, and cost-effective radiometers that are composed of a filter, photodetector, wide-range electrometer, analog-to-digital converter (ADC), microprocessor, and digital interface. Microradiometers were originally developed for in-water profiling systems and were adapted to the requirements of OSPREy applications by increasing their dynamic range to over 10 orders of magnitude with excellent (better than 1%) linearity over this interval. The devices now support measurements of both very bright sources like the solar disk and comparatively very dim sources like the ocean, calibration targets, and lunar disk. The circuitry was further modified to handle both silicon diodes for UV-VIS measurements and InGaAs photodetectors for measurements in the SWIR domain. The Multiple Microradiometer System (MMS) architecture allows clusters of up to 19 tightly-packed microradiometers to be networked together

using an aggregator, such that the multitude of sensors can be controlled as a solitary device. The aggregator also provides an interface to external devices, such as temperature controllers and filter-wheel stepping motors used in EMR instruments. Compared to legacy platforms, the new technology offers lower cost, fully automated manufacturing, higher reliability, smaller size, and higher detector densities while maintaining excellent performance characteristics.

3.   SWIR Cosine Collector Design and Evaluation

The irradiance collectors used with EMR sensors require small cosine errors and high transmission for wavelengths within 305–1,640 nm (UV–SWIR range). To satisfy this objective, a new irradiance collector was designed by selecting diffuser materials optimized for this spectral range and by modifying the shape of the existing irradiance collector originally developed for the UV-VIS range of legacy sensors. Laboratory tests indicated that a composite diffuser made of one layer of generic polytetrafluoroethylene (PTFE) sheet and one layer of porous PTFE (pPTFE) material produces the best characteristics. The tests also confirmed that a small cosine error can only be achieved with a shaped diffuser (for instance, a diffuser with a trapezoidal cross-section). A numerical model was developed to optimize the dimensions of the composite diffuser (e.g., height, plus top and bottom diameters of the diffuser) and its support structure (e.g., diameters and heights of two shadow rings surrounding the diffuser). Based on the results of material testing and modeling, a prototype irradiance collector was manufactured and tested. For wavelengths in the UV-VIS range, the cosine error of the new collector is less than $\pm 3\%$ for incident angles up to $75°$ and does not depend on wavelength and azimuth angle. Cosine errors at SWIR wavelengths are larger (e.g., -5% at 1,020 nm for an incident angle of $74°$), but are still within acceptable limits for OSPREy applications.

4.   Radiance Field-of-View Specifications

The field of view of EML (radiance) instruments used for OSPREy applications, specified here in terms of the full view angle (FVA), must be optimized to accurately measure a variety of different radiometric sources: the direct solar irradiance when pointing the instrument at the Sun; the total radiance emanating from the sea surface, the sky radiance, and the radiance of a calibration plaque. The optimum FVA was determined based on the following considerations: a) the FVA must encompass the entire solar and lunar disks when performing direct measurements under all observation conditions; b) compliance with recommendations for sun photometers issued by the World Meteorological Organization (WMO); c) an FVA large enough to allow accurate measurements of low-intensity sources (e.g., calibration plaques, the sea surface, and the lunar disk); d) an FVA small enough to permit statistical filtering of

surface and capillary wave effects when measuring the sea surface; and e) a reasonable overall instrument length. The latter are needed to ensure accurate pointing and control of the sensor, particularly by the sun tracker; easier handling during servicing and the types of activities that take place during those events (e.g., monitoring the stability of the sensors with a portable source); and minimization of wind loading. After taking all considerations into account, it was concluded that an FVA of $2.5°$ combined with a slope angle of $0.7°$ is the optimal configuration. These geometric parameters were translated into a fore-optic design consisting of Gershun tubes with an overall length of 182 mm, a front aperture of 4 mm, and three internal baffles for straylight suppression.

5.   Sun Tracker Performance Evaluation

An OSPREy system requires a pointing device or *tracker* to accurately direct radiance radiometers at relevant targets, including the Sun, Moon, sky, sea surface, calibration sources, and monitoring devices. Of all applications, the measurement of the direct Sun requires the highest pointing accuracy. Based on the angular size of the Sun, the geometry of radiance fore optics, and alignment uncertainties, it was determined that a pointing accuracy to within $0.2°$ is required. The tracker should be small in size with a low power requirement, and must also be weather and corrosion resistant for use in the marine environment. A market analysis was performed, which resulted in three candidate instruments. Based on specifications provided by the manufacturers, it was concluded that the PTU-D300 pan-tilt unit from FLIR Motion Control Systems would be the most suitable tracker for OSPREy applications. A test unit was procured and installed on the roof platform at BSI. The pointing accuracy was tested by mounting a video camera on the device for tracking the Sun. Software was developed to capture and examine the images of the video camera. The software was able to find the center of the Sun in the video images with an accuracy of $0.01°$. The method is a viable and cost-effective alternative to the use of quadrant detectors for Sun finding. Image analysis, later confirmed with a test deployment of an EML (radiance) sensor, showed the PTU-D300 unit can track the Sun with a sufficient accuracy of to within $0.1°$.

6.   Lamp Library Performance

Twenty-one 1,000 W tungsten-halogen FEL lamps were chosen to become part of the OSPREy lamp library. Nine lamps were calibrated by NIST, while the rest are uncalibrated, but seasoned lamps (by the supplier). These lamps were operated for periods ranging from 4–35 h to assess their stability. Changes in brightness were typically in the range of $\pm 0.02\%$ per hour with a few lamps exhibiting slightly larger drifts. These lamps should be seasoned for an additional 8–30 h to improve their stability. The calibration laboratory at BSI was upgraded to operate lamps

S.B. Hooker, G. Bernhard, J.H. Morrow, C.R. Booth, T. Comer, R. Lind, and V. Quang

of the OSPREy lamp library at the highest level of accuracy achievable. Upgrades included a new system for powering the lamps, which allows regulation of the lamp current to within a precision of $50\,\mu A$ (or 0.0006% for a target current of 8.2 A). Other facilities required for accurate lamp transfers were also upgraded to reduce uncertainties caused by stray light, misalignment, and temperature variations. Three radiometers are available for maintaining optical standards: an OXL instrument calibrated at BSI, an OXE instrument currently awaiting results of a NIST SIR-CUS calibration (and not used for the results presented in this chapter), and a transfer radiometer based on the BSI ground-based UV (GUV) class of radiometers that is called an XGUV. A comprehensive uncertainty analysis showed the use of moderate-bandwidth radiometers, such as the XGUV and OXL, are suitable to transfer calibrations of FEL lamps. Uncertainties related to the relatively large bandwidth of these instruments are on the order of 0.3%. All NIST lamps were intercompared and agreed to within $\pm 2\%$, which is a very good result considering that some lamps are rather old and were calibrated against different NIST scales. A protocol on the usage of the lamp library was developed with the goal of preserving the spectral irradiance scale over a timescale of 15 years or more.

7.   Spectrograph Testing and Review

EMR sensors are hybridspectral instruments with 19 fixed wavelength microradiometers plus an integrated spectrograph. Requirements for these devices are challenging, because they represent two sensing technologies in one housing, which must both sample a very wide dynamic range—the very bright Sun and the relatively much darker ocean. Candidate devices must be sufficiently sensitive to detect the low signals inherent in OSPREy work in the red region of the spectrum above seawater, exhibit sufficiently accurate spectral selection, stable dark noise, and good temperature stability. A review of commercial spectrograph manufacturers identified a large number of instruments, from which 10 spectrographs were obtained and systematically tested. The latter included two from Hamamatsu, three from Avantes, four from Zeiss/Tec5, and one from B&W Tek. Testing protocols included the analysis of the following: a) wavelength range, b) spectral resolution, c) slit function, d) dynamic range, e) out-of-band rejection, f) stray light, g) saturation, h) change of dark signal with integration time and temperature, i) spectral responsivity, j) noise equivalent irradiance or radiance, and k) linearity. The test results indicate that an ideal instrument does not exist, but workable candidates are available. For example, all instruments suffer from stray light and nonlinearity to some degree, which limits their usable dynamic range and measurement accuracy. After considering all tests results and other factors relevant for operation and system integration, it was determined that the MMS UV-VIS II and MMS1† spectrographs from Zeiss/Tec5 were the most suitable devices for OSPREy applications.

8.   The Integrated OSPREy System

The previous chapters describe the major elements in the radiometers used in an OSPREy system: a microradiometer cluster with necessary modifications to support OSPREy design criteria, a spectrograph, optical collectors (both radiance and irradiance), primary (housing) and secondary (spectrograph) thermal regulation, and accessories like the tracker and shadowband. This chapter describes how these components—plus housing design, primary and secondary temperature control, and other support electronics—are integrated to make the radiometers used in OSPREy systems. These include radiance and irradiance field sensors, and a similar pair designated as transfer radiometers. The fully integrated system provides an unprecedented capability in a single housing. The spectrograph provides hyperspectral resolution over a subset of the complete spectral range, while the microradiometers provide a larger dynamic range in responsivity, higher sampling speeds, better sensitivity, and sampling across the entire OSPREy spectral range (290–1,670 nm). The two sensor technologies supplement each other. For example, spectrograph data can be used to detect potential degradation of the interference filters used by the microradiometer channels, while the microradiometers help to correct dark-current drifts and nonlinearity in spectrograph measurements. The capability of radiance sensors is further enhanced by a nine-position filter wheel and integrated camera. In the standard configuration, the filter wheel permits hyperspectral polarimetric measurements, direct-Sun viewing, stray-light correction, dark current measurements, and a home position. The video camera is used for locating the Sun and verifying the condition of all targets (cloud-free solar and lunar disks, cloud presence in sky data, and sea surface debris or foam detection). The components of each radiance and irradiance sensor type are integrated in a common housing that is environmentally sealed, nitrogen purged, and temperature controlled. Synchronous and asynchronous sampling modes measure the sea, Sun, and sky, across a wide spectral range (UV–SWIR). The OSPREy architecture is modular and scalable, which permits the configuration (sensor inventory) and complexity (sampling redundancy) to be matched with science objectives and resource allocations. The modularity allows the observing system to expand or contract as mission requirements evolve. These measurements support an unprecedented number of current and next-generation satellite missions involving both atmospheric and oceanic data products.

---

† Note that "MMS" with regards to the MMS UV-VIS II and MMS1 from Zeiss/Tec5 is defined as the "Monolithic Miniature-Spectrometer," and is not to be confused with the MMS from Biospherical Instruments Inc., which is the Multiple Microradiometer System.

Chapter 1

The OSPREy System Concept

STANFORD B. HOOKER
NASA Goddard Space Flight Center
Greenbelt, Maryland

JOHN H. MORROW
Biospherical Instruments Inc.
San Diego, California

ABSTRACT

The primary objective of the OSPREy activity is to develop and deploy a new class of commercial radiometers to support existing and next-generation NASA ocean color satellites. An EPIC sensor is a *hybridspectral* device combining measurements of spectral irradiance and radiance from recently developed microradiometers with a commercially available hyperspectral spectrograph plus a pointing system. Over common parts of the spectrum, fixed-wavelength microradiometers and the spectrograph can be continuously intracompared to maintain stability and accuracy of the system. Radiance sensors have a nine-position filter-wheel assembly in line with the spectrograph fiber optics to permit hyperspectral polarimetric measurements (three polarized filters), direct-Sun viewing (neutral density filters), stray-light correction (395 nm cut-on filter), and dark current measurements (opaque disk). Radiance sensors also have an integrated camera for locating the Sun and Moon (in lieu of a quadrant detector), as well as verifying the condition of all targets (cloud-free solar and lunar disks, cloud presence in sky data, and sea surface debris or foam detection). All sensors include thermal stability control to increase filter and detector stability and reduce drift. The field sensor suite includes shadowband accessories to the solar irradiance sensors, which are combined with radiance observations of the Sun, Moon, sea, and sky across a wide spectral range—the UV, through the visible (VIS) and into the short-wave infrared (SWIR); 305–1,640 nm is the full spectral range for radiance, as well as irradiance because of a new cosine collector design. The diversity of targets and measurement types provides an unprecedented number of near-simultaneous atmospheric and oceanic data products. This new sampling capability is expected to improve a) the atmospheric correction of ocean color data; b) the accuracy in satellite data products, particularly in optically complex (coastal) waters; and c) the understanding of the interaction between the ocean and atmosphere. The combination of wide spectral and dynamic ranges with accurate pointing are also anticipated to have application to terrestrial observations.

1.1 Introduction

Global ocean color satellites provide a revolutionary capability for understanding Earth. Within a of couple days, significant portions of natural systems are sampled, and within only one week, even the vastness of the world ocean—which covers about two-thirds of Earth's surface—is sampled with relatively minor cloud contamination. Although now considered a routine accomplishment, such a global *snapshot* of the oceanic ecosystem still cannot be assembled with traditional sampling tools even if all the ship-based measurements throughout history are combined.

The ability to assess the world synoptically makes satellites an appealing tool for studying the oceanic contribution and response to climatic change. This approach requires a longevity and quality of the data in keeping with the problem set, however, which means decadal and longer time series are needed. Satellite missions are short in comparison; most have a five-year design lifetime, so sequential, multiple missions are needed. With sufficient mission overlap and properly characterized sensors, one mission can be properly intercompared to the next to ensure an uninterrupted time series of CDRs.

Understanding how climatic change will influence oceanic systems is a major research theme of the NASA Ocean Biology and Biogeochemistry (OBB) research program†.

---

† The long-term OBB programmatic objectives and research requirements are articulated in a comprehensive Advance Science Plan, *On the Shores of a Living Ocean: The Unseen World*, and is available from the following Web site: `http://oceancolor.gsfc.nasa.gov/DOCS`.

S.B. Hooker, G. Bernhard, J.H. Morrow, C.R. Booth, T. Comer, R. Lind, and V. Quang

Global monitoring of the oceanic biosphere is accomplished through the determination of radiometric variables. Specifically, the spectral radiances measured at the top of the atmosphere, from which (after atmospheric correction), the spectral radiances emerging from the surface of the ocean, $L_W(\lambda)$, are derived (λ denotes wavelength). Considerable emphasis is placed on the accurate determination of these so-called *water-leaving radiances*, because they are the primary parameters in the inversion algorithms to derive the CDRs. For the latter, the most common algorithm is the chlorophyll a (Chl a) concentration (O'Reilly et al. 1998), denoted [Chl a]†.

The development of a decadal time series has been highlighted in a number of reports (Space Studies Board 2000). Although time series of key biogeochemical parameters date back to the 1978 launch of the Coastal Zone Color Scanner (CZCS), the CZCS was a proof-of-concept mission and is unsuitable for initiating a CDR time series. Almost 20 years later, a sequence of sophisticated ocean color missions were launched including the Sea-viewing Wide Field-of-view Sensor (SeaWiFS) in 1997, followed by the Moderate Resolution Imaging Spectroradiometer (MODIS) on the Earth Observing System (EOS) Terra and Aqua platforms in 2000 and 2002, respectively (denoted MODIS-T and MODIS-A, respectively). The development and maintenance of CDRs derived from these and other missions must incorporate a sophisticated set of requirements before and throughout the lifetime of the satellite. The tasks involved are usually organized into a single activity called *calibration and validation* (Hooker and McClain 2000).

In remote sensing applications, calibration is frequently defined as *the prelaunch characterization followed by the continuing analysis of the onboard sensor calibrators once on-orbit operations commence,* and validation is usually thought of as *the development of data processing schemes (e.g., atmospheric correction and derived quantities), plus the verification of product accuracies using in situ data.* The OSPREy activity is primarily concerned with calibration, although aspects of the envisioned system are applicable to validation activities.

Aside from absolute system response versus radiance calibration, several characteristics must be quantified for each instrument channel prior to launch: polarization, temperature, linearity, stray light, electronic crosstalk, band-to-band spatial registration, and response versus scan angle. Uncertainties in these parameterizations are almost impossible to separate on orbit because their effects are convolved and many are a function of solar and sensor viewing geometries. All of these tasks are important, and in most cases properly planned before launch, but the pressures to launch on time usually result in a compromised

understanding of sensor performance. The severe launch conditions and the harshness of space can alter the anticipated capabilities of the spaceborne sensor, regardless of how thoroughly it was characterized before launch. Consequently, a vicarious calibration is performed after a sufficient time permitting the collection of an adequate number of ground-truth—more properly, sea-truth—observations. Approximately 30 contemporaneous matchups of clear-sky *in situ* measurements and glint-free satellite images are typically needed to derive a fixed set of calibration gains.

1.1.1 Vicarious Calibration

Regardless of how sea-truth data are acquired, accurate measurements are required. The most recent Sea-WiFS validation results show the satellite normalized L_W (412–555 nm) and [Chl a] values are within 5% and 8% of observed values, respectively, for waters deeper than 1,000 m (Bailey and Werdell 2006). This level of agreement significantly satisfies the performance specification first established for SeaWiFS (Hooker and Esaias 1993) and adopted by most missions thereafter.

A likely reason for the success of SeaWiFS is simply good planning. Early in the mission, the SeaWiFS Ocean Optics Protocols (hereafter referred to as the Protocols) were drafted to ensure the potentially large variety of field measurements were in keeping with the remote sensing accuracy requirements. The Protocols initially adhered to the Joint Global Ocean Flux Study (JGOFS) sampling procedures (JGOFS 1991) and defined the standards for SeaWiFS calibration and validation activities (Mueller and Austin 1992). Over time, the Protocols were initially revised (Mueller and Austin 1995), and then updated on essentially an annual basis (Mueller 2000, 2002, and 2003).

The methodology for vicarious calibration began with the Protocols. Some of the procedures are best described as assertions, i.e., *they were not the direct result of a field or modeling exercise that quantitatively established why certain practices had to be adopted—they were simply stated.* Some assertions were not applied and were discarded. For example, the original vicarious calibration concept required radiometric profiles to be collected during a dedicated cruise shortly after launch when routine satellite operations had commenced (Clark et al. 1997 and Gordon 1998). The long-term stability of the gains from the *initialization cruise* were to be monitored with a radiometric buoy. Initialization cruises were only executed for SeaWiFS and both MODIS instruments, but the data were ultimately used for validation purposes—not vicarious calibration—and all three satellites relied on Marine Optical Buoy (MOBY) data (Clark et al. 1997) to set the first, and all subsequent, gains.

The evolution of MOBY from a monitoring instrument into the only source of vicarious calibration data establishes the concept that the entire process can—*and probably should*—evolve. Recent attempts to continue the

---

† In fact, radiometric inversions to derive chlorophyll are made with respect to the total chlorophyll a concentration, which is denoted [TChl a]; the latter are typically determined using high performance liquid chromatography (HPLC).

evolutionary process includes the study by Werdell et al. (2007) who demonstrated the feasibility of using a Case-1† model to derive ocean-surface reflectance for determining the target $L_W(\lambda)$ values for vicarious calibration. More recently, Bailey et al. (2008) used data from COTS profiling radiometers (Werdell and Bailey 2005) and a buoy with COTS sensors (Antoine et al. 2008) to show: a) satellite gains from COTS instruments are comparable to those from MOBY (the uncertainties for both are essentially the same); b) a simulated COTS version (multispectral 10 nm bands) of the hyperspectral MOBY data produced gains very similar to the full resolution data; c) even without addressing a finite near-infrared (NIR) radiance, data from waters with [Chl a] up to $0.7\,\mathrm{mg\,m^{-3}}$ can be used, and if any NIR radiance is appropriately removed, [Chl a] as high as 1–$3\,\mathrm{mg\,m^{-3}}$ is satisfactory; and d) aerosol type and concentrations are not as critical as current criteria suggests. In summary, *a number of the key vicarious calibration requirements, specifically those for low chlorophyll waters, low aerosol atmosphere, and radiometric resolution sufficient to match the spectral response functions for the satellite instrument to be calibrated, can be relaxed without seriously compromising the calibration effort.*

A large number of sea-truth and satellite data pairs are needed for statistical confidence in both calibration and validation activities. For most latitudes, coverage is every other day and clouds interfere significantly, so a site with continuous operation is an advantage. To produce the needed matchups in a reasonable time period, multiple sites are preferred. For nontilting satellites, additional data is lost from sun glint during a substantial part of the year. For these missions, sites in both hemispheres are advantageous, which means an easily replicated capability—both in terms of hardware and cost—is desirable. In addition, if a sensor has an uncharacterized geometric sensitivity (e.g., polarization), the vicarious calibration from a particular site will be tuned to the restricted range of geometries encountered at that location; an easily replicated and deployable system will probably be needed to collect data across the full range of geometries to address the problem.

1.1.2 Above- and In-Water Sampling

A simple strategy to ensure replicability is to be able to buy the needed equipment outright from an existing supplier, which also lowers the cost. The basic requirement of providing accurate $L_W(\lambda)$ values can be satisfied by making above- or in-water radiometric measurements. As discussed in more detail in App. A, the average level of agreement between contemporaneous above- and in-water

determinations of $L_W(\lambda)$ is to within a) the uncertainty of the instrument intercalibrations (2–3%), and b) the intercomparisons derived from simultaneous in-water deployments (also 2–3%).

Returning to the need for a system easily deployed to multiple sites or new locations, a compact system satisfies this need more readily than a large and cumbersome system. Above-water systems are inherently the easiest to deploy, because they are mounted on existing offshore structures; in-water instruments, in comparison, usually must provide their own mounting platform, which is usually a very large buoy. In terms of a cost-benefit analysis, an above-water approach offers several other advantages:

- Deploying the radiometers on an existing offshore tower already built and maintained by another group or agency ensures significant cost savings;

- A tower provides a very stable platform and deterministic solar geometry for mounting instruments, so there are no ill effects from sensor motion, and additional instruments can be readily deployed to ensure the most comprehensive data set possible;

- Fouling is a minor problem, and if the sensors are *stowed* after use, the particle deposition is minimized;

- Acquiring high-quality data in the red, as well as the near-infrared, parts of the spectrum is easier to achieve with an above-water system; and

- An offshore structure offers substantial protection for the instruments against foul weather and maritime hazards (most buoys have experienced long data gaps because of storm damage or ship collisions).

The latter is a significant cost advantage. In-water moorings, for example, are usually replaced more than once, if deployed for any length of time, from ship collisions.

The follow-on requirements for the system introduced in this section are derived from a) the mission concepts and research questions already discussed; b) the aforementioned recent results obtained from actual and simulated COTS instrumentation, as well as the ocean-surface reflectance model (ORM); and c) the need to satisfy existing protocols for vicarious calibration, but reinterpreted in terms of viable COTS alternatives to the MOBY paradigm (App. B). Given the trade-offs between all of the different possible ways of measuring $L_W(\lambda)$, it seems most reasonable to use a method that is the least likely to have any inherent biases and to check it with as many other methods as possible. If this is the objective, *an above-water approach is the least likely to have any biases, because it has almost no fouling and the derivation of $L_W(\lambda)$ has almost no subjective parameters.* The asserted best approach—an in-water buoy—is probably the most likely to have biases, because of fouling and surface effects on the shallow sensors; it is also the most likely to have data losses, because of bad weather, recreational boaters, and ship collisions.

Quantifying the capability of towers equipped with an above-water instrument is an important achievement, but

---

† By definition, the optical properties of Case-1 waters are solely determined by the phytoplankton and its derivative products (Morel and Prieur 1977), whereas Case-2 optical properties are also determined by other material, e.g., from terrestrial or bottom origin.

it is made more convincing if results can be confirmed using a different procedure and with a vicarious calibration objective. A system for acquiring autonomous above-water radiance data, based on a commercial sun photometer and called the SeaWiFS Photometer Revision for Incident Surface Measurements (SeaPRISM), was field commissioned at a tower (Hooker et al. 2000) and assessed for the validation of satellite products in coastal waters (Zibordi et al. 2002b). A one-year time series was compared with simultaneous in-water measurements for a wide variety of conditions. The average relative percent difference (RPD†) values between the two $L_W(\lambda)$ determinations were less than 2% in the 412–555 nm spectral interval (Zibordi et al. 2004b). More importantly, *the vicarious calibration gains for SeaWiFS derived from MOBY and SeaPRISM data agreed to within 1% in the 412–555 nm domain, and to within 2% at 670 nm.*

1.1.3 Future Challenges

Accurate vicarious calibration is not the only prerequisite in the production of CDRs; accurate atmospheric correction is equally important, because a) it is convolved with the vicarious calibration process, and b) the oceanic signal is an order of magnitude less than the total radiance observed by the satellite sensor. Two unresolved issues in the ocean color data processing are the detection and correction of moderate concentrations of absorbing aerosols and finite NIR reflectance in turbid waters‡. Methods are being developed to address both, but limitations due to the sensor designs exist and some methods are simply too computationally intensive to use in a routine global processing capability. For example, the NIR reflectance issue may be addressed in MODIS processing by using bands above 1.2 μm (SeaWiFS has no bands above 865 nm), even though these bands do not have the desired signal-to-noise ratios (SNRs) for this application (McClain et al. 2006).

A future challenge will be to maintain the level of success achieved in deep-ocean, so-called Case-1, waters in the coastal ocean and marginal seas—The Advanced Science Plan, for example, has many mission themes and research questions associated with the coastal zone. This emphasis on shallower water means investigating the optically more complex Case-2 environment and understanding the influence of dissolved and particulate constituents will be increasingly important (Hooker et al. 2007).

Bio-optical algorithms (e.g., Chl *a*) primarily rely on empirical relationships and have inherent limitations because of absorbing substances that do not covary with

the parameter of interest (Siegel et al. 2005). As coastal research matures, it is anticipated that UV wavelengths might be exploited to distinguish the absorption signals of colored dissolved organic matter (CDOM), Chl *a*, detritus, and minerals (because of high UV absorbance by CDOM relative to the other components), yielding new algorithms for coastal waters. Furthermore, UV bands may promote the detection of harmful algal blooms, such as red tides, because they produce UV absorbing compounds known as mycosporine-like amino acids (Laurion et al. 2003).

The shortest wavelength used by SeaWiFS and both MODIS instruments, as well as their successor the National Polar Orbiting Environmental Satellite System (NPOESS) Visible and Infrared Imaging Radiometer Suite (VIIRS), is 412 nm. Future missions will need to include additional measurements down to about 345 nm, to improve the separation of various pigments and the contributions of covarying constituents. In addition, future algorithms will be based on semi-analytical models and inherent optical properties (IOPs). Although this evolution might ultimately alter the vicarious calibration approach, the immediate future will require a continuation of relying on direct measurements of the apparent optical properties (AOPs) of seawater. A benefit from adding UV bands will be the possibility of using them to flag and improve atmospheric correction algorithms in the presence of absorbing aerosols.

Despite their many valuable contributions, legacy ocean color sensors use a measurement approach developed in the 1970s, while the scientific and analytical capabilities being applied have evolved substantially. The next generation of satellites, which does not include VIIRS because its specifications have already been set, will require a technological maturation in remote sensing.

Two of the most important objectives currently being planned for future ocean color missions are *a) an improved ability to accurately separate the living and nonliving components of marine ecosystems, and b) a clear understanding of the interaction between the ocean and atmosphere.* The National Academy of Sciences (NAS) Earth Science Decadal Survey acknowledged the importance of these objectives by proposing the Aerosol-Clouds and Ecosystems (ACE) mission, which includes the added capability of also measuring the cloud contribution to atmospheric forcing. Regardless of the final satellite mission configuration, both of these future objectives are the most challenging in coastal (heterogeneous) waters where the scales of motion are necessarily shorter, so an enhanced spatial or temporal sampling capability is anticipated.

Also important is extending the range and resolution of the measurement wavelengths, while including a suite of ground-truth sensors to simultaneously characterize atmospheric aerosols and oceanic optical properties. The culmination of a coupled ocean–atmosphere observational system is expected to allow investigators to correlate changes in ocean ecosystems with individual components and environmental forcing, and then to integrate that understanding into biogeochemical models.

---

† The RPD is computed as the difference between an observation (x_o) and reference (y_r) value, normalized by the reference value, and then expressed as a percent: $100(x_o - y_r)/y_r$.

‡ In open-ocean waters, the NIR signal is negligible and this *black* response was used in the past (e.g., with CZCS) to produce a simplified atmospheric correction scheme.
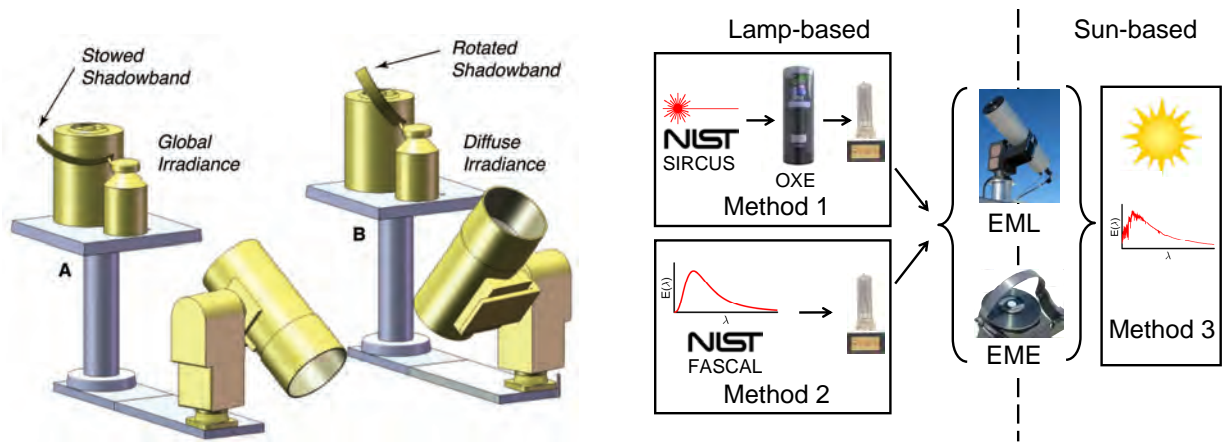
Fig. 1. The OSPREy system from an instrument and calibration perspective showing (left) two dyads of sensors (denoted A and B), each containing one irradiance sensor (with shadowband accessory) and one radiance sensor, and (right) the three calibration methods. The pedestal mounting is for illustrative purposes, as are the pointing angles and shadowband positions. The shrouds on the radiance sensors are not illustrative; they minimize unwanted scattering of direct sunlight on the detector during sky measurements.

1.2 System Concept

Based on the increased likelihood of combined oceanic–atmospheric satellite missions, the established capabilities of COTS radiometers, and the demonstrated success obtained with above-water radiometry, the primary objective of an OSPREy system is to satisfy all three of these aspects as design requirements for vicarious calibration and algorithm validation (Fig. 1). OSPREy system configurations are based on EPIC radiometers, which have a cluster of microradiometers (Morrow et al. 2010a) combined with a spectrograph to increase spectral resolution, primary and secondary thermal regulation to enhance accuracy, and other unique features (Sect. 1.3).

As noted earlier, legacy sensors were built primarily for specific light sources and sampling targets, whereas an OSPREy system has a tracker to allow sampling of a multitude of sources and targets. For brevity and specificity, an individual radiance (L) and irradiance (E) instrument from this so-called EPIC Multitarget Radiometer (EMR) product line is denoted as EML and EME, respectively. This same naming approach is also used for a radiance and irradiance sensor within the OSPREy Transfer Radiometer (OXR) instrument class as the OXL and OXE, respectively.

The system configuration for the development activity (Fig. 1) has the following design elements and capabilities:

- Two duplicate EMR sensor pairs intercompared to enhance data quality and minimize temporal gaps (Sect. 1.5.5.2), recalling that intracomparisons are possible within an instrument with two overlapping detector systems;

- Programming scenarios (Sects. 1.3.2 and 8.6) preventing any loss of data products if one or more radiometers in a set malfunctions (some of the intercomparison capabilities will be lost);

- Extensively characterized and intercompared calibration facilities for the radiometric sensors (App. C);

- Three EML or EME calibration methods, wherein two are based on lamps (SIRCUS calibration transfer to a lamp with an OXE and a FASCAL lamp calibration) and one based on the Sun (Langley method);

- Traceability to NIST with the OXR, which is also based on enhanced COTS instrumentation (Chap. 2), plus a lamp library (Chap. 6) is used to help maintain the calibration of OXR instruments;

- A set of ancillary sensors for meteorological measurements useful to calibration and validation activities and for detecting hazardous conditions (App. D);

- Biospherical Shadowband Accessory for Diffuse Irradiance (BioSHADE) accessories on the irradiance sensors support atmospheric measurements (App. E and Morrow et al. 2010a);

- A pointing and tracking unit (Chap. 5) to provide the needed metrology for sea and sky radiance measurements (App. A), plus Sun and Moon data products;

- Monthly calibration monitoring in the field with a portable light source;

- Autonomous operations using hybrid (e.g., solar and wind) power and COTS data telemetry (App. F); and

- Prototype testing at a controlled and easily accessed site (App. G) and operational deployment on an offshore structure to reduce infrastructure costs and enhance survivability (App. H).

OSPREy systems are complex with many nuances to understand. To aid the reader, an FAQs section is provided.

In addition to developing hardware, an objective of the OSPREy activity is to develop a well-documented method for providing high-quality calibration and validation data

S.B. Hooker, G. Bernhard, J.H. Morrow, C.R. Booth, T. Comer, R. Lind, and V. Quang
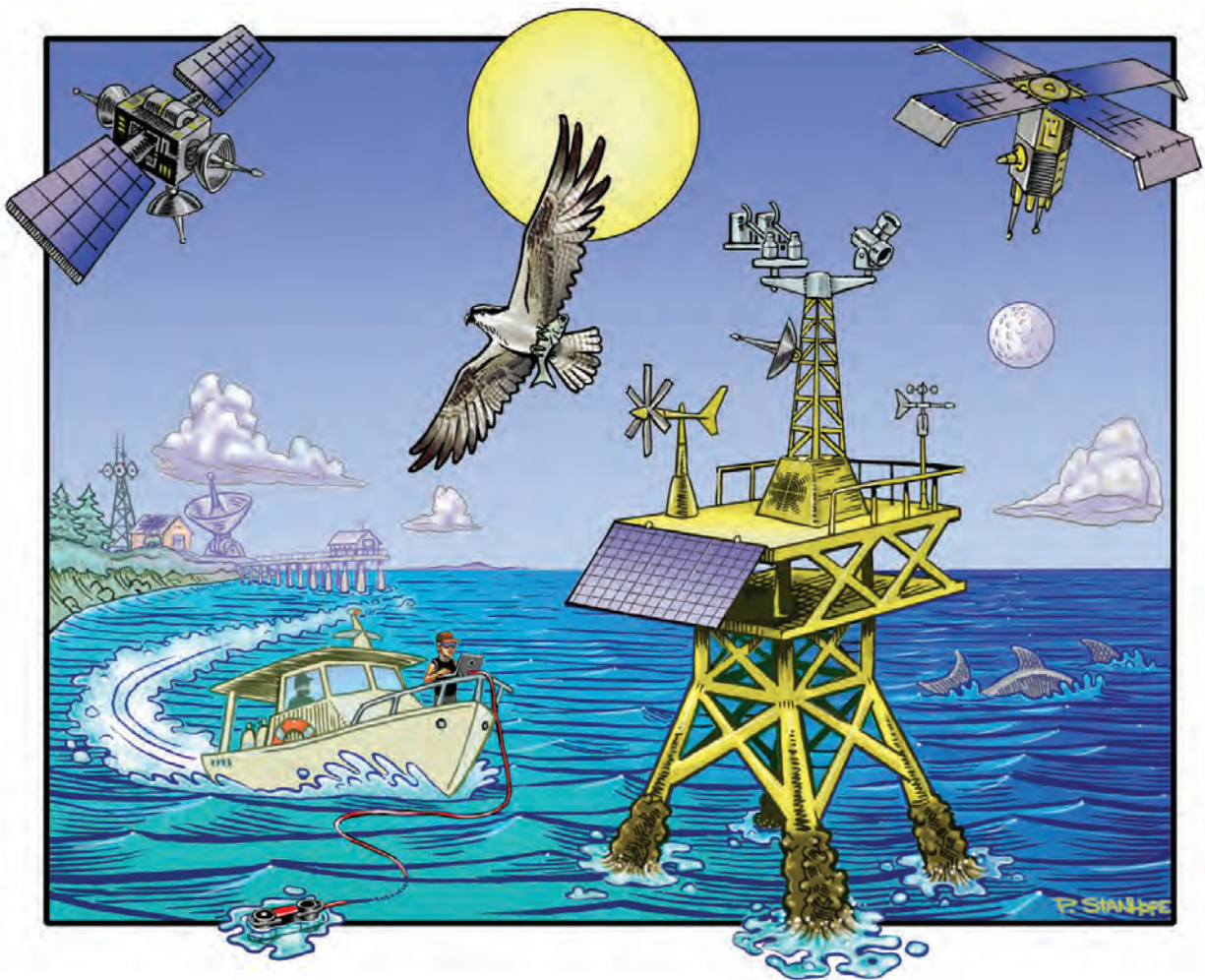
Fig. 2. Deployment of the OSPREy system with many of the components required for operations: two EMR dyads at the top of an offshore tower measuring the atmosphere and the ocean; an ocean color satellite (SeaWiFS) sampling the on- to off-shore gradient (green to blue) in productivity; the Sun and Moon as calibration targets for SeaWiFS and OSPREy; a telecommunications satellite for data telemetry from the platform sensor suite (including meteorological sensors), which are all powered by solar panels and a wind generator; a shore-based calibration and logistical support facility, including test capabilities at a pier; and monthly validation (including in-water AOP profiles) and maintenance visits with a small boat.

from remote (offshore) platforms. The important subelements of this development are an extension of the sea-truth data collection into the SWIR domain to support future NASA missions; a capability for producing atmospheric, in addition to oceanic, data products; and the incorporation of a stronger methodology for calibrating radiometers used in satellite calibration and validation (App. I).

The improved calibration approach helps ensure the uncertainties in the measurements are properly minimized (App. J). The adopted technique—the production of a transfer radiometer—involves a shift in methodologies from lamp-based to detector-based references used for calibrating field radiometers, which is more aligned with current practices at NIST. Another aspect of the main objective is the production of a protocol that can provide the needed parameters, complete with analysis and quality-controlled data delivery, at significantly lower costs. A summary de-

piction of two EMR dyads deployed on a platform is presented in Fig. 2 (recalling that platform-induced perturbations must be avoided, as described in App. K) with an anticipated third spare set of calibrated sensors available for deployment if needed on the monthly maintenance visits (not shown). An example of an appropriate site is presented in App. L.

1.3 Sensor Descriptions

The enhancements to the COTS sensors to produce EMR sensors involves the following:

1. The newest three-gain-stage microradiometer design (Chap. 2);

2. Channels in the SWIR domain for applicability to future missions with a modified cosine collector and new detector filter combinations;

11

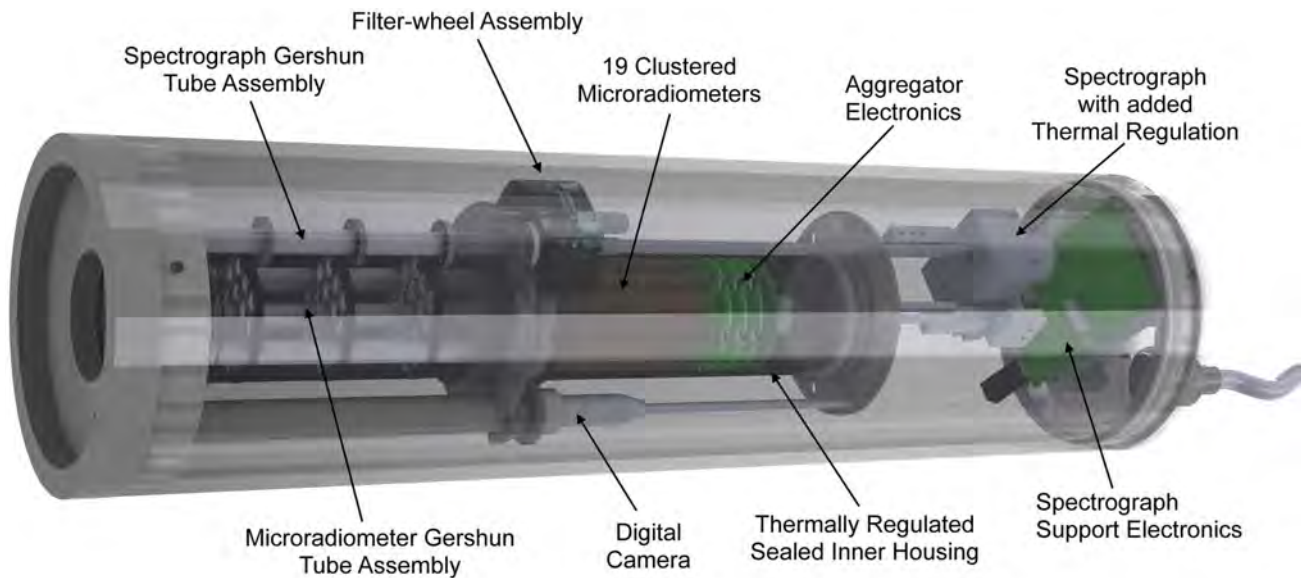**Fig. 3.** An EMR configured for radiance measurements, or EML, shown without a shroud and revealing the 19 microradiometers arranged in a central cluster, which is thermally regulated, with the Gershun-tube assembly to the left and the aggregator electronics to the right. The spectrograph with thermal regulation connects to a nine-position, filter-wheel assembly with a fiber-optic cable and has its own Gershun-tube assembly. The digital camera has an exit aperture on the other side of the filter-wheel assembly. The end cap also contains the spectrograph support electronics.

3. A new diffuser design for the irradiance sensors permitting a single cosine collector (Chap. 3) to cover the UV to SWIR spectral domain (290–1,670 nm);

4. Modification of the radiance entrance optics for a smaller FVA of 2.5° (Chap. 4) in compliance with sun photometry requirements (WMO 2003);

5. A spectrograph with an optical fiber front-end sampling through the entrance optics (Chap. 7);

6. Thermal stability control to increase filter and detector stability and reduce drift;

7. A pressure transducer to monitor the internal pressure of the positively-pressurized, dry-nitrogen atmosphere of radiometer housings;

8. An integrated camera for locating the Sun and Moon (in lieu of a quadrant detector), as well as verifying the condition of all targets, i.e., cloud-free solar and lunar disks, cloud presence in sky data, and sea surface debris or foam detection (although an irradiance sensor can also detect if clouds are obscuring the solar and lunar disks†); and

9. A nine-position, filter-wheel assembly positioned in front of the spectrograph fiber optics to provide hyperspectral polarimetric measurements (three polar-

ized filters), direct-Sun viewing (ND filters), stray-light correction (395 nm cut-on filter), and dark current measurements (opaque disk).

All but the last two items are also incorporated into the functionally similar OXR instruments, which are designed for application in the calibration laboratory. Aspects of the very last item are also provided by an anticipated all-sky camera for OSPREy systems.

An engineering drawing of an EML (radiance) sensor is presented in Fig. 3. An irradiance sensor has only 18 aggregated microradiometers—as do all OXR units—because one of the microradiometer positions is replaced with the fiber optics for the spectrograph. An irradiance sensor does not have the filter-wheel assembly or the integrated camera (as well as the Gershun-tube assembly).

1.3.1 Hardware

The addition of the spectrograph permits sampling of the spectrum in regions not covered by the filtered detector channels, and allows the spectrum of calibration sources to be scanned for unwanted emission lines. Furthermore, *the advantage of the higher resolution of the spectrograph can be combined with the superiorities of the fixed wavelength microradiometers—greater dynamic range, lower stray light, improved SNR, and higher scan speed—to provide a sensor combination superior to either of the individual constituents alone.*

Future satellite missions are planned that will push the spectral coverage toward both shorter wavelengths, as well

---

† The direct irradiance in the long wavelengths changes dramatically when clouds move in front of the Sun or Moon. By monitoring changes in the 1,640 nm channel when pointing at the Sun or Moon, a quantitative measure for cloud contamination is obtained.

as out into the SWIR region. To gain experience with this expanded spectral requirement, the complete band set for both types of prototype EMR sensors is as follows: 340, 380, 412, 443, 490, 510, 532, 555, 589, 625, 665, 683, 710, 780, 875, 1,020, 1,245, and 1,640 nm. The EML sensor has an additional 395 nm channel.

Environmental control is critical for longevity of interference filters, in particular, and electronics, in general. Because interference filters are composed of complex layers of differing materials, some mismatch in coefficients of expansion are inevitable; oxygen can also cause degradation through oxidation. For sensors built with MMS technology, the interference filters are manufactured with ion deposited TiO_2, which BSI has found to have superior—although not perfect—stability. To improve upon this stability, two enhancements are used: a) protecting against temperature transients by using custom thermal regulation from additional insulation and a temperature controller; and b) maintaining an internal atmosphere devoid of oxygen and moisture, which is made possible with hermetic seals and internal pressure monitoring.

The electronics are installed in a weatherproof enclosure, and selected for low power dissipation to avoid active cooling requirements. OSPREy dyads are controlled by ruggedized microprocessors selected for low power consumption. The microprocessors are controlled by a master computer, that coordinates the measurements of all sensors (Sect. 1.3.2), stores the data, and transfers it via the Internet. If no high-bandwidth Internet connection exists (e.g., on a remote platform), data can be written to an external hard drive which is swapped during monthly visits.

An OSPREy system is monitored by a security camera known as an *IP camera*, because it connects directly to an Internet connection. The camera is mounted above the plane of the EMR sensors (several meters away and not in the direct-Sun path), and is able to zoom in to inspect both radiance windows and irradiance collectors for signs of contamination. The camera can generate an event (start a recording and e-mail a photo) when something moves in the field of view (FOV). The degree of motion can be set, and it should be able to respond to bird activity, unauthorized visitors, etc. Prior to site visits or in the event of system failures, it can aid in diagnosing problems (e.g., a radiance sensor does not point correctly).

The camera also addresses a coastal sampling problem: towers and buoys are known by fisherman as fish attraction devices (FADs), because they attract fish. Having the camera record the ocean viewed by the radiometer can help explain anomalous measurements. Furthermore, it should enable engineers back at BSI to aid in site repairs or monitor site visits if local staff are used.

1.3.2 Software

The OSPREy system is designed with a variety of sampling modes optimized for coincident measurements during stable illumination and satellite overpass. Additional modes are used for producing the greatest number of quality assurance (QA) and quality control (QC) opportunities. For example, intercomparing data from the various radiometers, checking their calibration via the Langley method, and retrieving secondary data products, such as AOD. A summary of the modes in each sampling scenario is provided in Table 1.

Table 1. Examples of when each operational mode would be executed as a function of the anticipated sampling scenario.

Scenario	1	2	3	4
Night (nominal radiance)				×
Satellite overpass (±60 min)	×			
Overcast (homogeneous)	×	×		
Clear-sky (no overpass)	×	×	×	
Overcast (night, irradiance)				×
Rain or extreme weather				×

During a satellite overpass, operation would be primarily mode 1, which is the usual mode for $L_W(\lambda)$ measurements. This requires sky, $L_i(\lambda)$, and sea, $L_T(\lambda)$, observations at the appropriate geometry with respect to the Sun, as well as the correct nadir and zenith metrology (recalling the previously established platform-perturbation avoidance criteria). Shadowband observations are used primarily to acquire the global irradiance, $E_d(\lambda)$, and the diffuse irradiance, $E_i(\lambda)$, from which the ratio of direct-to-global irradiance can be computed†. The latter is useful in the derivation of atmospheric data products.

During other clear-sky conditions, modes 2 and 3 would be run alternatingly. During overcast conditions, specialized versions of mode 2 would be executed, viewing either the overcast sky or the sea. After an episode in this mode, operation would continue with mode 1. Mode 4 is primarily associated with scenarios when the sensors would be stowed, e.g., during severe weather.

During platform visits, additional modes would be activated to facilitate sensor evaluations (e.g., the portable light source) and calibrations. Additional modes, either to increase the data products or add additional redundancy, can be added for special experiments (e.g., characterization of skylight polarization).

1.4 Data Products

The field radiometers used in an OSPREy system measure quantities that can be directly compared with satellite data, as well as secondary products, which can be used

---

† The global irradiance is the sum of the direct plus diffuse irradiance. The direct beam, $E(\lambda)$, must be multiplied by the cosine of the solar zenith angle, θ_s, to obtain the radiation for a horizontal surface. Omitting the wavelength dependence for brevity, $E_d = E\cos(\theta_s) + E_i$, and the ratio of direct-to-global irradiance is $E/E_d = (1 - E_i/E_d)/\cos(\theta_s)$.

for atmospheric corrections of satellite retrievals. The full suite of data products are partitioned according to their radiometric sources.

1.4.1 Stationary Sensors

The primary data products of the stationary radiometers are downward global, diffuse, and direct (global minus diffuse) irradiance between 340–1,640 nm. The spectrograph integral to irradiance radiometers measures the solar spectrum from 305–785 nm with a resolution of 7 nm, and the spectrograph integral to radiance radiometers measures the solar spectrum from 305–1,100 nm with a resolution of 9 nm. When occluding the Sun, a shadowband also blocks a portion of the sky. The resulting systematic uncertainty can be quantified by additional measurements where the shadowband is positioned at $\pm 10°$ away from the solar disk. This method is routinely applied for correcting measurements of rotating shadowband radiometers (Harrison et al. 1994 and Wesely 1982). A new and more accurate correction method was recently developed (Bernhard et al. 2010), whereby the shadowband is moving at a constant rate over the cosine collector. This method is used with all OSPREy shadowband units.

Secondary data products include AOD and cloud optical depth, which are estimated from the difference of global measurements for overcast and clear skies. The clear-sky reference can be estimated from long-term measurements or from radiative transfer (RT) calculations. The latter method is well established and has been applied to measurements of multifilter radiometers (Dahlback 1996) and spectroradiometric measurements (Bernhard et al. 2004).

1.4.2 Rotating (Sun-Tracking) Sensors

The primary data products of the radiometers on the sun trackers are water-leaving radiances, direct-normal Sun irradiance, and sky radiance for arbitrary zenith and azimuth angles. Secondary data products include the AOD, aerosol single scattering albedo (SSA), total column, and precipitable water vapor (PWV). The ratio of direct-to-global irradiance can be calculated by comparison with global irradiance measured by the stationary radiometers. AOD is determined via the Langley technique or by applying the Beer-Lambert law to individual direct-normal measurements. Both methods are well established (Schmid and Wehrli 1995, and Schmid et al. 1999).

Aerosol Ångström parameters are calculated from AOD measurements. Aerosol SSA is calculated from sky scans along the principal plane and almucantar. Inversion algorithms were developed for the AERONET activity (Holben et al. 1998) network and can be adopted for OSPREy (Dubovik and King 2000). These algorithms also allow for the calculation of higher-level aerosol data products such as the aerosol scattering phase function, the aerosol refractive index (real and imaginary parts), aerosol size distributions,

and the radiative forcing induced by aerosols. Using the polarization measurement capability of the spectrograph, the polarization (Stokes vector) of sky and total sea surface radiance can be determined. Alternatives for calculating the SSA using look-up tables are being explored.

1.5 Quality Assurance Plan

Providing high-quality data with minimal uncertainties requires a comprehensive QA and QC plan. The OXR instruments (Chap. 6) are initially characterized by BSI, calibrated by NIST, and a rigorous uncertainty analysis is performed (Sect. 1.5.1 and App. J). The calibration is then transferred at BSI to other EMR instruments, as well as to a set of lamp standards (Chap. 6) to preserve the NIST scale of irradiance over the time span of the project. All field radiometers, plus other major hardware components, are redundant. The radiometers are automatically intracompared (microradiometers and spectrograph) and intercompared (one instrument versus another) on a daily basis to detect performance outside of selected control limits (e.g., elevated dark currents or calibration drifts) on the day of occurrence (Sect. 1.5.3.). A portable light source is used to monitor the radiometric calibrations during monthly site visits (Sect. 1.5.4).

In addition, natural targets including the Sun, Moon, clear sky, and homogeneous clouds are regularly scanned to verify correct operation across the dynamic range of the sensors (Sect. 1.5.5). The applicable above-water data products are also intercompared with in-water AOP products produced during monthly maintenance visits, short-term intercomparisons with existing field sensors (e.g., a SeaPRISM unit), as well as radiometers used in other networks for cross-network performance review (Sect. 1.5.5.2). Software will ultimately be implemented that automatically generates alerts if individual instrument parameters are outside control limits, or if sensor measurements do not agree within control limits.

Finally, data will be reviewed by a scientist once per week, corrected for known systematic uncertainties, compared with results from RT models, and reprocessed if necessary. Performance metrics will be published in operations reports available on the Internet, and in peer-reviewed papers for external review. The QA and QC plan will be based on experience gained during 20 years of operating the UVSIMN for the NSF (App. M).

1.5.1 Uncertainty Budget

The uncertainty of irradiance and radiance measurements of OXR and EMR sensors is composed of uncertainties related to the following:

1. Responsivity calibrations of the OXR by the NIST SIRCUS facility;

2. OXR calibration transfers to EMR sensors (App. I);

3. Changes in responsivity over time;

4. Collector contamination (fouling);

5. The non-ideal cosine response of irradiance diffusers;

6. Transferring laboratory calibrations to field measurements (App. I) of $E_d(\lambda)$, $E_i(\lambda)$, sky radiance $L_i(\lambda)$, and the total radiance at the sea surface $L_T(\lambda)$ for a prescribed viewing angle (usually $40°$ or $45°$);

7. The nonlinearity of radiometer signals; and

8. Photon and electronic noise.

Additional uncertainties arise from the conversion of $L_T(\lambda)$ and $L_i(\lambda)$ to $L_W(\lambda)$, with the latter defined as the radiance emerging from the sea at nadir viewing. Uncertainties in this conversion procedure are related to the following:

9. Corrections for natural reflectance sources (e.g., glint from Sun, sky, and clouds);

10. Corrections for anisotropy of the upwelling radiance due to different viewing geometries for L_T and L_W;

11. Perturbation from the observation platform; and

12. Surface waves plus other environmental effects.

A quantitative summary of the uncertainty contributions by all 12 of these sources is provided in Table 2, and additional detail concerning the computation of uncertainties is given in App. J. The combined uncertainties range is estimated to be 1.6–3.1%, with or without the contribution of environmental factors, which meet the specifications required by the Protocols.

Table 2. Uncertainty budget for the OSPREy measurement parameters and principal radiometric data product (L_W). All uncertainties refer to a 95% confidence level.

Uncertainty Source	E_d	E_i	L_i	L_T	L_W
1. SIRCUS calibration	0.2	0.2	0.2	0.2	0.2
2. Calibration transfer†	0.2	0.2	0.2	0.2	0.2
3. Responsivity changes	1.0	1.0	1.0	1.0	1.0
4. Collector contamination	2.0	2.0	1.0	1.0	1.0
5. Non-ideal cosine‡	1.0	2.0			
6. Calibration transfer§	0.5	0.5	0.5	0.5	0.5
7. Nonlinearity	0.5	0.5	0.5	0.5	0.5
8. Photon and electronic noise¶	0.1	0.1	0.1	0.1	0.1
9. Surface reflectance					0.7
10. Platform perturbation					0.3
11. Anisotropy correction					0.6
12. Environmental factors					2.5
1–11 *Quadrature sum*	2.6	3.1	1.6	1.6	1.9
1–12 *Quadrature sum*	2.6	3.1	1.6	1.6	3.1

† Transfer of the SIRCUS calibration to BSI.

‡ For solar zenith angles less than $70°$; the E_i value is larger in the SWIR domain where the diffuse irradiance is very small.

§ Transfer of a laboratory calibration to the field.

¶ The E_d and E_i values are larger for the SWIR channels, because the diffuser is thicker.

1.5.2 Absolute Calibrations

Although not completed in time for this publication because of difficulties with personnel, scheduling, and equipment, calibration of the OXE instrument was initiated at the NIST SIRCUS facility as part of the development activity. The calibration of the OXR and EMR sensors will be published as a separate report (Bernhard et al. 2012). A subsequent calibration of the OXL instrument is anticipated. A principal purpose of the OXE unit is to calibrate six 1,000 W FEL lamps, which have three functions: a) preserving the SIRCUS scales of irradiance over time, b) calibrating other EMR sensors, and c) monitoring and correcting temporal changes in the calibration of field radiometers.

Using calibration information obtained in the laboratory, conversion factors are calculated to convert the radiometric raw data obtained *in situ* (typically measured in volts or digital counts) to spectral irradiance or radiance. The method takes into account the change of the solar spectrum within the bandpass of the individual instrument channels, as well as the variation of this change as a function of atmospheric constituents (e.g., ozone and water vapor), sensor biases such as residual cosine error, as well as components in the water (e.g., Chl a and CDOM concentrations).

OXR instruments are used on a recurring basis to monitor the calibration of EMR instruments deployed in the field, when the latter are returned to BSI for calibration and maintenance. The absolute calibrations of field radiometers in the field are checked on a monthly basis with the portable light source, and the portable light source is checked before and after field use with the OXR sensors. Daily checks for changes in responsivity are performed by comparing the various EMR instruments. The number of comparisons depends on the system configuration. The simplest is an intracomparison of the spectrograph and microradiometers, followed by redundant sensor intercomparisons (i.e., two types of instruments that are the same), and then two types of instruments that are different (i.e., radiance and irradiance), but can be used to produce the same data product. More details on absolute calibrations and the transfer of lamp calibrations to solar measurements are provided in App. I.

1.5.3 Hardware Redundancy

Redundancy is a central aspect of the built-in reliability of the OSPREy system being built for the development activity. In addition to the functional security duplicate hardware provides (radiometers, shadowbands, and tracking systems), a high level of intercalibration between the instruments can be supported by replicating the data products with simultaneous individual measurements. The latter is effective in calibration QA, and also in detecting most kinds of sensor drift, mechanical problems in the tracking

mechanisms, and certain types of system wiring and power problems.

An additional layer of functional redundancy is provided if a third set of fully characterized radiometers is available for exchange during monthly maintenance and sampling visits, either in response to unanticipated problems or scheduled replacement (to minimize the chance of failures). Rotating new sensors into the system allows a sensor set with a fresh calibration to be automatically compared with the older sensors. Note, when multiple OS-PREy systems are deployed in the future, the third set of radiometers (and other spare components) can be shared between installations.

To control cost and complexity, not all components of an OSPREy system are redundant, because commercially manufactured components such as personal computers, satellite downlink terminals, and power distribution systems can be designed and tested to ensure a reasonable degree of robustness. In this case, computers with redundant, high-quality power supplies and a redundant array of independent drives (RAID) are used. Power generation redundancy can be designed into the solar and wind components so that a failure in one part of the power system still permits partial OSPREy system operation at reduced power levels.

1.5.4 Portable Light Source

For lengthy deployment time periods, a portable light source is useful for monitoring instrument response in the field. For OSPREy, the source needs to be usable with both the radiance and irradiance EMR sensors, over the full spectral range of interest (UV–SWIR). To facilitate use on a remote platform, it needs to be fully self-contained (except power), and able to be modified to match the OS-PREy kinematic mounts. In addition to the support electronics (regulated power supply), the portable source needs monitoring photodetectors to ensure the output is stable and repeatable.

Several portable sources have been produced, which are based principally on the SeaWiFS Quality Monitor (SQM), which was developed with NIST more than a decade ago (Johnson et al. 1998). Although shown to be capable of monitoring radiometric performance to within 1% (Hooker and Aiken 1998), the SQM design was not as portable as desired for OSPREy systems, and it did not have sufficient flux in the UV and blue parts of the spectrum for the wavelength range of interest now.

A likely portable source to be used for the OSPREy activity is the Portable Universal Radiometer Light Source (PURLS) manufactured by Hydro-Optics, Biology & Instrumentation Laboratories, Inc. (Tucson, Arizona). The PURLS device uses light-emitting diodes (LEDs) to provide a tunable output with a whiter spectrum than can be achieved with an incandescent source. It provides sufficient flux across 340–875 nm, but does not support the UV-B and SWIR wavelength domains in its default configuration.

The PURLS unit also has minimal power consumption (150 W for full-spectrum output), rugged and weather-resistant construction, minimal weight (15 kg), small size ($30 \times 30 \times 30$ cm^3), and easy adaptability to both irradiance and radiance sensors. It has an "auto-adjust" feature to improve its long-term stability. Preliminary tests indicate that the feature can keep the output constant to within $\pm 0.2\%$ over a time period of six months. The device is currently still under evaluation (results will be published in a subsequent report).

1.5.5 Product Validation

Validation of the various radiometers and their corresponding data products are conducted during all test deployments (App. G), where possible, and in particular during the operational testing phase (App. H); the latter includes a platform-perturbation mapping of the selected offshore structure (App. K). The primary sources of validation data are natural targets under a variety of illumination conditions, to ensure the full dynamic range of the sensors are validated, plus above- and in-water intercomparisons with independent observational systems.

1.5.5.1 Natural Targets

The stability of the EMR field instruments is monitored with the portable source plus regular scanning of natural targets including the Sun and the Moon, as well as homogeneous skies during twilight, overcast, and cloud-free conditions. By measuring the direct-Sun irradiance with the tracker-mounted radiometer and the shadowband radiometer at different air masses, the irradiance at the top of the atmosphere, $E_0(\lambda)$, is regularly calculated based on the Langley technique (Schmid and Wehrli 1995). This method is operationally used by the UV monitoring of the U.S. Department of Agriculture (USDA) network for tracking calibration changes of rotating shadowband radiometers over time (Slusser et al. 2000, and Bigelow and Slusser 2000), and can identify changes in responsivity of approximately 1% per year.

This same technique is also applied to direct-Moon measurements for monitoring stability at low light levels. Measurements at twilight, low Sun, and overcast conditions are used to detect any changes in the linearity of the radiometers. For example, consecutive measurements with different gain settings allow the detection of drifts in amplifier offsets and scale factors. By scanning across the solar disk in small angular increments, the tracking accuracy of the sun tracker is regularly checked.

1.5.5.2 Validation Intercomparisons

Because EMR radiometers are capable of making a wide variety of measurements, there are necessarily a diversity of options for validating OSPREy measurements. The

following instruments can be used to provide independent observations of EMR measurements:

- The SUV-100 spectroradiometer, which is a part of the UVSIMN and installed at the BSI rooftop facility. The instrument measures $E_d(\lambda)$ between 280–600 nm with a 1.0 nm bandwidth (Booth et al. 1994). Data are corrected for the instrument's cosine uncertainty and have a wavelength accuracy to within 0.02 nm (Bernhard et al. 2004).

- A sun photometer designed to measure solar irradiance and AOD. Possible applicable instruments include the CIMEL CE-318 photometer of the type used in the AERONET activity and a Middleton Solar SP02 instrument used by the NOAA Earth System Research Laboratory (ESRL).

- The Multi-Filter Rotating Shadowband Radiometer (MFRSR) for measuring global and diffuse irradiance at seven channels in the visible domain built by Yankee Environmental Systems (Turners Falls, Massachusetts) to validate the BioSHADE approach.

- An above-water radiometric sampling system such as an automated SeaPRISM or the Biospherical Surface Optical Reflectance System (BioSORS), which is manually pointed (Hooker et al. 2010a).

- An in-water system called the Submerged Biospherical Optical Profiling System (SuBOPS), which is radiometrically identical to BioSORS (Hooker et al. 2010b), or the newer Compact-Optical Profiling System (C-OPS), which is built from microradiometers (Morrow et al. 2010b). These instruments are floated away from the deployment platform to avoid perturbations to the light field. The buoyancy can be adjusted using a so-called *hydrobaric* system for a very slow descent rate and the vertical orientation can be trimmed using counterbalances (floats, weights, and the sensor orientation), which provides excellent vertical resolution (approximately 1 cm or less) and a capability to collect data in shallow water.

All these instruments exist, but the principal automated instrument in use to derive $L_W(\lambda)$ using the above-water L_T and L_i approach is the eight-channel SeaPRISM unit.

1.5.5.3 Comparative Technology Assessment

Following are the OSPREy technologies that enable it to have significantly better performance than the technologies presently available for validation:

1. EML microradiometers measure all wavelengths simultaneously more than an order of magnitude faster, which allows L_T filtering for surface wave effects (a SeaPRISM unit has a data sampling rate that is too slow for significant filtering).

2. For two radiance sensors in a dyad (Fig. 1), L_T and L_i can be measured simultaneously, which reduces glint correction uncertainties. For one radiance sensor (a SeaPRISM analog), L_T and L_i are measured to within 5 s, because of the high angular velocity of the tracker ($50° \, s^{-1}$).

3. OSPREy systems permit seamless integration of a solar reference. By measuring $E_d(\lambda)$ rather than estimating it from direct-Sun data (as is the case with SeaPRISM), normalized $L_W(\lambda)$ data products (e.g., the remote sensing reflectance, R_{rs}), have smaller uncertainties.

4. The use of InGaAs detectors for the SWIR domain allows OSPREy channel options to span 340–1,640 nm (the CE-318 uses a single silicon detector, which is radiation insensitive beyond 1,100 nm).

5. OSPREy spectrograph measurements offer a more accurate mechanism to interpolate between the measurements of the filter wavelengths than is possible with SeaPRISM.

6. OSPREy has three polarizers (0, 45, and 90°) for sky and sea Stokes vector determinations (SeaPRISM can have one polarization wavelength, but that reduces the wavelengths to six).

The only commercial shadowband unit that is similar to an OSPREy EME instrument is the aforementioned MFRSR from Yankee Environmental Systems. The MFRSR is used in the USDA UV-B Monitoring and Research Program (Harrison et al. 1994), but OSPREy shadowbands have a higher sampling rate, larger spectral range, more channels, and larger dynamic range.

Chapter 2

Application of Microradiometers to EMR and OXR Sensors

Randall N. Lind, Charles R. Booth, Germar Bernhard, and John H. Morrow
Biospherical Instruments Inc.
San Diego, California

Stanford B. Hooker
NASA Goddard Space Flight Center
Greenbelt, Maryland

Abstract

Microradiometers are small, fast, reliable, and cost-effective radiometers that are composed of a filter, photodetector, wide-range electrometer, analog-to-digital converter (ADC), microprocessor, and digital interface. Microradiometers were originally developed for in-water profiling systems and were adapted to the requirements of OSPREy applications by increasing their dynamic range to over 10 orders of magnitude with excellent (better than 1%) linearity over this interval. The devices now support measurements of both very bright sources like the solar disk and comparatively very dim sources like the ocean, calibration targets, and lunar disk. The circuitry was further modified to handle both silicon diodes for UV-VIS measurements and InGaAs photodetectors for measurements in the SWIR domain. The Multiple Microradiometer System (MMS) architecture allows clusters of up to 19 tightly-packed microradiometers to be networked together using an aggregator, such that the multitude of sensors can be controlled as a solitary device. The aggregator also provides an interface to external devices, such as temperature controllers and filter-wheel stepping motors used in EMR instruments. Compared to legacy platforms, the new technology offers lower cost, fully automated manufacturing, higher reliability, smaller size, and higher detector densities while maintaining excellent performance characteristics.

2.1 Introduction

The initial plan for the OSPREy development activity was to build the needed radiometers by enhancing the existing capabilities of the PRR-800 class of instruments from BSI. Although developed in the late 1990s, the mostly handmade PRR-800 sensors and associated sampling systems continue to provide outstanding value in terms of the sampling speed, measurement accuracy, and dynamic range. While the OSPREy activity was under review, BSI had just completed development of a new approach to radiometer design—the microradiometer—which was funded by the NASA Small Business Innovation Research (SBIR) program.

Priority objectives in the microradiometer development included lower cost, fully automated manufacturing with built in QA and QC functions, potentially higher reliability (by reducing the number of handmade components), smaller size, and higher detector densities (or packing efficiencies). Details concerning the development of the microradiometer (Fig. 4) are documented by Booth et al. (2010), so only summary information is presented here.
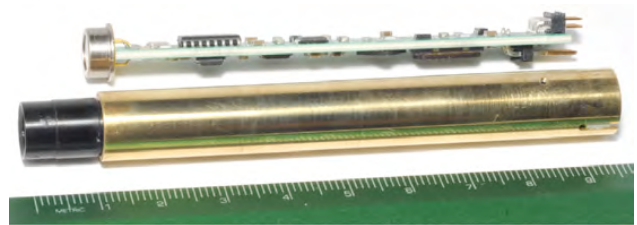
Fig. 4. A side view of a microradiometer (top) showing the two-sided circuit board design, and a sleeved unit with fore optics attached (bottom). The ruler is marked in centimeters.

At the start of the OSPREy activity, microradiometers were being commercially manufactured and had been successfully integrated into the Compact-Optical Profiling System (C-OPS), a NASA in-water profiling instrument (Morrow et al. 2010b). An engineering analysis was performed to determine if the OSPREy activity would be better served using microradiometers, the newest advanced technology, or to use PRR-800 legacy technology. The comparison was approached from the perspective of managing risk. The microradiometers were thought to be more
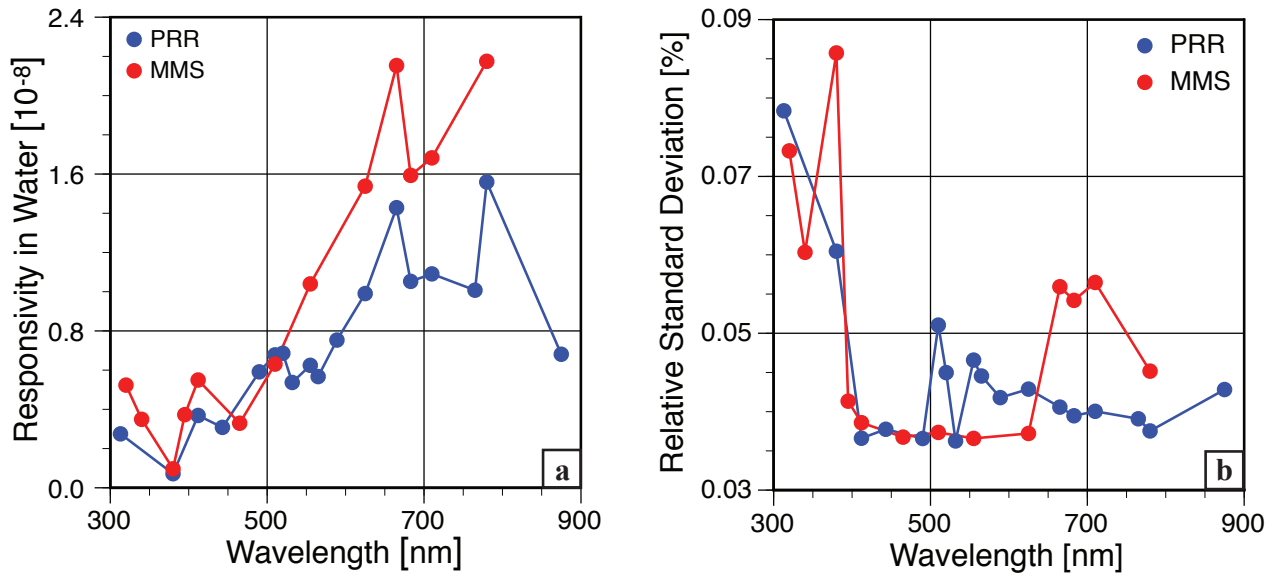
Fig. 5. A comparison of legacy PRR-800 performance with an MMS cluster: **a)** in-water radiance responsivity (in amps per $\mu W\, cm^{-2}\, nm^{-1}\, sr^{-1}$), and **b)** the noise levels for radiance calibration.

capable, but riskier to use given how few systems had been built with them, whereas the PRR-800 sensors had been used successfully for more than a decade, but were less flexible to adapt to new requirements (e.g., the smaller size and packaging configuration of the microradiometer architecture allowed somewhat smaller overall size, and enabled full integration of spectrograph and filter radiometers, particularly in the irradiance configuration).

The PRR and MMS systems have similar input optics and use similar filters and photodetectors, but substantially different electronics (Booth et al. 2010). The individual channels of the PRR electronics feature three electrometer gain stages sharing a single 16 bit ADC multiplexed to all channels. Microradiometers also feature three electrometer gain stages, but each detector has a dedicated 24 bit ADC, simplifying calibration, and enhancing stability. Although similar in expected performance, comparisons of the legacy PRR and new MMS technologies show the MMS to have somewhat better responsivity and similar noise characteristics (Fig. 5).

Between the start of the OSPREy development activity and the conclusion of the engineering analysis involving PRR and MMS capabilities, an increasing number of C-OPS instruments were sold to scientists. The emerging success and experience being achieved with C-OPS, and by extension with microradiometers, added to the list of advantages inherent in using the microradiometer as the basis of instruments for OSPREy systems. A significant practical advantage of the MMS architecture was it was mostly machine assembled and tested, so many of the commissioning problems experienced with handmade legacy sensors were not realized with microradiometer instruments. A simple consequence of the handmade versus machine-made approach is easily seen in Fig. 6, wherein the MMS

sensor (on the right) has no internal cabling. Consequently, it was decided to move the OSPREy activity ahead using microradiometers rather than the legacy PRR technology.
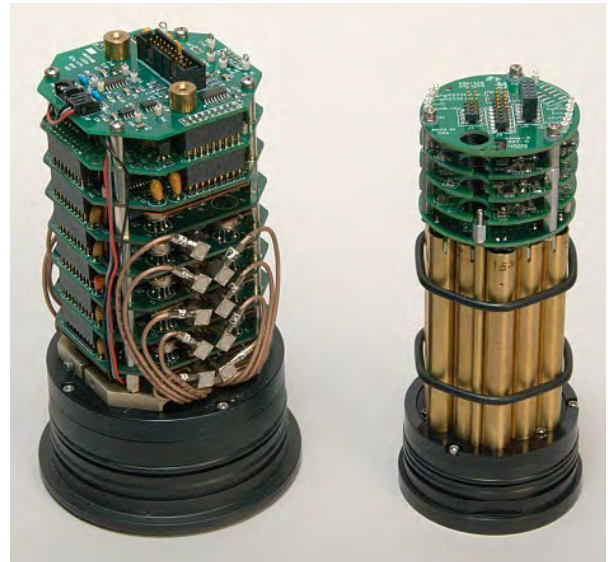
Fig. 6. A side-by-side comparison of a legacy PRR sensor (left) and a new MMS sensor (right).

2.2 Microradiometer Modifications

Several engineering tasks had to be addressed in order to adapt the MMS architecture to the design requirements for EMR and OXR sensors. These tasks included extending the signal range within the lowest resistor setting (i.e., largest signal) in the gain amplification, adapting the circuitry to handle SWIR detectors, and adapting the microradiometer support electronics to support additional tasks, such as temperature regulation and filter-wheel integration.

19

Operated over the SWIR and visible regions of the electromagnetic spectrum, EML sensors must be able to measure the sky radiance, the total radiance above the sea surface, the radiance of a reflectance plaque, as well as the direct solar and lunar irradiances. These applications require a dynamic range spanning more than nine orders of magnitude, with good linearity (less than 1% departure) and no saturation. The original microradiometer as implemented in C-OPS used two automatically selected gain stages. This limited the upper signal range, which would saturate if the sensor was pointed directly at the Sun. To extend the upper signal range, the current-to-voltage conversion front end of the microradiometer was redesigned to add a third gain stage.

Adding a third gain stage had several advantages: a) the factor between gains was reduced from 1,000 to 200, which decreased the stabilization time after a gain change; b) the voltages at which gains increase were raised by a factor of 2.5, resulting in a decrease of the medium and low gain offset uncertainty; and c) the photocurrent signal range was increased to accommodate 40 times higher saturating signal levels ($160\,\mu A$). The analog front end of the three-gain microradiometer was redesigned with different components, but the physical package outline and connections are identical.

The circuit architecture is very similar in the two- and three-gain microradiometers. The photodetector is connected to a high-performance operational amplifier. The amplifier is configured as a current-to-voltage converter, with the gain set using a resistor and capacitor combination that is selected with an analog switch. The resulting voltage is digitized by a 24 bit ADC normally running at 125 Hz. The three-gain microradiometer has an ADC resolution of $0.5\,\mu V$, and at maximum gain, a current resolution of less than 1 fA. A microprocessor controls the switch and ADC, implements autoranging, and calculates a running average.

By operating at 125 Hz, range changes can usually be made, and time can be allowed for settling, while maintaining an uninterrupted stream for multiple instruments, at sampling rates as high as 20 Hz. Before each reading is averaged, it is corrected for offset and gain and expressed as a floating point number, which is then added to the average. If a range change occurs during an averaging period, readings can be dropped while still being able to calculate and report an average, thereby minimizing data gaps at signal regions where gain changes occur. The firmware contains modes for automatically determining dark offsets at each gain, gain ratios when exposed to appropriate light levels, and configuring various operational modes, e.g., ranging mode, switch points, and other parameters. It is also possible to program the system for manual gain, different ADC sample rates ranging from 4–125 Hz, and sample averaging periods from less than 0.05 s to 60 s.

Both the two- and three-gain versions of the microradiometer contain a temperature sensor, and circuitry to monitor the supply voltages. When configured for radiance measurement at 490 nm, 1 s averaging, and using entrance optics with 14° field of view, a three-gain microradiometer has a detection limit of $0.14\,pW\,cm^{-2}\,nm^{-1}\,sr^{-1}$ and a saturation radiance of $8.5\,mW\,cm^{-2}\,nm^{-1}\,sr^{-1}$, corresponding to a dynamic range of approximately 6×10^{10}.

2.3 Linearity Tests

Linearity testing is particularly important with respect to the EMR and OXR instruments, because they must operate over an extremely large signal range. As an example, the signal measured by the 340 nm microradiometer channel when pointing at the direct Sun is approximately 5×10^6 times greater than the signal measured by the same channel when pointing at the laboratory source used for radiance calibrations (a reflectance plaque). At 700 nm, the signal from the direct Sun is about a factor of 3×10^7 larger than the signal generated by the water-leaving radiance. Microradiometers are typically linear over a range of larger than 10^9 as discussed below.

The principal apparatus for testing linearity was the so-called *lineator*, which consists of multiple LED light sources coupled to a fiber optic bundle with a three-in-four-out beam combining and splitting mixer. The multiple LED light sources are operated at intensities set by a 16 bit computer-controlled power supply, and each of the LEDs has a significantly different brightness when operated at the maximum level. One of the output fiber optics was coupled to a silicon photodiode of the same type used in microradiometers, and the output of that photodiode was digitized by a Keithley 6485 Picoammeter.

By controlling each individual LED, the signal level was varied over a range of approximately three decades. Using one LED, the test currents ranged from 10 pA to 1 μA (in subsequent testing, the test system was expanded to characterize 19 microradiometers over photocurrent ranges of 1 pA to 100 μA). Another source gave a slightly higher range, between 100 pA and 10 μA and spanned both range-change points. Linearity testing (Fig. 7) suggests increasing nonlinearity at signal levels greater than 10 μA, which is the maximum signal level achieved from the lineator. This level is 16 times smaller than the 160 μA saturation level of a three-gain microradiometer.

Linearity at higher light levels not supported by the lineator was tested using an apparatus based on a beam conjoiner principle (Sanders 1962). Two LEDs operating in constant current mode (sources A and B) were arranged on an optical bench such that the two beams would enter a 50% beam splitting cube, with both beams exiting through the opposite two sides of the cube. In theory, each exit beam receives 50% of the flux from each LED source. Shutters were installed so that the LEDs could remain on constantly during each test sequence in order to maximize stability. The shutters can independently block the beams of the two LEDs to measure the dark signal, the signal of either of the LEDs, or both LEDs.
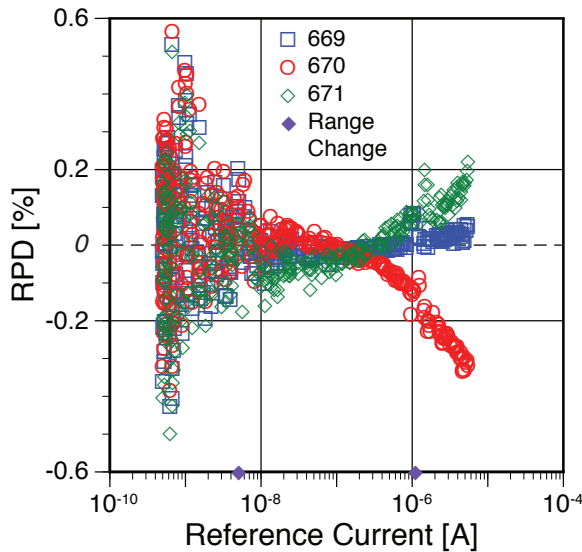
Fig. 7. Lineator test results for the mid-intensity source. Microradiometer gain change points are marked with diamonds on the x-axis.

If the device under test is linear, the net signal measured with both LEDs unblocked should be identical to the arithmetic sum of the net signals of the LEDs measured separately. By changing the intensity of the two LEDs and repeating the test, linearity can be tested with this apparatus over a dynamic range of approximately five orders of magnitude up to the saturation level.

A sample test result for a microradiometer equipped with a silicon detector is presented in Fig. 8, which indicates that the device is linear to within 1% between 20 nA and 160 µA (the highest point is on the verge of saturation).
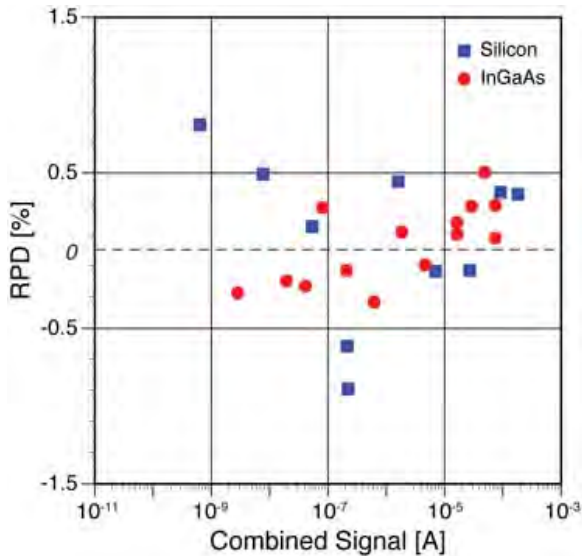
Fig. 8. Beam conjoiner linearity test results at high flux levels using silicon and InGaAs (SWIR) photodetectors.

Figure 8 also presents a similar result for a microradiometer equipped with an InGaAs detector using LEDs with a peak wavelength at 1,550 nm. The test indicates that the system is linear to within 0.5%. By combining the results of the lineator and the beam conjoiner, linearity could be examined over ranges from 160 µA down to signals approaching the noise level.

2.4 Microradiometer Clusters

Arrays of microradiometers are operated in conjunction with associated interface circuitry that is collectively referred to as an aggregator. The aggregator is a pivotal component of the MMS architecture, because in addition to providing the basic networking bus, an aggregator provides regulated +5 V digital and ±5 V analog supplies to the microradiometers, conditions the logic level data streams, and provides the Recommended Standard (RS) interfaces (RS-232 and RS-485).

An aggregator also provides measurements of sensor attitude (two-axis angular orientation), supply current and voltage, plus internal housing temperature and pressure. With respect to data reporting, aggregators coordinate all microradiometer data frames into a single data stream for acquisition. The latest model aggregator used with OXR and EMR instruments is considerably smaller than the original design (Fig. 9), and significantly smaller than could have been possible with the PRR-800 components.
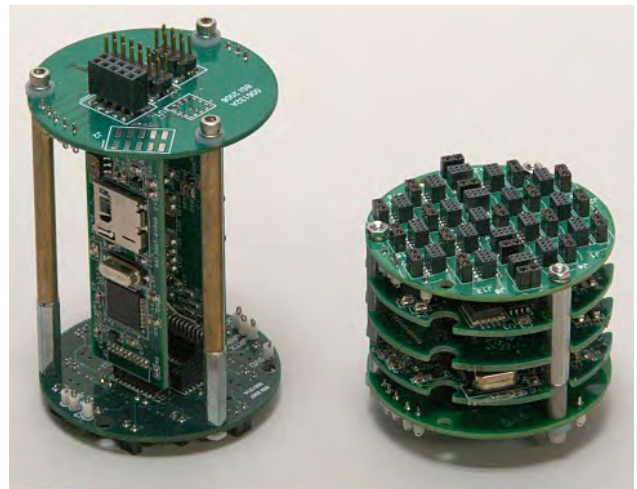
Fig. 9. The old aggregator (left) shown next to a new aggregator assembly (right) oriented to reveal an unpopulated 19-channel microradiometer backplane (top). From top to bottom, the boards under the backplane are as follows: power supply, microprocessor and communications, temperature and depth, and connections.

To support the OSPREy radiometric requirements, additional aggregator capabilities were added, including interfaces to external devices. For example, to support the integration of a spectrograph (Chap. 7), a programmable

voltage source was added to the aggregator. The source is used to set the target temperature of a precision temperature controller, which is used for temperature stabilization. To support the filter wheel that is integrated into radiance radiometers (Chap. 8), a motor driver and command set were incorporated into the aggregator. Lastly, the circuit board assembly that implements the aggregator functions was redesigned for a smaller form factor and to allow the spectrograph fiber optics to be integrated into the irradiance collector.

The power supply board creates all of the voltages necessary to run the sensor (+5 VDC digital, +5 VDC analog, and −5 VDC analog) and includes a pressure transducer that measures the internal housing pressure (to monitor the nitrogen backfill). The microprocessor- and communications board is the *brain* of the sensor and contains the RS-232 and RS-485 drivers. The temperature and depth board (so named because of the heritage that the first microradiometer sensors were for in-water sampling) includes two *microradiometer* circuits configured to measure high resolution temperature and depth (for above-water EMR sensors, the depth channel is converted into a second high resolution temperature channel). Finally, the connections board provides connection back to the deck box, as well as connection of the water temperature and depth transducers.

Chapter 3

SWIR Cosine Collector Design and Evaluation

Germar Bernhard and Randall L. Lind
Biospherical Instruments Inc.
San Diego, California

Stanford B. Hooker
NASA Goddard Space Flight Center
Greenbelt, Maryland

Abstract

The irradiance collectors used with EMR sensors require small cosine errors and high transmission for wavelengths within 305–1,640 nm (UV–SWIR range). To satisfy this objective, a new irradiance collector was designed by selecting diffuser materials optimized for this spectral range and by modifying the shape of the existing irradiance collector originally developed for the UV-VIS range of legacy sensors. Laboratory tests indicated that a composite diffuser made of one layer of generic polytetrafluoroethylene (PTFE) sheet and one layer of porous PTFE (pPTFE) material produces the best characteristics. The tests also confirmed that a small cosine error can only be achieved with a shaped diffuser (for instance, a diffuser with a trapezoidal cross-section). A numerical model was developed to optimize the dimensions of the composite diffuser (e.g., height, plus top and bottom diameters of the diffuser) and its support structure (e.g., diameters and heights of two shadow rings surrounding the diffuser). Based on the results of material testing and modeling, a prototype irradiance collector was manufactured and tested. For wavelengths in the UV-VIS range, the cosine error of the new collector is less than $\pm3\%$ for incident angles up to 75° and does not depend on wavelength and azimuth angle. Cosine errors at SWIR wavelengths are larger (e.g., -5% at 1,020 nm for an incident angle of 74°), but are still within acceptable limits for OSPREy applications.

3.1 Introduction

The EMR sensors used with the OSPREy activity include radiometers for measuring irradiance across the 305–1,640 nm domain—an unprecedented spectral range for a legacy sensor using a single optical collector. Ideally, these instruments should have a *cosine response*, meaning that the signal from the radiometer should vary with the cosine of the angle of incidence (defined as the angle between the normal vector of the fore optics and the direction of the light source to be measured). The fore optics of BSI production irradiance radiometers consist of a thin (e.g., 0.02 in) PTFE sheet acting as a *primary diffuser*, which is supported by a solid piece of quartz glass to maintain the geometric shape. A second PTFE sheet placed at the bottom of the quartz glass acts as the *secondary diffuser*, ensuring that the emission from the fore optics is independent of the azimuth direction of the source radiation.

Research has shown that PTFE sheet is an ideal material to construct diffusers for measuring solar light over the UV–VIS range, because of its good scattering properties, low absorption, high inertness, and excellent long-

term stability. The scattering properties of PTFE sheet, however, deteriorate rapidly for wavelengths longer than 600 nm. Thin sheets of PTFE become virtually translucent at SWIR wavelengths and cannot be used as diffusers beyond 1,000 nm. This chapter documents the research leading to the development of a unique new diffuser design, optimized for operation over the wavelength range of 305–1,640 nm.

3.2 Selection of Diffuser Material

Early engineering analyses concentrated primarily on using thicker pieces (e.g., 4 mm or several sheets) of PTFE material to compensate for the loss in scattering at longer wavelengths. The resulting design was used successfully for building a prototype irradiance sensor with two channels at 1.55 μm and 1.65 μm, but the increased thickness resulted in low transmission at wavelengths below 1.0 μm, so the design was eventually discarded. A search for a new diffusing material uncovered a pPTFE sheet that was available commercially and showed increasing scattering at
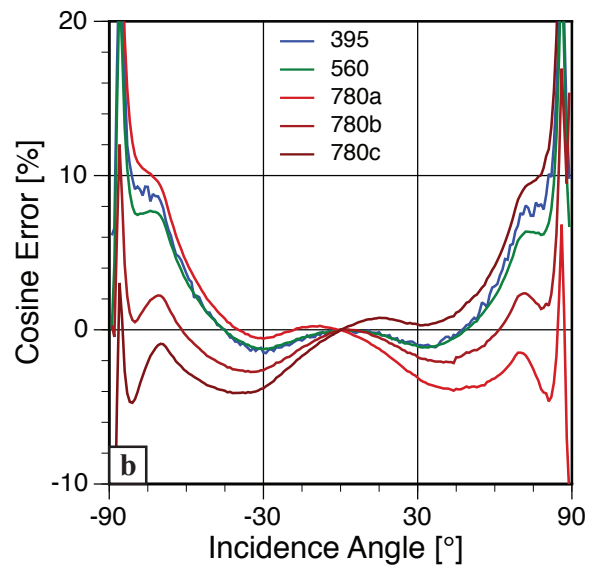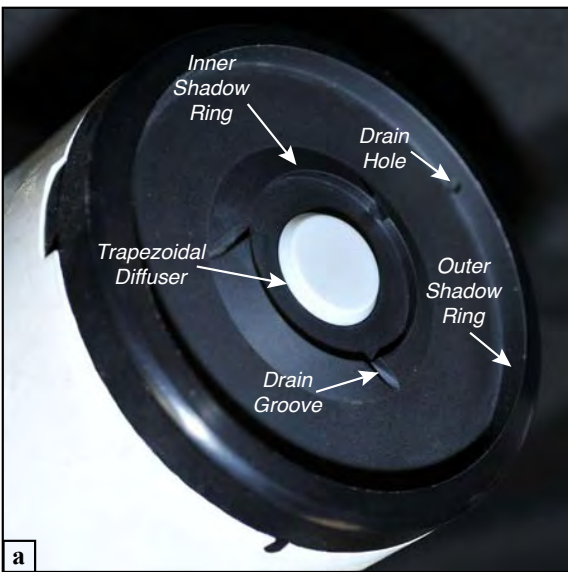
Fig. 10. A production-line irradiance radiometer, based on design characteristics for a legacy cosine collector, showing **a)** a photograph of the diffuser (left), and **b)** the cosine error for wavelengths between 380–780 nm (right). Water shedding is accomplished with three drain grooves cut into the inner shadow ring (oriented to prevent vignetting) and four drain holes in the outer shadow ring (only one is visible). To help discern the effect of detector positioning outside the visible region of the spectrum, the sensor used for the cosine error analysis had three 780 nm channels, one in the center of the microradiometer cluster and two at the perimeter, at opposing sides.

SWIR wavelengths, but that was thin enough to allow sufficient flux at 600 nm for satisfactory performance in the UV and visible domains. The manufacturer's data sheet indicated that this new material should have good scattering properties for wavelengths up to at least 2.5 μm.

Using a directional test bench consisting of a 1,000 W FEL tungsten lamp and a rotary table under computer control, the response for incidence angles between −90° and +90° of PTFE and pPTFE samples of various thicknesses were measured over wavelengths from 305–1,550 nm. This was accomplished by placing the samples in front of two microradiometers, one equipped with a silicon detector (sensitive from 300–1,100 nm) and the other with an InGaAs detector (sensitive between 700–1,700 nm). Wavelength selection was accomplished using interference filters at 305, 710, 780, 1,015, 1,300, and 1,550 nm sequentially placed between the material samples and the microradiometers for each directional scan.

One disadvantage of pPTFE is its porous structure, which makes it unsuitable for outdoor use without protection from dust and the elements. Consequently, a multi-layered diffuser consisting of a top layer of PTFE overlying a layer of pPTFE was developed. The angular response of the composite diffuser shows that the cosine error is similar to that of a single sheet of generic PTFE material for wavelengths ranging from 305–780 nm. For wavelengths from 1,015–1,550 nm, the cosine error of the composite diffuser resembles that of a single piece of pPTFE, at least up to an incidence angle of 65°. At larger angles, the cosine error is somewhat larger.

3.3 Irradiance Collector Design

Among other issues, reflection (Fresnel) losses at the air–diffuser interface cause the angular response of any diffusing material to depart from the ideal cosine response, particularly for incidence angles larger than 40°. A common solution for this problem is to design the collector such that the effective area, as viewed from the light source, increases with increasing incidence angle. This can be accomplished by shaping the diffuser in the form of a dome (Bernhard and Seckmeyer 1997), a cylinder (Harrison et al. 1994), or a trapezoid (Morrow et al. 1994). A trapezoidal cross-section is used by BSI, because it provides the optimal shape for underwater collectors that must withstand high pressure while presenting a well-defined reference plane for calibrations. One or more shadow rings surrounding the diffuser are often required to avoid excessive response at angles larger than approximately 50°.

A picture of the diffuser end of an irradiance sensor based on microradiometers is shown in Fig. 10a. The collector features a diffuser with a trapezoidal cross-section, plus inner and outer shadow rings surrounding the diffuser. The two rings limit the angular response at very large incidence angles by casting a shadow on the diffuser. Grooves in the inner rings (slanted to prevent vignetting) and four holes (not all visible) in the outer ring ensure proper water drainage. The angular response of this sensor for wavelengths between 380–780 nm is presented in Fig. 10b. Departures from the cosine law depend very little on wavelengths between 300–600 nm. The secondary diffuser made

of generic PTFE is not suitable for removing the azimuth asymmetry at wavelengths beyond 600 nm, and the cosine error of the three 780 nm channels depends on the location of the detector within the microradiometer cluster.

3.4 Optimized Cosine Collector

Calculations of the effective area of a diffuser as a function of incident angle, coupled with the measured angular response of a diffusing material, were used to model the response of a cosine collector design. Model parameters included the following:

1. Diameter of the diffuser top,

2. Height of the diffuser,

3. Diameter of the diffuser bottom,

4. Diameter of the outer shadow ring,

5. Diameter of the inner shadow ring, and

6. The distance between the inner shadow ring and the top of the diffuser.

To optimize the collector geometry, the model parameters were varied until the desired response was achieved.

A comparison of the modeled and measured cosine response of an optimized cosine collector design, compared to the departures from cosine for a flat plate collector made from PTFE, is shown in Fig. 11. In this example, increasing the height of the inner shadow ring in the model by 0.45 mm reduced the cosine error associated with the modeled angular response to less than 3.5% for incidence angles smaller than 85°. The measured values are very similar to the modeled, and any remaining deviations can be explained by the uncertainty of the estimate.
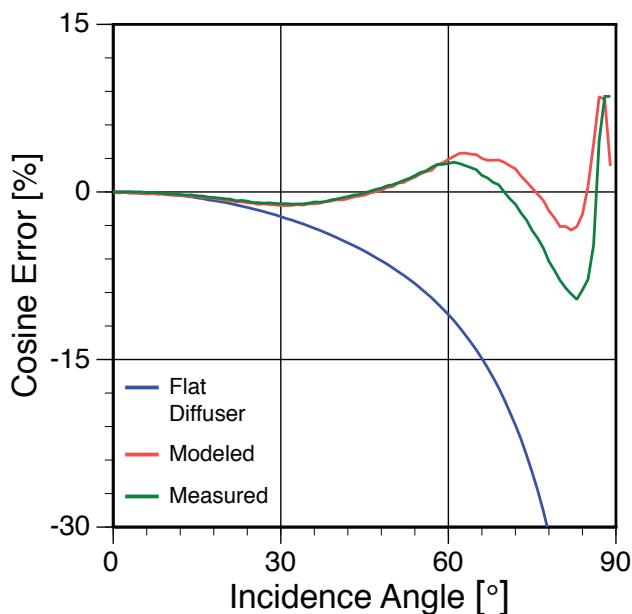
Fig. 11. Modeled and measured cosine error of the new collector compared with the cosine error from using a PTFE flat sheet as a collector.

3.5 Final Collector Design Test

A form with the optimized dimensions of an irradiance collector was machined out of aluminum. The pPTFE composite diffuser was then fitted into the form to shape the diffuser into the desired shape of the collector. The new collector was attached to a sensor composed of 18 microradiometers and equipped with filters for 380, 395, 412, 443, 490, 510, 532, 555, 560, 670 nm (one filter per wavelength), six filters for 1,020 nm, and two filters for 1,610 nm. Because pPTFE is relatively inflexible, a piece of the material was fashioned in a star-burst pattern (Fig. 12 top) and pressed into the outer diffuser layer made of generic PTFE (Fig. 12 bottom). A pPTFE sheet was also used as a secondary diffuser.
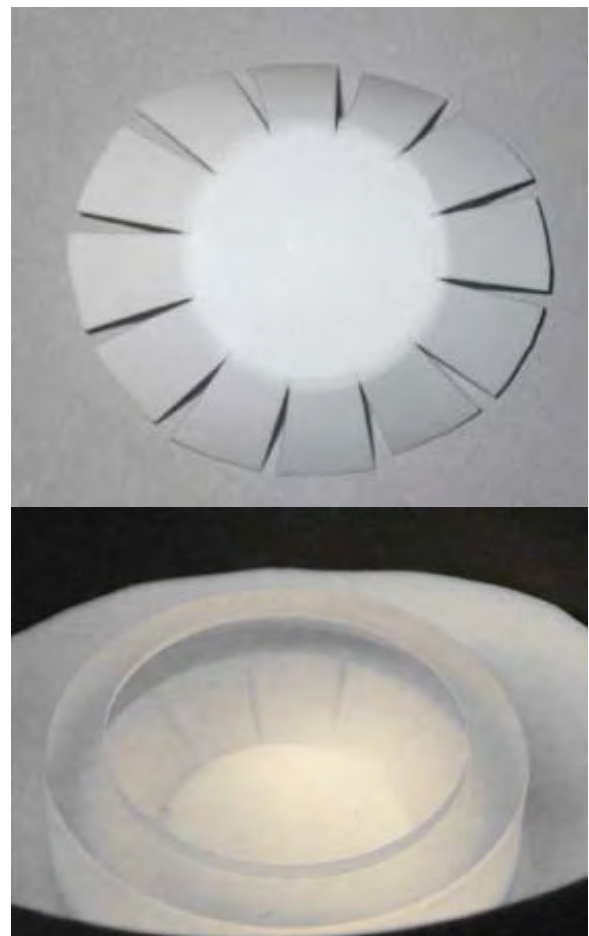
Fig. 12. The pPTFE material insert cut into a star-burst pattern (top) and viewed through the back of the quartz glass support (bottom).

Measurements indicated that the angular responses for the six 1,020 nm channels were virtually identical (i.e., the differences involved were to within 1% for incidence angles up to 80°), thereby confirming the angular response for this wavelength does not depend on the position of the detector within the cluster of 18 microradiometers. Measurements

of the two 1,610 nm channels agreed to within 0.3%. Measurements of the other wavelengths (380–670 nm) did not show a significant difference as a function of azimuth angle and wavelength (systematic variations were to within 0.5%). These results confirmed that the secondary diffuser is able to satisfactorily remove dependence of the angular response on azimuth angle that may have existed in the light field exiting the primary diffuser.

As shown in Fig. 13, the cosine error for the 490–670 nm wavelength range is to within 3% for incidence angles up to 75°. The maximum cosine error is −10% at 84°. The angular response of the channels at 1,020 and 1,610 nm are generally lower, because of a gradual deterioration of the scattering properties of the composite diffuser as the wavelength increases. For the six 1,020 nm channels, the cosine error is smaller than −5% for incident angles up to 74°. The maximum cosine error is −16% at 84°. For the two 1,610 nm channels, the cosine error is smaller than −10% for incident angles up to 70°, and the cosine error at 84° is −25%.

Fig. 14. A photograph of the new cosine collector highlighting important features of the design, including perpendicularly placed drain holes in the outer and inner shadow rings.

3.6 Conclusions

Tests using sheets of PTFE and pPTFE showed that one layer of generic PTFE sheet and one layer of pPTFE is an acceptable composite material for constructing an irradiance collector suitable for measurements at wavelengths spanning 305–1,640 nm. A numerical model was used to optimize the dimensions of a trapezoidal cross-section irradiance collector (originally designed for measurements for the UV-VIS) to extend its usable range to SWIR wavelengths. A new collector was machined, fitted with the composite diffuser, and tested.

The angular response of the new collector does not depend on azimuth angle and wavelength for 350–670 nm. The cosine error for this wavelength range is to within 3% for incident angles up to 75°. Cosine errors at 1,020 and 1,610 nm are larger because of the deterioration of scattering properties of PTFE for SWIR wavelengths. In terms of the knowledge base presented here, alternative materials with better scattering properties are not available. Consequently, the new collector represents the best broadband angular response possible with current diffuser technology.

Additional modeling results indicate that the angular response at SWIR wavelengths could be improved by modifying the dimensions of the collector design (e.g., by increasing the height of the diffuser), but this modification would degrade the angular response in the UV-VIS domain. To achieve the best accuracy, OSPREy systems can be equipped with two irradiance radiometers, one fitted with an irradiance collector optimized for the UV-VIS range, while the other is equipped with a collector optimized for SWIR wavelengths. Such an optimization might be particularly useful for systems deployed at high-latitude locations where the solar elevation is low year-round.

Fig. 13. The average cosine error of the test radiometer for which measurements at azimuth angles of 0 and 180° were averaged.

A picture of the new cosine collector is presented in Fig. 14 and has the same overall shape as the legacy collector shown in Fig. 10a. The irradiance sensor shown in Fig. 14 is without any insulation or end cap, i.e., the inner part of the instrument is shown. The two shiny objects to the top left and right are the ends of threaded rods that hold everything together, and normally they are hidden by the end cap. The inner shadow ring is undercut such that the drain holes do not cause azimuthal dependence in the angular response. The ability for water to drain away from the collector is an important design feature, because it allows rain to keep the collector clean, that is, rain water flushes particles off the collector and as long as they can drain away, they are not redeposited on the collector.

Chapter 4

Radiance Field-of-View Specifications

GERMAR BERNHARD, RANDALL N. LIND, CHARLES R. BOOTH, AND JOHN H. MORROW
Biospherical Instruments Inc.
San Diego, California

STANFORD B. HOOKER
NASA Goddard Space Flight Center
Greenbelt, Maryland

ABSTRACT

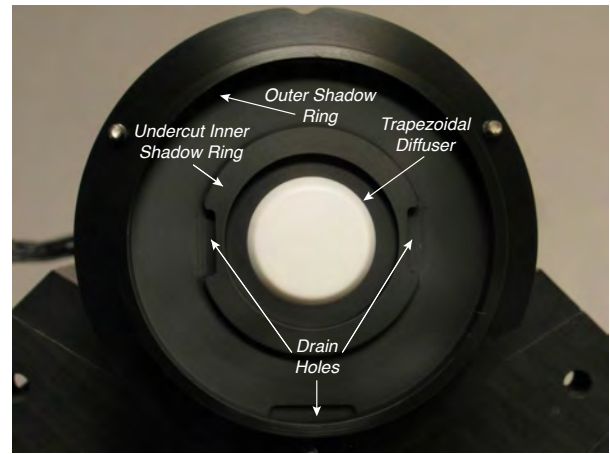The field of view of EML (radiance) instruments used for OSPREy applications, specified here in terms of the full view angle (FVA), must be optimized to accurately measure a variety of different radiometric sources: the direct solar irradiance when pointing the instrument at the Sun; the total radiance emanating from the sea surface, the sky radiance, and the radiance of a calibration plaque. The optimum FVA was determined based on the following considerations: a) the FVA must encompass the entire solar and lunar disks when performing direct measurements under all observation conditions; b) compliance with recommendations for sun photometers issued by the World Meteorological Organization (WMO); c) an FVA large enough to allow accurate measurements of low-intensity sources (e.g., calibration plaques, the sea surface, and the lunar disk); d) an FVA small enough to permit statistical filtering of surface and capillary wave effects when measuring the sea surface; and e) a reasonable overall instrument length. The latter are needed to ensure accurate pointing and control of the sensor, particularly by the sun tracker; easier handling during servicing and the types of activities that take place during those events (e.g., monitoring the stability of the sensors with a portable source); and minimization of wind loading. After taking all considerations into account, it was concluded that an FVA of 2.5° combined with a slope angle of 0.7° is the optimal configuration. These geometric parameters were translated into a fore-optic design consisting of Gershun tubes with an overall length of 182 mm, a front aperture of 4 mm, and three internal baffles for stray-light suppression.

4.1 Introduction

EML radiometers must be able to measure sky radiance, the total radiance L_T emanating from the sea surface, the radiance of a calibration plaque, and the direct irradiance from the Sun and Moon. These tasks have different entrance optics requirements for the instrument, and the resulting design is, inevitably, a compromise. When measuring the direct solar irradiance, for example, the FVA of the radiometer should ideally be smaller than 1° to minimize circumsolar radiation contributions (i.e., photons scattered in the direction of the radiometer by air molecules or aerosols). In contrast, the FVA has to be sufficiently large to support accurate measurements at low light levels, e.g., the UV radiance of the calibration plaque and L_T measurements in the near infrared (NIR). The original OSPREy objectives established that the fore optics of radiance radiometers should have an FVA between 1.5–2.5° (Sect. 1.3). This chapter presents the engineering analysis behind selecting the optimal FVA within this range.

4.2 Engineering Considerations

There are two preliminary engineering considerations that help define an optimized value for the FVA: stray-light suppression and overall instrument length. Direct sunlight is several orders of magnitude brighter than sky radiance, so any contamination from stray light is maximal when sky radiance is measured in close proximity to the Sun. Consequently, the design of the fore-optics for the sensor must include baffles to control stray light. A final engineering consideration is that the fore optics should not be more than 20 cm long to keep the overall length of the instrument within reasonable limits. These limits are needed to ensure accurate pointing and control of the sensor, particularly by the sun tracker. Minimization of the size of the sensor is also important for reducing wind loading and ensuring easier handling during servicing and the types of activities that take place during those events (e.g., monitoring the stability of a radiometer with a portable source).

The EMR field instruments are designed to measure the total radiance above the sea surface, which is a combination of photons that have exited the air–sea interface from below (the water-leaving radiance, L_W), and photons reflected by the sea surface (e.g., glint from the sky and Sun). Waves, white caps, sea spray, and glint may lead to an inhomogeneous radiance within the FVA of the sensor. Data points affected by sea glint and other factors can be filtered out, but only if the FVA is small and the sensor sampling rate is high (e.g., 6 Hz or more). This suggests that the chosen FVA should be as small as possible.

As a starting point in the numerical specifications of a design, EMR sensors should also have an FVA that is comparable to other sun photometers currently in use. Table 3 shows that the FVA values of such instruments are between 1.2–2.5°.

Table 3. A summary of the FVA of commercial sun photometers. Both of the PFR and SP02-L units have a 0.7° slope angle.

Manufacturer	Model	Used By	FVA
Cimel Electronique	CE-318	NASA AERONET	1.2°
YES†	SPUV-6/10		2.5°
PMOD/WRC‡	PFR	PMOD/WRC WMO/GAW	2.5°
Kipp & Zonen	POM-01		2.0°
Carter-Scott Middelton Solar	SP02-L	NOAA/ESRL GMD§	2.5°

† Yankee Environmental Systems
‡ *Physikalisch-Meteorologisches Observatorium Davos* (PMOD), World Radiation Center (WRC)
§ NOAA Earth System Research Laboratory (ESRL), Global Monitoring Division (GMD)

To establish the FVA required to measure the direct solar irradiance when pointing the instrument at the Sun, the first consideration is the angular size of the Sun when viewed from Earth. Over the course of the year, the angular size of the Sun varies from 0.527–0.545°. In practice, the FVA of a sun-viewing radiometer must be considerably larger than these values such that the complete solar disk is viewed by the instrument during all operating conditions. The latter must include compensation for the pointing inaccuracies of the sun tracker, the instrument, and positional uncertainties associated with the physical mounting of the instrument. For example, the finite step-resolution of the tracker, alignment differences in individual channels of the radiometer, and positional uncertainties where the instrument is installed (perhaps caused by environmental or platform vibrations), respectively. Based on these considerations, it was determined that the optimal sun-viewing FVA should not be smaller than 1.5°.

EMR field sensors must also be in compliance with the recommendations and specifications for sun photometers as issued by cognizant authorities. The *WMO Guide to Meteorological Instruments and Methods of Observations* (WMO 2008), for example, requires that modern pyroheliometers designed for making direct solar shortwave radiation observations should only measure "radiation from the Sun and a narrow annulus of sky." The resulting half-angle (half of the FVA) is "about 2.5°." The WMO Global Atmosphere Watch (GAW) aerosol measurement procedures guidelines and recommendations require that direct-beam radiometers have a "full opening angle of 2.5°" (WMO 2008), i.e., an FVA of 2.5°.

The FVA of an EMR sensor must also be large enough to allow accurate measurements of all sources considered by the OSPREy activity, including low-light applications. The signal of a radiance sensor, from a uniform source fully filling the field of view, is proportional to the solid angle Ω associated with the FVA. For small FVA values, Ω changes quadratically with FVA (Table 4). For example, changing the FVA from 17°, a baseline value established for the Ocean Optics Protocols (Mueller and Austin 1992), to 2.5° (a factor of 0.1471) changes Ω by a factor of 0.0218. In consequence, a decrease in the FVA greatly reduces the radiative flux reaching the photodetector, which in turn affects the detection limit for the instrument.

Table 4. The relationship between FVA and solid angle.

Full View Angle	Half Angle	Solid Angle Ω [sr]	Relative Solid Angle†
1.5°	0.75°	0.000538	0.0078
2.5	1.25	0.001471	0.0218
17.0	8.50	0.069000	1

† Relative to the solid angle for an FVA of 17°.

The noise equivalent radiance (NER) of an instrument, $\mathbf{N}_L$, is defined as

$$\mathbf{N}_L(\lambda) \; = \; \frac{\widehat{\sigma}_L(\lambda)}{\gamma_L(\lambda)} \tag{1}$$

where $\widehat{\sigma}_L(\lambda)$ is the standard deviation of the dark signal and $\gamma_L(\lambda)$ is the responsivity. The responsivity of a radiance sensor, from a uniform source fully filling the field of view, is proportional to Ω, and NER for a hypothetical system with a smaller FVA can be estimated by scaling with Ω (the right-most column in Table 4). The increase in NER with decreasing FVA can partly be compensated by increasing the integration time of the instrument, but $\widehat{\sigma}_L(\lambda)$ cannot be reduced by endlessly increasing the averaging time because of many factors, e.g., dark current drifts (which can be caused by small temperature changes). For measurements at the 1% accuracy level, radiances of artificial and natural targets should be at least 2.5 orders of magnitudes larger than the NER of the instrument, and this limit establishes the required FVA.
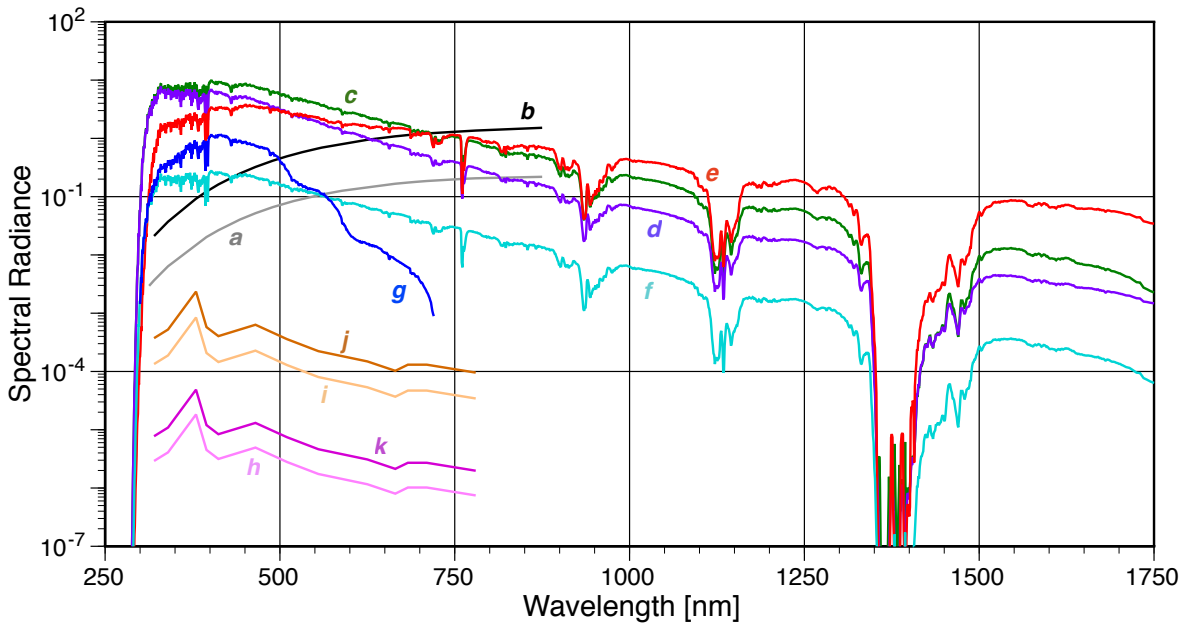
Fig. 15. Spectral radiances, in units of $\mu\mathrm{W\,cm^{-2}\,nm^{-1}\,sr^{-1}}$, of various sources compared with NER values for BSI microradiometers. The 11 data sets (**a**–**k**) are described in the text (Sect. 4.3).

4.3 Results and Discussion

Figure 15 compares radiances of various sources with the NER of microradiometers for data sets **a**–**k**:

a. The radiance of a Spectralon plaque that is mounted 287.1 cm from a 1,000 W FEL standard of spectral irradiance (the typical BSI configuration).

b. The radiance of the plaque (**a**), but mounted 107 cm from the calibration standard (used historically for calibrating radiometers with large NER).

c. The sky radiance modeled for a zenith angle of 40°, offset by 90° in azimuth from the solar principal plane. Radiance was calculated with the radiative transfer model `UVSPEC` (Mayer and Kylling 2005), for a solar zenith angle (θ_s) of 40°, cloudless sky, and aerosol optical depth of 0.5 at 500 nm.

d. The **c** data, but with no aerosols.

e. The **c** data, but for $\theta_s = 80°$.

f. The simulated radiance ΔL of the sea surface originating from the sky radiance defined by **c** data and reflected by the sea surface (assuming a surface reflectivity of $\rho = 0.028$).

g. Omitting any spectral dependencies for brevity, L_W, is calculated according to:

$$L_W = 0.54\, R(0^-)\, 0.965\, E_d(0^+)\, Q^{-1}, \qquad (2)$$

where the 0.54 term is the radiance transmittance of seawater, $L_W/L_u(0^-)$, for which $L_u(0^-)$ is upwelling radiance; $R(0^-)$ is the irradiance reflectance, $E_u(0^-)/E_d(0^-)$, where $E_u(0^-)$ is the upward irradiance and $E_d(0^-)$ is the downward irradiance at

null depth; 0.965 is the irradiance transmittance of sea water, $E_d(0^-)/E_d(0^+)$; $E_d(0^+)$ is downward irradiance above the water surface (the global solar irradiance); and Q is the irradiance-to-radiance ratio, $E_u(0^-)/L_u(0^-)$. Assuming $Q = 4$, R is set for a chlorophyll concentration of $0.045\,\mathrm{mg\,m^{-3}}$ using data adopted from Morel and Maritorena (2001); and $E_d(0^+)$ is modeled for a $\theta_s = 40°$, cloudless sky, and aerosol optical depth of 0.5 at 500 nm.

h. The NER of a microradiometer with an FVA of 17° and a sampling frequency of 5 Hz, as determined with the **a** data.

i. The hypothetical NER of the **h** microradiometer, but equipped with an FVA of 2.5°.

j. The hypothetical NER of the **h** microradiometer, but equipped with an FVA of 1.5°.

k. The same as **i**, but calculated for data averaged over a period of 60 s.

Figure 15 illustrates that sky radiances (**c**–**e** data) can be expected to be more than three orders of magnitude larger than NER values (**h**–**k** data). At this level of flux, even an instrument equipped with an FVA of 1.5° and sampling at 5 Hz can accurately measure sky radiance for solar zenith angles as large as 80°. In comparison, radiance emanating from the sea surface resulting from the reflection of sky radiance alone (**f** data) is about 2.5 orders of magnitude larger than NER for the fore optics with FVA equal to 1.5°. This difference is at the limit of the criterion discussed earlier. Because accurate measurements of sea surface radiances are of paramount importance for the OSPREy activity, an FVA larger than 1.5° should be

chosen. Averaging measurements over longer time periods is not an option because of the rapidly changing light field (caused by surface waves).

Conservative estimates of water-leaving radiances (**g** data) suggest an FVA of 2.5° or larger is required for wavelengths longer than about 550 nm, because the expected NER is less than 2.5 orders of magnitude smaller than the light field. For wavelengths shorter than 550 nm, water-leaving radiances are likely more than 2.5 orders of magnitude larger than the NER.

For an FEL lamp mounted 287.1 cm from a plaque, the radiance of the plaque is $0.003\,\mu\mathrm{W\,cm^{-2}\,nm^{-1}\,sr^{-1}}$ at 320 nm (**h** data). This value is only one order of magnitude larger than the NER of the fore optics with an FVA equal to 1.5°. While the difference could be increased by moving the lamp closer to the plaque or by averaging the radiometer signal, it is thought that choosing a fore optics with the FVA equal to 2.5° is a more conservative approach.

Based on these considerations, it was concluded that the fore optics of the instrument should have an FVA of 2.5°. To keep the length of the fore optics at or below 20 cm, a slope angle of 0.75° or smaller is required. A slope angle of 0.7° is used, because this angle is also used by some existing sun photometers (Table 3).

4.4 Fore Optics Design

The geometry and dimensions of the fore optics are defined by the FVA, the slope angle, and the size of the active area of the photodiodes used for each channel (Fig. 16). Photodiodes with an active area of $3.5 \times 3.5\,\mathrm{mm}^2$ were selected. To avoid any azimuthal asymmetry, photodetector mounts must have a circular opening with a radius r_p of 1.75 mm. The half-angle is defined as the $\arctan(r_a/d_p)$, where r_a is the radius of the front aperture and d_p is the distance between the front aperture and the photodetector. The slope angle is $\arctan\left[(r_a - r_p)/d_p\right]$. Setting r_p to 1.75 mm, the FVA to 2.5°, and the slope angle to 0.7°, results in $r_a = 3.98$ mm and $d = 182.25$ mm.
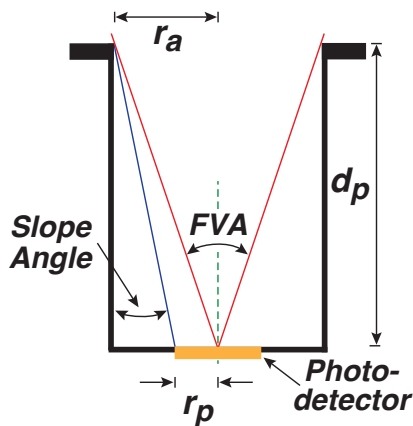
Fig. 16. An illustration of a single Gershun tube and definition of FVA and slope angle. The center line of the aperture is shown dashed.

The fore optics of sun photometers are typically Gershun tubes that include two or three internal baffles (e.g., Wehrli 1989). The EML instruments also use this design (Fig. 17). Baffles divide the tube in sections determined by ray trace paths of direct and scattered light. Considerable effort has gone into the details specifying baffle placement. The radius of the baffle apertures is chosen such that the baffles do not interfere with the FVA defined by r_a, r_p, and d_p, but at the same time are as small as possible for efficient stray-light suppression.

Fig. 17. The initial assembly of the first of four layers of Gershun tubes, made from hollow black cylinders, which are stacked to control the FVA.

Figure 18 shows a side-view drawing of the 19-channel Gershun tube and baffle arrangement needed to achieve the desired narrow FVA. The chamfers (beveled edges) surrounding the knife edges of the outermost baffle are oriented towards the eternal light field. Chamfers surrounding the knife edges of the interior baffles are oriented towards the detectors. Only three out of 19 possible Gershun tubes are depicted for clarity.

Fig. 18. A drawing of the four layers of Gershun tubes, and baffle placement for a 2.5° FVA.

4.5 Conclusions

The optimal FVA for EML instruments was determined based on the differing measurement requirements associated with the diversity of data products that were first anticipated for radiance measurements. The principal data products were associated with direct observations of the Sun and Moon for AOD data products, plus sea and sky measurements for oceanic data products. It was concluded that an FVA of 2.5° combined with a slope angle of 0.7° is the optimal combination. These geometric parameters were translated into a fore-optic design consisting of Gershun tubes with an overall length of 182 mm, a front aperture radius of 4 mm, and four internal baffles for stray-light suppression.

The data product suite can be expanded from sky photometry sampling scenarios, but an additional design requirement associated with measuring the sky close to the Sun is required. At the aperture end of an EML radiometer is an 8 in (20 cm) long by 4 in (10 cm) cylindrical shroud that serves multiple purposes. The design dimensions and placement of internal baffling help minimize off-angle stray light reaching the radiance entrance optics of the instrument and associated spectrograph and camera ports. The system also provides protection from swirling debris that can stick to the optical surfaces and cause scattering artifacts, especially when directed to the stowed position where the entrance port is oriented downward. The shroud is removable to enable cleaning of the entrance optics of the instrument.

Chapter 5

Sun Tracker Performance Evaluation

Germar Bernhard, Charles R. Booth, and Vi Quang
Biospherical Instruments, Inc.
San Diego, California

Stanford B. Hooker
NASA Goddard Space Flight Center
Greenbelt, Maryland

Abstract

An OSPREy system requires a pointing device or *tracker* to accurately direct radiance radiometers at relevant targets, including the Sun, Moon, sky, sea surface, calibration sources, and monitoring devices. Of all applications, the measurement of the direct Sun requires the highest pointing accuracy. Based on the angular size of the Sun, the geometry of radiance fore optics, and alignment uncertainties, it was determined that a pointing accuracy to within 0.2° is required. The tracker should be small in size with a low power requirement, and must also be weather and corrosion resistant for use in the marine environment. A market analysis was performed, which resulted in three candidate instruments. Based on specifications provided by the manufacturers, it was concluded that the PTU-D300 pan-tilt unit from FLIR Motion Control Systems would be the most suitable tracker for OSPREy applications. A test unit was procured and installed on the roof platform at BSI. The pointing accuracy was tested by mounting a video camera on the device for tracking the Sun. Software was developed to capture and examine the images of the video camera. The software was able to find the center of the Sun in the video images with an accuracy of 0.01°. The method is a viable and cost-effective alternative to the use of quadrant detectors for Sun finding. Image analysis, later confirmed with a test deployment of an EML (radiance) sensor, showed the PTU-D300 unit can track the Sun with a sufficient accuracy of to within 0.1°.

5.1 Introduction

A primary innovation for the OSPREy above-water system is the ability to make atmospheric as well as oceanic measurements. The former is best exploited if each radiance sensor can also function as a sun photometer, which means an ability to track and locate the Sun is required. Although a custom-built device is a solution, in keeping with other aspects of the OSPREy activity, a commercial source provides potential cost savings.

The OSPREy system has other metrology requirements that a *tracker* must satisfy. The radiometers need to be potentially pointed at a variety of targets—including the Moon, sky, ocean, and a monitoring device—and in each case at a specified angle. The primary measurements, however, are the direct-normal Sun irradiance, sky radiance for a multitude of zenith and azimuth angles, and the total radiance emanating from the sea, L_T, at a prescribed geometry with respect to the Sun. From these measurements, secondary data products can be derived, including

the AOD, the SSA, the ratio of direct-to-global irradiance, and the water-leaving radiance, L_W.

The material presented here establishes the requirements for a tracker, provides an overview of commercially available systems, and gives the rationale for selecting the model PTU-D300 tracker from FLIR Motion Control Systems, Inc.† (Burlingame, California). Test results indicate that this tracker meets the requirements for the OSPREy activity. Suggestions for improving the performance of the tracker are also provided.

5.2 Tracker Requirements

EML radiometers must be able to measure sky radiance, the total radiance emanating from the ocean surface, and direct solar irradiance when pointing the instrument at the Sun. Of all applications, measurements of the direct Sun require the highest pointing accuracy of the tracker. For these measurement tasks, the entire Sun

---

† Formerly called Directed Perception.

must be within the field of view of the radiometer that is mounted on the tracker.

Minimum requirements for the pointing accuracy of the tracker were calculated from the geometric properties of the radiometer's fore optics and the angular size of the Sun. The fore optics of EML sensors have a half angle of 1.25° and a slope angle of 0.7° (Chap. 4). The latter specification means that a point source, which is infinitely distant from the radiometer, fills the entire area of the radiometer's photodetector even if the radiometer is misaligned by 0.7°. The actual pointing accuracy must be significantly better, because the Sun is not a point source: it has an angular diameter of 31.6′ (0.5266°) on 4 July (aphelion) and 32.7′ (0.545°) on 3 January (perihelion). This means that the pointing accuracy must be at least $\pm 0.7° - \frac{1}{2}0.545°$ or $\pm 0.4275°$.

In practice, the accuracy must be even better still, because of radiometric diffraction effects at the sensor's front aperture and possible departures of the field of view from the (theoretical) design specifications. In addition, the radiometer is made up of separate Gershun tubes for each channel, and small differences in the pointing direction of those tubes (e.g., 0.1°) further restrict the required pointing accuracy of the tracker. *Based on these considerations, it was determined that a pointing accuracy to within 0.2° is required.* The repeatability of the tracker should be considerably better than this value, e.g., to within 0.05°.

Radiances of the sky, ocean, and calibration sources change very little (less than 1%) with small variations (less than 1°) of the pointing direction. A tracker that is adequate for measuring the direct Sun is, therefore, also suitable for other OSPREy measurements.

In addition to good pointing accuracy, the OSPREy requirements for a Sun tracker include the need for surviving long exposure times in the marine environment, low power consumption, small size (to reduce platform space requirements and wind loading), and low cost. An analysis of existing tracker manufacturers was performed based on these considerations, which resulted in three candidate instruments:

- Model 2AP-GD, Kipp & Zonen, Inc. (Bohemia, New York);
- Model PTU-D300, FLIR Motion Control Systems, Inc. (Burlingame, California); and
- Model ASTX-1, Prede Co., Ltd. (Tokyo, Japan).

The latter had the most number of unknown operating specifications.

5.3 Tracker Selection

The Kipp & Zonen 2AP-GD tracker, commonly used in European sun photometry applications, is based on a spur gear primary plus a final double-involute worm gear. The primary products of FLIR Motion Control Systems use a worm gear pan-tilt design, and are sold for surveillance, antenna positioning, lidar mounting, and other applications.

The FLIR units are designed to military specifications for harsh outdoor environments and vehicle-mounted applications, and are equipped with a slip ring and military-style hardware. Information concerning number and type of users for the ASTX-1 tracker from Prede was not available.

A comparison of the three trackers that were considered for OSPREy systems (Table 5) showed the PTU-D300 from FLIR would be the most suitable sun tracker for OSPREy applications†. Its main advantages over the other units are high rotational velocity (required for quickly changing observing modes), superior specifications for harsh environments (including exposure to sea spray), and lower price. It is also compact, relatively light, and typically does not consume as much power. Its resolution is not as good as the 2AP-GD, but is considerably better than the requirements for sun photometry discussed above. Based on these considerations, a PTU-D300 (Fig. 19) was procured, installed, and tested.

Table 5. A summary of the three sun tracking systems considered for OSPREy. A blank entry indicates an unknown specification.

Specification	2AP-GD	PTU-D300	ASTX-1
Communications	RS-232	RS-232	RS-232
Resolution	0.0025°	0.0064°	0.0036°
Pointing Accuracy	< 0.05°	0.01°	0.01°
Repeatability	< 0.02°	0.01°	
Zenith Range	210°	180°	90°
Velocity [°/s]	1.8	50	
Azimuth Range	540°	360°	300°
Torque [N m]	40		
Power [W]	50	18.2‡	10
Payload [kg]	65	31.7	10
Weight [kg]	30	11.8	27
Environment	Outdoor	IP67§	Outdoor
Operating Temp. [°C]	−50 to 50¶	−30 to 70	
Price	$21,640	$11,540	

‡ Typical consumption; up to 49.2 W peak.

§ Up to 6 mm of ice buildup, sustained exposure to blowing dust and sand, and sustained operation in salt-spray environments.

¶ With heater.

† A list of the specifications for the model PTU-D300 pan-tilt unit from FLIR Motion Control Systems is available at http://www.dperception.com/pdf/specs-ptu-d300.pdf.

Fig. 19. The PTU-D300 pan-tilt unit from FLIR Motion Control Systems, which is approximately $7.1 \times 11.6 \times 8.5 \, in^3$. The perforated plate extending to the right away from the control housing is the payload (radiometer) mounting bracket.

5.4 Test Protocol

The PTU-D300 was mounted on the BSI rooftop platform with sturdy Unistrut framing (Fig. 20a). A video surveillance camera (Sony model SNC-Z20N) was installed inside a protective housing and fastened to the tracker's mounting bracket (Fig. 20b). The camera has a resolution of 640 (horizontal) by 480 (vertical) pixels and is equipped with a telephoto lens (magnification 1–18×).
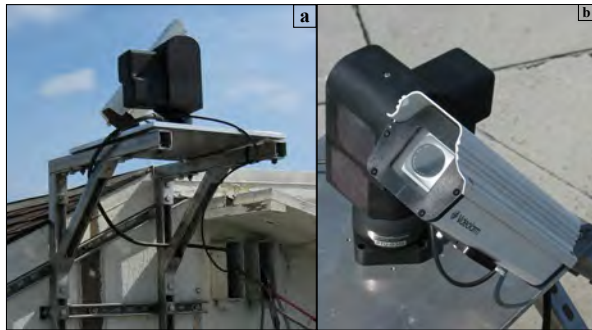
Fig. 20. The mounting of a PTU-D300 on the BSI rooftop platform showing **a)** support provided by stainless steel Unistrut framing, and **b)** the Sony SNC-Z20N video camera mounted on a PTU-D300.

All settings, including exposure time and zoom, are computer controlled. A neutral density filter was installed in front of its lens to prevent overexposure. The tracker was programmed to point the camera at the Sun by implementing the ephemeris algorithm by Wilson (1980). Additional software was developed to capture and analyze the images of the video camera. This software implements a Hough Transform (Ballard 1981) for finding the center of the Sun. The pixel coordinates of the Sun's center are displayed on the screen (Fig. 21) and also written to a database at a rate of 3 Hz. Data are automatically rejected from further analysis if the Sun is obscured by clouds.
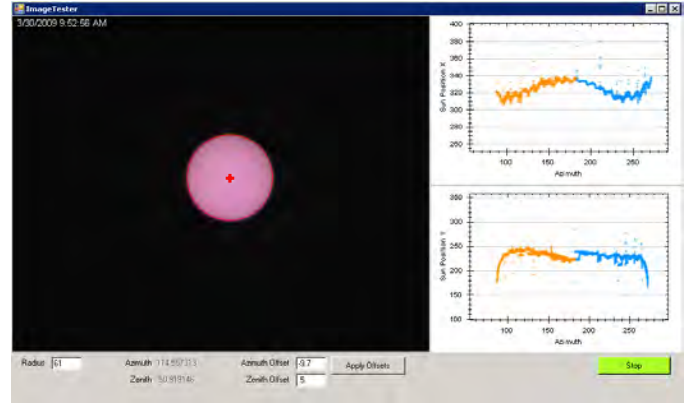
Fig. 21. A screen shot of a program to determine the center of the Sun. The left panel shows the image of the Sun captured by the video camera and the center of the Sun as determined by the software (red cross). The top right panel shows the horizontal pixel position of the Sun's center as a function of azimuth angle calculated by the ephemeris algorithm. Morning and afternoon data are displayed in different colors. The bottom right panel shows similar results for the Sun's vertical position. The radius of the Sun, and tracker zenith and azimuth offsets are configurable by the user.

5.5 Results

The pixel position of the Sun's center, as determined with the software, should ideally be independent of the solar azimuth angle. The first test results, taken between 13 and 16 March 2009, showed this was not the case. The horizontal position (x_p) of the center pixel varied between 273–361, and the vertical position (y_p) of the center pixel varied from 129–344. The data from the four days almost entirely overlay one another, however, indicating that the tracker's position is very reproducible from day to day.

Because the diameter of the Sun is known ($0.5391°$ on 14 March), the positional data can be converted to angular variation (denoted by the subscript a) via the equations:

$$x_a \;=\; 0.5391 \, \frac{x_p \;-\; 320}{122}, \tag{3}$$

and

$$y_a \;=\; 0.5391 \, \frac{y_p \;-\; 240}{122}, \tag{4}$$

where 320 and 240 are the center pixel in the x and y directions, respectively, and 122 is the pixel diameter of the Sun for 14 March. Figure 22 shows the result of the conversion. The diurnal variation in the image of the Sun's
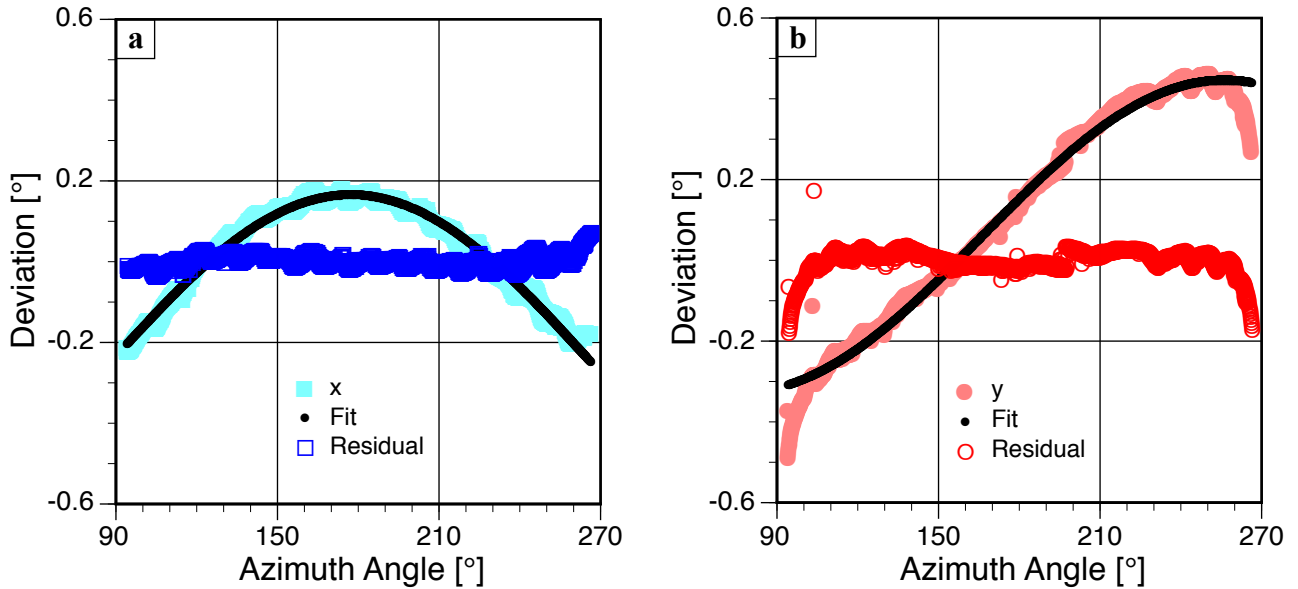
Fig. 22. The angular position of the center of the Sun with the fit to the data and the resulting residuals for **a)** the horizontal direction, and **b)** in the vertical direction.

center is $\pm 0.2°$ in the horizontal and $\pm 0.45°$ in the vertical directions. This variation is likely due to small leveling uncertainties of the instrument. For example, if the instrument mounting plate was tilted by $0.4°$ towards the western horizon, the image of the Sun would be low by $0.4°$ in the morning and correspondingly high in the evening. It can be expected that the image position varies with the cosine of the azimuth angle ϕ for other times.

Harmonic functions of the form $a + b\cos(\phi - c)$ were fitted to the measured data. These fit functions, as well as their residuals, are shown in Fig. 22. It is evident that the functions provide an excellent fit, because the residuals (i.e., ratio of measurement to fit) are typically smaller than $\pm 0.03°$. Much of the remaining variability is made up by a small-scale variation on the order of $\pm 0.015°$ with a periodicity of approximately $10°$ in the azimuth angle. This variability is likely correlated to a full resolution of the tracker's worm drives. Imprecisions in the manufacturing of the worm drives provide the ultimate limitation in the pointing accuracy.

Closer inspection of Fig. 22b reveals that residuals exceed $0.05°$ for solar azimuth angles smaller than $100°$ or larger than $260°$. For these azimuth angles, $\theta_s > 78°$. At these large zenith angles, the position of the Sun becomes dependent on refraction by Earth's atmosphere, which is not implemented in the ephemeris program. These departures are, therefore, not related to inaccuracies of the tracker but rather are related to simplifications in the calculation of the Sun's position.

As a next step of instrument characterization, the two fit functions shown in Figs. 22a and 22b were included in the tracker software, and the tests were repeated. The results are shown in Fig. 23, and should match with the residuals shown in Fig. 22. A comparison of Figs. 22 and 23

indicates that implementation of the fit functions resulted in a significant improvement of the tracker's accuracy.

Fig. 23. The angular position of the center of the Sun for the horizontal and vertical directions as measured after the fit functions in Fig. 22 were implemented in the tracker software.

Both the vertical and horizontal deviations in Fig. 23 closely match the residuals of Fig. 22. For horizontal tracking, maximum deviations are smaller than $\pm 0.1°$; for vertical tracking, maximum deviations are smaller than $\pm 0.06°$, except at either very small or large azimuth angles where atmospheric refraction becomes important. These deviations are below the required accuracy of $\pm 0.2°$ specified in

Sect. 5.2. The day-to-day variability, which is indicated by the vertical spread of the data points in Fig. 23, is about ± 0.02, which is also better than the target limit of ± 0.05.

All tests discussed above are based on measurements where the tracker was following the Sun in a continuous motion from the morning to the evening. The tracker gears were loaded from one side only and any possible "play" (or backlash) in the worm drives would not show up in these tests. To investigate whether backlash of the drives would appreciably compromise tracker accuracy, a modified test was performed. The tracker was commanded at the top of every hour to point to the zenith or various points on the horizon. Results of this modified test are presented in Fig. 24, for which the same correction functions determined from Fig. 22 were implemented.
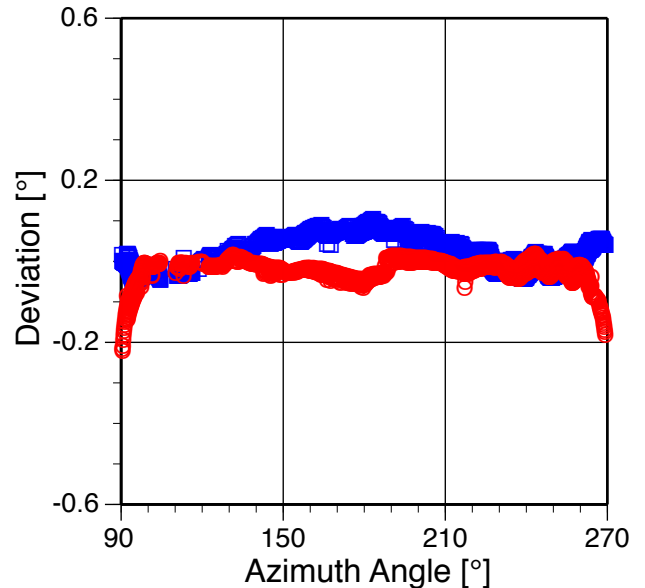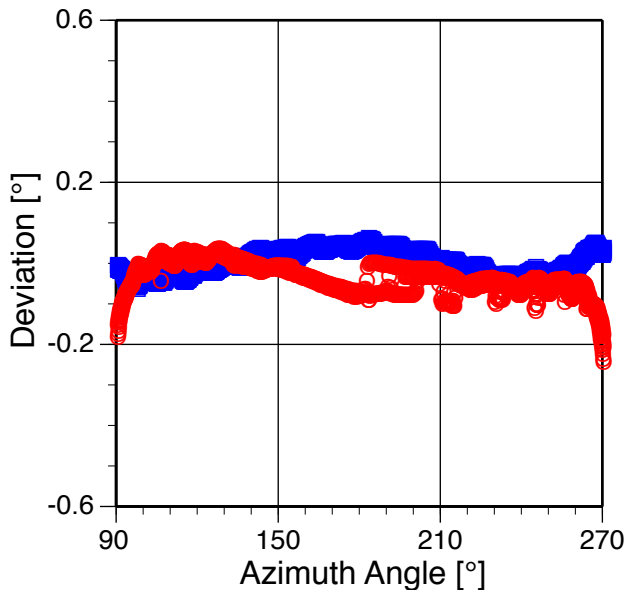

Fig. 24. The angular position of the center of the Sun for the horizontal and vertical directions as measured during the backlash testing.

Figures 23 and 24 are very similar for the horizontal direction (blue), indicating that changing the azimuth before resuming Sun tracking does not have an appreciable influence on the data. This means that there is no detectable backlash in the gears for the azimuth position. This is not the case for the vertical direction. Figure 24 shows discontinuities in the vertical direction at azimuth angles of $182°$, $190°$, $212°$, $231°$, and $245°$ at times when the tracker was briefly pointing to either the zenith or horizon before resuming Sun tracking. These discontinuities are about $0.1°$ (i.e., an order of magnitude larger than the specified accuracy of the system), and are likely related to backlash of the zenith drive.

The backlash test results were discussed with the manufacturer, who acknowledged that the observed amount of backlash is beyond the specified limits. The company suggested that the system be returned for adjustment of the gears. This advice was followed, and the system was retested after refurbishment. The angular precision (calculated as the standard deviation of repeat measurements) of the serviced systems was $0.008°$, both in the zenith and azimuth directions. This value is close to the theoretical limit defined by the PTU-D300 pan and tilt resolution of $0.0064°$. Consequently, the refurbished system met the pointing accuracy specification of $0.01°$ (Table 5).

5.6 Conclusions

Based on a market analysis, it was determined that the PTU-D300 unit is the most suitable tracker for OSPREy applications. Its specifications meet OSPREy requirements in terms of tracking accuracy, resolution, speed, range of motion, payload, power consumption, size, and weather resistance. In addition, its price is substantially less than that of comparable systems. A PTU-D300 was subsequently procured, installed on the BSI rooftop facility, and tested by pointing a video camera at the Sun and analyzing the data recorded.

The tests verified most of the specifications provided by the manufacturer, however, it was determined that the zenith drive of the system is affected by a backlash of about $0.1°$. The manufacturer acknowledged this value does not meet specification and readjusted the drive mechanism. The angular precision (calculated as the standard deviation of repeat measurements) of the refurbished unit was $0.008°$, both in the zenith and azimuth directions. This value is close to the theoretical limit defined by the pan and tilt resolution of $0.0064°$.

Sun trackers for OSPREy require a pointing accuracy of better than $\pm 0.2°$, and the refurbished system met the pointing accuracy specification of $0.01°$ (Table 5). Even if backlash were to reappear after additional months of operation, its effect could be mitigated by adjusting the measurement protocol accordingly. For example, the tracking software could be modified such that a specific angular position is always approached from the same direction. By mounting the payload slightly off balance, gravity also helps to load the zenith gear in one direction.

Tests also indicated that the range of motion for the tracker is $\pm 89.5°$ in the zenith direction and $\pm 175°$ in the azimuth direction. These values are somewhat smaller than specified. It is, therefore, not possible to point to the zenith (directly overhead) and nadir (directly below). Radiometers attached to the tracker could be mounted with a small offset, however, so that observations of the zenith sky are possible. The ability to point downward is desirable for "safing" or "stowing" the instrument (e.g., during inclement weather), and for measuring dark currents during daylight (e.g., when a light-tight enclosure is installed at the base of the instrument). These measurements could also be performed at a zenith angle of $-89°$, and the ability to point to the exact nadir is, therefore, not a requirement for OSPREy.

There is an azimuth range of about $\pm 5°$, nominally towards North, that cannot be accessed. This is not a problem for OSPREy applications because measurements in this direction are not required. The PTU-D300 provides cable pass-throughs for the payload, which reduces the risk that cables from a radiometer mounted to the instrument get entangled or damaged, e.g., during periods of high wind.

The software for finding the center of the Sun is very reliable and fast. Determinations of the Sun's center are reproducible to within $\pm 0.01°$. Using a video camera in combination with this software is a viable and cost-effective alternative to quadrant detectors, which are typically used for Sun trackers, such as the 2AP-GD unit. The tracker-mounted EML sensors are equipped with a small video camera, and the integrated approach improves the tracking accuracy from about $\pm 0.05°$ for the test system, to better than $\pm 0.01°$. The accuracy is only limited by the step resolution of the tracker, which is $0.0064°$. Active tracking using a video camera extends the tracker's range to $\theta_s > 80°$, where refraction by the atmosphere limits the accuracy of the ephemeris algorithm. Subsequent tests with an EML radiometer confirmed the suitability of this tracker for OSPREy systems.

Chapter 6

Lamp Library Performance

Germar Bernhard and Charles R. Booth
Biospherical Instruments Inc.
San Diego, California

Stanford B. Hooker
NASA Goddard Space Flight Center
Greenbelt, Maryland

Abstract

Twenty-one 1,000 W tungsten-halogen FEL lamps were chosen to become part of the OSPREy lamp library. Nine lamps were calibrated by NIST, while the rest are uncalibrated, but seasoned lamps (by the supplier). These lamps were operated for periods ranging from 4–35 h to assess their stability. Changes in brightness were typically in the range of ±0.02% per hour with a few lamps exhibiting slightly larger drifts. These lamps should be seasoned for an additional 8–30 h to improve their stability. The calibration laboratory at BSI was upgraded to operate lamps of the OSPREy lamp library at the highest level of accuracy achievable. Upgrades included a new system for powering the lamps, which allows regulation of the lamp current to within a precision of 50 µA (or 0.0006% for a target current of 8.2 A). Other facilities required for accurate lamp transfers were also upgraded to reduce uncertainties caused by stray light, misalignment, and temperature variations. Three radiometers are available for maintaining optical standards: an OXL instrument calibrated at BSI, an OXE instrument currently awaiting results of a NIST SIRCUS calibration (and not used for the results presented in this chapter), and a transfer radiometer based on the BSI ground-based UV (GUV) class of radiometers that is called an XGUV. A comprehensive uncertainty analysis showed the use of moderate-bandwidth radiometers, such as the XGUV and OXL, are suitable to transfer calibrations of FEL lamps. Uncertainties related to the relatively large bandwidth of these instruments are on the order of 0.3%. All NIST lamps were intercompared and agreed to within ±2%, which is a very good result considering that some lamps are rather old and were calibrated against different NIST scales. A protocol on the usage of the lamp library was developed with the goal of preserving the spectral irradiance scale over a timescale of 15 years or more.

6.1 Introduction

The radiance and irradiance scales for OSPREy are linked to the NIST SIRCUS radiometric scale. Two OXR sensors were planned to be calibrated by SIRCUS, and the calibrations transferred to OSPREy field instruments. The OXE sensor was sent to NIST for SIRCUS calibration in 2010 and is awaiting the calibration report. Pending final results, the OXL unit may also be calibrated at SIRCUS. Calibration details of the radiometers used in the OSPREy activity is provided by Bernhard et al. (2012).

While OXR instruments are designed for maximum short- and long-term stability that is achievable with current technology, small drifts of the instrument's responsivity over time can be expected, as is the case for any radiometer. To maintain the calibration of OXR radiometers for long periods of time (e.g., one decade), a cost-effective approach is to transfer the scale to standards of spectral irradiance, which are commonly realized by 1,000 W tungsten halogen lamps of type FEL.

Lamps, like radiometers, change over time. To avoid drifts in the spectral radiance and irradiance scales over time, it is essential to transfer the scale to several lamps, which are regularly intercompared to ensure consistency of their calibrations. This suite of lamps is called the OSPREy lamp library.

Ensuring the stability of radiometric scales to within 1% over the long term, either using radiometers or lamps, is a demanding task. To achieve this goal, lamps must be operated with specialized equipment in a well-characterized dark room. The laboratory at BSI was, therefore, upgraded with state-of-the-art equipment, including precision power supplies, laser alignment tools, and additional baffles to reduce stray light as much as possible. The lamp library currently consists of 21 lamps, some of which were

Table 6. A summary of the OSPREy lamp inventory. The specified number of amps indicates the calibration current for the lamp. Lamps with a blank calibration scale entry are provided uncalibrated by the supplier (lower half of table). The date of first use is at BSI and is with respect to establishing the OSPREy lamp library.

S/N	Manufacturer	Owner	Supplier	Amps	Scale	First Use	Tested
F-137	General Electric	NASA	NBS†	8.0	Unknown	Jan. 2010	OXR
F-182	General Electric	NASA	NIST	7.9	NIST 1990	Jan. 2010	OXR, XGUV
F-473	Osram Sylvania	BSI	NIST	8.2	NIST 1990	1997	OXR, XGUV
F-474	Osram Sylvania	BSI	NIST	8.2	NIST 1990	1997	OXR, XGUV
F-527	General Electric	NASA	NIST	7.9	NIST 1990	Jan. 2010	OXR
F-550	General Electric	NASA	NIST	8.2	NIST 1990	Jan. 2010	OXR
F-614	Osram Sylvania	NASA	NIST	8.2	NIST 2000	Jan. 2010	OXR, XGUV
F-615	Osram Sylvania	NASA	NIST	8.2	NIST 2000	Jan. 2010	OXR, XGUV
F-616	Osram Sylvania	NASA	NIST	8.2	NIST 2000	Jan. 2010	OXR, XGUV
V-017	Osram Sylvania	NASA	CUCF‡	8.2		Apr. 2008	Not Tested
V-018	Osram Sylvania	NASA	CUCF	8.2		Apr. 2008	OXR
V-019	Osram Sylvania	NASA	CUCF	8.2		Apr. 2008	OXR
V-020	Osram Sylvania	NASA	CUCF	8.2		Apr. 2008	XGUV
V-021	Osram Sylvania	NASA	CUCF	8.2		Apr. 2008	OXR
V-022	Osram Sylvania	NASA	CUCF	8.2		Apr. 2008	OXR
GS-1019	Osram Sylvania	BSI	Gamma Scientific	8.0		Aug. 2008	Not Tested
GS-1024	Philips Electronics	BSI	Gamma Scientific	8.0		May 2008	XGUV
GS-1025	Philips Electronics	BSI	Gamma Scientific	8.0		May 2008	XGUV
GS-1026	Philips Electronics	BSI	Gamma Scientific	8.0		May 2008	XGUV
GS-1027	Philips Electronics	BSI	Gamma Scientific	8.0		May 2008	XGUV
GS-1028	Philips Electronics	BSI	Gamma Scientific	8.0		May 2008	XGUV

† The National Bureau of Standards (NBS) was the precursor Federal agency to NIST.

‡ The NOAA Central UV Calibration Facility (CUCF) is a joint activity with NIST.

calibrated by NIST FASCAL, which issues calibrated FEL standard lamps. It is possible, therefore, to compare the radiometric scales provided by SIRCUS and FASCAL using the lamp library and OXR instruments.

6.2 Lamp Inventory

Twenty-one FEL lamps were chosen to establish the OSPREy lamp library (Table 6). All lamps are potted in bi-post bases compatible with the recommended NIST kinematic lamp socket (Zalewski et al. 1972). Not all lamps are calibrated by NIST, because it would have been cost-prohibitive to base the lamp library exclusively on NIST lamps. Two NIST lamps (F-473 and F-474) have been in use at BSI since 1997 and their calibration refers to the NIST FASCAL irradiance scale from 1990 (Walker et al. 1987). Lamps F-182, F-527, and F-550, which belong to NASA, are also traceable to the NIST 1990 scale.

Standard lamp F-137 was calibrated by NBS in 1982 against DXW standards. The traceability of this lamp is unknown. Three lamps (F-614, F-615, and F-616) were acquired from NIST specifically for the OSPREy activity,

and their calibration is traceable to the latest NIST irradiance scale, which was established in 2000 (Yoon et al. 2002). The NIST irradiance scale of 2000 has a smaller uncertainty than the NIST 1990 scale (Table 7) and is about 1.0–1.5% larger in intensity (Yoon et al. 2002).

Table 7. Typical irradiance values (in units of $\mu W\,cm^{-2}\,nm^{-1}$) and uncertainties as a function of wavelength (λ) for NIST spectral irradiance standards (Yoon et al. 2002). The uncertainties are relative expanded uncertainties ($k = 2$, where k is the coverage factor) and are shown for the 1990 and 2000 NIST scales.

λ [nm]	Typical Value	Uncertainty 1990	2000
250	0.02	1.8%	1.56%
350	0.85	1.1	1.12
655	17.0	0.7	0.63
900	23.0	1.1	0.47
1,600	12.0	1.4	0.33
2,400	4.00	4.4	0.57

FEL lamps have a limited calibration lifetime of about 50 h. To preserve the NIST scale over longer periods, it is necessary to transfer the irradiance scale to other lamps. Consequently, six lamps were procured from the NOAA Central Ultraviolet Calibration Facility (CUCF) and added to the lamp library (GS-017 through GS-022, inclusive). The CUCF† (Boulder, Colorado) is a joint project between NOAA and NIST whose mission is to provide highly accurate standards for UV monitoring networks in the US.

Because the quality of FEL lamps has deteriorated over the last years, the CUCF has refined methods to pot, screen, and season 1,000 W FEL lamps (Disterhoft 2005). CUCF procured and tested 50 lamps from Osram Sylvania and found the batch of lamps was very stable and did not exhibit emission lines of aluminum, which were observed in many lamps tested during the last years (pers. comm., Patrick Disterhoft, CUCF). The six lamps procured from CUCF showed excellent stability during their seasoning at CUCF, and it was confirmed that they do not exhibit any anomalous emission lines. These lamps were believed to be the best quality attainable at the time of purchase.

To add to the lamp library, six lamps were procured from Gamma Scientific (San Diego, California) who are one of a few vendors of potted and seasoned FEL lamps. The procured lamps were seasoned for 20 h before they were potted, and an additional 10 h after potting before they were shipped to BSI. Additional lamps from other vendors are currently being tested for possible inclusion in the lamp library.

Ohno (1997) stated that new incandescent lamps decrease in luminous intensity by 10% or more in the first few percent of their life, and that standard lamps must be seasoned at the rated operation current for more than 5% of the rated life. For FEL lamps, Ohno suggests seasoning at the rated current for 24 h, followed by more than 48 h at the operating current. The CUCF lamps were seasoned at the CUCF facility for more than 20 h before they were shipped to BSI. Seasoning times of the "V" and "GS" lamps are shorter than those recommended by Ohno (1997).

All of the uncalibrated lamps (starting with "V" or "GS") were operated for periods ranging from 4–35 h using the software described in Sect. 6.3.1. Lamp current and voltage were recorded and lamp irradiance was monitored with either the XGUV or OXR (Sect. 6.4). A summary of this lamp validation activity is provided in Fig. 25 and Table 8, which show a comparison of changes in irradiance ("drifts") that were calculated for all lamps from the radiometric measurements. In the visible, lamp drifts ranged between approximately −0.03% and +0.03% per hour, whereas in the UV, the drifts ranged between about −0.04% and +0.01% per hour. Although all lamps were

seasoned, drifts were typically larger during the first hours of testing. These results indicate some lamps should be seasoned for another 10–30 h before a calibration transfer.
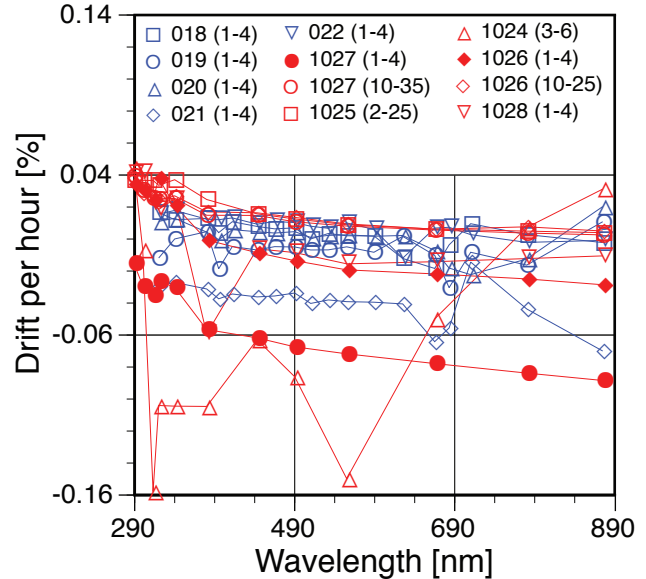
Fig. 25. The drifts in the uncalibrated "V" and "GS" lamps (blue and red, respectively) that are part of the OSPREy lamp library. Lamps that were tested twice are denoted with a solid symbol.

Table 8. A summary of lamp output drifts (in units of percent change per hour) for the uncalibrated lamps in the lamp library as a function of the UV and visible spectral domains.

Serial Number	Time On [h]	Drift	
		UV	Visible
V-017†			
V-018	4	0.011	−0.001
V-019	4	−0.006	−0.007
V-020	4	0.007	−0.001
V-021	4	−0.031	−0.042
V-022	4	0.014	0.005
GS-1019†			
GS-1024§	4		
GS-1025	25	0.034	0.009
GS-1026	25	0.027	0.010
GS-1027	35	0.027	0.008
GS-1028	4	0.015	−0.011

† Not tested.

§ Requires additional seasoning before establishing the long-term performance.

NIST asserts that well-seasoned FEL lamps should be stable to within 0.3% over a 24 h period. This translates to drifts less than 0.0125% per hour. This drift rate compares well to the drift rate of lamps of the "V" series. Lamps of the "GS" series show somewhat larger drifts, in particular below 350 nm. It appears prudent to season these lamps for an additional 10–30 h before calibrating them.

---

† Additional information concerning the CUCF and their joint mission with NIST is available on the following Web site: http://www.srrb.noaa.gov/calfacil/cucfhome.html.

6.3 Lamp Operation

Operating FEL standards of spectral irradiance at the highest level of accuracy entails demanding requirements for lamp setup and operation. Important factors to address include accurate control over the drive current for the lamp, meticulous lamp alignment, and good stray light suppression in the calibration dark room.

6.3.1 Control of Lamp Current

The output of an FEL lamp at 300 nm changes by about 1% per 0.1% change in the current used to power the lamp (Kostkowski 1997). To achieve the desired accuracy of better than 0.1% in the output of the lamp, the current has be controlled to better than 0.01%. This is not achievable with COTS digitally-controlled power supplies, because of the low resolution of these devices. Consequently, BSI developed a customized control system for powering a lamp, which consists of the following components:

- Power supply with analog control input (Agilent 6654A);
- High-precision voltage source (National Instruments NI-9263);
- High-quality digital multimeter (Agilent 34401A) for measuring the voltage drop across the shunt;
- High-accuracy shunt (Isabellenhuette ISA-PLAN Precision Resistor Type RUG-Z) and;
- Custom LabVIEW software (National Instruments) to set, monitor, and control the lamp current.

Current is supplied to the lamp posts, and lamp voltage is monitored at the opposite (kinematic) contacts. A high-capacity uninterruptible power supply (UPS) is integral to the system to prevent sudden power losses or fluctuations at the lamp in case of a power outage, brownout, or surge.

With this system, it is possible to set and maintain the lamp current to within a precision of $\pm 50\,\mu A$ (0.0006% for a target current of 8.2 A). The accuracy of the current is only limited by the calibration uncertainty of the shunt of less than $\pm 0.002\%$. LabVIEW software was developed that allows the system to execute the following:

1. Linearly ramp up the lamp current over several minutes using the digital input of the power supply to a point 25 mA below the specified current.

2. Finely tune the lamp current to within $\pm 50\,\mu A$ using the analog programming terminals of the power supply and a 16-bit ADC reading the voltage across the shunt.

3. Monitor the voltage at the lamp terminals, plus the temperatures of several key components (multimeter, laboratory, and shunt).

4. Display the lamp current, voltage, and power plus deviation from established lamp voltage.

5. Write all measurements and ancillary information (e.g., cumulative lamp usage time) into databases.

A screenshot of the software in operation is provided in Fig. 26, which is divided into three columns. The left column is used to select the shunt and lamp, to turn on the lamp, and to actuate the shutter used for dark current measurements. The center panel gives an overview of the lamp current, voltage, and power, and indicates whether the lamp has reached a stable state. The current and voltage reported by the power supply, plus lamp usage times are also displayed. The right column provides time-series plots of temperature at several locations in the laboratory, as well as lamp voltage, current, and power.
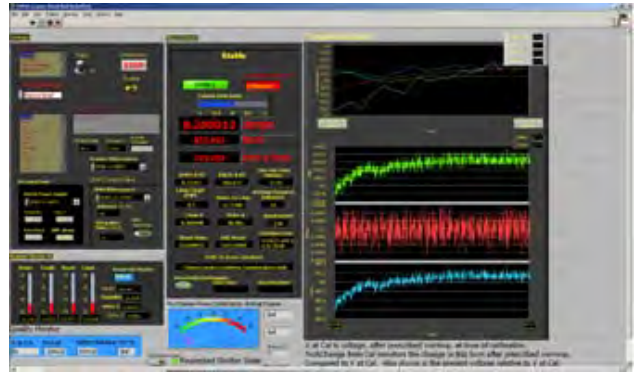
Fig. 26. The software control panel for operating FEL lamps.

6.3.2 Laboratory and Lamp Setup

The BSI calibration laboratory was upgraded in 2009 to meet the requirements for high-accuracy calibration transfers. Materials (e.g., paints, walls, and curtains) with low reflection in the infrared were selected to reduce uncertainties from stray light in the SWIR wavelengths. The laboratory is temperature stabilized to within 1°C. The temperature and humidity are measured at several locations including the lamps, bases, and radiometers; and air flow disturbance from air conditioning vents is minimized.

6.3.2.1 Irradiance Bench

A new irradiance optical bench was designed and constructed. Using occulting devices placed in the direct optical path between the lamp and collector, stray light contributions at all wavelengths was confirmed to be less than 0.1%. Transfer radiometers are positioned in kinematic mounts, which allow reproducible instrument removal and reinstallation. Lamps are mounted in a kinematic lamp socket designed by NIST (Zalewski et al. 1972), which is attached to a stack of linear and tilt stages allowing precise alignment with respect to six degrees of freedom. Baffles between the lamp and radiometer were designed using NIST guidelines (Yoon and Gibson 2011) to further minimize stray light. The laboratory back wall is covered with black fabric tested for minimum reflectivity to reduce on-axis reflections and is 2 m away from the lamp.

A computer-controlled shutter was installed between the lamp and radiometer for automated dark-current measurements. A laser alignment system was added to allow fast and reliable alignment of lamps and transfer radiometers. Correct alignment of a radiometer can be verified by placing a mirror placed in front of the radiometer and confirming that the laser beam reflects back on the laser aperture. Similarly, a standard lamp alignment jig, having a window with etched crosshairs to mark the location of the lamp, can be inserted in the lamp holder to verify the lamp is correctly positioned (Fig. 27). The distance between the lamp and radiometer is adjusted with the aid of an aluminum rod that is precisely machined to 50 cm.
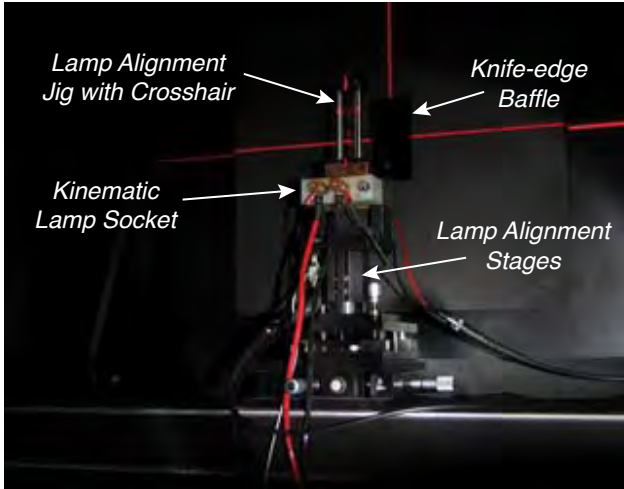
Fig. 27. The irradiance bench lamp alignment assembly. The red lines are generated by the alignment laser, which defines the optical path and is used to center the crosshair of the alignment jig.

6.3.2.2 Radiance Bench

The BSI radiance optical bench was also improved. The lamp is mounted 290 cm away from a Spectralon plaque made by Labsphere, Inc. (North Sutton, New Hampshire). The bidirectional reflectance distribution function (BRDF) of the plaque is regularly calibrated by Labsphere. Black baffles held in place with flat-black frames are mounted between the lamp and plaque to reduce stray light. Black curtains, which were selected to have low reflectivity in the visible and infrared, were installed to block light paths other than the direct path from lamp to plaque.

Dual mounts were designed and installed, which enable reproducible radiometer alignment and accurate pointing to the center of the plaque from opposite sides at 45° angles. The setup allows for the installation of two radiometers at the same time wherein one radiometer can be a monitoring device, which stays in place during an entire series of calibration transfers. The second holder can accommodate radiometers to be calibrated or recalibrated. The radiance test bench is also equipped with a laser alignment system and a computer-controlled shutter for automated dark-current measurements.

6.4 Lamp Transfer Radiometers

The individual lamp library lamps were characterized with the XGUV and the OXL instruments. These radiometers can also be used to transfer irradiance scales from one lamp to another. The XGUV has been in service at the BSI calibration facility for several years, is optimized for UV transfers with a 290–875 nm spectral range, and is used on the irradiance optical bench. The OXL instrument spans 340–875 nm with microradiometers and 325–790 nm with a spectrograph, which is normally mounted on the radiance calibration bench; and the OXE instrument spans 320–1,640 nm with microradiometers and 250–785 nm with a spectrograph.

The OXE instrument was not used for the lamp characterizations and is presented to complete the description of the OXR instrumentation developed for the OSPREy activity (it is the companion sensor to the OXL). The centroid wavelengths for the XGUV and OXL instruments are presented in Table 9.

Table 9. Nominal (left column) and centroid wavelengths of the XGUV and OXL sensors used as lamp transfer radiometers.

λ [nm]	XGUV [nm]	OXL [nm]
289	291.29	
300	301.13	
313	311.24	
320	319.18	318.19
340	339.12	339.12
380	379.92	379.33
395		395.64
412		411.06
443	442.62	441.92
465		464.07
490	489.08	488.96
510		509.26
532		530.40
555	554.43	553.21
589		588.55
625		624.46
665	665.46	663.87
683		682.98
710		708.06
780	779.46	777.63
875	875.07	873.42

6.4.1 The XGUV

The XGUV is based on PRR electronics and GUV-2511 radiometers, and has 12 channels. Spectral response functions of each channel were measured with the BSI spectral tester (Bernhard et al. 2005) and their centroid wavelengths λ_i^c were calculated. Nominal and centroid wavelengths are summarized in Table 9. The XGUV is

equipped with a cosine collector and temperature stabilized to ±0.1°C.

6.4.2 The OXL

The OXL is a laboratory instrument designed to monitor and transfer radiance calibrations. It combines filter-photodetector technology at 18 discrete wavelengths (Table 9) with a high-resolution spectrograph, Hamamatsu model C9407MA (Bridgewater, New Jersey). The OXL is temperature stabilized to about ±0.1°C, and the radiance fore optics have a 17° FVA. The spectrograph spans 325–793 nm, with bandwidths of 7 nm in the UV and 5 nm in the visible, and has a complementary metal oxide semiconductor (CMOS) detector with 256 pixels and 16 bit digitization. The OXL is a very stable, hybridspectral radiometer; ideal for radiance measurements of calibration sources such as a 1,000 W FEL irradiance standard used in conjunction with a calibrated reflectance plaque.

6.4.3 Software for Lamp Spectra

Data measured by transfer radiometers are written to a centralized Structured Query Language (SQL) database. Software was developed to parse this database and calculate a summary of a measurement sequence. The results include the means and standard deviations of *light* and *dark* data sequences. These measurements are also compared with the previous usage of a given lamp, and the ratio of the two measurements is graphically displayed. This feature allows real-time assessment of lamp drifts while the lamps are still being used. Queries of the databases can also be used to retrieve the lamp usage history, current and voltage stability, and laboratory conditions (temperature and humidity) during calibration activities.

6.5 Lamp Transfer Uncertainties

Comparisons of lamp library FEL standards, as well as the transfer of an irradiance scale between lamps, should ideally be performed with a radiometer that has an infinitesimally small bandwidth. From a practical point of view, such a radiometer cannot be designed and manufactured. Instead, this section discusses uncertainties associated with using moderate-bandwidth radiometers, such as the XGUV and OXR. The channels of these radiometers have approximately a rectangular (box-shaped) slit function with a nominal bandwidth of about 10 nm.

6.5.1 Setup of Analytical Functions

Systematic uncertainties from a moderate-bandwidth instrument depend mostly on differences in the shape of the spectrum associated with the FEL lamp†. For this

---

† If two lamps with different brightness, but identical spectral shape are compared, the bandwidth of the instrument would not affect the transfer.

analysis, analytical functions $\Phi(\lambda)$ were fitted to the irradiance values $E(\lambda)$ of several FEL lamps from various manufacturers (Table 10). These functions formed the basis of the analysis presented in the following subsections.

Table 10. The lamps used for uncertainty estimates.

Lamp	Manufacturer	Amps	Origin
F-614	Osram Sylvania	8.2	NIST
F-615	Osram Sylvania	8.2	NIST
F-616	Osram Sylvania	8.2	NIST
91537	General Electric	7.9	Gamma Scientific
BSI-1	Ushio	8.2	Gamma Scientific
BSI-2	Ushio	8.2	Gamma Scientific
HEC-1631	Unknown	8.0	Hofmann
HEC-1632	Unknown	8.0	Hofmann
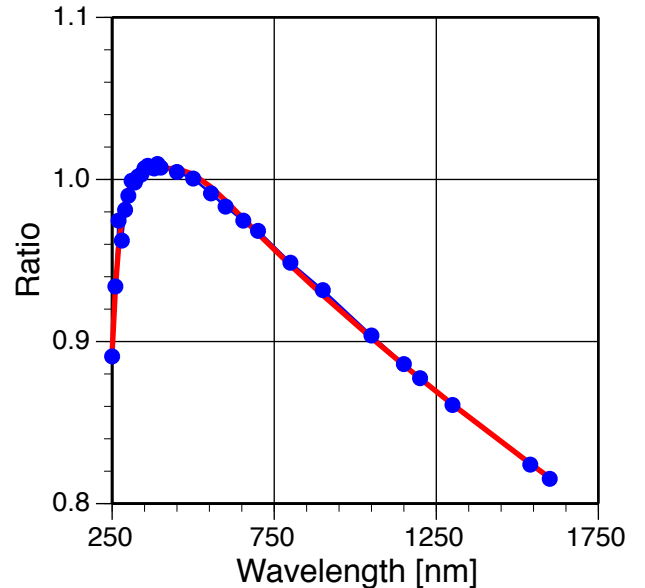
Fig. 28. The ratio of irradiance calibration values for NIST lamp F-616 to a black-body fit (blue). The red line is the inverse of the fit function $f(\lambda)$.

To determine $\Phi(\lambda)$, black-body (or Planck) functions, $P(\lambda)$, were fitted to the lamps' irradiance tables. In a second step, functions of the form

$$f(\lambda) = 1 + \eta_1 e^{-\eta_2(\lambda-\eta_3)} + \frac{\eta_4 + \eta_5\lambda + \eta_6\lambda^2}{1 + e^{-(\lambda-\eta_7)/\eta_8}} \quad (5)$$

were fitted to the ratio of $P(\lambda)$ and $E(\lambda)$, where λ is wavelength, and η_i are eight fit coefficients. Figure 28 shows
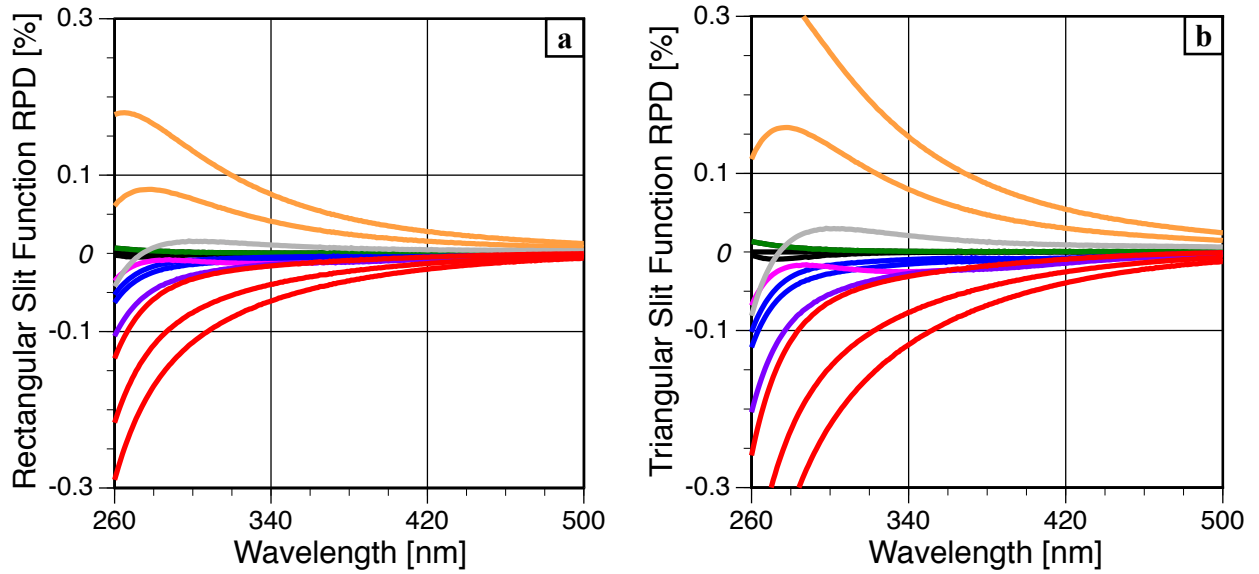
Fig. 29. The systematic uncertainties involved when using a hypothetical spectroradiometer for lamp transfers that has two different slit functions of 10 nm FWHM: **a)** rectangular (or box-shaped), and **b)** triangular. The uncertainties are computed with NIST lamp F-614 as the reference in the RPD calculation (Sect. 1.1.2). The lamps involved are shown in groups. The *real* lamps are NIST FELs 614, 615, and 616 (black); 91537 (green); BSI lamps 1 and 2 (blue); HEC-1631 (violet); and HEC-1632 (purple). The black-body functions are shown as a function of temperature ranging from 2,800–2,900 K (orange), 3,000 K (gray), and 3,100–3,300 K (red).

the ratio $E(\lambda)/P(\lambda)$ and the associated inverse of the fit function $f(\lambda)$ for NIST lamp F-616. The fit was equally good for all lamps, indicating that functions of the type $\Phi(\lambda) = P(\lambda)/f(\lambda)$ are an excellent analytical representation of FEL irradiance tables.

6.5.2 Effect of Bandwidth

Figure 29a shows the effect of using a hypothetical spectroradiometer that has a rectangular (box-shaped) slit function of 10 nm full-width at half-maximum (FWHM). The first eight data sets were calculated based on the real lamps described above. The remaining data sets are based on black-body functions with color temperatures ranging between 2,800–3,300 K. All data sets are with respect to NIST lamp F-614. Figure 29b shows a similar figure for a hypothetical instrument with a triangular slit function of 10 nm FWHM (20 nm at the base). In both figures, the maximum uncertainty at 300 nm is smaller than 0.3%, and smaller than 0.1% for wavelengths larger than 370 nm. These uncertainties are considerably smaller than the uncertainty of lamp irradiance tables issued by NIST. It can therefore be concluded that moderate-bandwidth radiometers such as the OXR radiometers are more than adequate for the transfer of calibrations from one FEL lamp to another.

6.5.3 Calibration Transfer Simplifications

The signal (amplitude) A of channel i of a moderate-bandwidth radiometer measuring a lamp is proportional to

$$A(\lambda_i) = \int \gamma(\lambda_i)\, E(\lambda)\, d\lambda, \qquad (6)$$

where $\gamma_i(\lambda)$ is the spectral response function of channel i and $E(\lambda)$ is the spectral irradiance of the lamp. When comparing two lamps with irradiance $E_1(\lambda)$ and $E_2(\lambda)$, the ratio Υ of the signals is:

$$\Upsilon(\lambda_i) = \frac{\int \gamma(\lambda_i)\, E_1(\lambda)\, d\lambda}{\int \gamma(\lambda_i)\, E_2(\lambda)\, d\lambda}. \qquad (7)$$

In practice, this ratio is not evaluated. Instead the simplified ratio Υ' is calculated, which is defined as:

$$\Upsilon'(\lambda_i) = \frac{E_1(\lambda_i^c)}{E_2(\lambda_i^c)}, \qquad (8)$$

where λ_i^c is the centroid wavelength of channel i calculated from the response function $\gamma(\lambda_i)$.

An analysis of the systematic uncertainty introduced by this simplification was made by computing the ratio of $\Upsilon'(\lambda_i)$ to $\Upsilon(\lambda_i)$. The data were once again referenced to NIST lamp F-614. The uncertainty was found to be largest at the shortest wavelengths. For the comparison of *real* lamps, the uncertainty was less than 0.2% at all wavelengths. The uncertainty only exceeded 0.3% when lamps with color temperatures below 2,900 K or above 3,300 K were used. The latter is likely not an issue when comparing FEL lamps, but could become an issue when lamps of another type are used in the lamp library in the future

(recalling that the lamp library cannot remain a static inventory, because lamps have finite lifetimes and inevitably are replaced). It was concluded that the *centroid* method was adequate for lamp comparisons.

6.5.4 Uncertainties

The measurement of response functions is affected by uncertainties, and this may also lead to some uncertainty in the calculation of the centroid wavelength for each instrument channel. To study this effect, spectra of all test lamps were shifted by 1 nm and compared to the unshifted spectra, and following the procedure used in earlier (Sect. 6.5.2), the computations are with respect to NIST lamp F-614. The results are presented in Fig. 30 following the presentation scheme established for Fig. 29 (but note the change in scales). For wavelengths above 300 nm, systematic uncertainties due to 1 nm wavelength shifts are smaller than 0.5% in all cases. For the subset of *real* lamps, uncertainties are smaller than 0.15%.
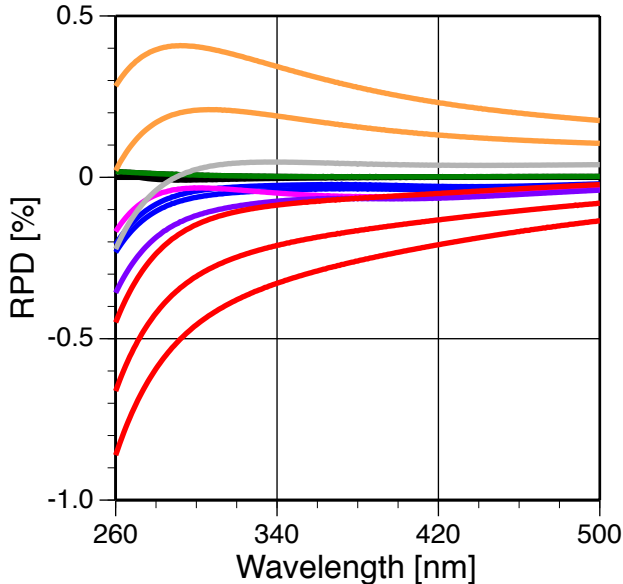

Fig. 30. The uncertainty (expressed as the RPD with respect to NIST lamp F-614) caused by a 1 nm shift in the centroid wavelength.

An uncertainty of 1 nm in the centroid wavelength for a particular channel is, therefore, adequate. The BSI spectral tester allows measurements of spectral response functions of the multichannel instruments with uncertainties of approximately 0.1 nm. Uncertainties resulting from the wavelength mapping of spectral response function measurements are, therefore, a negligible contribution to the overall lamp transfer uncertainty.

6.6 Lamp Usage Protocol

Prior to using a lamp, the correct alignment of the test setup is verified using the laser alignment system (Sect. 6.3.2.1). The FEL to be used is inserted into the lamp holder, with its identification tag facing away from the sensor. The computer-controlled power supply is turned on and slowly ramped up (to avoid thermally shocking the filament) until the proper operating current for the particular lamp is achieved.

Following a warm-up time of at least 15 min, the shutter of the test bench is closed and dark-current measurements are taken for a 1 min period. The shutter is then opened and *light* measurements are recorded. Lamp currents, voltages, and other parameters provided by the LabVIEW software (Sect. 6.3.1), as well as measurements of the transfer radiometer are written to SQL databases. On completion, the lamp current is slowly ramped down (to avoid thermally shocking the filament), and the lamp is removed from the holder only after it has cooled down completely.

6.7 Lamp Comparisons

All lamps of the OSPREy lamp library that have a calibration certificate were compared on both the radiance and irradiance optical benches. Lamps were powered using the LabVIEW software and allowed to warm up for at least 20 min. After the warm-up period, the dark currents of the transfer radiometers were measured for 1 min, followed by 1 min of *light* measurements. Lamp V-020 was measured on both calibration benches at the beginning and end of the comparison sequences to verify that the calibration setup (transfer radiometers, lamp power, alignment, and stray light in the laboratory) remained stable. These measurements indicated that the system did not change by more than ±0.15% over the course of the experiment.

As an example comparison, all of the measurements with lamp V-020 that were performed on the radiance bench are considered. The lamp was measured five times: in the morning and evening of the first day of measurements, and then three times on the following day. Ratios of all measurements with the OXR relative to the first measurement show the OXR microradiometer channels changed by less than ±0.1%, with the exception of the 710 nm channel, which had one outlier at 0.15%.

Measurements with the spectrograph were consistent at the same level, however, some data were affected by the spectrograph's *hot pixels* (i.e., pixels with locally higher dark value than their neighbors), most notably at 374.4, 406.5, and 656.5 nm. Spectrograph data were also affected by considerably more signal noise in the UV compared to the microradiometer channels. The relative uncertainty $u'(\lambda)$, which is caused by signal noise, is shown in Fig. 31, and is determined by

$$u'(\lambda) \;=\; \frac{\sqrt{\sigma^2(\lambda) + \widehat{\sigma}^2(\lambda)}}{\mu(\lambda) - \widehat{\mu}(\lambda)}, \qquad (9)$$

where $\mu(\lambda)$ and $\widehat{\mu}(\lambda)$ are the mean light and dark signals, respectively, and σ and $\widehat{\sigma}$ are the corresponding standard

deviations. For the microradiometer channels, $u'(\lambda)$ is smaller than 0.1%, except for the 380 nm channel, whose filter has lower transmission than that of other channels. For the spectrograph, $u'(\lambda)$ exceeds 1% for wavelengths smaller than 380 nm. This demonstrates that the spectrograph is less suitable for performing accurate lamp transfers in the UV at these radiance levels.
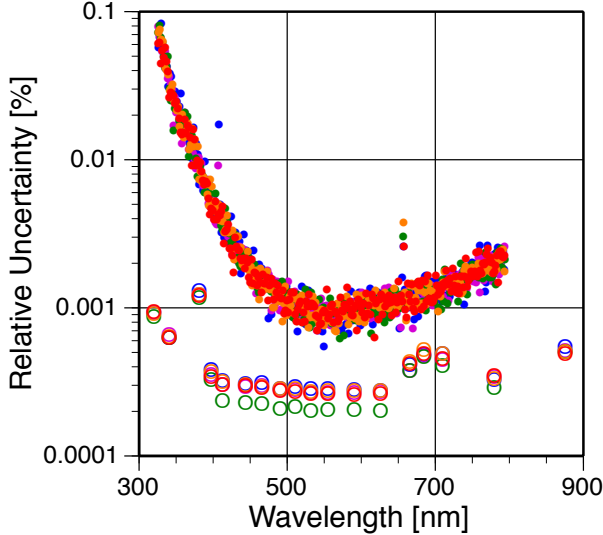
Fig. 31. The relative uncertainty of measurements in the OXR microradiometer channels (open circles) and the spectrograph (solid circles) determined from five measurements (different colors).

Lamps were compared relative to the NIST standard F-616, which is considered to be the most trustworthy lamp of the lamp library. First, it is traceable to the NIST 2000 scale, and second, the voltage drop when powered up agrees best with the value specified by NIST. The lamps were compared by calculating the so-called Γ_l values, which are ratios defined as

$$\Gamma_l(\lambda_i) \;=\; \frac{\mu_l(\lambda_i) - \widehat{\mu}_l(\lambda_i)}{\Phi_l(\lambda_i^c)} \left[\frac{\mu_r(\lambda_i) - \widehat{\mu}_r(\lambda_i)}{\Phi_r(\lambda_i^c)} \right]^{-1}, \quad (10)$$

where μ_l and $\widehat{\mu}_l$ are the 1 min means of light and dark measurements, respectively, of the transfer radiometer when measuring lamp l with channel λ_i; $\Phi_l(\lambda_i^c)$ is the value of the fit function of lamp l at the centroid wavelength that is associated with channel i; and r denotes the reference lamp (F-616). The denominator (the terms in brackets) of Γ_l includes similar quantities for the reference lamp.

Ten-parameter functions of the type introduced in Sect. 6.5.1 were fitted to the irradiance tables of all lamps. Figure 32 shows the residuals to these fits, expressed as the ratio of the fit functions, $\Phi(\lambda)$, to the irradiance values that are tabulated in the lamp certificates. Residuals are typically smaller than 0.25%. There is some variability at the shorter wavelengths in Fig. 32, which is due to *noise* in the tabulated values. Because the fit functions smooth this noise, it is believed that these functions provide values closer to the actual spectral irradiance of the lamps than the values of the certificates.
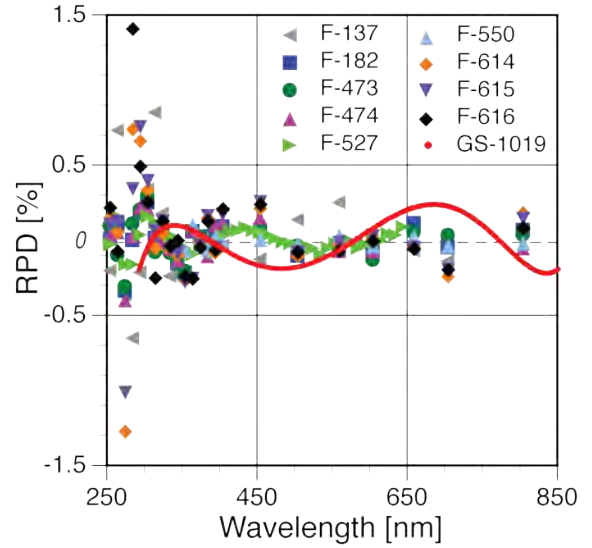
Fig. 32. The residuals of the 10-parameter fit, expressed by the ratio of fit functions $\Phi(\lambda)$ to the tabulated irradiance values $E(\lambda)$ of all lamps.

6.7.1 Irradiance Bench Comparison

Figure 33 shows Γ_l values determined from measurements using the irradiance bench and the XGUV as the transfer radiometer, but expressed as RPDs, by subtracting 1 from the ratio in (10) and multiplying by 100. There is excellent (better than 0.3%) agreement between lamps F-615 and F-616. Measurements of lamp F-614 are 0.5–1% too high. These high values were expected because the voltage drop across the contacts of the lamp was 108.107 V, which is 1.2% larger than the value reported by NIST (106.83 V). It is likely the lamp changed during transport from NIST to BSI (although the lamps were hand transported on an airline, not shipped by common carrier).
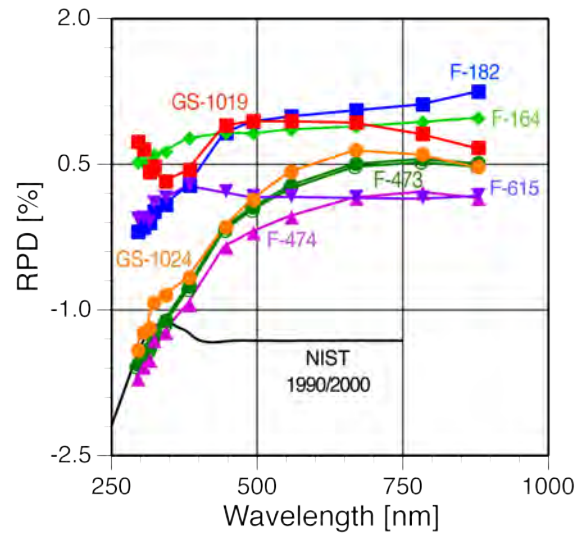
Fig. 33. The $\Gamma_l(\lambda_i)$ values for seven lamps expressed as an RPD and determined with irradiance bench comparisons using the XGUV.

The calibrations of all other lamps are with respect to the NIST 1990 scale. As expected, these lamps are lower in the UV by about 1.5% (see also the black line labeled NIST1990/NIST2000 in Fig. 33). The two measurements of lamp F-473 are very consistent. Lamp GS-1024 was calibrated against F-473 in August 2008 and not used since. The figure indicates that the irradiance scales of the two lamps were still in very good agreement on 7 January 2010. Measurements of lamp GS-1019 were high, even though it was also calibrated against F-473 in August 2008. In contrast to lamp GS-1024, it was used for 18 hours and the difference likely reflects its aging over time.

6.7.2 Radiance Bench Comparison

Figure 34 shows a similar comparison for measurements performed on the radiance bench using the OXR. Measurements for all lamps agree to within ±2%, except lamp F-137, which was not run on the irradiance bench. This lamp is very old; it was calibrated in 1982 against a DXW lamp, and some time ago during an intercomparison exercise, another laboratory wrapped the lamp in plastic while it was still hot. Some of the plastic melted on the glass envelope. When used for the trials presented here, no plastic was visible, but it is possible that the glass envelope was permanently damaged. It was included in the lamp library to set an end-member state as to what can be expected from a mishandled lamp.
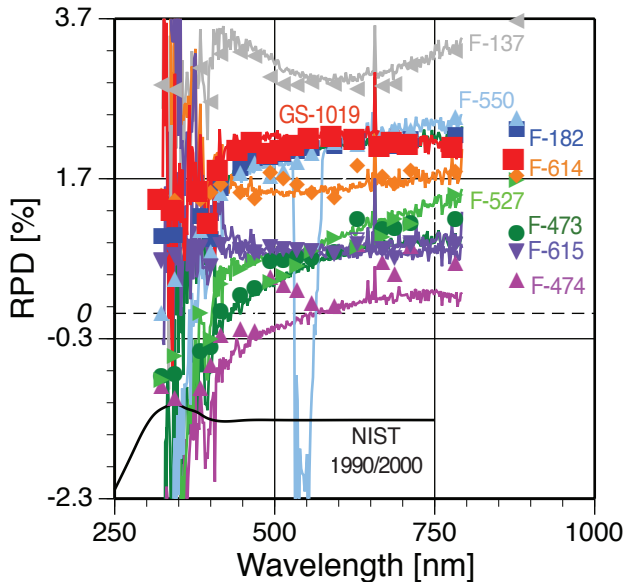
Fig. 34. The $\Gamma_l(\lambda_i)$ values for nine lamps expressed as an RPD and determined with the radiance bench using the OXR. Measurements of OXR microradiometer channels are indicated by symbols, and measurements of the spectrograph are indicated by the color-matched lines.

Lamp F-550 has the highest irradiance of all undamaged lamps (excluding F-137). The spectrograph saturated

between 530–580 nm when measuring this lamp (light blue line in Fig. 34). The hot spectrograph pixel at 656.5 nm is visible for most lamps as a notable spike in the data. Because of the many data sets plotted in Fig. 34, it is difficult to compare measurements of microradiometer channels and the spectrograph. Subsets of the figure were therefore redrawn, and are shown in Fig. 35.

Figure 35a shows the Γ_l values expressed as RPDs for lamps F-137, F-182, and F-527. The Γ_l values for microradiometer channels and the spectrograph generally agree well, with the exception of the UV wavelengths of lamp F-527 for which the spectrograph measurements are lower than the corresponding microradiometer measurements by up to 2%. This difference is likely caused by changes in the dark current for the spectrograph. The spectrograph is close to its detection limit at these wavelengths, and even small changes in dark current can have a significant relative effect.

Also note that there is a dip of about 0.5% in the Γ_l values for all three lamps at 395 nm, which is seen in both the microradiometer channels and the spectrograph. This dip is caused by an emission line of aluminum that is affecting lamp F-616, according to the lamp certificate issued by NIST. Disterhoft et al. (2005) reported that aluminum emission lines at 308, 309, 394, and 396 nm have become common in recent FEL lamps, while they were mostly absent in older lamps, such as F-137, F-182, and F-527. The lines are caused by aluminum that has been added to the tungsten alloy during production to improve its anti-sag properties.

Figure 35b shows the Γ_l values expressed as RPDs for lamps F-474, F-615, and GS-1019. The Γ_l values for the microradiometer channels and the spectrograph are very consistent for lamps F-615 and GS-1019. There is considerable variability in the measurements of the microradiometer channels for lamp F-474, which is not apparent in the spectrograph measurements. The reason for this variation is unknown, but it is possible the feature is caused by a combination of anisotropic lamp output and the fact that OXR channels do not point to the same spot of the plaque. The sensitivity of OXR measurements to the pointing direction is further discussed in Sect. 6.7.4. The effect of the aluminum line is also visible in the Γ_l values of the three lamps.

Figure 35c shows the Γ_l values expressed as RPDs for lamps F-473, F-550, and F-614. For lamp F-614, Γ_l values for the microradiometer channels and the spectrograph differ sharply at wavelengths below 380 nm. This difference is caused by dark-current drifts of the spectrograph. While for all other lamps "dark" and "light" currents were measured immediately after the other, measurements of lamp F-614 were 1.5 h apart. The Γ_l values of lamp F-614 does not indicate a dip from an aluminum emission line. Lamps F-614 and the reference lamp F-616 are likely affected by this line equally, and the effect cancels when forming the ratio. Spectrograph measurements of lamp F-550 saturated as discussed earlier.
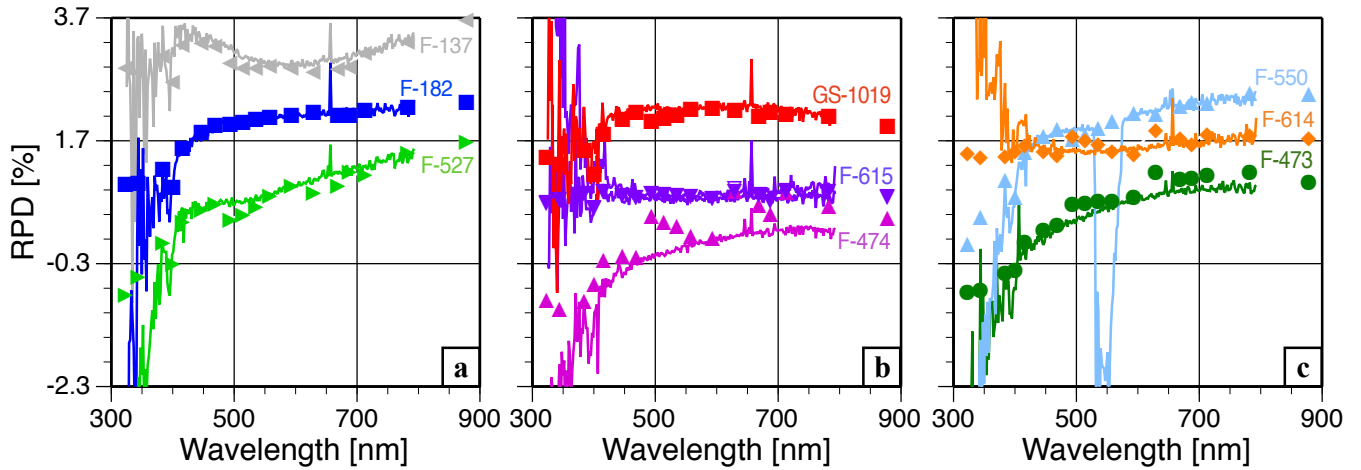
Fig. 35. a) Same as Fig. 34, but for subsets of the lamps: **a)** F-137, F-182, and F-527; **b)** F-474, F-615, and GS-1019; and **c)** F-473, F-550, and F-614.

6.7.3 Comparison of Measurements

Figure 36 compares $\Gamma_l(\lambda_i)$ values expressed as RPDs determined with both the irradiance and radiance benches. The pattern is generally similar, for example, Γ_l values for lamps F-473 and F-474 show a comparable increase with wavelength on both benches. The Γ_l values determined on the radiance bench tend to be higher by 0.5–1.2% than those for the irradiance bench.
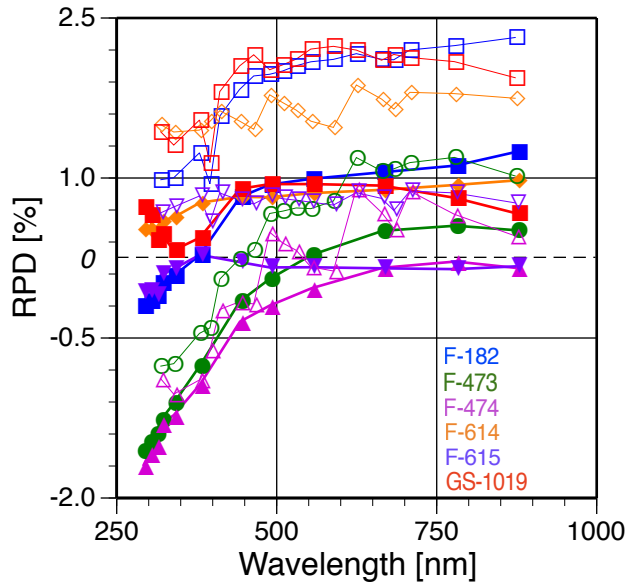
Fig. 36. A comparison of $\Gamma_l(\lambda_i)$ values expressed as RPDs determined with the irradiance (solid symbols) and radiance (open symbols) benches. Measurements with the same lamp are shown in the same color.

The reason for the higher values on the radiance bench is likely rooted in the common reference, lamp F-616. The voltage drop across the lamp terminals was monitored with

the LabVIEW software on both benches and agreed to within $11\,\mathrm{mV}$ (or 0.01%). It is believed that the radiative output was virtually identical during both uses of the lamp. One explanation of the discrepancy is a possible anisotropic output of the lamp. After the measurements were completed, it was discovered that the lamp holder was rotated by 1°. If the radiant intensity of lamp F-616 were different by 0.5–1% at 1°, compared to its normal orientation while other lamps have a more isotropic output, the difference could be explained.

The excursion from the aluminum line at 395 nm is only apparent in OXR measurements. The XGUV used on the irradiance bench does not have a channel at 395 nm (Table 9), so the aluminum line cannot be detected.

6.7.4 Effect of OXR Pointing Direction

The microradiometer channels of the OXR are arranged within a hexagonal grid, so each channel points to a slightly different spot on the plaque. Channels on the outer rim are approximately $2\,\mathrm{cm}$ away from the channel in the center, and point to a spot of the plaque that is approximately $3\,\mathrm{cm}$ away from its center. It can be expected that signals change when the instrument is rotated. First, the plaque should be brightest in the center because this point is closest to the lamp. The distance between lamp and plaque is approximately $280\,\mathrm{cm}$. The center of the plaque should be a factor of $(280^2 + 3^2)/280^2 = 1.00011$ brighter than a spot $3\,\mathrm{cm}$ away from the center. The difference of 0.011% can be considered negligible. Second, if the radiant intensity of a lamp is not isotropic, the illumination pattern of the plaque differs from that expected from a point source. Finally, the BRDF of the plaque may not be completely homogeneous.

To measure the effect of the pointing direction, the OXR was rotated in its holder in steps of 90°, and measurements at 0°, 90°, 180°, and 270° were compared. Results indicate that rotation changes the instrument's signal

by up to 1.7%. This is much larger than the change expected from the variation in plaque brightness calculated from a point source. This indicates that the radiant intensity of the test lamp (V-020) is indeed anisotropic. This anisotropy contributes to uncertainties of lamp transfers using the radiance bench. These uncertainties can be reduced by reducing the distance between transfer radiometer and plaque, or by reducing the FVA of the transfer radiometer.

6.8 Usage of OSPREy Lamp Library

Lamps of the OSPREy lamp library have to be intercompared at regular intervals (e.g., annually) to confirm that the irradiance preserved by these standards is constant in the long term. Some lamps of the library are used regularly to validate the calibration of EMR sensors in OSPREy systems, and it is particularly important to ensure that these lamps are stable. The frequency of lamp intercomparisons is based on the following:

- NIST standards should be operated as infrequently as possible to preserve their calibration over the long term (e.g., 15 or more years), so the annual operating time should ideally be not more than 2 h (thereby not exceeding their recommended calibration lifetime of about 50 h).

- Lamps that are used to calibrate radiometers used in the OSPREy activity should be intercompared with each other and NIST lamps after 20 h of usage or less (more frequent checks may be necessary if a lamp's voltage changes by more than 0.3%).

- Lamps should ideally be used in pairs for radiometer calibrations so that any inconsistency becomes immediately obvious.

- Whenever lamps are intercompared, the lamp that is run at the beginning of the test series should also be run at the end to confirm stability of the transfer radiometer.

A complete operation of a lamp—including ramp up, measurement, and cool down—takes about 1 h. It is, therefore, not practical to compare more than 10 lamps in one day.

Based on these considerations, the following "OSPREy Lamp Library Usage Protocol" was established and used for all lamps in the lamp library:

1. Operate every uncalibrated lamp of the OSPREy lamp library ("V" and "GS" lamps) for another 10–30 h to confirm their stability with either the XGUV

or OXR. This is necessary because preliminary tests reported in Sect. 6.2 suggest some lamps are still drifting at a rate larger than typical for this lamp type.

2. Compare all lamps using the OXR radiometers on the irradiance and radiance benches, and transfer calibrations to the "V" and "GS" lamps. This establishes a baseline value for each lamp over the full wavelength range (300–1,600 nm). This also allows for a comparison of the NIST SIRCUS irradiance scale that will eventually be transferred to OXR instruments with the NIST FASCAL scale of the FEL standards.

3. Divide the "V" and "GS" series of lamps into three categories:
   - Category 1 lamps are routinely used to check the radiometers used in the OSPREy activity.
   - Category 2 lamps are only used if measurements of "Category 1" lamps are inconsistent.
   - Category 3 lamps are considered long-term standards and should only be used every five years or if "Category 2" lamps become inconsistent.

   Note: "Category 1" lamps should be used in pairs such that inconsistencies that would require double checking with "Category 2" lamps become immediately apparent.

By using this protocol and its hierarchical approach, the amount of time a NIST standard is powered on can be reduced considerably. The goal is to compare lamps only when necessary to minimize lamp usage.

6.9 Conclusions

Twenty-one lamps were identified to become part of the OSPREy lamp library. This library, in combination with the OXR instruments, helps maintain the spectral irradiance scale for a time period of 15 years or more. Some lamps of the "V" and "GS" series should be seasoned for some additional hours until drift rates are within the expected range of this lamp type. Systems for powering and operating lamps, and the radiometers used, proved more than adequate to reliably transfer irradiance scales from one lamp to another. Problems in the existing setup, such as the rotation-dependence of OXR measurements, were identified, and experience gained from operating and comparing lamps helps to further improve the setup.

Chapter 7

Spectrograph Testing and Review:
An Engineering Analysis of COTS Spectrographs

Germar Bernhard, Vi Quang,
Thomas Comer, Charles R. Booth, and John H. Morrow
Biospherical Instruments Inc.
San Diego, California

Stanford B. Hooker
NASA Goddard Space Flight Center
Greenbelt, Maryland

Abstract

EMR sensors are hybridspectral instruments with 19 fixed wavelength microradiometers plus an integrated spectrograph. Requirements for these devices are challenging, because they represent two sensing technologies in one housing, which must both sample a very wide dynamic range—the very bright Sun and the relatively much darker ocean. Candidate devices must be sufficiently sensitive to detect the low signals inherent in OSPREy work in the red region of the spectrum above seawater, exhibit sufficiently accurate spectral selection, stable dark noise, and good temperature stability. A review of commercial spectrograph manufacturers identified a large number of instruments, from which 10 spectrographs were obtained and systematically tested. The latter included two from Hamamatsu, three from Avantes, four from Zeiss/Tec5, and one from B&W Tek. Testing protocols included the analysis of the following: a) wavelength range, b) spectral resolution, c) slit function, d) dynamic range, e) out-of-band rejection, f) stray light, g) saturation, h) change of dark signal with integration time and temperature, i) spectral responsivity, j) noise equivalent irradiance or radiance, and k) linearity. The test results indicate that an ideal instrument does not exist, but workable candidates are available. For example, all instruments suffer from stray light and nonlinearity to some degree, which limits their usable dynamic range and measurement accuracy. After considering all tests results and other factors relevant for operation and system integration, it was determined that the MMS UV-VIS II and MMS1 spectrographs from Zeiss/Tec5 were the most suitable devices for OSPREy applications.

7.1 Introduction

The radiometers used in the OSPREy activity are hybridspectral instruments with fixed wavelength microradiometers plus an integrated spectrograph. The addition of the spectrograph permits sampling of spectra in regions not covered by filtered detector channels. Spectrograph data can be used to account for any spectral features in measurements of water-leaving radiance that are caused by absorbing and scattering compounds in the water, which cannot be spectrally resolved by the microradiometer channels. The spectrum can then be convolved with the spectral response of the satellite channels, and the resulting values can be compared with satellite measurements. Furthermore, the addition of a spectrograph allows for the detection of unwanted emission lines in spectra of calibration sources. The advantage of the higher resolution of the spectrograph can be combined with the superiorities of the filter radiometers—greater dynamic range, lower stray light, better SNR, and higher sampling speed—to provide a sensor combination superior to either of the individual constituents alone.

Spectrograph requirements for OSPREy applications are challenging, because they must sample a very wide dynamic range—the very bright Sun and the relatively much darker ocean. Candidate devices must be sufficiently sensitive to detect the low signals inherent in OSPREy work in the red region of the spectrum above seawater, exhibit sufficiently accurate spectral selection, stable dark noise, and good temperature stability. This chapter presents the results of a detailed engineering analysis of candidate spectrographs available for integration into OSPREy.

A review of spectrograph manufacturers identified a large number of instruments, from which 10 spectrographs

were obtained and systematically tested. The list includes two from Hamamatsu (models C9407MA and C9408MA), three from Avantes (AvaSpec models 1024, 2048×14, and 2048), four from Zeiss/Tec5 (MCS PDA, MCS CCD, MMS UV-VIS II, and MMS1), and a BTC112E from B&W Tek. Because some instruments were only available for a limited amount of time (e.g., one week), not all tests could be performed with all instruments. A photograph of a Zeiss/Tec5 MMS spectrograph with the fiber optic bundle (i.e., the "fiber optics") is shown in Fig. 37.

Fig. 37. The Zeiss/Tec5 MMS spectrograph with the fiber optics shown alongside a microradiometer for scaling purposes. A fully assembled microradiometer, with metal sleeve and front-end optics, has a dimension of $0.435 \times 3.79 \, \text{in}^2$.

7.2 Test Protocols

The instruments were tested in the BSI calibration facility. Wavelength range was first established by mapping wavelength versus pixel and then determining the wavelengths of the first and last pixel. This was done by using polynomial mapping functions provided by the manufacturer or by establishing these functions through scanning the spectrum of a mercury wavelength standard.

The spectral resolution of a spectrograph depends on the number of rules per millimeter of the grating, the width of the entrance slit, and the number of adjacent pixels of the array that are averaged. Slit functions were determined from scans of mercury and argon lines of a low-pressure wavelength standard. Gaussian functions of the type $a \exp \left[-b(\lambda - c)^2 \right]$ were fitted to the measured data points for comparison. Bandwidth (FWHM) of all instruments was calculated from available mercury and argon lines, as well as the 633 nm line of a HeNe Laser.

Out-of-band rejection is defined as the background radiation level when measuring a spectral line at wavelengths far from that line. It is quantified here as the ratio of the far-field background signal to that of the spectral line. When measuring a light source with a continuous spectrum (e.g., a tungsten lamp or the Sun), the background signal results from the combined contributions of a large wavelength band. If the radiation level at a given wavelength is

very small, the out-of-band *stray light* contribution can become as large as the signal. This is a common occurrence for solar measurements in the UV-B, because absorption by atmospheric ozone causes a very rapid decrease of spectral irradiance for shorter wavelengths. Stray light can also cause large calibration uncertainties.

The out-of-band stray light for each spectrograph was evaluated using the 632.816 nm line of a HeNe laser. Side modes were *cleaned up* by pointing the laser beam on a grating and directing the beam that was diffracted towards a slit. The beam exiting the slit was directed onto a diffuser made of PTFE that was mounted in front of the entrance optics of the instrument to be tested. For each instrument, these laser scans were *stitched* together from measurements at two integration times to extend the dynamic range of the units. For example, a short integration time is needed close to the peak of the laser line to avoid saturation, while a long integration time is required away from the peak to measure stray light with sufficient detail.

Saturation and stray-light levels for solar measurements were determined by pointing the optical fiber connected to the candidate spectrographs directly at the Sun. No attempt was made to calibrate these spectra, because of the difficulties in obtaining an accurate irradiance calibration to fiber fore optics not equipped with a cosine diffuser. Measurements were performed with different integration times. When the signal of a spectrograph saturated at the shortest integration time possible, measurements were repeated by placing an ND filter of optical depth (OD) between 0.5–3.0 in front of the fiber optics.

At wavelengths below 320 nm, the solar irradiance is effectively absorbed by Earth's ozone layer and no signal is detectable below about 290 nm. The cutoff provided by ozone absorption can therefore be used to quantify stray light that is detected below 290 nm, but originates from photons with wavelengths in the visible and infrared.

The dark signal (i.e., no light enters the sensor aperture) generally depends on the array pixel and integration time, and is temperature dependent. Drifts in dark signal affect the detection limit of radiometers equipped with these detectors. Consequently, in addition to recording the dark values as a function of integration time, the temperature sensitivity of the dark signal of all spectrographs was characterized. Most test devices were not equipped with internal temperature sensors and an external sensor was mounted as closely as possible to the detector.

The spectral responsivity for each of the candidate spectrographs was determined both for irradiance and radiance calibrations. Spectral responsivity was determined by dividing net signals with the irradiance produced by the FEL lamp. It is important to note that spectral responsivity calculated this way is only accurate if the stray-light contribution to the net signal is negligible. As is shown below, this is generally not the case for any of the test instruments in the ultraviolet range. At short wavelengths, the stray-light contribution can be more than two orders of

magnitude larger than the signal resulting from photons of the desired wavelength. This problem makes the calibration a challenge and requires the use of *cut-on* filters to determine the spectral dependence of stray light. If the stray-light contribution is large (e.g., greater than 10% of the net signal), uncertainties of the stray-light correction may prevent accurate determination of the responsivity.

Radiance responsivity was determined using the candidate device's *bare* fiber (no fore optics attached), oriented towards the center of a Spectralon plaque with Lambertian characteristics, or with an FOV-limiting baffle arrangement. Bare fibers typically have a numerical aperture of 0.22, which translates into an FVA of about 25°. The baffle arrangement had an FVA of 2.5°, which is the designed FVA for radiometers used in the OSPREy activity. The plaque was illuminated by a calibrated FEL lamp mounted 287.1 cm away.

To determine responsivity for measuring irradiance, flat PTFE diffusers were fitted to the instrument's fore optics and placed a distance of 50 cm from a calibrated 1,000 W FEL lamp. Net signal was determined by subtracting *dark* measurements where any light reaching the diffuser was occluded and *light* measurement, where the entire lamp was visible from the diffuser. Measurements were performed at integration times ranging between several milliseconds and several seconds. Several light and dark scans were averaged together to reduce noise when calculating responsivity and its standard deviation. At integration times smaller than 10 ms, typically 100–200 samples were averaged. For integration times larger than 1,000 ms, 20 samples were averaged. Spectral responsivity was determined by dividing net signals with the irradiance produced by the FEL lamp.

Following (1), noise equivalent irradiance (NEI) of the spectrograph, $\mathbf{N}_E(\lambda)$, determines the smallest spectral irradiance that can be measured with a radiometer. NEI is defined here as the standard deviation of the dark signal, $\widehat{\sigma}$, relative to the irradiance responsivity:

$$\mathbf{N}_E(\lambda) \;=\; \frac{\widehat{\sigma}_E(\lambda, t_i)}{\gamma_E(\lambda, t_i)}, \tag{11}$$

where λ is wavelength, t_i is the integration time, γ is the responsivity, and the E subscript designates irradiance. NEI was calculated for all candidate spectrographs, and was not corrected for stray light. Noise equivalent radiance (NER) of the spectrograph, $\mathbf{N}_L(\lambda)$, is defined as the standard deviation of the dark signal to radiance responsivity (expanded here for completeness):

$$\mathbf{N}_L(\lambda) \;=\; \frac{\widehat{\sigma}_L(\lambda, t_i)}{\gamma_L(\lambda, t_i)}, \tag{12}$$

where the L subscript designates radiance. The wavelength range was also assessed for all instruments for which NER is sufficiently small to allow accurate calibrations with and without FOV-limiting fore optics.

Linearity of the candidate instruments was tested using a variety of approaches, some specific only to individual candidates. Because of the instrument-specific nature of the approach, the testing protocol is presented with the specific result for each spectrograph.

7.3 Candidate Instruments

The results from a market survey to select the best spectrograph for integration with OXR and EMR instruments resulted in the following potential COTS sources:

- Avantes (`www.avantes.com`) provides an extensive lines of fiber optic spectroradiometers using a symmetrical Czerny-Turner design. Six different detector arrays (photodiode, CMOS, and CCD†), and six gratings can be chosen. All models (except those equipped with Peltier coolers) have the same size, form factor, and software interface.

- B&W Tek (`www.bwtek.com`) offers a variety of array spectroradiometers equipped with CCD detectors. The most suitable model for OSPREy is the BTC112E series of spectrometers, equipped with a 2,048 pixel Peltier-cooled CCD array built into a small housing of $108 \times 95 \times 42 \, \text{mm}^3$.

- Hamamatsu (`www.hamamatsu.com`) makes so-called *mini-spectrometers*, which cover a wavelength range from 200–2,200 nm with a spectral resolution ranging from 1–9 nm. The available sensors include linear CMOS image sensors for the UV and visible, back-thinned CCD, and InGaAs linear sensors for wavelengths between 900–2,200 nm.

- Horiba/Jobin Yvon (`www.horiba.com`) makes the model VS-140 linear array spectrometer, which is a high-throughput $f/2.4$ system. The VS-140 features an aberration-corrected concave holographic grating and can be equipped with either a CCD or photo-diode array (PDA) detector for the wavelength range of 190–800 nm with 2.3 nm bandwidth.

- Ocean Optics (`www.oceanoptics.com`) supplies a variety of turnkey universal serial bus (USB) systems for a variety of applications ranging from absorbance, fluorescence, and Raman spectroscopy to spectroradiometric measurements.

- Labsphere (`www.labsphere.com`) markets a mini-spectrometer similar to the USB4000 spectrometer from Ocean Optics. This recently introduced unit uses a Sony linear silicon CCD array with 2,048 pixels and covers the wavelength range 200–1,100 nm.

- StellarNet (`www.stellarnet-inc.com`) builds several different ruggedized miniature fiber optic spectrometers, and the model EPP2000C would be the

---

† CCD is defined as charge-coupled device.

most suitable for OSPREy. It uses a concave grating, provides a CCD array detector with 2,048 pixels, and allows measurements between 280–900 nm with a resolution of about 1 nm.

- Zeiss/Tec5 (`www.tec5usa.com`) spectrographs are based on a monolithic body made of a patented ceramic structure, and they are all equipped with an aberration-corrected concave grating. The MCS and MMS models would be the most suitable for OSPREy. The MCS is available with a thermoelectrically cooled CCD array from Hamamatsu. MMS models are attractive because of their small size of $70 \times 60 \times 40 \, \text{mm}^3$.

In addition to the market survey, a literature search was conducted regarding the use of miniature spectroradiometers in atmospheric research. For example, Herman et al. (2006) used an Avantes AvaSpec-1024 spectrometer to measure atmospheric trace gases, and Kouremeti et al. (2008) built a spectroradiometer based on a Zeiss/Tec5 MCS module to measure solar irradiance and sky radiance in the UV spectral domain.

The specifications of the various models were subsequently compared to determine which units were the most promising for OSPREy. The following 10 demonstration models were acquired for testing, and are presented in Table 11:

- Hamamatsu models C9407MA and C9408MA;
- Avantes AvaSpec models 1024, 2048×14, and 2048;
- Zeiss/Tec5 models MCS PDA, MCS CCD, MMS UV-VIS II, and MMS1; and
- B&W Tek model BTC112E.

The two models from Hamamatsu are attractive because of their small size and comparatively low price. The three models from Avantes have almost identical optics, but are equipped with different detectors, either a CMOS linear image sensor (AvaSpec-1024) or CCD detectors (AvaSpec-2048x14 and AvaSpec-2048). While CMOS sensors are less sensitive than CCD arrays, they offer a considerably better SNR and can be used at higher light levels. One objective of the tests was to determine the better technology for OSPREy applications. Instruments by Zeiss/Tec5 promised the best wavelength stability and ruggedness, because of their monolithic design; the MMS UV-VIS II and MMS1 models were particularly attractive, because of their small size. The BTC112E from B&W Tek looked promising because of its integrated Peltier cooler.

7.4 Results

Table 11 presents the determinations for spectral range (λ_R) of each of the candidate instruments. Note that detectors based on silicon are relatively insensitive beyond 1,150 nm, and the usable wavelength range may, therefore, be smaller than shown.

7.4.1 Resolution and Slit Function

The Avantes AvaSpec models 1024 and 2048×14 spectrographs had 50 μm entrance slit widths. The spacing of array cells (i.e., the *pixel pitch*) was 25 μm for the model 1024 and 14 μm for the 2048×14. In order to get slit functions with the desired triangular or gaussian shape, the effective width of the exit slit of a spectroradiometer should match that of the entrance slit. Following the advice of the manufacturer, two pixels were averaged when using the AvaSpec-1024, three pixels for the AvaSpec-2048, and five pixels for the AvaSpec-2048×14. Measurements of all other units were not averaged.

Determinations of the slit functions for the Zeiss/Tec5 MCS CCD at 296.728, 435.833, 546.074, and 912.297 nm are shown in Fig. 38, which indicates good agreement between the measurements and the matching gaussian function. The slit functions are symmetrical, but the bandwidth increases substantially with wavelength. Slit functions of all other instruments, except those of the Avantes AvaSpec-2048 and the B&W Tek BTC112E, could also be well characterized with gaussian functions. The slit function of the BTC112E unit was very asymmetrical, in particular in the visible. It is possible the test unit was misaligned, but this could not be confirmed.
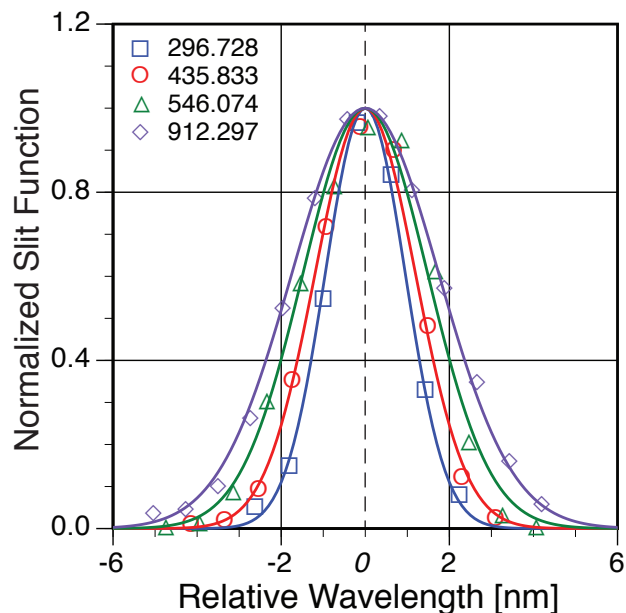
Fig. 38. The determinations of the slit functions for the Zeiss/Tec5 MCS CCD at four different wavelengths (in nanometers).

The bandwidths for the Avantes AvaSpec-2048 and the Zeiss/Tec5 MCS PDA units vary from 1.7–3.6 nm. The bandwidth of the Zeiss/Tec5 MCS CCD unit has a peculiar pattern, with a local maximum at 546 nm and a large increase towards longer wavelengths in the infrared. This pattern is consistent with test results of a similar unit reported by Kouremeti et al. (2008). The Hamamatsu

Table 11. The specifications of candidate spectrographs tested at BSI for the OSPREy activity. The Zeiss/Tec5 MCS PDA unit is referred to by the manufacturer as MCS; the MCS PDA designation used here is for better differentiation from the MCS CCD unit. The complete model name for the UV-VIS II unit is MMS UV-VIS II. Blank entries indicate a specification is either unknown or not specified by the manufacturer. The wavelength range is denoted λ_R and the wavelength resolution is denoted $\delta\lambda$.

Unit Specification	Hamamatsu		Avantes (AvaSpec)			MCS PDA	Zeiss/Tec5		MMS1	B&W Tek
	C9407MA	C9408MA	1024	2048×14	2048		MCS CCD	UV-VIS II		BTC112E
Layout	Czerny-Turner	Czerny-Turner	Symmetrical Czerny-Turner[a]	Symmetrical Czerny-Turner[a]	Symmetrical Czerny-Turner[a]	Concave Grating Spectrometer	Concave Grating Spectrometer	Concave Grating Spectrometer	Concave Grating Spectrometer	Crossed Czerny-Turner
TE Cooled	No	No	No	No	No	Optional	Yes	No	No	10–15°C
λ_R Avail.[b] λ_R Tested[d]	340–780 nm 340–780 nm	640–1,050 nm 640–1,050 nm	200–1,100 nm 200–1,100 nm	200–1,100 nm 200–1,100 nm	200–1,100 nm 200–1,100 nm	190–1,015 nm 300–720 nm	190–1,015 nm 190–995 nm	250–785 nm 250–785 nm	300–1,150 nm 300–1,150 nm	300–850 nm[c] 300–780 nm
$\delta\lambda$ Avail.[b] $\delta\lambda$ Tested[d]	9 nm 9 nm	9 nm 9 nm	0.15–20 nm 2.9–3.5 nm	0.04–20 nm 2.9–3.5 nm	0.04–20 nm 1.7–2.3 nm	2.4 nm[e] 2.4 nm	2.4 nm[e] 2.5–6 nm[f]	7 nm 6–8 nm	10 nm 9–10 nm	0.3–20 nm ~1.5 nm
Stray Light	<0.5%	<0.5%	<0.1%	<0.1%	<0.1%	0.1%	0.1%	<0.3%	<0.8%	0.05%[g]
Detector	CMOS Hamamatsu S8378-256N	CMOS Hamamatsu S8378-256N	CMOS Hamamatsu	CCD[h] Hamamatsu	CCD Sony	NMOS Hamamatsu S3904-512	CCD Hamamatsu S7031-1006	NMOS Hamamatsu S3904-256Q	NMOS Hamamatsu S3904-256Q	CCD
Pixels	256	256[i]	1,024	2,048×14	2,048	512[j]	1,048×64	256	256	2,048
Sensitivity[k]			120	16,000	20,000	1,000–10,000[l]	≫10,000[l]		≫10,000[l]	
Signal to Noise			2,000:1	500:1	200:1					
ADC	16 bit	16 bit	16 bit[m]	16 bit	16 bit	16 bit	16 bit	15 bit[n]	15 bit[n]	16 bit
Integration Time	5 ms–10 s	5 ms–10 s	2.2 ms–10 min	2.2 ms–10 min	1.1 ms–10 min	1 ms–6 s	1 ms–6 s	2 ms–6.5 s	2 ms–6.5 s	5 ms–17 min
USB Interface	1.1	1.1	2.0	2.0	2.0	1.1. or 2.0	1.1. or 2.0	2.0	2.0	2.0
Dimensions [mm]	75×53×46	75×53×46	175×110×44	175×110×44	175×110×44	140×105×75[o]	140×105×75[o]	67×60×40[o]	70×60×40[o]	108×95×42
Estimated Weight	400 g	400 g	716 g	716 g	716 g	2,500 g	2,500 g	125 g	125 g	500 g
OEM Unit Available	Yes	Yes	Yes	Yes	Yes	Is An OEM	Is An OEM	Is An OEM	Is An OEM	Yes
Estimated Cost	$1,850	$1,850	$4,200	$5,000	$3,500	$7,582	$12,000	$4,271	$4,271	

a With a 75 mm focal length.
d The demonstration unit as tested by BSI.
g At a wavelength of 600 nm.
j A unit with 1,024 pixels is available as an option.
m The unit tested at BSI had a 14 bit ADC.

b Can be provided by the manufacturer.
e Specification is 3.0nm in the UV-NIR.
h A back-thinned CCD.
k In units of counts per microwatt per millisecond.
n Plus a sign bit.

c For a unit equipped with the NIR option.
f About 2.5 nm for $\lambda < 800$ nm; 6 nm for $\lambda = 950$ nm.
i Infrared enhanced.
l With 14 bit ADC.
o Dimensions do not include the electronics module.

C9407MA and the two MMS units from Zeiss/Tec5 have bandwidths ranging between 5 and 11 nm. The bandwidth of the C9408MA varies between 8.5 nm at 650 nm to about 6.5 nm at 1,000 nm.

7.4.2 Out-of-Band Rejection

A comparison of measurements of the 632.816 nm line of a HeNe laser using several candidate spectroradiometers is presented in Fig. 39. The out-of-band rejection of the spectrographs at 100 nm away from the laser line is between 5×10^{-4} and 3×10^{-5}. For comparison, a scan of the 325 nm line of the HeCd laser using a BSI high-resolution SUV-150B spectroradiometer is also shown in Fig. 39 (but shifted by 308 nm for clarity). This instrument is based on a scanning double monochromator.
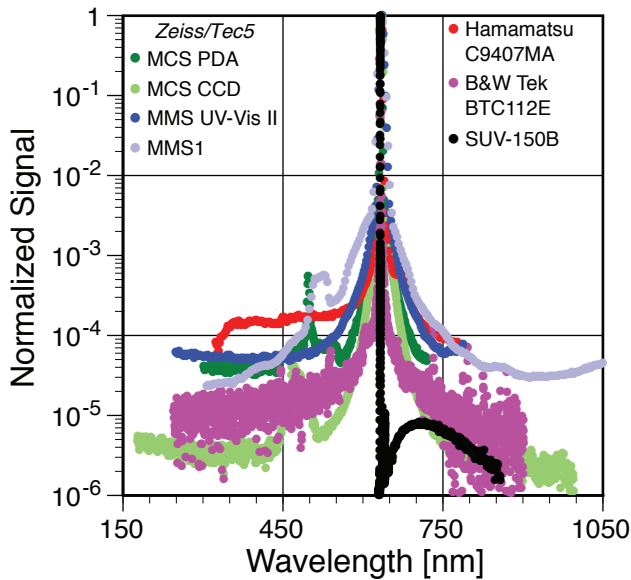

Fig. 39. A comparison of measurements of the 632.816 nm line of a HeNe laser using several candidate spectroradiometers.

In terms of stray-light rejection, the Zeiss/Tec5 MCS CCD and B&W Tek BTC112E units are the best, and smaller units are poorer (e.g., the Hamamatsu C9407MA and the two Zeiss/Tec5 MMS devices). Some Zeiss/Tec5 units show secondary peaks, and according to the manufacturer, these features are caused by *recycled* light that is reflected by the detector array back to the grating, and then diffracted a second time by the grating and measured by the sensor.

Spectrograph units with similar optical layouts, nonetheless had different levels of out-of-band rejection. For example, the stray-light rejection of the MMS UV-VIS II is significantly better than the MMS1, and the stray-light level of the MCS CCD is below that of the MCS PDA, but all these devices are from the same manufacturer. It is not clear from the experiments whether these differences

are caused by the small changes in the optical layout of the units or some variation between individual units of the same model. For example, contamination during the manufacturing process could conceivably raise the stray-light level. Measurements of the three devices from Avantes fall within the range of the other units. Notably, the stray-light levels of all instruments tested were better than the specifications provided by the manufacturers.

The out-of-band rejection of the SUV-150B device is at least 5×10^{-8}. Some fluorescence from (or caused by) PTFE contamination is indicated five orders of magnitude below the level of the excitation line. Note that fluorescence cannot typically be detected with the spectrographs discussed here, because it is well below the observed stray-light levels.

7.4.3 Stray-Light Levels

Stray light was present for all of the spectrographs when measuring the solar spectrum. Below about 300 nm, the measured spectra do not decrease exponentially, as they should, but stay either constant or increase with decreasing wavelength. The stray-light level ranges between 0.1–1% of the maximum signal value and was the smallest for the Zeiss/Tec5 MCS CCD and Avantes AvaSpec 2048×16 units. Curiously, the stray light level is considerably higher, and also spectrally dependent, for the two other units manufactured by Avantes.

The starting wavelength of the Hamamatsu C9407MA plus the Zeiss/Tec5 MCS PDA and MMS1 devices are at 300 nm or higher, so stray-light assessment using the ozone cutoff is not possible. Repeated measurements with a Schott GG-385 filter shows stray light becomes apparent below 353 nm for these instruments, and ranges between 0.2–0.5%. The stray-light level depends on wavelength, indicating it is not sufficient to subtract a constant value from a measured spectrum to correct for stray light.

7.4.4 Saturation

Except for the Zeiss/Tec5 MCS PDA, all of the spectrographs saturated—even at the shortest integration times that the instruments were capable of—when the fiber optic bundle was pointed at the Sun with no ND filter. Instruments equipped with CCD detectors are more sensitive than those with PDAs and are more affected by saturation. While the Zeiss/Tec5 MCS PDA could in theory be used without an ND filter, it is not advisable because the instrument would have to be operated at integration times between 1–5 ms. Much longer (e.g., 2,000 ms) integration times are necessary for calibration.

Results discussed below indicate that none of the instruments tested, including the MCS PDA, is linear with integration time. It would therefore be difficult to operate the MCS PDA without an ND filter for OSPREy sun photometer applications. These results suggest that an ND filter is necessary for all instruments.

7.4.5 Dark Signal

The dark signal characteristics of the test units were very different. The dark signal data for the Hamamatsu C9407MA spectrograph consists of two components: a constant component and one increasing strongly with integration time, with additional large pixel-to-pixel variability that increases with integration time. At 10,000 ms, the dark signal of some pixels was as high as 40,000, or 61% of the maximum signal of 65536 (16 bit). The same variability is also present when the unit is exposed to light. Most of the variability is, therefore, removed when the dark measurement is subtracted from light measurement to calculate the net current. The large dark signal, however, substantially limits the dynamic range of the instrument.

The Hamamatsu C9408MA and C9407MA use similar detectors and have similar dark signals, but the former has fewer hot pixels. Hot pixels are also a problem for the Avantes AvaSpec-1024. The two CCD models from Avantes have no hot pixels, but the AvaSpec-2048 dark signal shows a general downward trend with pixel number. The dark signals of all Zeiss/Tec5 units show very little dependence on pixel number and are more than one order of magnitude below their saturation threshold, even at the longest integration time.

The temperature sensitivity of the dark signal for all spectrographs was also characterized. As an example, the Hamamatsu C9407MA dark signal increased by about a factor of 16 over a temperature range of 5–56°C. The relative increase depends weakly on wavelength. Notably, the majority of pixels saturate at temperatures higher than 45°C, and several pixels saturate at lower temperatures. Spectrographs for the OSPREy activity are heated to a constant temperature of 40°C to maintain the temperature stability. At this temperature, several pixels of the C9407MA are already saturated. Operating the Hamamatsu C9407MA spectrograph at such a high temperature would severely affect the performance of the device. The dark signals of the two Zeiss/Tec5 MCS PDAs changed by a factor of 115 over a 12–60°C temperature range without saturating. The change is exponential, which suggests the instrument should be operated at low temperatures. The tests indicated that a temperature of 40°C with a temperature stabilization to within 0.05°C is acceptable, however.

The large temperature dependence of dark signals observed for all units suggests instrument responsivities are also affected by temperature. Testing with the Avantes AvaSpec-2048×14 and the Zeiss/Tec5 MCS PDA as a function of temperature while exposed to a 100 W tungsten lamp showed that the signal varied strongly with temperature, as predicted. The results also indicated, however, that most of the temperature dependence was the result of the temperature effect on the dark signal.

Temperature-related drifts in the dark signal can be tolerated if the dark signal is measured frequently (e.g., every minute). EML radiometers have a computer-controlled filter wheel with an opaque position to allow automated dark measurements. Such a device is not available for irradiance radiometers. The dark signal tests show excellent temperature stabilization is necessary to operate spectrographs in irradiance radiometers to meet the accuracy levels required by the OSPREy activity. Tests with an analog temperature controller confirmed that temperature stabilization to within 0.03°C level is achievable.

7.4.6 Spectral Responsivity

The spectral responsivity of each candidate spectrograph was determined for irradiance and radiance calibrations. The Avantes AvaSpec-2048×14 saturates for integration times larger than 100 ms, and reports a signal even at wavelengths below 180 nm because of stray light. The net signal increases linearly with integration time when the ratio of net signal divided by integration time is between 100–400, but there are differences below and above this range. Measurements with an integration time of 50 ms are about 2% smaller in the center of the wavelength range. At large signal levels, the unit tends to underestimate the actual irradiance. Below 400 or above 1,100 nm, where signal levels are small, there is a large discrepancy between the different data sets, which is a clear indication that there are significant departures from linearity. A similar analysis was performed for all candidate spectrographs. The relationship between net signal and integration time was nonlinear for all units, but the effect varied in magnitude. For some units, the effect was barely noticeable because the signals at short integration times were affected by noise, which partly obscured the nonlinear effect.

Nonlinear behavior at low signal levels is mostly observed at wavelengths that are also affected by stray light. Stray light is an optical phenomenon, however, and the signal generated by stray light should scale linearly with integration time. Linearity of the Zeiss/Tec5 MCS CCD determined with a monochromatic light source indicated that the system is linear to within 1.5%, i.e., within the uncertainty of the experiment. The measurement of monochromatic light sources is not a OSPREy application, however, so the value of these test results is limited.

The spectral responsivity of all units was determined by dividing the net signal by the known irradiance of the FEL calibration lamps. For example, the responsivity of the Avantes AvaSpec-1024 is about one order of magnitude greater in the UV than in the NIR, whereas the responsivity of the AvaSpec-2048×14 is relatively uniform across the entire wavelength range. Generally, spectrographs with CCD arrays have a much larger spectral responsivity than those using PDAs.

7.4.7 Dynamic Range

The candidate spectrographs were equipped with either 15 or 16 bit analog-to-digital converter (ADC) capabilities, which is equivalent to a dynamic range of approximately 3.3×10^4 or 6.6×10^4, respectively. Spectrographs

installed in EML radiometers require a dynamic range of more than 100×10^4 to accurately measure high-intensity sources, such as direct sunlight, and low-intensity sources, such as the radiance of the sea surface or the radiance of a calibration plaque.

In theory, the dynamic range of a spectrograph can be increased beyond that offered by the ADC capability by either measuring at different integration times or using ND filters to reduce the signal from high-intensity sources. The nonlinear behavior described above limits the ability to extend the dynamic range via the use of different integration times. Spectrographs for EML sensors are, therefore, equipped with a filter wheel with two ND filters. The dynamic range for EME sensors is less demanding than for radiance sensors. For irradiance sensors, sunlight and calibration sources can be measured at the same integration time, so the use of ND filters is not necessary.

7.4.8 Noise Equivalent Irradiance

The NEI for the MMS UV-VIS II equipped with a PTFE diffuser plate that is 0.02 in thick is presented in Fig. 40. NEI varies between $0.001\,\mu\mathrm{W\,cm^{-2}\,nm^{-1}}$ at $t_i = 200\,\mathrm{ms}$ and $0.3\,\mu\mathrm{W\,cm^{-2}\,nm^{-1}}$ at $t_i = 2\,\mathrm{ms}$. Longer integration times (which would lead to lower NEI) are not possible because the unit would saturate. For accurate results, NEI ideally has to be lower by at least 1.5 orders of magnitude than the spectrum to be measured. For the sample spectra shown in Fig. 40, this can be achieved for integration times equal to, or longer than, 100 ms and for wavelengths above 310 nm.
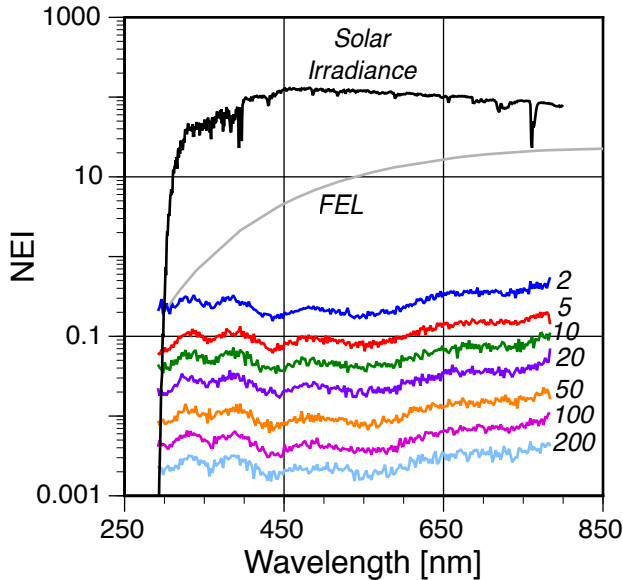
Fig. 40. The NEI, in units of $\mu\mathrm{W\,cm^{-2}\,nm^{-1}}$, for the Avantes AvaSpec-1024 as a function of t_i values from 2–200 ms. The spectrum of a 1,000 W FEL lamp at 50 cm distance and a spectrum of solar global irradiance at a 45° zenith angle are shown for comparison.

In theory, NEI should decrease proportional to $\sqrt{t_i}$, if the noise contribution is dominated by photon statistics. Multiplying all Fig. 40 data sets by $\sqrt{t_i}$ shows this is not the case for the Avantes AvaSpec-1024 spectrograph, for which the NEI is approximately proportional to t_i. The reason for this unexpected behavior is not known, but was confirmed by the manufacturer. Similarly, the NEI of all the other units was proportional to t_i rather than $\sqrt{t_i}$. NEI can either be improved by averaging several spectra at a given integration time, or measuring one spectrum over a long integration time. NEI determined with the former should decrease proportionally to $\sqrt{t_i}$, while the latter is proportional to t_i as the data indicate. Consequently, it is advantageous to always use the longest integration time possible.

A comparison of the Avantes AvaSpec-1024 with the AvaSpec-2048 may suggest that instruments using CCD detectors have a smaller NEI and are, therefore, preferable for OSPREy applications. Tests with other units, however, reveal that this is not the case. For example, an NEI of $0.001\,\mu\mathrm{W\,cm^{-2}\,nm^{-1}}$ is achievable with the Zeiss/Tec5 MMS UV-VIS II. For this unit, the accuracy of the calibration is limited by dark signal drifts and stray light, rather than signal noise.

7.4.9 Radiance Responsivity

The spectral pattern of radiance responsivity was similar to that for irradiance responsivity for all instruments, because the transmission of the diffuser used for the latter was not highly dependent on wavelength. As in the case of irradiance, radiance responsivity should change linearly with integration time. The BSI tests indicate that this is not the case for all test units, albeit the degree of nonlinearity differs from unit to unit. Ratios of net currents, with and without the baffle arrangement, varied between 0.015–0.070, and did not show much dependence on integration time for most instruments.

7.4.10 Noise Equivalent Radiance

For the Zeiss/Tec5 MCS CCD equipped with a *bare* fiber and using a 200 ms integration time, NER is more than 2.5 orders of magnitude smaller than the radiances from the sky or a calibration plaque. This indicates that signal noise is not a limiting factor for accurate calibrations and solar measurements. The minimum NER (at 5,000 ms) when equipped with the 2.5° FVA fore optics is about $0.0001\,\mu\mathrm{W\,cm^{-2}\,nm^{-1}\,sr^{-1}}$. This is the best (lowest) value of all instruments tested. With the fore optics installed, the radiance of the plaque is more than two orders of magnitude larger than NER for wavelengths longer than 360 nm. At 340 nm, the radiance of the plaque with the lamp 287.1 cm away is about 1.5 orders of magnitude larger than the NER for the longest integration time. Accurate determination of responsivity at this wavelength is,

Table 12. An abbreviated summary of the spectrograph testing performed at BSI. All numerical wavelength range entries show the reduced wavelength range, with respect to the full range given in Table 11, determined to be usable for a given characteristic. For stray light, the range is defined as the interval where stray light contributes less than 10% to the total signal. For noise and linearity, the range is defined as the interval for which the error is smaller than 2.5%.

Unit Specification	Hamamatsu (MA)		Avantes (AvaSpec)			Zeiss/Tec5 (MCS)		Zeiss/Tec5 (MMS)		B&W Tek
	C9407	C9408	1024	2048×14	2048	PDA	CCD	UV-VIS II	MMS1	BTC112E
Stray Light	350–380 nm	N/A	378–965 nm	377–1,100 nm	395–1,100 nm	Not Tested	330–995 nm	348–785 nm	380–930 nm	442–780 nm
Attenuator Required	Yes	Yes	Yes	Yes	Yes	Maybe	Yes	Yes	Yes	Yes
NEI Calibration	Full Range	Not Tested	320–1,100 nm	Full Range	Full Range	Full Range	Full Range	Full Range	Full Range	Full Range
NER Calib. Bare Fiber	Full Range	Full Range	350–1,100 nm	350–1,100 nm	Not Tested	340–720 nm	Full Range	Not Tested	Not Tested	Not Tested
NER Calib. 2.5° FOV	430–700 nm	Full Range	500–600 nm	441–1,100 nm	Not Tested	600–700 nm	Full Range	Not Tested	Not Tested	Not Tested
Nonlinearity Irradiance	Not Tested	Not Tested	Noise Limited	470–1,025 nm	360–1,100 nm	Noise Limited	360–995 nm	350–785 nm	350–1,050 nm	340–780 nm
Quality Slit Function	Yes	Yes	Yes	Yes	No	Yes	Yes	Yes	Yes	No
Satisfactory Dark Signal	No	Yes	No	Yes	Yes	Yes	Yes	Yes	Yes	No
Temp. Stabil. Required	Yes	Yes	Yes	Yes	Yes	Heating is Sufficient for Quality Data				Yes

therefore, challenging. If the lamp is moved to a distance of 100 cm, however, calibration becomes possible.

The wavelength range for which NER is sufficiently small to allow for accurate calibrations, with and without FOV-limiting fore optics, was assessed for all instruments (Table 12). Without FOV-limiting optics, calibrations are possible over the full wavelength range for most instruments. Limiting the FOV to 2.5° makes calibrations in the UV challenging.

7.4.11 Linearity

Stray-light tests revealed that signals of all instruments do not scale linearly with integration time, in particular at short wavelengths (or small signal levels). This nonlinearity—together with stray light and drifts of the dark signal—limits the dynamic range of the instruments. Spectrographs using CCD detectors seem to be more affected, but this may not, in fact, be the case because nonlinear behavior of PDA systems tends to be obscured by signal noise. The effect was further investigated by repeating the stray-light measurements using PTFE diffusers of different thicknesses in front of the instrument fiber optics. If a thicker diffuser is used, a lower signal is expected, but the ratio of measurements with a thick and a thin diffuser should be independent of integration time.

The ratios of measurements from the Avantes AvaSpec-1024 made with a diffuser 0.03 in thick to that of a diffuser 0.02 in thick are presented in Fig. 41. The responsivity with the thicker diffuser is 20–30% lower in the UV and

visible, and up to 65% lower in the NIR. The reason for the wavelength dependence is probably due to the wavelength-dependent scattering properties of PTFE. Measurements for integration times of 500, 1,000, and 2,000 ms are consistent between 340–1,100 nm (indicating good linearity), and affected by noise outside this range.
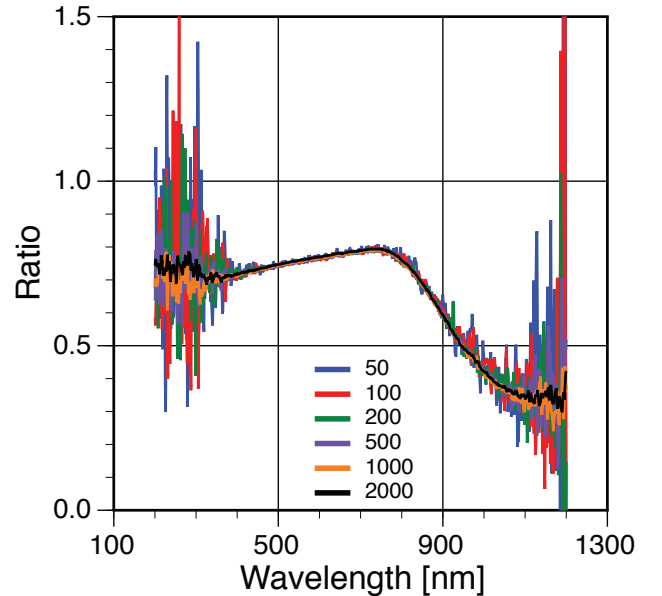

Fig. 41. The ratios of measurements from the Avantes AvaSpec-1024 made with a diffuser 0.03 in thick to that of a diffuser 0.02 in thick, as a function of t_i (colored lines) in milliseconds.

A similar analysis for the Avantes AvaSpec-2048×14 is presented in Fig. 42. The ratio of the two responsivities is far less affected by noise. The magnitude of the difference is similar to that determined with the AvaSpec-1024, but ratios for different integration times are less consistent than they were for the AvaSpec-1024. At short wavelengths, the ratio is smaller for measurements at short integration times. Between 1,050–1,200 nm, the pattern is reversed. This suggests that the signal at a given pixel depends on the signal of pixels sampled prior to that pixel when reading out the array.
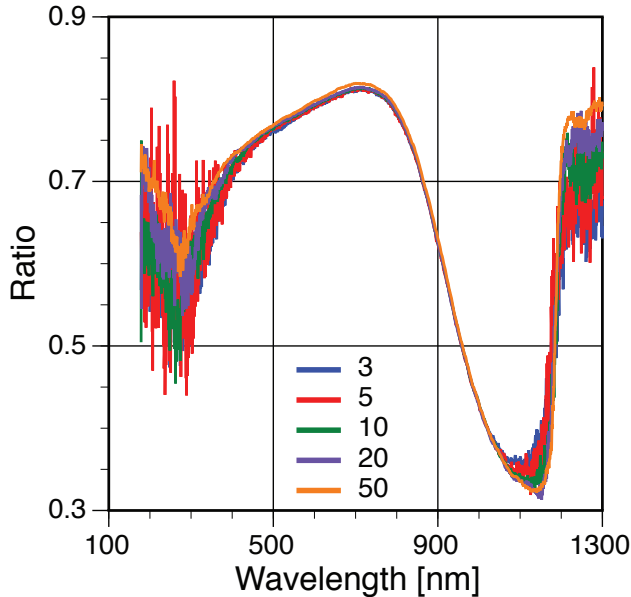

Fig. 42. An analysis similar to the one shown in Fig. 41 (note, however, the difference in *y*-axis scaling), but for the Avantes AvaSpec-2048×14.

The signal dependency as a function of pixel number leads effectively to nonlinearity, which becomes dependent on integration time and the spectral pattern of the source being measured. This artifact is very difficult to correct and would be a serious obstacle if the unit were to be used for the OSPREy activity. Measurements with the Zeiss/Tec5 MCS CCD uncovered a similar nonlinear behavior. On the other hand, measurements with the MCS PDA for integration times between 50–1,000 ms were consistent to within 0.5% down to 300 nm.

Linearity of the Avantes AvaSpec-2048×14 was also tested using a purpose-built *beam combiner* designed and built by BSI. This apparatus combines the beams of two light sources using a cubical beam splitter. For testing the AvaSpec-2048×14, one light source was a bright white-light LED and the other was a 100 W halogen lamp coupled with a fiber optic bundle. The beams of the two light sources can be blocked independently to measure dark signal, signal of either of the sources, or both sources. If an instrument is linear, the signal measured with both

light sources unblocked should be identical to the arithmetic sum of the signals of the two sources measured separately. The output of the two sources can be adjusted independently to achieve the desired signal levels close to saturation. In the test, the ratio of the arithmetic sum of the signals of the two sources and the signal measured with both light sources unblocked deviated by up to 2% between 500–700 nm. These measurements confirmed the nonlinear performance of the unit.

All of the tests above were performed with polychromatic light sources, i.e., lamps or LEDs. The Zeiss/Tec5 MCS CCD was also tested with a quasi-monochromatic radiation at 555 nm, which was produced by the BSI spectral source (Bernhard et al. 2005). This source consists of a 1,000 W Xenon lamp focused on the entrance slit of a 50 cm double monochromator with prism pre-disperser. Radiation exiting the system is *pure*, for all practical purposes, with no measurable contribution of stray light. It was directed on a diffuser connected to the MCS CCD via a fiber optic bundle. Measurements were performed at integration times between 3–5,000 ms. The response of the spectrograph was linear to within 1.5%.

A second experiment with the Zeiss/Tec5 MCS CCD was designed to test whether detected radiation at a given wavelength depends on radiation at other wavelengths. For example, the CCD pixels are read sequentially by the system electronics. If the read-out mechanism was dependent on the charge of pixels read prior to the pixel in question, the signal would be biased. This would result in nonlinearity if the bias depended on integration time. The test involved three monochromatic light sources: in addition to the BSI spectral source (set to 480 nm), radiation from a HeCd laser (325 nm) and a HeNe Laser (633 nm) were directed onto a diffuser connected to the fiber optics. Linearity at 480 nm was quantified depending on whether or not any (or both) of the lasers were turned on. Results indicated the system was linear to within 0.6%, regardless of the configuration, suggesting that the CCD read-out mechanism is not responsible for the nonlinearity observed with polychromatic light sources.

A third test investigated the hypothesis that nonlinearity depends on the light intensity entering the fiber optics. The test was set up like an irradiance calibration, but with ND filters involving transmissions ranging between 10^{-3} and 1 placed in front of the diffuser. These tests indicated that the observed nonlinearity is not affected by the light intensity.

A fourth and final test was performed with the use of *cut-on* filters, which are opaque at wavelengths below a certain wavelength. Examples are shown in Fig. 43a with no filter and Fig. 43b with a GG-400 filter, which is opaque below 380 nm. In the latter case, signals measured at wavelengths below 380 nm are entirely caused by stray light and nonlinearity is almost entirely restricted to this region.
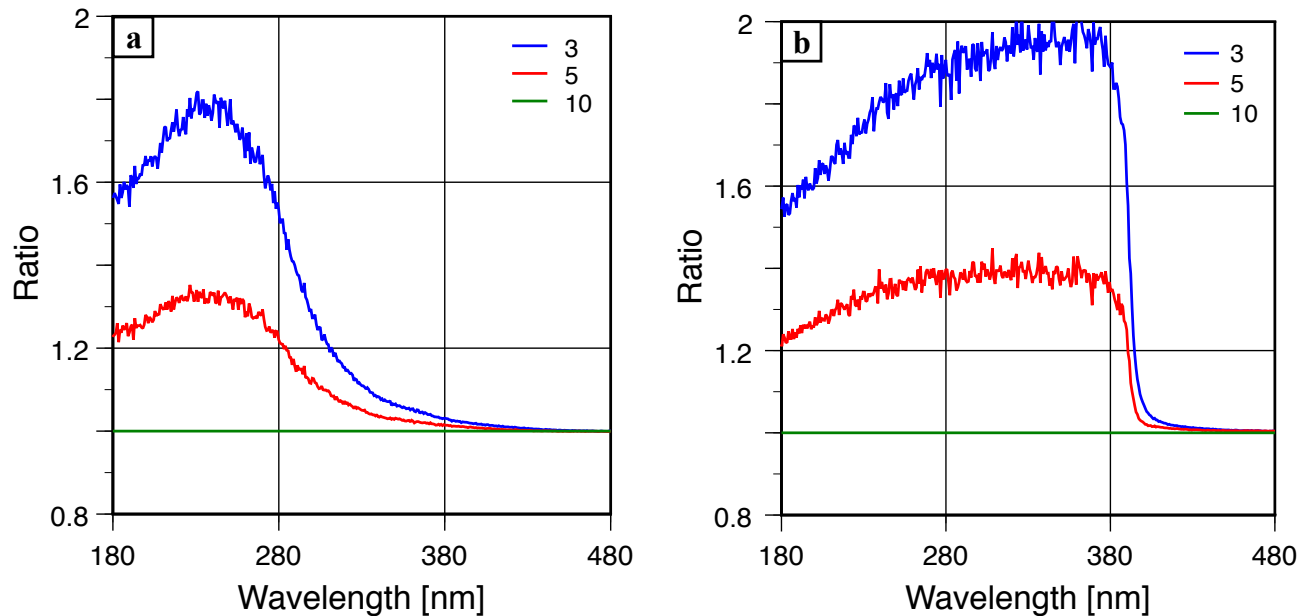
Fig. 43. Linearity test results of the Zeiss/Tec5 MCS CCD performed without and with a *cut-on* filter: **a)** no filter, and **b)** the GG-400 filter, which is opaque below 380 nm. The plots show the net signal measured by the Zeiss/Tec5 MCS CCD divided by integration time (3, 5, or 10 ms) and normalized to the measurement with 10 ms integration time. This ratio should be equal to 1 and independent of integration time for a linear system.

These tests confirmed that nonlinearity is only a problem when polychromatic light sources are measured. They also suggest that the effects of nonlinearity can be reduced (if not, perhaps, completely eliminated) if the stray light contribution to the net signal is removed by post processing the data. It has yet to be shown whether this is true or not.

7.5 Conclusions

A side-by-side comparison of the spectrographs that were tested is provided in Table 12, which is organized as a function of nine unit specifications. Note that the organization of the table follows the presentation scheme established with Table 11, although it is partitioned a little differently.

Wavelength range testing showed the wavelength range of all test units is sufficient for OSPREy applications. The wavelength range of most units can be optimized for the needs of OSPREy by selecting an appropriate grating. The two Hamamatsu units have fixed gratings, covering the range of 325–1063 nm by using both units together.

Spectral resolution and slit function testing showed the bandwidth of the 10 test units varied between 2–10 nm. The Zeiss/Tec5 MMS UV-VIS II and MMS1 models plus the Hamamatsu C9407MA and C9408MA models represent the four smallest units, and they have bandwidths ranging between 6–10 nm. The comparatively low spectral resolution of these units may not be sufficient for some OSPREy applications. All spectrographs have symmetrical gaussian-shaped slit functions, with the exception of the Avantes AvaSpec-2048 and the B&W Tek BTC112E. The optics of these two test units may have been misaligned.

Out-of-band rejection and stray light testing showed the far-field out-of-band rejection of the test units varied between 0.04% and 0.0004%. Characterizing out-of-band rejection with a monochromatic light source is not sufficient to characterize stray light characteristics relevant for solar measurements. The dynamic range of solar measurements is typically limited by stray light to 2.5–3.0 orders of magnitude. Stray light is also a problem for calibration scans and limits the dynamic range to between 1.5 (AvaSpec-1024) and 3.0 (MCS CCD) orders of magnitude. The spectral distribution of stray light can be determined with cut-on filters, and a correction can be applied. This correction extends the usable dynamical range for calibrations by more than one order of magnitude.

Saturation testing showed that with the exception of the Zeiss/Tec5 MCS PDA spectrograph, all instruments saturate when their fiber optics are pointed at the Sun. While the MCS PDA does not saturate at 1 ms integration time, other data suggest that the instrument is not linear at this short integration time. This means that ND filters have to be used to measure direct sunlight for all instruments.

Change of dark signal with integration time testing showed the dark signal increases substantially with integration time for all instruments. The Avantes AvaSpec-1024, the B&W Tek BTC112E, and the two Hamamatsu units exhibit a large pixel-to-pixel variation in the dark signal,

S.B. Hooker, G. Bernhard, J.H. Morrow, C.R. Booth, T. Comer, R. Lind, and V. Quang

which increases with integration time. Most of this variability is removed when subtracting "dark" from "light" measurements, however, the dynamic range for long integration times is limited by these "hot" pixels. The pixel-to-pixel variability of the two CCD-equipped Avantes units and the four Zeiss/Tec5 units is very low in comparison.

Change of dark signal with temperature testing showed the dark signal of all instruments depends strongly on temperature. Changing the temperature from $10°C$ to $60°C$ increased the dark signal by factors between 16 and 115. For long integration times, the dark signal of some pixels of the Hamamatsu units and the Avantes AvaSpec-2048x14 saturated for temperatures above $45°C$. These results show that all instruments should be operated in a temperature-stabilized—preferably cooled—housing. The detectors of the B&W Tek BTC112E and the Zeiss/Tek5 MCS CCD units are thermo-electrically cooled. The testing showed, however, that the instruments are not insensitive to variations in ambient temperature. Consequently, it is necessary to temperature stabilize the enclosure where these instruments would be installed. This is a challenge, because the excess heat of the thermo-electric coolers would have to be properly dissipated.

Irradiance responsivity and NEI testing showed all instruments exhibited some nonlinear behavior when measurements at different integration times were compared. Stray light prevented determination of responsivity at short wavelengths. NEI was calculated by dividing the standard deviation of dark current measurements by the responsivity. When using the longest integration time that does not lead to saturation, the NEI of the test units ranged between 0.0006 and $0.01 \, \mu W \, cm^{-2} \, nm^{-1}$. For some instruments, NEI is not small enough to calibrate these units with sufficient accuracy in the UV.

Radiance responsivity testing confirmed problems with nonlinearity and stray light. When limiting the field-of-view to $2.5°$ full-angle, it became a challenge to determine responsivity for several instruments. This problem could be alleviated by moving the lamp closer to the plaque.

Linearity testing showed all instruments suffer from some nonlinearity. The problem is most severe for instruments equipped with CCD detectors, e.g., the Avantes AvaSpec-2048 and AvaSpec-2048x14. The testing indicates that departures from linear behavior of these two instruments may exceed 5% at large signals and 40% at low signals. The Zeiss/Tec5 MCS CCD is also affected by nonlinearity when tested with a polychromatic light source. It is linear to within 0.6% (i.e., within the measurement uncertainty) when tested with a monochromatic light source. The reason for the conflicting results is not understood. As calibrations are performed with polychromatic light sources, nonlinearity remains a challenge.

The primary conclusions of the spectrograph testing, organized in order of importance to OSPREy objectives, are as follows:

1. Of the instruments tested, the two Zeiss/Tec5 MCS units have the best optical properties and operational characteristics. The main disadvantages of the instruments are their large size and high price. Like all other instruments tested, the two instruments are affected by nonlinearity when exposed to polychromatic radiation, which limits the usable dynamic range of the instruments.

2. The Zeiss/Tec5 models MMS UV-VIS II and MMS1, as well as the Hamamatsu C9407MA and C9408MA (used together) units, are also possible options for OSPREy. The main advantage of the four units is their small size while still providing acceptable optical characteristics. Their main disadvantage is their comparatively large, wavelength-dependent bandwidth of 5–9 nm. The two Hamamatsu units also suffer from an excessively high dark current with large pixel-to-pixel variability.

3. All Zeiss/Tec5 spectrographs are made from a monolithic body, which provides superior ruggedness and wavelength stability.

4. The two Hamamatsu units are only equipped with the USB 1.1 interface and two spectrographs cannot be operated at the same time on one computer.

5. Instruments equipped with CCD detectors have favorable sensitivity. Unfortunately, the signals of these units change in a nonlinear way with integration time and flux level. These nonlinearities are difficult to correct and pose a challenge for OSPREy integrations.

6. Good temperature stabilization is necessary for all units because of the large temperature dependence of the dark offset with the spectrograph component. This is a challenge considering space and power are recurring limitations.

7. None of the spectrographs are able to cover the dynamic range required for direct observations of the solar disk, calibration scans, and measurement of other natural targets (e.g., radiance emanating from the ocean). Possible solutions to this problem are to a) use ND filters mounted on a filter wheel under computer control to attenuate the signal when viewing the Sun, b) use a fixed ND filter in combination with a large field-of-view (e.g., $17°$ instead of $2.5°$), or c) to not use spectrographs for Sun measurements. For the latter, EML radiometers use a filter wheel.

Chapter 8

The Integrated OSPREy System

Charles R. Booth, Randall N. Lind, John H. Morrow, and Germar Bernhard
Biospherical Instruments Inc.
San Diego, California

Stanford B. Hooker
NASA Goddard Space Flight Center
Greenbelt, Maryland

Abstract

The previous chapters describe the major elements in the radiometers used in an OSPREy system: a micro-radiometer cluster with necessary modifications to support OSPREy design criteria, a spectrograph, optical collectors (both radiance and irradiance), primary (housing) and secondary (spectrograph) thermal regulation, and accessories like the tracker and shadowband. This chapter describes how these components—plus housing design, primary and secondary temperature control, and other support electronics—are integrated to make the radiometers used in OSPREy systems. These include radiance and irradiance field sensors, and a similar pair designated as transfer radiometers. The fully integrated system provides an unprecedented capability in a single housing. The spectrograph provides hyperspectral resolution over a subset of the complete spectral range, while the microradiometers provide a larger dynamic range in responsivity, higher sampling speeds, better sensitivity, and sampling across the entire OSPREy spectral range (290–1,670 nm). The two sensor technologies supplement each other. For example, spectrograph data can be used to detect potential degradation of the interference filters used by the microradiometer channels while the microradiometers help to correct dark-current drifts and nonlinearity in spectrograph measurements. The capability of radiance sensors is further enhanced by a nine-position filter wheel and integrated camera. In the standard configuration, the filter wheel permits hyperspectral polarimetric measurements, direct-Sun viewing, stray-light correction, dark current measurements, and a home position. The video camera is used for locating the Sun and verifying the condition of all targets (cloud-free solar and lunar disks, cloud presence in sky data, and sea surface debris or foam detection). The components of each radiance and irradiance sensor type are integrated in a common housing that is environmentally sealed, nitrogen purged, and temperature controlled. Synchronous and asynchronous sampling modes measure the sea, Sun, and sky, across a wide spectral range (UV–SWIR). The OSPREy architecture is modular and scalable, which permits the configuration (sensor inventory) and complexity (sampling redundancy) to be matched with science objectives and resource allocations. The modularity allows the observing system to expand or contract as mission requirements evolve. These measurements support an unprecedented number of current and next-generation satellite missions involving both atmospheric and oceanic data products.

8.1 Introduction

OSPREy systems use EMR sensors composed of a cluster of fixed wavelength microradiometers and a spectrograph. The sensors include radiance and irradiance versions, with a similar pair designated as transfer radiometers. Previous chapters presented major elements in the hybrid designs: microradiometers and necessary OSPREy modifications (Chap. 2); optical collectors, for both irradiance (Chap. 3) and radiance (Chap. 4); the tracker used with the radiance sensors (Chap. 5); and selection of a spectrograph (Chap. 7). This chapter describes how these components—plus housing design, primary and secondary temperature control, and other support electronics—are integrated in OSPREy systems built with EMR sensors.

The spectrograph component provides hyperspectral resolution over a subset of the complete spectral range, while the microradiometers provide a larger dynamic range in responsivity, higher sampling speeds, better sensitivity, and sampling across an observational spectral range of 340–1,640 nm. The two sensor technologies supplement each other through intracomparisons. For example, spectrograph data can be used to detect potential degrada-

S.B. Hooker, G. Bernhard, J.H. Morrow, C.R. Booth, T. Comer, R. Lind, and V. Quang

		Starter System	Measurements, Data Products, and Mission Advantages
a		Starter System • 8–19 channels • One radiance sensor (SeaPRISM analog) • Manual or fixed options	• Sun, sea, sky, and Moon radiance measurements (290–1,670 nm) • Thermal regulation, hyperspectral, video camera, and 9-position filter-wheel assembly (3-axis polarimetry, cut-on filter, etc.) • QA and QC from microradiometer-spectrograph intracomparison
b		Minimum System • Radiance and irradiance (16–37 channels) • Some redundancy • Shadowband optional	All of the Above, and in Addition: • Global irradiance plus diffuse component (using shadowband) • Direct-to-global irradiance ratio (used for cosine-error correction) • Improved data products plus cloud detection and optical depth • Enhanced QA and QC from two (redundant) solar measurements
c		Spectral System • Two irradiance sensors with shadowbands • One radiance sensor • Improved accuracy	All of the Above, and in Addition: • Two optimized cosine collectors for high irradiance accuracy from UV to SWIR (290–1,100 nm and 1,000–1,670 nm) • Up to 36 channels for irradiance or enhanced redundancy • Synchronous and asynchronous shadowband operation
d		Operational System • Up to 74 channels of radiance and irradiance • Synchronous and asynchronous data products	All of the Starter and Minimum Systems, and in Addition: • Redundancy minimizes risk (data loss from sensor malfunction) • Synchronous sampling enhances QA, QC, and data products • Asynchronous sampling also enhances data products (e.g., the detection of thin cirrus clouds)
e		Maximum System • Two complete triads • Maximum redundancy and spectral coverage • Maximum data quality	All of the Above, and in Addition: • Maximum risk reduction (full instrument redundancy) • Maximum number of synchronous and asynchronous scenarios • Maximum QA and QC (faulty sensor or device quickly identified) • Maximum number and quality of data products

Fig. 44. The SHALLO architecture applied to the EMR sensor suite to produce the following field systems (in order of increasing complexity and capability): **a)** starter system, **b)** minimum system, **c)** spectral system, **d)** operational system, and **e)** maximum system. The wavelength ranges are examples and can be configured to the research objectives—they are not predetermined.

tion of the interference filters used by the microradiometer channels while the microradiometers can help to correct dark-current drifts and nonlinearity in spectrograph measurements, while greatly extending the dynamic range.

The capability of EML (radiance) sensors is further enhanced by a filter-wheel assembly and integrated camera. The nine-position filter-wheel assembly is mounted in line with the spectrograph fiber optics and can be custom populated. In the standard configuration, the filter wheel permits hyperspectral polarimetric measurements (three polarized filters), bright-target viewing (two ND filters), stray-light correction (395 nm cut-on filter), dark current measurements (opaque disk), dim-target viewing (open), and a *home* position. The video camera is used for locating the Sun (in lieu of a quadrant detector) and verifying the condition of all targets, i.e., cloud-free solar and lunar disks, cloud presence in sky data, and sea surface debris or foam detection (although an irradiance sensor can confirm cloud-free solar and lunar disks).

The OSPREy field radiometers are EMR sensors, and the laboratory sensors are from the OXR instrument class. A fully supported deployment of an OSPREy system involves radiance and irradiance sensors from both instrument classes being used in the field and in a calibration facility. Although the sensors are similar, there are differences, as summarized in the following:

1. OXR sensors are anticipated to be used exclusively in the laboratory (calibration transfer), while EMR sensors are anticipated to be used only in the field.

2. OXR sensors have a maximum of 18 fixed wavelengths, because the spectrograph fiber replaces one microradiometer for both radiance and irradiance instruments; for EMR sensors, this is also true for EME sensors—EML sensors have 19 channels.

3. EML sensors have a nine-position filter wheel and a video camera.

Although designed for laboratory use only, OXR sensors are nonetheless designed to be rugged and can be shipped to remote calibration facilities.

An important aspect of EMR sensors is their scalability. One part of this unique functionality results directly from the modularity of microradiometers, but the principal scalability comes from the Scalable Hydro-optical Applications for Light-Limited Oceanography (SHALLO) design philosophy established for all instrument classes built with microradiometers, including above-water sensors (Morrow et al. 2010a). This philosophy recognizes that there is always a part of the spectrum that is light limited for all water masses, although the portion of the spectrum involved likely changes with water type. Consequently, a high-quality sensor technology that can be easily and cost effectively reconfigured—i.e., microradiometers—is needed to span and adapt to the dynamic range of the problem.

The SHALLO architecture codifies this philosophy by establishing a sequence of modular capabilities and a stepwise upgrade pathway for the instruments built with microradiometers (Fig. 44). For EMR sensors and their antic-
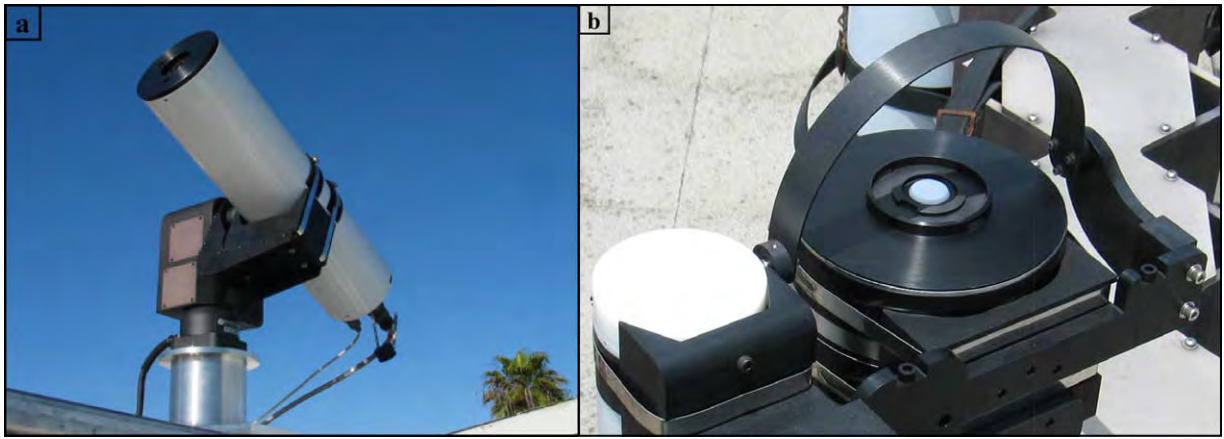
Fig. 45. The testing of EMR sensors on the BSI rooftop facility: **a)** an EML sensor (without a shroud) in solar-tracking mode, and **b)** an EME sensor with the shadowband deployed and shading the cosine collector. The customized bracket holding the radiance sensor fastens to the arm of the PTU-D300 tracker.

ipated use in the OSPREy activity, five system configurations are available. The five systems establish a hierarchy in the level of accomplishment that can be achieved , both in terms of the accuracy and diversity of the resulting data products. The five systems also establish a range in complexity and, thus, a range in resources needed to deploy and support the systems. Within this matrix of functionality and cost, the starter system requires the least, and the maximum system provides the most.

The ensuing sections introduce the common design features for EML and EME sensors (Fig. 45) followed by the specifics of what is needed to produce each system configuration. To ensure all systems are completely commercial products, all the radiometers and necessary support electronics or mechanisms are constructed with COTS components. Some of these components are discussed in detail in prior chapters of this document or in Morrow et al. (2010a) and are mentioned only briefly here. The short- and long-term stability of an EMR sensor is of great importance to OSPREy applications. It is achieved primarily through the selection of stable components, thermal regulation, nitrogen-purged and sealed housings, plus rugged designs that can withstand potential shocks during transport.

8.2 Common Design Features

All EMR and OXR sensors, whether built to measure radiance or irradiance, have three common design features: a fixed wavelength microradiometer cluster, a hyperspectral spectrograph, and a support electronics component. Radiance sensors are further distinguished by having a filter-wheel assembly and a video camera. All radiometric components are mounted inside a nitrogen-purged sealed inner housing, which is temperature regulated to within $40 \pm 0.1°C$ using a primary heater element and analog proportional-integral (PI) controller. The housing is an anodized aluminum cylinder with an outer diameter of 6.0 in

(15.2 cm) and a length of 22.9 in (58.2 cm) for EML sensors and 19.7 in (50.0 cm) for EME sensors.

The spectrograph fiber-optic bundle is 9.4 in (24.0 cm) long and enters the inner housing via a sealed coupling. The tip of the fiber optics is in the same plane as the microradiometer photodetectors such that the fiber optics and the photodetectors have the same view of the back of the irradiance collector. Custom temperature regulation from a secondary heater element integrated with the spectrograph supports stable temperatures to better than $\pm 0.03°C$.

An EMR sensor set is defined as a single radiometer (Fig. 44a), a radiance and irradiance pair (Fig. 44b), or a radiance radiometer with dual irradiance radiometers (Fig. 44c). Each sensor set plus accessories and ancillary sensors are connected to a Power and Component Scheduler (PCS) unit (Sect. 8.2.4), which provides power and houses the needed support electronics for instrument scheduling and data acquisition. Consequently, the redundant configurations shown in Figs. 44c and 44d, require two PCS units. A separate Archive and Communications Master (ACM) coordinates the measurements of all sensors in the system configuration and archives the data collected by the PCS units (Sect. 8.2.4).

8.2.1 Microradiometer Component

The microradiometer section of EMR sensors consists of the fore optics to support irradiance (Chap. 3) or radiance (Chap. 4) measurements, the cluster of microradiometers with integrated filters for wavelength selection, and the aggregator. The waveband set used to initiate the OSPREy activity was based on a variety of factors. Because the fixed-channel wavelengths of EMR instruments are based on microradiometer technology, it is easy to change the set of wavelengths in response to requirements for a specific satellite mission or research requirement, so the initial configurations are easily modified if necessary.

The selected wavelengths for the OXR and EMR sensors produced for the OSPREy development activity are presented in Table 13.

Table 13. The wavelengths (10 nm bandwidths, except as noted) used in the OXR and EMR sensors for the OSPREy development activity (L denotes the radiance sensor and E the irradiance sensor).

Nominal Center Wavelength [nm]	OXR		EMR	
	L	E	L	E
320	×			
340, 380	×	×	×	×
395	×		×	
412, 443	×	×	×	×
465	×			
490, 510, 532, 555	×	×	×	×
589	×	×	×	×
625, 665, 683, 710, 780, 875	×	×	×	×
1,020, 1,245†, 1,640‡		×	×	×

† 15 nm bandwidth.   ‡ 30 nm bandwidth.

The criteria used to select the wavelengths in Table 13 were based on the following considerations:

- Because the primary objective of the OSPREy activity is to validate satellite measurements of water-leaving radiance, filters were selected at wavelengths where absorption by atmospheric trace gases such as oxygen and water vapor is minimal. This is particularly important because the oceanic signal is an order of magnitude less than the total radiance observed by a satellite sensor. Selecting bands void of atmospheric absorption is also important for accurate retrievals of aerosol parameters.

- Wavelengths were selected to match current and next-generation ocean color satellite missions.

- SWIR wavelengths were included to improve atmospheric correction algorithms. The ocean is radiometrically *black* in the SWIR domain, so the contribution of the atmosphere to the backscattered signal can be accurately measured and extrapolated to the visible domain.

- In anticipation of a future focus on coastal zones, UV wavelengths were included because they might be used to distinguish the absorption signals of CDOM, Chl *a*, detritus, and minerals. UV bands may also promote the detection of harmful algal blooms, such as red tides, because they produce UV absorbing compounds known as mycosporine-like amino acids (Laurion et al. 2003). Furthermore, UV bands are helpful for flagging data affected by absorbing aerosols, which are a challenge for atmospheric correction.

- The spacing of the chosen wavelengths is approximately equal throughout the UV and visible domains.

- OSPREy systems are composed of as many COTS elements as possible. To keep costs down, wavelengths were selected from a pool of wavelengths commonly stocked at BSI.

The OXR sensors include a 320 nm channel to allow for comparisons of standards of spectral irradiance below the shortest wavelengths of the EMR field instruments as initially configured (340 nm). This is important, because the spectra of the calibration lamps may deviate significantly from a black-body function for wavelengths in the UV-B. The spectrum of a lamp does not change linearly with wavelength, so knowledge of the spectral irradiance below 340 nm is needed to accurately interpolate lamp spectra between the two shortest wavelengths used by the field instruments (i.e., 340 and 380 nm).

Each microradiometer is assembled with custom, ion-deposited, five-cavity, interference filters with 6 OD blocking over the detector range, and is designed for minimum fluorescence. Additional broad-band blocking filters are included in most microradiometer assemblies to provide additional out-of-band blocking. These are selected after reviewing the interference filter performance and the target source spectral distributions. Each EMR sensor is spectrally measured to verify blocking and center wavelength (Fig. 46). All data were deconvolved to correct for the finite bandwidth of the slit function for the spectral tester, as described by Bernhard et al. (2005). The centroid wavelength λ^c of each channel is calculated as

$$\lambda^c = \frac{\int \gamma(\lambda)\lambda \, d\lambda}{\int \gamma(\lambda) \, d\lambda}, \quad (13)$$

which is then used in the data analysis.

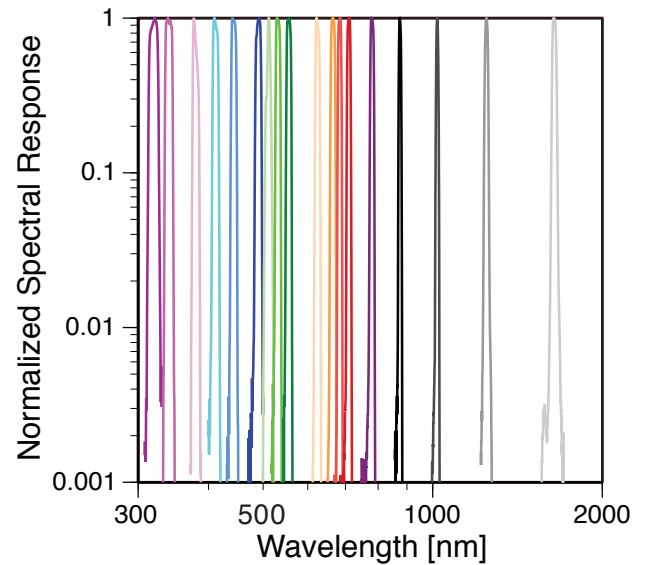**Fig. 46.** The normalized spectral response functions of the OXE sensor (Table 13). Note the logarithmic *x*-axis.

8.2.2 Spectrograph Component

The inclusion of a spectrograph permits sampling of the spectrum in regions between the filtered detector channels. The advantage of the higher resolution of the spectrograph can be combined with the superiorities of the filter radiometers—greater dynamic range, lower stray light,

better SNR, and higher scan speed—to provide a sensor combination superior to either of the individual constituents alone. Based on a detailed engineering analysis (Chap. 7) the COTS models MMS UV-VIS II and MMS1 UV-VIS from Zeiss/Tec5 were selected for OSPREy. The MMS UV-VIS II has a spectral range of 245–785 nm and is used with the OXE and EME instruments. The MMS1 has a spectral range of 300–1,150 nm and is used for the EML instruments.

The irradiance and radiance radiometers use different spectrographs, because of differences in how dark corrections are made. Radiance sensors have a filter-wheel assembly for which one position contains an opaque disk for measuring the dark current. Irradiance sensors do not have a filter-wheel assembly, and it would have been both challenging and cost prohibitive to integrate a mechanical shutter in this design for automated dark measurements of the spectrograph. Consequently, a different technique for applying the dark correction was necessary.

For irradiance radiometers, fixed wavelength channels and the fiber optics of the spectrograph share common fore optics (Fig. 47), including the cosine diffuser. In this design, one microradiometer of the fixed wavelength cluster is replaced by a pass-through of the spectrograph fiber optics. Although the spectrograph is temperature stabilized with an analog controller to better than ±0.03°C when used in the field, data analysis indicates that the remaining variation in temperature still leads to noticeable variation in the dark current of the spectrograph.
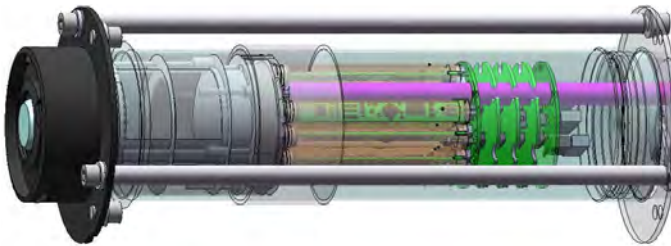
Fig. 47. The front (aperture) section of an OXE or EME radiometer showing how the spectrograph fiber optic (pink) replaces one of the microradiometers, so both sensing technologies view the cosine collector.

Because the atmosphere is opaque below 290 nm, spectrograph data from 245–290 nm can be used to monitor variations in the dark offset, which can then be used to correct the observational data. This correction is possible because tests indicate that changes in the dark offset are nearly independent of the spectrograph pixel, which means that information from the 245–290 nm range can be used to correct measurements in the UV-A and visible wavelengths.

If the MMS1, which does not measure below 300 nm, had been selected for irradiance radiometers, corrections for drifts in the dark offset would have been challenging,

perhaps not even possible. The use of the MMS UV-VIS II in irradiance units is, therefore, necessary to meet the accuracy requirements for OSPREy applications. An additional advantage of the MMS UV-VIS II is its smaller bandwidth of 7 nm provides superior spectral resolution compared to 9 nm for the MMS1.

In radiance instruments, fixed wavelength channels and the fiber optics of the spectrograph use independent Gershun tubes defining their FOV. This design allows a physical separation of the two components and the implementation of a filter wheel between the spectrograph fiber optics and the Gershun tube for the spectrograph (Fig. 48). The filter wheel also includes an opaque disk position for automated dark current measurements. Drifts in dark current can be corrected by moving the filter wheel periodically to the opaque disk position, and measurements below 290 nm are not needed. Consequently, the MMS1 is used for radiance instruments to take advantage of their ability to measure at wavelengths beyond 785 nm.
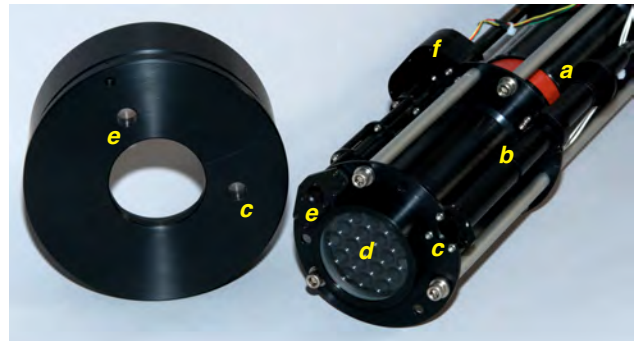
Fig. 48. The front (aperture) section of an OXL radiometer with the environmental housing removed (right), and the cover plate with all apertures visible (left). The exposed components include **a)** the primary instrument heating element (red), **b)** the microradiometer Gershun tubes, **c)** the video camera exit aperture, **d)** the array of 19 microradiometers on a hexagonal grid, **e)** the spectrograph exit aperture, and **f)** the filter-wheel assembly (with separate Gershun tube).

8.2.3 Support Electronics Component

All sensors and controls are accessible via a single all-weather connector on the end cap of the radiometer, which is used to route the spectrograph data acquisition and control functions via a Tec5 interface to the Zeiss spectrometer. This connection also provides communications with the microradiometers and their aggregator, secondary temperature control for the spectrograph, and a flash drive for storing calibration data. In the case of the EML (radiance) sensor, control of the filter wheel and telescopic camera are also routed through the connection. The internal electronics and spectrograph temperature control use 12 VDC power; the primary instrument temperature control uses a separate 15 VDC power source.

A commonly used device for instrument temperature stabilization is the digital proportional-integral-derivative (PID) controller, which switches a heater on and off at high frequency. Rapid switching can cause electrical interference that may cause noise in measurements made by sensitive devices. To prevent any adverse effects, the spectrographs in OXR and EMR sensors are temperature stabilized using an analog proportional-integral (PI) controller, which smoothly adjusts the current to the heater strip attached to the device without switching.

Measurements of the spectrograph temperature of an OXR sensor that was tested in the laboratory over a time period of 10 h showed variations in temperature had a standard deviation of 0.0011°C, indicating the excellent performance of the controller. Temperature variations of a system installed outside were larger, about ±0.03°C, because solar heating caused temperature gradients across the radiometer. Gradients across the spectrograph component are minimized by thermal insulation, but cannot be completely avoided and have an effect on the spectrograph's dark current. For the most accurate measurements, it is therefore necessary to measure the dark current several times throughout the day.

The nine-position filter wheel (Fig. 49) is mounted in front of the spectrograph fiber and uses an index (*home*) position to establish the following hyperspectral measurements: three axes of polarization, dark offsets (opaque disk), bright-target (Sun) viewing (two different ND filters), dim-target (Moon) viewing (open), and stray-light correction (395 nm cut-on filter).
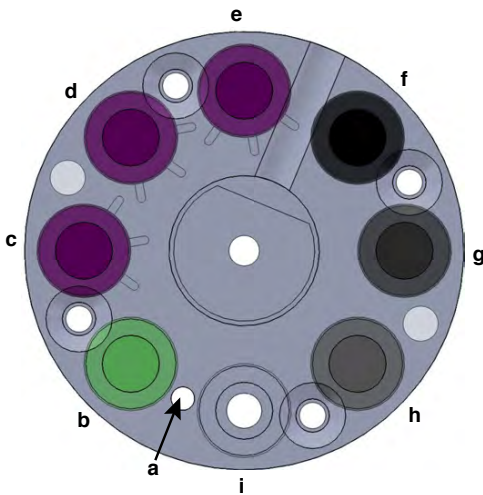
Fig. 49. The EML sensor filter wheel: **a)** index (home) position, **b)** cut-on filter, **c)** 90° polarizer, **d)** 45° polarizer, **e)** 0° polarizer, **f)** opaque disk, **g)** 3.0 ND filter, **h)** 1.5 ND filter, and **i)** open.

The wheel measures 30 mm in diameter and is driven by a high resolution stepping motor controlled by the aggregator electronics. Recent testing has shown that the components are sufficiently light tight that high-quality dark measurements can be obtained by making the dark measurement in between two disk positions. This frees up a position in the filter wheel for another purpose, if needed.

The integrated video camera is a USB Webcam fixed-focus camera modified with the addition of telescopic optics and ND filters optimized for direct viewing of the Sun. The video camera is used for locating the Sun (in lieu of a quadrant detector) and verifying the condition of all targets, i.e., cloud-free solar and lunar disks, cloud presence in sky data, and sea surface debris or foam (although an irradiance sensor can confirm cloud-free solar and lunar disks).

External to the instrument housing, located a short distance away (less than 5 m) in an all-weather enclosure is an acquisition control computer based on a low-power Intel Atom processor, solid state disk drive, and high-efficiency AC-to-DC power supplies for the computer and the remote field radiometer. Also in this enclosure is an Ethernet hub allowing the computer to connect to the Internet, other field radiometers, and field laptops, which may be brought to the site for calibration and other maintenance duties. Other interface modules for connecting additional sensors (meteorological sensors, for example) can also be provided. Typically, this enclosure would be mounted at the base of the pedestal mounting the radiometer.

8.2.4 System Scheduling and Archiving

In an observational system built with EPIC radiometers (Fig. 44), each EMR sensor, as well as ancillary external devices that do not connect directly to an EMR sensor, connects to an automated Power and Component Scheduler (PCS), which is housed with additional support electronics (described below) in a stainless steel control box for long-term weather resistance. The enclosure was selected with an emphasis on maintaining a reasonable internal thermal environment for the electronics in all seasons, as well as ease of field maintenance in the event of a component failure.

The enclosure is a National Electrical Manufacturers Association (NEMA) 4X type, which provides certified protection from the worst environments with an ingress protection (IP) rating for the connectors (IP67) and suitable cables. The control box is designed to be located up to 5 m from the external devices, and is resistant to the external formation of ice on the enclosure. It is also rated for protection against corrosion, falling dirt, rain, sleet, snow, windblown dust, and splashing water. PCS power is supplied from 85–264 VAC at 47–63 Hz (200 W maximum). Options are available for DC power from solar panels or other power sources (e.g., a wind turbine).

Custom OSPREy software written as Microsoft .NET Framework modules control the system and provides autonomous operations under a user-programmable schedule. Included in the PCS are high stability, low-noise power supplies, thermal control circuitry, an integrated GPS receiver, and auxiliary sensors (e.g., a rain detector) as desired. The PCS design is predicated on adaptability; for

example, radiance instrument position is controlled by the tracking system, and the operation of the shadowband is likewise controlled by an automated positioning system, either of which is powered by a Phoenix TRIO power supply mounted on a standard mounting rail†. The internal components were carefully selected for reliability in each purpose. OSPREy system operations are controlled by an Intel DW525 Atom dual core imbedded PC with 4 GB random access memory (RAM) plus a 120 GB solid-state disk (SSD), under Windows Embedded 7, as configured for OS-PREy. A block diagram overlaid on a picture of control box internal components is provided in Fig. 50 (the optional surge protector and Ethernet hub are not shown).
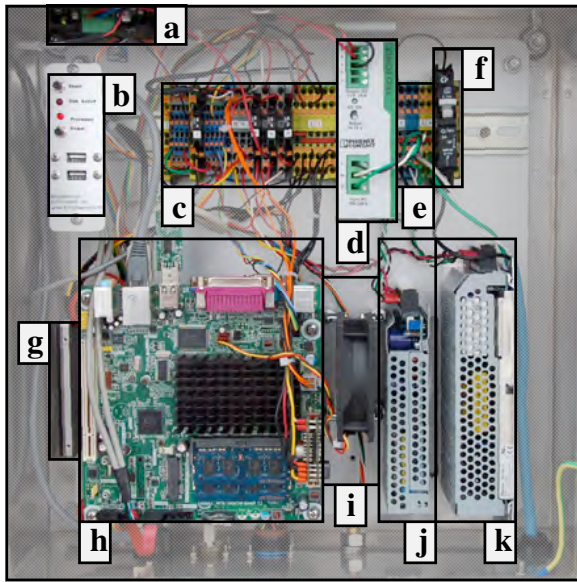
Fig. 50. The control box internal components for an EMR observational system, like OSPREy (the heat sink and GPS antenna are not shown, because they are mounted on the top exterior of the enclosure), grouped into functional units: **a)** primary housing temperature controller (Wavelength Electronics); **b)** power switch and USB expansion hub; **c)** DIN rail with terminal blocks; **d)** power supply (Phoenix) for the embedded PC and tracker or shadowband accessory; **e)** 110 VAC bus; **f)** circuit breaker; **g)** 120 GB SSD (Intel); **h)** D525MW Atom dual-core embedded PC (Intel); **i)** secondary cooling fan; **j)** ultra-low-noise power supply for main instrument power and spectrograph secondary temperature controller (Daitron); and **k)** ultra-low-noise power supply for primary housing temperature controller (Daitron).

Data collection software running on each PCS is driven by a scheduler (task), which specifies the component and

mode of data collection as a function of time. The scheduler is implemented as a table in American Standard Code for Information Interchange (ASCII) format and is regularly updated by the Archive and Communications Master (ACM), which coordinates the measurements of all EMR sensors. Because all computer clocks are synchronized, measurements can be performed in synchronous and asynchronous modes as directed by the ACM.

If the connection between a PCS and the ACM is severed (e.g., because the communications connection is lost or there is a failure with the ACM), the affected PCS system will run the schedule it last received from the ACM until new communications establish otherwise. The scheduler specifies all parameters relevant for system operation including the mode of the shadowband (e.g., stowed shadowband, shadowband in front of Sun, or shadowband sweeping between predefined angles), the mode of the solar tracker (e.g., Sun tracking using ephemeris algorithm, Sun tracking using video camera, Moon tracking, sky scan, sea surface viewing, etc.), the position of the filter wheel in EML (radiance) sensors, the integration time of the spectrograph, and others.

All data records are time stamped, and acquired in an ASCII comma-separated format in the measurement units reported by the sensors (e.g., volts, counts, or pixel number). Separate files are produced for system logs, the spectrograph (if present), and microradiometer components. Data are recorded on the SSD, and are intended to be ingested daily by the ACM on a defined, but programmable, schedule (most likely at night when system activity is usually at a minimum).

The ACM is a computer located close to the EMR sensors, or remotely situated, depending on the bandwidth of the available communications channels to the deployment site. A variety of tools for system monitoring, QA and QC, as well as data analysis are under development. These tools are being designed to apply calibrations and produce a variety of data products, with the initial set of tools based on an operational system and its resulting data products (Fig. 44d).

8.3 Starter System

The simplest OSPREy configuration—or *starter system*—uses a single EML radiance sensor as a starting point for automated above-water radiometry and sun photometry, as well as an advanced replacement for a SeaPRISM unit (Fig. 44a). With respect to the latter, SeaPRISM units are not hyperspectral, have many fewer channels (eight), are not capable of intracomparisons for QA and QC (unless duplicate filter channels are installed, which further reduces their limited spectral resolution), do not have a video camera, and cannot measure channels simultaneously. In addition, any polarization capability also reduces the spectral resolution.

The starter system is a low-cost, entry system into the OSPREy suite of instruments, which can be incrementally

---

† A *Deutsches Institut für Normung*, or German Institute for Standardization, (DIN) metal rail widely used for mounting circuit breakers and industrial control equipment inside equipment racks is used.

improved as resources or objectives evolve. For example, a single EML sensor can be used as an algorithm validation system or a monitoring device, for atmospheric, terrestrial, and oceanic applications. The front end of an EML radiometer is shown in Fig. 48, and a cutaway drawing is presented in Fig. 51. The narrow FOV of the instrument determines the length of the Gershun tubes and results in a slightly longer housing than an irradiance instrument. A customized FOV for different sampling objectives is possible and would change the overall length of the instrument. Similarly, customized lengths of the fiber optics can alter the length of the instrument.

Fig. 51. A simplified technical drawing of an EML radiometer. The *core* of the design is the cluster of microradiometers (brown) left of the aggregator stack (green) with filter-wheel assembly above, fiber and spectrograph (pink) to the right, and camera below. The electronics positioned near the end cap primarily support the spectrograph. Some details are omitted (e.g., wiring and insulation) for clarity.

A sampling scenario for a starter system may include measurements of direct solar irradiance, $E(\lambda)$, followed by $L_i(\lambda)$ and $L_T(\lambda)$, to derive $L_W(\lambda)$. Because of the high angular velocity of the tracker (up to $50°\,\mathrm{s}^{-1}$), a complete sequence can be executed within $30\,\mathrm{s}$ and may be repeated several times per hour. Direct solar measurements allow the determination of the AOD, which is needed for computing the normalized water-leaving radiance (Zibordi et al. 2004b), $\left[L_W(\lambda)\right]_\mathrm{N}$. Once or twice per hour, almucantar and principal plane scans can be performed for characterizing additional aerosol properties, e.g., the aerosol SSA and phase function.

During the night, the measurement scenarios can include direct measurements of the Moon. A time series of such measurements permits a Langley calibration of the sensors and derivation of the AOD. The sequence of measurements can be reconfigured and tailored to the specific research objectives. For example, a starter system can replace sun photometers used in the AERONET work and sampling scenarios can be adapted to the AERONET protocol.

8.4 Minimum System

The addition of an EME sensor with a shadowband accessory to a starter system defines a *minimum system* configuration (Fig. 44b). The front end of an EME (or OXE) sensor is shown in Fig. 47 and a cutaway depiction is provided in Fig. 52. An EME sensor consists of a cluster of 18

microradiometers with fixed wavelengths and the fiber of the Zeiss/Tec5 MMS UV-VIS II spectrograph occupies the position normally used by the nineteenth microradiometer. The microradiometer cluster is coupled to the irradiance collector via a plano-convex lens specially designed for use with the parallel geometry of microradiometers (Booth et al. 2010).
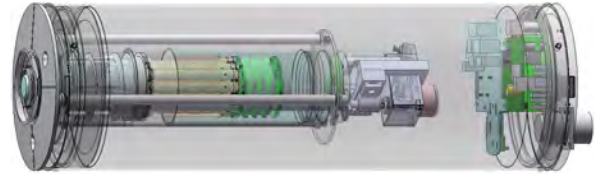
Fig. 52. A simplified technical drawing of an EME (or OXE) following the approach in Fig. 51. The primary new component is the plano-convex lens (white) immediately left of the microradiometers (brown) and the cosine collector on the aperture end plate (blue).

The benefits of the minimum system configuration are the enhanced QA and QC capabilities, which is provided by having two (radiance and irradiance) independent measurements of the Sun and Moon plus the intracomparisons between the microradiometers and spectrograph in each sensor. By itself, the irradiance radiometer provides measurements of the global solar and lunar irradiance, which can be used to detect the presence of clouds across the solar and lunar disks. The shadowband accessory permits the measurement of the diffuse component of the global irradiance, which is used to establish the direct-to-global irradiance ratio. The greater diversity in measurements provides improved data products (e.g., better cosine-error correction), as well as new data products (e.g., cloud optical depth).

A variety of sampling scenarios can be implemented with a minimum system. For oceanic observations, the EME sensor typically measures $E_d(0^+, \lambda)$ while the EML sensor alternates between $L_T(\lambda)$ and $L_i(\lambda)$ measurements. The $E_d(0^+, \lambda)$ data are used to convert $L_W(\lambda)$ derived from the EML sensor to $\left[L_W(\lambda)\right]_\mathrm{N}$. Measuring $E_d(0^+, \lambda)$ directly, rather than estimating it from $E(\lambda)$, as is done for the starter system (or a SeaPRISM unit), is more accurate and this is a fundamental advantage of the minimum system configuration.

A typical sampling scenario for atmospheric observations includes EML measurements of $E(\lambda)$ while the EME sensor measures $E_d(0^+, \lambda)$ and $E_i(\lambda)$ in an alternating sequence using the shadowband. The direct irradiance computed from the E_d and E_i measurements can be used to validate the data from the EML sensor. As an alternative, the EME sensor can be making shadowband measurements to determine the direct-Sun irradiance, while the EML sensor performs almucantar and principal plane scans. An additional feature of the minimum system is its ability to

Table 14. The sampling modes for the OSPREy operational system. The first column refers to the two redundant EMR dyads, labeled "A" and "B". Mode 1 is the standard mode for measuring $L_W(\lambda)$ and is distinguished by two different ("a" and "b") versions, wherein the role of the two dyads is reversed. Mode 2 has three versions, each of which has both dyads making the same measurements: Sun, sky, and sea. Mode 3 is for sky radiometry and Mode 4 is stowed. The $\perp$ symbol denotes viewing perpendicular to the solar plane.

Instrument	Mode 1a	Mode 1b	Mode 2a	Mode 2b	Mode 2c	Mode 3	Mode 4
A: *Radiance*	L_i	L_T	Direct-Sun†	L_i	L_T	Direct-Sun	Stowed, dark
A: *Tracker*	Sky, $\perp$ Sun	Sea, $\perp$ Sun	Tracks Sun	Sky, $\perp$ Sun	Sea, $\perp$ Sun	Tracks Sun	Stowed
A: *Irradiance*	E_d, E_i	E_d, E_i	E_d, E_i	E_d	E_i	E_d, E_i	E_d, dark
A: *Shadowband*	Cycling	Cycling	Cycling	Stowed	Active	Cycling	Stowed
B: *Radiance*	L_T	L_i	Direct-Sun†	L_i	L_T	L_i	Stowed, dark
B: *Tracker*	Sea, $\perp$ Sun	Sky, $\perp$ Sun	Tracks Sun	Sky, $\perp$ Sun	Sea, $\perp$ Sun	Sky scans	Stowed
B: *Irradiance*	E_d, E_i	E_d, E_i	E_d, E_i	E_d	E_i	E_d, E_i	E_d, dark
B: *Shadowband*	Cycling	Cycling	Cycling	Stowed	Active	Cycling	Stowed
Duration [min]	15	15	15	5	5	15	> 60

† Or direct-Moon measurements.

estimate cloud optical depth by comparing measurements of E_d during overcast illumination with reference data for clear-sky conditions. As with the starter system, lunar data collection scenarios are also possible.

8.5 Spectral System

A refinement to the minimum system is accomplished by having two EME sensors. This so-called *spectral system* (Fig. 44c) uses two individually optimized cosine collectors to ensure the lowest cosine errors over the two spectral regions. The two regions are established by the cosine collectors and the accompanying selection of the spectrograph. The two cosine collector designs are optimized for the 290–1,100 nm and 1,000–1,670 nm spectral ranges, and the corresponding wavelength ranges for the spectrographs are 250–780 nm and 300–1,150 nm, respectively.

The overlap in wavelengths of the two spectrographs provides redundancy in the measurement suite across a subset of the full spectral range. The microradiometer components of the two irradiance sensors can be set up to add to, or complete, the desired level of redundancy— the complete extent of which establishes how much minimization of risk is built into the system. Dual irradiance sensors allow more sophisticated sampling scenarios using synchronous and asynchronous protocols, which further enhances data products and the number and types of QA and QC products. The latter are an important part of managing the uncertainty budget for the system.

In synchronous operation, the two irradiance sensors work in tandem and the spectral system is essentially equal to a minimum system with a larger number of wavelengths. In this configuration, all sampling scenarios of the minimum system can also be applied to the spectral system. In asynchronous operation, one irradiance sensor is measuring E_d while the other measures E_i using the shadowband. For channels common to both sensors, the ratio of

diffuse-to-global irradiance can be measured directly. This method has smaller uncertainties compared to the alternative approach where this ratio is determined from sequential measurements of diffuse and global irradiance.

8.6 Operational System

Balanced proportions of enhanced accuracy and risk minimization are achieved with an *operational system* (Fig. 44d), which is composed of two EML and EME dyads. This system configuration was built as part of the OSPREy development activity. Although each sensor type could be configured slightly differently, the perspective here is that the radiance sensors are duplicates as are the irradiance sensors. The use of two identical dyads (recalling that a radiance and irradiance sensor pair must differ by one fixed wavelength channel) provides maximum redundancy, which minimizes risk and maximizes enhanced data products from the use of synchronous and asynchronous sampling scenarios. Consequently, the operational system is anticipated to be suitable for the highest-quality validation exercises, as well as for vicarious calibration.

Within the hierarchy of the most simple to the most complex system configurations (Figs. 44a–44e), the operational system is the first system to provide the greatest diversity in sampling modes, as shown in Table 14). This diversity also provides the most extensive QA and QC opportunities, through redundancies in equipment (two copies of one instrument type) and data products (alternative measurement approaches for the same data product). Ultimately, the diversity is primarily due to the fact that the dual EML and EME sensors permit synchronous and asynchronous sampling for both sensor types, during the day and night.

Modes 1a and 1b are the usual modes for $L_W(\lambda)$ measurements with one radiance sensor viewing the sky and the other viewing the water at the correct angles with respect to the Sun and the platform-perturbation avoidance

criteria. The shadowband accessories cycle through measurements of global irradiance (E_d), diffuse irradiance (E_i), and special measurements, wherein the shadowband is either positioned at 10° on either side of the Sun or slowly *sweeps* over the collector (Bernhard et al. 2010). The latter are used to correct for the partial shading of the sky when E_i is measured with the shadowband occulting the Sun. The shadowbands of the two dyads operate asynchronously such that there is always a measurement of E_d.

Modes 2a–2c are designed primarily for sensor intercomparisons. In Mode 2a, both EML instruments measure direct-normal irradiance and either track the Sun (day) or Moon (night). The EME sensors cycle through independent measurements of direct-normal irradiance. In Mode 2b, the tracked systems make synchronous measurements of sky radiance (L_i) while the EME sensors measure E_d. In Mode 2c, the EML instruments point at the sea and the EME sensors measure E_i. These modes allow for the intercalibration of both radiometer types, with the EML sensors exposed to flux levels representative of Modes 1 and 3.

Mode 3 is designed to characterize the sky radiance field for sun photometry, and is used for retrieving more comprehensive data products, such as the SSA. This is done with one EML sensor scanning the sky at a constant solar zenith angle and varying the azimuth (almucantar scan), or by scanning the sky in a vertical plane containing the Sun and the radiometer (principal plane scan). During the latter, the second sensor is pointing at the Sun. Two modes could be used here for redundancy, but given the redundancy in the second set of modes, this seems unnecessary. During sky-radiance characterizations, the shadowband devices are cycling. There can also be an alternative scan wherein one EML sensor scans the entire sky.

Mode 4 is a night mode and is used primarily to determine the dark offsets. During this mode, the radiometers are exercised at each of the three gain settings while measuring the dark signals. Mode 4 is also executed during severe weather for safeguarding the sensors.

8.7 Maximum System

The culmination of redundancy and sampling opportunities occurs with the *maximum system*, which uses two identical triads (Fig. 44e). The triads are formed by using one EML sensor and two EME sensors to ensure the highest accuracy in the irradiance measurements. Once again, spectral diversity can be optimized by using different spectral configurations in the multiple sensor systems, while remembering that common wavelengths provide redundancy for the most important wavelengths and enhance QA opportunities. The use of a maximum system is anticipated for vicarious calibration activities requiring the highest accuracy possible, and for specialized exercises wherein a portion of the spectral domain requires a unique configuration.

8.8 Transfer Radiometers

Although a separate class in the architecture of instruments built with microradiometers (Morrow et al. 2010c), OXL and OXE instruments are of a similar design to their EMR equivalents, and in fact, the irradiance sensors in both product lines are the same. The principal differences between the two are in the radiance sensors: compared to an EML, an OXL unit does not have a video camera nor a filter-wheel assembly, and has one less microradiometer (18). Although built and envisioned as laboratory devices, OXR sensors can collect data outdoors. The OXL spectrograph, however, saturates if pointed at a very bright target (e.g., the Sun), because of the absent ND filter (due to the missing filter wheel).

For the OSPREy activity, the main purpose of OXR sensors is to a) ensure a high-accuracy transfer of the radiance and irradiance scales established by the NIST SIRCUS facility (Brown et al. 2000 and Eppeldauer et al. 2000) to the BSI calibration laboratory, b) preserve these scales for the long term, and c) transfer these scales to OSPREy field sensors and the OSPREy lamp library (Chap. 6). OXR sensors are compatible with the kinematic mounting fixtures used in the BSI calibration laboratory to ensure reproducible positioning.

The long-term stability of OXR units is very important. For the OSPREy activity, the instruments are anticipated to remain in the BSI calibration facility under controlled environmental conditions (temperature and humidity) at all times with the exception of travel to NIST for SIRCUS calibration. The OXR radiance instrument is also used for monitoring the stability of the BRDF of the reflectance plaque used for radiance calibrations (App. I). Because the BSI radiance calibration bench (Sect. 6.3.2.2) has fixtures on both sides of the reflectance plaque, the OXR radiance sensor can be used for direct comparison with other radiance sensors (Fig. 53). In this case, the calibration of the lamp illuminating the plaque is not critical.

Fig. 53. A view from the plaque of the radiance bench toward the calibration standard (dimly lit for clarity). The OXL prototype is on the left side and an EML sensor is on the right side with the spectrograph aperture oriented downward (6 o'clock position). Both instruments are positioned with kinematic mounts. All reflections are caused by the camera flash.

8.9 Radiometer Performance

An OXE and an EML sensor were calibrated in the BSI calibration laboratory. The OXE sensor was set up on the irradiance bench (Sect. 6.3.2.1) and illuminated by a calibrated FEL lamp 50 cm from the cosine collector (as measured from the lamp posts). The EML sensor was set up facing the center of a Spectralon reflectance plaque, which was illuminated by a calibrated FEL lamp positioned 287.1 cm away from the center of the plaque.

Because both of the OXR and EMR instruments are nontraditional—*hybridspectral*—devices, a new lexicon incorporating a unique symbology and vocabulary is needed to provide the specificity for the calibration and the resulting data products that can be produced from the instrument measurements. This new lexicon is important and becomes even more important once the radiometers are exposed to the diversity of targets in the field, wherein data products can be produced from different instrument types (radiance or irradiance).

8.9.1 Iconographic Symbology

The so-called *iconographic symbology* presented here is based on providing accents on variables, both above and below, to denote the important aspect of data acquisition, e.g., sea viewing, shadowband, FEL calibration, etc. In most cases, the accents are designed to be *visual clues* regarding what was recorded. The simplest variable is associated with recording a signal amplitude, denoted A, and is used to introduce the symbology. In most cases, A is recorded from either fixed wavelength microradiometers or hyperspectral spectrographs, and the spectral channel for the former or pixel number for the latter is denoted λ_i. The center wavelength associated with either is λ_i^c. To simplify the ensuing presentation, any spectral dependence is omitted for the time being.

There are two types of optical measurements to distinguish: radiance and irradiance. Radiance measurements usually involve targeting, and the sensor is pointed at a light source. Irradiance measurements usually do not involve pointing, except they are usually made with respect to an established planar geometry, which requires the instrument to be properly positioned or leveled (a form of pointing). Radiance measurements usually have an arrow accent, whereas irradiance measurements usually do not. An exception for the latter is during calibration, wherein the cosine collectors are pointed at a light source (e.g., an FEL lamp). Consequently, the only time irradiance measurements have an arrow is to denote calibration (denoted by leftward overhead arrow accent).

There are four recurring kinds of variables and the presence or absence of the accents provide the needed distinction among the four: a) a calibration recording, b) an ideal value, c) a true value, and d) a field measurement:

$\overleftarrow{A}$ A calibration value signal amplitude is identified by the leftward overhead arrow accent.

$\underset{=}{A}$ An ideal value signal amplitude is identified by the vertical parallel bars accent under the variable.

$\underset{=}{A}$ A true value signal amplitude is identified by the horizontal parallel bars accent under the variable.

A field measurement, which is the most predominant type of measurement, is identified by the absence of the above three accents. Whether or not the measurement is radiance or irradiance, as well as microradiometer or spectrograph, is established below after more of the distinctive types of measurements are presented.

A principle distinction in variable type, as established in Chaps. 6 and 7, is whether the variable represents a *light* or *dark* measurement. For a light measurement, the sensor aperture is unobstructed with respect to the intended target, whereas for a dark measurement the sensor aperture is obstructed, occluded, or capped. Following the approach established above, wherein the most recurring value is not accented, dark measurements are denoted by the presence of a filled-in (dark) circle or square:

$\overset{\bar{\blacksquare}}{A}$ The capped dark signal amplitude obtained with an opaque cover over the sensor aperture.

$\overset{\rightharpoonup\blacksquare}{A}$ The *background* dark signal amplitude obtained by closing a shutter between the lamp (while it is operating) and the radiometer.

$\overset{\bullet}{A}$ The night (dark) signal amplitude.

$\overset{\bullet\bullet}{A}$ The *ambient* or occluded calibration dark signal amplitude.

Consequently, any variable without the filled-in (dark) circle is, by definition, a light measurement.

For irradiance sensors equipped with the BioSHADE accessory, a unique type of dark measurement can be made:

$\overset{\bullet}{A}$ The shadowband night (dark) signal amplitude.

This dark value can be subtracted from an irradiance night (dark) value to establish a QA assessment of the night dark (which shows how a radiance and irradiance dyad leads to enhanced QA, because radiance sensors alone cannot make this measurement).

There is additional nuance in the dark data collected by microradiometers, which is important for certain analyses. The nuance is a result of microradiometers having multigain amplifiers. The very first microradiometers had two-stage amplifiers, and all subsequent models have three-stage amplifiers. The type of amplification circuit, i.e., two- or three-gain stages, is denoted by the number of the filled-in (dark) circles:

$\underset{\bullet\bullet}{A}$ The two-gain stage sensor dark signal amplitude.

$\underset{\bullet\bullet\bullet}{A}$ The three-gain stage sensor dark signal amplitude.

Only one two-gain system was built with microradiometers (the very first system), so the distinction between two- and three-gain systems is not expected to be significant, but is included for completeness.

When dark data are collected, microradiometers are taken out of autoranging gain control and commanded

to switch to specific gain stages, so dark values can be recorded for each gain stage. The particular gain stage being recorded is denoted by the presence and relative position of the filled-in (dark) circle within a sequence of circles, the number of which indicates the number of stages in the amplification circuit:

$\overset{..}{A}$ The high gain of a two-gain sensor signal amplitude.

$\overset{..}{A}$ The low gain of a two-gain sensor signal amplitude.

$\overset{...}{A}$ The high gain of a three-gain sensor signal amplitude.

$\overset{...}{A}$ The medium gain of a three-gain sensor signal amplitude.

$\overset{...}{A}$ The low gain of a three-gain sensor signal amplitude.

Combining the gain-stage information for a particular dark type provides a complete description of the dark measurement. Combining a capped sensor dark with gain information can yield the following, for example:

$\overset{...}{\bar{A}}$ The low gain (of a three-gain sensor) signal amplitude obtained with a capped sensor.

This level of detail is not needed in all applications. It is presented here for completeness and to show how a highly detailed symbology might be produced.

As noted earlier, radiance measurements are *targeted*, that is, the sensor is pointed at the light source to be measured. The currently anticipated targets for EMR radiometers include the following:

$\tilde{A}$ The sky signal amplitude.

$\breve{A}$ The sea signal amplitude.

$\overset{*}{A}$ The solar signal amplitude.

$\overset{\circ}{A}$ The lunar signal amplitude.

Note that the sky and sea arrows are not horizontal, so they do not indication calibration; the former is angled upwards and the latter downwards.

The direct components of the solar and lunar flux can be measured or derived and are designated as follows:

$\overset{|*|}{A}$ The direct-Sun signal amplitude.

$\overset{|\circ|}{A}$ The direct-Moon signal amplitude.

Note that two bounding small vertical bars are used in conjunction with the already established Sun and Moon accents to denote the value is directional.

For some of the OSPREy system configurations presented in Fig. 44, an irradiance sensor is equipped with a BioSHADE accessory, so the indirect (sky) component of the solar (or lunar) global irradiance can be determined. This diffuse component can be subtracted from the global measurement to yield the direct-Sun (or direct-Moon) irradiance component mentioned above. The shadowband variables for OSPREy systems are as follows:

$\widehat{A}$ The shadowband sky signal amplitude.

$\overset{*}{\widehat{A}}$ The shadowband solar global irradiance (Sun and sky) signal amplitude.

$\overset{\circ}{\widehat{A}}$ The shadowband lunar (Moon and sky) signal amplitude.

Recalling that a fourth shadowband dark measurement, $\overset{\bullet}{\widehat{A}}$, can also be made.

The anticipated calibration scenarios include the following:

$\overset{\leftarrow}{A}$ The FEL lamp calibration signal amplitude.

$\overset{*\leftarrow}{A}$ The solar calibration signal amplitude.

$\overset{\circ\leftarrow}{A}$ The lunar calibration signal amplitude.

$\overset{\square\leftarrow}{A}$ The reflectance plaque calibration signal amplitude.

All of these calibration scenarios can be executed at BSI or in the field.

8.9.2 Lexicon

Sensor performance was established using the statistics derived from dark and light measurements plus instrument characterization parameters, which have a spectral dependence (part of this nomenclature was presented in Sects. 6.7 and 7.2, and is repeated here for completeness):

$\mu(\lambda)$ The mean value of an acquisition sequence,

$\sigma(\lambda)$ The standard deviation of an acquisition sequence,

$\kappa(\lambda)$ The maximum (or saturation) signal level,

$\gamma(\lambda)$ The responsivity (calibration coefficient and applicable terms, e.g., the immersion factor).

The use of light or dark data is indicated by the absence or presence of a dark accent, respectively. In this case the capped darks accent is applicable. For example, the mean value of a dark data acquisition sequence is denoted $\bar{\mu}(\lambda)$, whereas the mean value of a data acquisition sequence collected with the aperture exposed to light is denoted $\mu(\lambda)$.

Considering a generalized parameter $\mathfrak{P}$, an indexing scheme is adopted wherein two indices, i and j, provide the needed specificity to uniquely identify the measurement and instrument type, respectively, $\mathfrak{P}_i^j$, as follows:

$i = E$ denotes irradiance data,

$i = L$ denotes radiance data.

$j = M$ denotes the microradiometer data, and

$j = S$ denotes the spectrograph data.

To continue with the earlier example, the mean value of a dark data acquisition sequence for the spectrograph data of a hybridspectral radiance sensor is denoted $\bar{\mu}_L^S(\lambda)$. This nomenclature also anticipates indices assigned for EMR spectrograph data involving the position of the filter-wheel assembly. Because they are not needed here, the information is suppressed for brevity. If a radiometer does not have more than one sensing technology, the superscript designation is not used (e.g., Sect. 7.2).

There are two other immediately useful parameters that need to be included, and they both involve sources (or targets), which are identified with the i subscript:

$i = F$ denotes measurements of an FEL lamp, and

$i = P$ denotes measurements of a reflectance plaque. The irradiance from an FEL lamp is designated E_F and the radiance from a plaque is designated L_P. In general, these designations are used with the standard symbology associated with radiance (L) and irradiance (E) variables. Note that E_i and L_i are the diffuse irradiance and sky radiance, respectively, unless indicated within a generalized discussion of parameter indices. For generalized parameter discussions, the radiometric parameter of interest should be indicated by the fraktur or euler typefaces (e.g., $\mathfrak{P}$ or $\mathcal{P}$, respectively) to avoid confusion; the euler typeface is reserved for hybridspectral sensors, so it is clear that two different sensor technologies might have been used for the observation of interest.

Some data products (e.g., direct-Sun irradiance) can be derived more than one way with more than one sensor, so accents are likely necessary to make it clear how a data product was derived. This diversity is part of the power of the OSPREy architecture, because it provides intrinsic QA assessments, particularly for autonomous systems. The level of detail needed to document data products is left to the user, and the presentation here is designed to show what a detailed approach might look like.

Ultimately, the variables of central interest with an OSPREy system are radiance (L) and irradiance (E), wherein the subscript notation $i = L$ and $i = E$, respectively, become redundant and can be ignored. This frees up the subscript location for the standard symbology for radiance and irradiance values, at which point, accents might no longer be needed for proper distinction and can also be ignored. For example, the total sea radiance from a hybridspectral sensor can be denoted $\mathcal{L}_T^j(\lambda)$, wherein $\mathcal{L}_T^M(\lambda)$ denotes the microradiometer data and $\mathcal{L}_T^S(\lambda)$ denotes the hyperspectral spectrograph data.

To characterize the performance of the OXE radiometer and an EML sensor, several dark and light measurements were performed and their mean (μ) and standard deviation (σ) values are part of the data products. From these data, the following three parameters were computed: the noise equivalent signal, $\mathbf{N}$; the signal noise, $\mathbf{S}$; and the maximum level of signal saturation, $\mathbf{M}$:

$$\mathbf{N}_i^j(\lambda) = \frac{\breve{\sigma}_i^j(\lambda)}{\gamma_i^j(\lambda)}, \tag{14}$$

$$\mathbf{S}_i^j(\lambda) = \frac{\sigma_i^j(\lambda)}{\mu_i^j(\lambda)}, \tag{15}$$

and

$$\mathbf{M}_i^j(\lambda) = \frac{\kappa_i^j(\lambda) - \breve{\mu}_i^j(\lambda)}{\gamma_i^j(\lambda)}. \tag{16}$$

These three parameters are central to describing instrument performance for hybridspectral instruments (as first introduced in Sect. 7.2).

8.9.3 OXE (Irradiance) Performance

For the specific case of the OXE sensor,

$$\mathbf{N}_E^j(\lambda) = \frac{\breve{\sigma}_E^j(\lambda)}{\gamma_E^j(\lambda)}, \tag{17}$$

$$\mathbf{S}_E^j(\lambda) = \frac{\sigma_E^j(\lambda)}{\mu_E^j(\lambda)}, \tag{18}$$

and

$$\mathbf{M}_E^j(\lambda) = \frac{\kappa_E^j(\lambda) - \breve{\mu}_E^j(\lambda)}{\gamma_E^j(\lambda)}, \tag{19}$$

where the j index designates the spectrograph or microradiometer channels (S and M, respectively).

The responsivity is calculated as

$$\gamma_E^j(\lambda) = \frac{\mu_E^j(\lambda) - \breve{\mu}_E^j(\lambda)}{E_F(\lambda)}, \tag{20}$$

where E_F is the spectral irradiance of the FEL lamp at 50 cm distance.

Measurements of the microradiometer channels were performed at a rate of 5 Hz, while an integration time of 5,000 ms was applied to the spectrograph measurements. Light and dark measurements were executed over a 1 min time period. These measurements were used to calculate $\mu_E^j(\lambda)$ and $\breve{\mu}_E^j(\lambda)$. Data analysis confirmed that individual measurements have a distribution that is approximately gaussian.

The standard deviation of the mean of a normal distribution is equal to $\sigma/\sqrt{N_s}$, where N_s is the number of samples. The mean $\mathbf{N}_E^M(\lambda)$ is designated $\overline{\mathbf{N}}_E^M(\lambda)$ and is computed for microradiometers based on a sampling at 5 Hz with a 60 s sampling period:

$$\begin{aligned}\overline{\mathbf{N}}_E^M(\lambda) &= \frac{\mathbf{N}_E^M(\lambda)}{\sqrt{5 \cdot 60}} \\ &= 5.77 \times 10^{-2}\,\mathbf{N}_E^M(\lambda).\end{aligned} \tag{21}$$

The corresponding formulation for the spectrograph using an integration time of 5 s and 60 s sampling is:

$$\begin{aligned}\overline{\mathbf{N}}_E^S(\lambda) &= \frac{\mathbf{N}_E^S(\lambda)}{\sqrt{60/5}} \\ &= 2.89 \times 10^{-1}\,\mathbf{N}_E^S(\lambda).\end{aligned} \tag{22}$$

One advantage resulting from the conversion of $\mathbf{N}_E^j$ to $\overline{\mathbf{N}}_E^j$ is that noise specifications for the filter channels and the spectrograph become comparable. Furthermore, the latter is the more relevant quantity to describe the instrument performance, because calibrations applied to solar measurements are typically based on a 60 s sampling of the light and dark signals when measuring the calibration source, as was done here.

The mean signal noise, $\overline{\mathbf{S}}$, for 60 s sampling is defined in a similar way as follows:

$$\overline{\mathbf{S}}_E^j(\lambda) = \frac{\mathbf{S}_E^j(\lambda)}{\sqrt{N_s}}, \tag{23}$$

where N_s is 300 for the microradiometer channels and 12 for the spectrograph.

Table 15 presents $\mathbf{M}_E^M(\lambda)$, $\overline{\mathbf{N}}_E^M(\lambda)$, and $\overline{\mathbf{S}}_E^M(\lambda)$ values for the microradiometer channels of the OXE sensor. The $\mathbf{M}_E^M(\lambda)$ and $\overline{\mathbf{N}}_E^M(\lambda)$ values are considerably larger in the UV compared to the VIS–SWIR wavelengths. This is partly a consequence of the transmission of the interference filters used for each microradiometer channel. For example, the peak transmission of the 380 nm filter is comparatively low, explaining the increased $\mathbf{M}_E^M(\lambda)$ at this wavelength. The $\overline{\mathbf{S}}_E^M(\lambda)$ values are less than 0.01% at all wavelengths, indicating that signal noise in light data is not a significant contributor to the overall uncertainty budget.

Table 15. Noise and saturation characteristics for the microradiometer channels of the OXE sensor. The E_F, $\mathbf{M}_E^M$, and $\overline{\mathbf{N}}_E^M$ values are given in units of $\mu W\,cm^{-2}\,nm^{-1}$; the $\overline{\mathbf{S}}_E^M$ values are in percent. The last row gives the scaling factor for the data in each column.

λ [nm]	E_F	$\mathbf{M}_E^M$	$\overline{\mathbf{N}}_E^M$	$\overline{\mathbf{S}}_E^M$
320	0.314	3.99	17.4	0.006
340	0.557	4.09	19.1	0.004
380	1.388	13.58	57.9	0.005
412	2.436	3.68	16.6	0.002
443	3.776	2.37	9.9	0.002
490	6.314	1.04	4.4	0.002
510	7.525	1.25	5.4	0.002
532	8.908	0.91	4.5	0.002
555	10.380	0.70	2.9	0.002
625	14.690	0.43	2.0	0.002
665	16.870	0.31	1.3	0.002
683	17.760	0.45	2.1	0.002
710	18.960	0.40	1.7	0.002
780	21.390	0.29	1.3	0.002
875	22.950	0.58	2.5	0.002
1,020	22.600	0.22	2.8	0.002
1,245	18.870	0.07	6.5	0.002
1,640	11.570	0.03	2.2	0.002
Scaling	1	$\times 10^6$	$\times 10^{-6}$	1

Figure 54 contrasts the noise and saturation characteristics of the microradiometers to those of the spectrograph and compares these quantities with a spectrum of global solar irradiance modeled for $\theta_s = 40°$, as well as the spectral irradiance of an FEL lamp at a distance of 50 cm from the sensor. The irradiance of both sources is more than four orders of magnitude larger than $\overline{\mathbf{N}}_E^M(\lambda)$, which indicates signal noise is not a significant factor in limiting the accuracy of the fixed wavelength measurements. The irradiance of both sources is also well below the saturation level, $\mathbf{M}_E^M(\lambda)$.
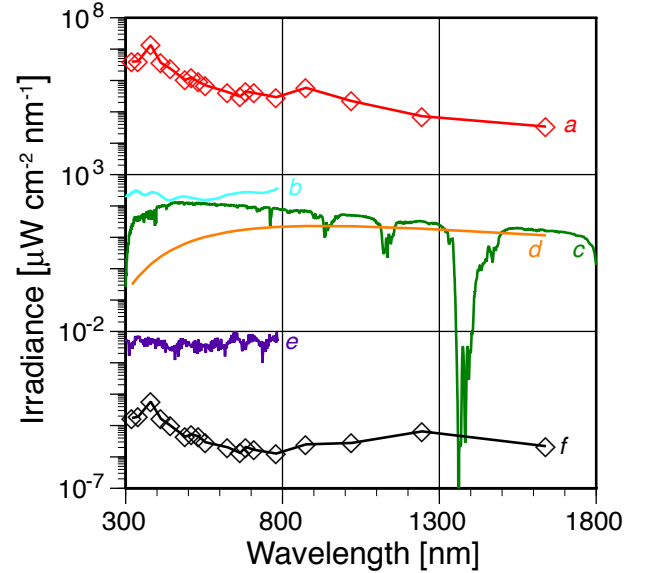
Fig. 54. The noise and saturation characteristics of microradiometer channels and the spectrograph of the OXE sensor: **a)** $\mathbf{M}_E^M(\lambda)$, **b)** $\mathbf{M}_E^S(\lambda)$ for $t_i = 5{,}000$ ms, **c)** global Sun irradiance, **d)** $E_F(\lambda)$, **e)** $\overline{\mathbf{N}}_E^S(\lambda)$, and **f)** $\overline{\mathbf{N}}_E^M(\lambda)$.

The noise and saturation characteristics of the spectrograph are notably inferior to those of the microradiometer channels. For example, at 320 nm, the lamp irradiance is only 1.5 orders of magnitude larger than $\overline{\mathbf{N}}_E^S(\lambda)$, indicating that signal noise limits the precision of lamp transfers using the spectrograph at this wavelength. The saturation irradiance $\mathbf{M}_E^S(\lambda)$ shown in Fig. 54 was calculated for an integration time of 5,000 ms and is barely larger than the irradiance of the solar spectrum. It is therefore possible that the spectrograph might saturate under certain circumstances (e.g., when reflections off of clouds lead to an enhancement of surface irradiance beyond the clear-sky limit). In these cases, saturation can be avoided by reducing the integration time. The system operation software has a build-in feature to automatically optimize the integration time to the radiation level of the source.

8.9.4 EML (Radiance) Performance

Noise and saturation characteristics of the EML sensor were determined in a similar way as those for the OXE instrument. The main difference is that the EML sensor was pointed to the center of a reflectance plaque, which was illuminated by a calibrated FEL lamp positioned 287.1 cm away from the center of the plaque. The radiance of the plaque was calculated based on the BRDF of the plaque. The $\mathbf{S}_L^j(\lambda)$ and $\mathbf{M}_L^j(\lambda)$ terms for the EML sensor follow

from (15) and (16), noting that the radiance responsivity becomes

$$\gamma_L^j(\lambda) \;=\; \frac{\mu_L^j(\lambda) \;-\; \bar{\mu}_L^j(\lambda)}{L_P(\lambda)}, \qquad (24)$$

where $L_P(\lambda)$ is the spectral radiance of the plaque. Following the practices established for the OXE performance analysis, mean quantities $\overline{\mathbf{N}}_L^j(\lambda)$ and $\overline{\mathbf{S}}_L^j(\lambda)$ were calculated by scaling with $1/\sqrt{N_s}$. The scaling factors for irradiance and radiance are identical, because both measurements use sampling periods of 60 s.

Table 16 presents $\mathbf{M}_L^M(\lambda)$, $\overline{\mathbf{N}}_L^M(\lambda)$, and $\overline{\mathbf{S}}_L^M(\lambda)$ for the EML channels. The wavelength dependence of the three quantities is very similar to those shown in Table 15 for irradiance. The main difference of the OXE and EML sensors is the irradiance collector used by the former. The similar wavelength dependence of the two devices confirms that the collector (specifically the diffuser material) is spectrally flat. The $\overline{\mathbf{S}}_L^M(\lambda)$ values are considerably larger than $\overline{\mathbf{S}}_E^M(\lambda)$ values, particularly in the UV. This is a consequence of the field-of-view limiting fore-optics of the radiance sensor, which reduces its responsivity considerably (Chap. 5).

Table 16. Noise and saturation characteristics for the microradiometer channels of the EML sensor following the format for Table 15. The units for the L_P, $\mathbf{M}_L^M$, and $\overline{\mathbf{N}}_L^M$ values are μW cm^{-2} nm^{-1} sr^{-1}; the $\overline{\mathbf{S}}_L^M$ values are in percent. The last row gives the scaling factor for the data in each column.

λ [nm]	L_P	$\mathbf{M}_L^M$	$\overline{\mathbf{N}}_L^M$	$\overline{\mathbf{S}}_L^M$
340	0.005	2.19	9.8	0.165
380	0.014	9.34	40.1	0.310
395	0.018	2.47	11.5	0.062
412	0.024	2.87	13.7	0.052
443	0.037	1.82	7.8	0.024
490	0.061	0.99	4.5	0.008
510	0.073	1.21	5.7	0.008
532	0.086	1.14	5.9	0.007
555	0.100	0.86	3.6	0.006
589	0.121	0.79	3.3	0.005
625	0.142	0.57	2.3	0.005
665	0.163	0.44	2.4	0.005
683	0.171	0.59	2.6	0.005
710	0.183	0.54	2.5	0.005
780	0.206	0.43	1.8	0.004
875	0.221	0.91	4.2	0.004
1,020	0.214	0.34	4.2	0.005
1,245	0.179	0.10	6.2	0.005
1,640	0.109	0.06	4.1	0.005
Scaling	1	$\times 10^6$	$\times 10^{-6}$	1

Figure 55 contrasts the noise and saturation characteristics of the microradiometer channels to those of the spectrograph and compares these quantities with the so-called *pseudo*-radiance of the direct Sun, the sky radiance

$L_i(\lambda)$, the water-leaving radiance $L_W(\lambda)$, and the radiance of the calibration plaque $L_P(\lambda)$.
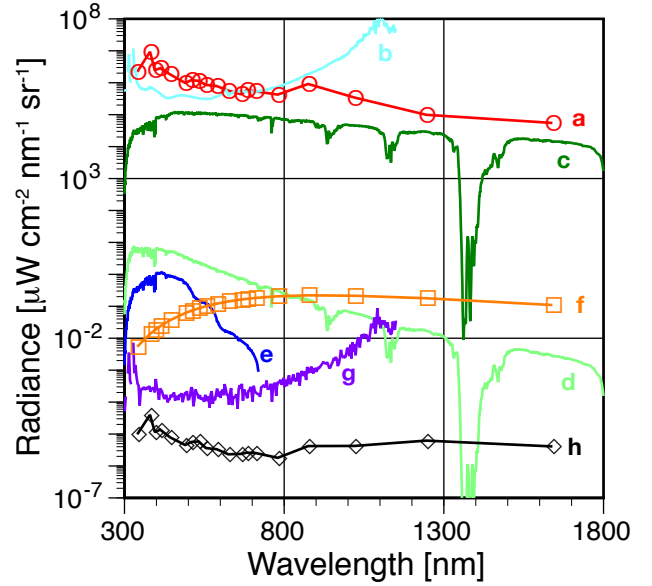
Fig. 55. The noise and saturation characteristics of the spectrograph and microradiometer channels for the OXE radiometer: **a)** $\mathbf{M}_L^M(\lambda)$; **b)** $\mathbf{M}_L^S(\lambda)$ for $t_i = 100$ ms; **c)** pseudo-Sun radiance; **d)** $L_i(\lambda)$ for $\theta_s = 40°$ and no aerosols; **e)** $L_W(\lambda)$ for $\theta_s = 40°$; **f)** $L_P(\lambda)$; **g)** $\overline{\mathbf{N}}_L^S(\lambda)$; and **h)** $\overline{\mathbf{N}}_L^M(\lambda)$.

Some of the Fig. 55 data sets require further explanation. The sky radiance data were calculated for $\theta_s = 40°$, a viewing zenith angle of 40°, and an azimuth angle 90° away from the solar azimuth (i.e., perpendicular to the Sun plane). The direct-Sun radiance was calculated by scaling the sky radiance by the factor $E_n(\lambda)/E_i(\lambda)$, where $E_n(\lambda)$ is the solar direct irradiance at the surface of Earth for overhead Sun, and $E_i(\lambda)$ is the integral of $L_i(\lambda)$ over the FVA of 2.5° of the EML sensor. The factor $E_n(\lambda)/E_i(\lambda)$ is equal to the expected ratio of signals of the sensor when pointing at the Sun and the sky. The pseudo-Sun radiance is so designated, because the radiance across the FVA when pointing at the Sun is not uniform. Consequently, this pseudo-radiance can be interpreted as a uniform radiance across the FVA that leads to the same signal as that produced by the direct Sun. The water-leaving radiance is computed identically to that used in Fig. 15.

The c–f radiances in Fig. 55 are more than 2.5 orders of magnitude larger than $\overline{\mathbf{N}}_L^M(\lambda)$. Calibrating the filter channels with a plaque located 287.1 cm away from an FEL lamp with sufficient precision is therefore possible. In contrast, $\overline{\mathbf{N}}_L^S(\lambda)$ is less than 2.0 orders of magnitude smaller than the radiance of the plaque for wavelengths below 400 nm. The calibration accuracy of the spectrograph is therefore compromised, and it may be necessary to move the plaque closer to the lamp for calibrating this wavelength range. Measuring water-leaving radiance with the

spectrograph for wavelengths above 600 nm also leads to significant uncertainties, whereas accurate measurements with the microradiometer channels can be performed at wavelengths beyond 700 nm. Measurements of sky radiance are not compromised by signal noise for either the filter channels or the spectrograph.

Figure 55 also indicates that pointing the instrument at the Sun does not saturate the microradiometer channels. Measurements of the spectrograph do saturate, so it is necessary to attenuate the signal. The Fig. 55b data indicates the saturation level of the spectrograph when the signal is attenuated by an ND filter of optical density 3.0 (attenuation by a factor of 1,000), and, in addition, the integration time is reduced to 100 ms. The filter wheel integral to the EML sensor includes two ND filters with an optical density of 1.5 and 3.0, which are rotated in front of the spectrograph fiber optics whenever direct-Sun measurements are performed.

8.10 Remote Sensing Applications

The marine biosphere is composed of a complex diversity of physical, chemical, biological, and ecological processes. Each process is an integral part of larger planetary biogeochemical cycles (e.g., carbon, nitrogen, phosphorous, silica, iron, etc.). These planetary cycles are coupled to, and influence climate through, feedback mechanisms. Despite significant research accomplishments from SeaWiFS and the two MODIS instruments onboard the Aqua and Terra spacecrafts, the oceanic processes, planetary cycles, and feedback mechanisms are insufficiently understood.

The National Research Council (NRC) Decadal Survey (NDS) emphasized the importance of satellite data for investigating oceanic processes and recommended three spaceborne observing systems designed to contribute to the acquisition of data regarding the distribution of marine biosphere properties (NRC 2007):

- Geostationary Coastal and Air Pollution Events (GEO-CAPE),
- Hyperspectral Infrared Imager (HyspIRI), and
- Aerosol-Cloud-Ecosystems (ACE).

The NASA Climate-Centric Architecture (CCA) report (NASA 2010) added the following:

- The National Polar Orbiting Environmental Satellite System (NPOESS) Preparatory Project (NPP) mission, and
- The recently announced Pre-Aerosol, Clouds, and Ocean Ecosystem (PACE) mission.

Because an OSPREy system can produce multiple (oceanic, terrestrial, and atmospheric) data products, the total number of satellite missions that can be supported—and made consistent—is necessarily larger. Restricting the list to example domestic missions, the following can

be added to the above: Aura, Aqua, Terra, and Cloud-Aerosol Lidar and Infrared Pathfinder Satellite Observations (CALIPSO).

The NDS advocates that the "validation of geophysical products inferred from satellite remote sensing is essential." Furthermore, for the development of CDRs, "validation should be an almost continuous component, providing an independent check on the performance of space-based sensors and processing algorithms." The CCA places special emphasis on global data sets created from multiple satellite platforms and notes: "it is incumbent on the providers of satellite data to take particular care that the consistency between related data sets is well documented." For the inevitable need to create comprehensive data products from diverse organizations and instruments, the CCA requires "calibration and validation throughout all stages of the process."

Both the NDS and CCA promote the use of ground networks for calibration and validation activities. The NDS recommends "the networks should also be expanded in geographic extent and the types of measurements made." Specifically, "the panel calls for the development of surface-based networks focused on climate observations and the development of the associated climate records as set forth in climate-stewardship principles." The compact size of even the most sophisticated OSPREy (maximum) system, and the availability of lower-cost configurations, makes an OSPREy network easier to implement than a network of traditional in-water moorings (which are typically very large and more expensive to purchase and maintain). More importantly, an OSPREy system can contribute to both oceanic and atmospheric (or terrestrial and atmospheric) climate records simultaneously.

The CCA recommends expanding ground networks, so they can be used "in validation activities required to establish inter-consistency between data from NASA and non-NASA satellites." Expanding the geographic extent of networks implies international partnerships, as does including foreign missions. The NDS recommends international partnering, because it, "spreads the cost burden, mitigates risks of gaps in particular data streams, encourages technical innovation by broadening the engineering expertise base, and increases the number of science users."

This philosophy of shared international participation is at the core of the OSPREy activity, which establishes a COTS software and hardware solution that is available to the worldwide scientific community. Indeed, the first exploitation of microradiometers, the recently introduced C-OPS in-water instrumentation (Morrow et al. 2010b), followed the same philosophy and is being used by US, French, Canadian, Polish, Chinese, and South African scientists, to name a few.

Examples of current and next-generation missions that OSPREy was designed to support, including the international Environmental Satellite (ENVISAT) launched by

Table 17. The applicability of OSPREy data products (derived from an operational system configuration) to representative domestic and international satellites that are currently operational or that are planned next-generation missions. (The row numbering is for referencing convenience.)

OSPREy Data Product	Aura	Aqua Terra	ENVI-SAT	CAL-IPSO	PAR-ASOL	NPP	PACE	GEO-CAPE	Hysp-IRI	ACE
1 Total ozone column	×		×							
2 Aerosol optical depth (AOD)	×	×		×	×	×	×	×		×
3 Aerosol absorption	×		×				×	×		×
4 AOD for fine and coarse mode aerosols							×			×
5 Aerosol size and effective radius		×			×	×	×			×
6 Aerosol phase function							×	×		×
7 Almucantar and principal plane scans							×			×
8 Refractive index (real and imaginary)							×			×
9 Cloud optical thickness			×			×				
10 Precipitable water vapor (PWV)		×	×	×			×	×		×
11 Global and diffuse spectral irradiance	×								×	
12 Aerosol scattering of spectral flux							×			×
13 Radiative forcing induced by aerosols							×			×
14 Degree of polarization, Stokes vector							×			×
15 L_W, R_{rs}, [TChl a], and turbidity		×	×			×	×	×	×	×
16 Suspended or dissolved matter		×	×			×	×	×	×	×
17 Terrestrial surface reflectance		×	×			×	×	×	×	×

Notes: [2] With the Ångström coefficients.   [3] The single scattering albedo.   [6] And the asymmetry parameter.   [7] Plus full scans at greater angular resolution.   [15] Plus normalized and exact forms of L_W.

the European Space Agency (ESA), are presented in Table 17. The table summarizes a representative diversity of oceanic, atmospheric, and terrestrial data products that a minimum OSPREy system (Fig. 44b) can provide based on the sensor capabilities of each mission:

- Total ozone column is derived from spectrograph measurements in the UV-B. The standard retrieval method uses direct-Sun measurements and is the method of choice for processing observations of Dobson and Brewer spectrophotometers.

- All aerosol products can be retrieved with a single radiance sensor, either by pointing the device at the Sun or by performing scans in the almucantar and principal plane directions.

- Cloud optical depth is determined from the attenuation of global irradiance by clouds.

- Precipitable water is determined from spectrograph measurements between 900–1,000 nm.

- Polarimetric data are provided by the spectrograph internal to radiance sensors.

- For comparison with satellite measurements, L_W is transformed to normalized forms, e.g., the radiance that would exit the ocean in the absence of the atmosphere and with the Sun at zenith and denoted $[L_W]_N$.

- The requirements for measuring terrestrial surface reflectance are similar to those for measuring L_W and its normalized forms.

Note, in particular, the comprehensive number of data products associated with the PACE and ACE joint oceanic and atmospheric missions.

The CCA also advocates for "opportunities for developing countries to participate more fully with NASA." In the not-too-distant past, many aspects of calibration and validation were very expensive customized solutions that were not commercially available, which prevented replication by a partner. For example, the high cost and lack of commercialization of the MOBY instrumentation, which was the main vicarious calibration source for SeaWiFS and MODIS (Clark et al. 1997), restricted its use to a single domestic site (off Lanai, Hawaii). The intrinsic vulnerability of one site results in data gaps, even with multiple copies of the observing system. More importantly, the utility of the data is compromised by unavoidable seasonal dependencies (e.g., sun glint, which is a recurring problem for sensors that do not tilt, like MODIS), as well as geometric limitations that restrict the kinds of on-orbit problems that can be addressed with the sea-truth observations (e.g., trying to understand and correct an inadequate prelaunch polarization characterization).

The CCA supports climate measurements and the expansion of "validation opportunities that leverage NASA investments and lower the development risk of key components vital for the instruments needed for climate measurements." The OSPREy approach presented here embraces this philosophy, as well as the need for international partnerships. To provide access for all interested partners, all of the sensor suites are commercially available. In addition, all major subsystems are COTS technologies (e.g., the sun

tracker), so the entire measurement suite is subjected to market forces to ensure cost competitiveness. Relying on COTS technology is not a detraction. Bailey et al. (2008) used data from COTS profilers (Werdell and Bailey 2005) and a buoy with COTS sensors (Antoine et al. 2008) to show satellite gains from COTS instruments are rather indistinguishable from MOBY.

8.11 Discussion and Conclusions

The satellite missions discussed above and summarized in Table 17 include both hyperspectral and fixed wavelength sensors. The latter includes individual spaceborne instruments with an arguably sufficient number of wavelengths to qualify as hyperspectral, and the summation of all such sensors certainly comprise a hyperspectral superset. This places a unique burden on the technologies used in the field as part of a comprehensive response to the required calibration and validation exercises to support these missions. Although individual field units could be deployed for each mission, such an approach increases the final uncertainty budget, because of sensor-to-sensor differences, particularly if the underlying technologies or radiometric scales are considerably different. A single sensor system that is part of a network of intercalibrated like sensors all traceable to the same radiometric scale can support the calibration and validation of multiple satellites while offering the unique opportunity to significantly reduce satellite-to-satellite uncertainties.

Also summarized in Table 17 is how an OSPREy system can produce multiple (oceanic, atmospheric, and terrestrial) data products and necessarily across a wide spectral domain, so the total number of satellite missions that can be supported spans domestic and international missions. The OSPREy approach fosters international partnerships, providing access to high-quality observations to all interested partners. As many of the subsystems as possible are COTS technologies (e.g., the sun tracker, the spectrographs, and the video camera), and the entire measurement suite is subjected to market forces to ensure cost competitiveness.

OSPREy systems are configured with hybridspectral radiometers combining a cluster of fixed wavelength microradiometers with a spectrograph. The spectrograph provides hyperspectral resolution over a subset of the complete spectral range, while the microradiometers provide a larger dynamic range in responsivity, higher sampling speeds, better sensitivity, and sampling across the entire OSPREy spectral range (305–1,640 nm). The two sensor technologies supplement each other. For example, spectrograph data can be used to detect potential degradation of the interference filters used by the microradiometer channels while the microradiometers can help to correct dark-current drifts and nonlinearity in spectrograph measurements, while greatly extending the dynamic range.

The capability of radiance sensors is further enhanced by a nine-position filter wheel and integrated camera. In the standard configuration, the filter wheel permits hyperspectral polarimetric measurements, direct-Sun viewing, stray-light correction, dark current measurements, and a home position. The video camera is used for locating the Sun and Moon, as well as verifying the condition of all targets, i.e., cloud-free solar and lunar disks, cloud presence in sky data, and sea surface debris or foam detection (although an irradiance sensor can confirm cloud-free solar and lunar disks). The components of each radiance and irradiance sensor type are integrated in a common housing that is environmentally sealed, nitrogen purged, and temperature controlled.

OSPREy field sensors are part of the EMR product line, and the OSPREy laboratory sensors are from the OXR instrument class. A fully supported deployment of the OSPREy technology involves radiance and irradiance sensors from both instrument classes being used in the field and in a calibration laboratory. An important aspect of EMR sensors is their scalability, which is derived directly from the modularity of microradiometers, but the principal scalability comes from the SHALLO design philosophy established for all instrument classes built with microradiometers (Morrow et al. 2010c). The SHALLO architecture codifies this philosophy by establishing a sequence of modular capabilities and a stepwise upgrade pathway for the instrument classes built with microradiometers. This scalability can be reversed to create a simpler system if resources or science objectives no longer require or can support, respectively, a more sophisticated system.

Five configurations are available for OSPREy systems (Fig. 44): the *starter system* establishes a significantly more advanced replacement for SeaPRISM units; the *minimum system* features radiance and irradiance, with a shadowband capability for the latter; the *spectral system* optimizes irradiance coverage from 290–1,670 nm; the *operational system* with dual radiance and irradiance sensors provides a compact, fully redundant, sampling capability; and the *maximum system* features two instrument triads for maximum spectral coverage, measurement redundancy, and data products. The five systems establish a hierarchy in the level of accomplishment that can be achieved for calibration and validation activities, both in terms of the accuracy and diversity of the resulting data products.

The upgradability of the OSPREy architecture has already been exploited as part of the development activity. The linear glass polarizing filters from Edmund Scientific (Rochester, New York) used to establish and test the filter-wheel assembly (Fig. 49) were inexpensive, but spectrally limited to 400–700 nm. Properly orienting the round filters in the filter holder was technically challenging. To provide polarimetry over the spectral range supported by the spectrograph, i.e., 300-1,150 nm an alternative technology and source for polarizers was needed.

Broadband polarizers (250–4,000 nm) using nanowire technology have recently become available. A set of Ultra Broadband Nanowire UBB01A polarizers from Moxtek (North Orem, Utah) were procured and the filter wheel

Table 18. The applicability and quality of OSPREy data products to the five SHALLO system configurations (Fig. 44) using the presentation established for Table 17. The quality is presented on a relative five-star scale, with five stars being the highest quality and one star the lowest. Data products that do not achieve a five-star rating for a maximum system configuration have a design component or compromise that requires more comprehensive testing than could be achieved with the field commissioning part of the OSRPEy development activity. In addition, distinguishing between four- and five-star systems remains to be completely determined, because the outcome of the cosine correction of the EME radiometer was better than originally anticipated. The line numbering is for referencing purposes. Note that the latter does not mean the device is inadequate for the measurement task—it simply means there are higher quality alternatives (which may or may not be necessary for consideration). A blank entry indicates the data product cannot be produced directly from the observations, although it might be modeled using one or more available parameters.

OSPREy Data Product	System Configuration				
	Starter	Minimum	Spectral	Operational	Maximum
1 Total ozone column	★★	★★★	★★★	★★★★	★★★★
2 Aerosol optical depth	★★	★★★	★★★★	★★★★	★★★★★
3 Aerosol absorption	★★	★★★	★★★★	★★★★	★★★★★
4 AOD for fine and coarse mode aerosols	★★	★★★	★★★★	★★★★	★★★★★
5 Aerosol size and effective radius	★	★★	★★★	★★★	★★★★
6 Aerosol phase function	★	★★	★★★	★★★	★★★★
7 Almucantar and principal plane scans	★★	★★★	★★★★	★★★★	★★★★★
8 Refractive index (both $\Re$ and $\Im$ parts)	★★	★★★	★★★★	★★★★	★★★★★
9 Cloud optical thickness		★★	★★★	★★★★	★★★★★
10 Precipitable water vapor	★★	★★	★★	★★★★	★★★★
11 Global and diffuse spectral irradiance		★★	★★★★	★★★	★★★★★
12 Aerosol scattering of spectral flux	★★	★★★	★★★	★★★★	★★★★
13 Radiative forcing induced by aerosols	★★	★★★	★★★★	★★★★	★★★★★
14 Degree of polarization, Stokes vector	★★	★★★	★★★	★★★★	★★★★★
15 L_W, R_{rs}, [TChl a], and turbidity	★	★★	★★★	★★★★	★★★★★
16 Suspended or dissolved matter	★	★★	★★★	★★★★	★★★★★
17 Terrestrial surface reflectance	★	★★	★★★	★★★★	★★★★

modified to accommodate these components (Fig. 56). The comparatively large size ($0.6 \times 0.6 \, \text{cm}^2$) and delicacy of the coatings presented a number of technical challenges. For example, the filters are so delicate, they cannot be touched or altered (e.g., cut to size) during installation. Orienting the filters in the filter holder was not difficult, because they have an orientation aligned to a square edge.
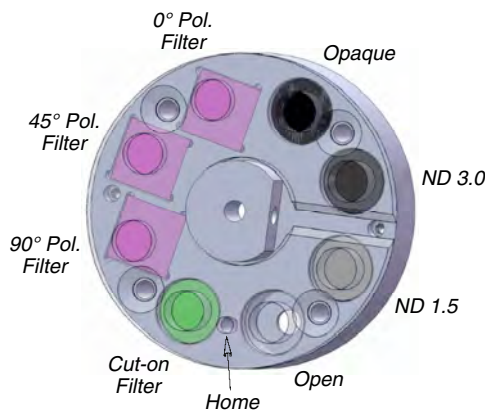
Fig. 56. The modified EML sensor filter wheel upgraded with Moxtek polarizers (pink) and following the presentation established in Fig. 49.

Table 18 provides an overview of the applicability and quality of OSPREy data products to the five SHALLO system configurations (Fig. 44). Most data products can be retrieved from measurements of a radiance sensor mounted on a pointing unit (the starter system). The addition of an irradiance sensor with the shadowband accessory (a minimum system) provides redundancy, reduced uncertainty, and the ability to measure additional data products such as cloud optical depth, and global and diffuse irradiance. The following are relevant with respect to the perspective of the data products and sensor configurations:

- Deriving total ozone column from direct-Sun measurements is only possible if the Sun is not obscured by clouds. When clouds are present, total ozone can be calculated from measurements of global irradiance, which can be performed with the minimum system.

- Although aerosol products only require a single radiance sensor, the addition of an irradiance sensor system provides redundancy and also offers an independent method to derive aerosol absorption properties. For example, the single scattering albedo can be estimated from the ratio of diffuse to global irradiance. The spectral and maximum systems allow

more accurate determinations of aerosol properties in the SWIR domain.

- Cloud optical depth requires at least one irradiance sensor, and in practice, is estimated by comparing measurements of global irradiance with results of a radiative transfer model using different optical depth values as model input parameters.

- Measurements of precipitable water cannot be made with irradiance sensors, because the spectrograph internal to these units has a terminal wavelength of 785 nm.

- Measurements with the three polarizers that are mounted in the filter wheel in front of the spectrograph fiber optics at orientations of $0°$, $45°$, and $90°$ can only be performed sequentially (unless the operational system with a second radiance sensor is used).

- The requirements for measuring terrestrial and sea surface reflectance are similar, resulting in an increase in data quality progressing from the starter system to the maximum system.

Because illumination conditions can change during the observation period for a radiance measurement, contemporaneous observations with an irradiance sensor can help to characterize these changes. A minimum system is, therefore, superior compared to a starter system even though irradiance sensors do not provide polarimetric measurements.

In general, the confidence in a measurement result can be improved if the same data product can be achieved with different methodologies. For example, AOD can either be determined from measurements of the radiance sensor pointing at the Sun or from data of direct solar irradiance that have been derived from global and diffuse measurements from an irradiance sensor. If results of the two approaches agree, confidence is significantly enhanced because it is unlikely that the same systematic error is affecting both methods equally.

The uncertainty of most data products can be reduced further as the sensor suite is expanded, resulting in the spectral, operational and maximum systems. Such a progression adds redundancy, the ability to measure different quantities simultaneously, and the use of irradiance collectors optimized for the spectral range of the measurement (spectral and maximum systems). Although applicable to almost all data products, the benefits in the ability to expand the sensor suite is well represented in the oceanic measurement requirements:

1. L_W and related data products can be measured with a starter system in a similar way as with a SeaPRISM instrument (except the individual channels are acquired simultaneously with OSPREy). Without an irradiance sensor, the normalization factor to convert L_W to $[L_W]_N$ must be estimated from measurements of direct solar irradiance, which is subject to uncertainty.

2. The irradiance sensor that is part of the minimum system allows the normalization factor to be measured directly, resulting in a smaller uncertainty of $[L_W]_N$. The irradiance sensor is also required for accurate R_{rs} values.

3. As in the case of atmospheric data products discussed above, the spectral system can provide more accurate measurements at SWIR wavelengths.

4. The use of two dyads in the operational system decreases uncertainties in measuring L_W, $[L_W]_N$, and R_{rs} further, because L_T and L_i can be measured simultaneously.

5. The use of two triads in the maximum system minimizes uncertainties with more accurate measurements at SWIR wavelengths.

Although the progression to more sophisticated systems provides increasingly powerful capabilities, the level of accomplishment with a solitary EML sensor is unprecedented, because of the hybridspectral architecture. The hyperspectral and fixed-wavelength observations of solar and lunar irradiances during clear-sky conditions with an EML sensor is presented in Fig. 57. The data were acquired at different zenith angles resulting in an air mass of about one for the solar data and approximately five for the lunar data. The two plots include annotations of atmospheric absorption bands from oxygen (O_2) and water (H_2O), as well as a calcium (Ca) band in the solar photosphere. The broad reduction in the UV domain from ozone (O_3) is noted on the figure, and the strong effect of Rayleigh reduction in the lunar observations from the longer atmospheric path length (large zenith angle and corresponding air mass) is also noted.
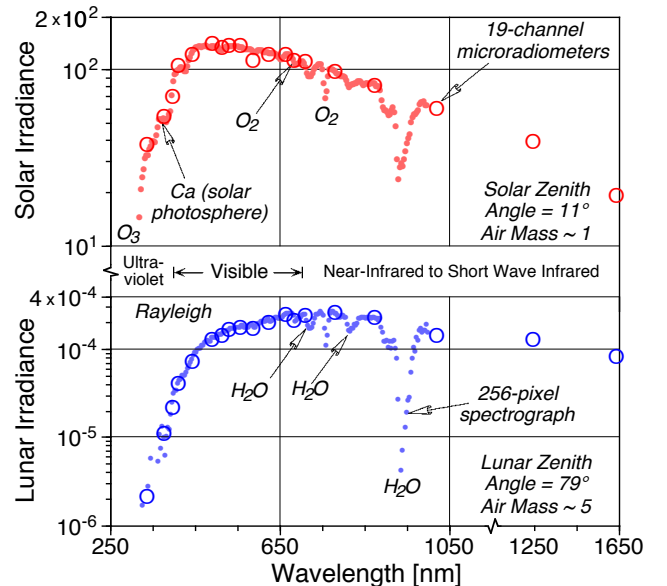
Fig. 57. EML irradiance observations (in units of $\mu W\,cm^{-2}\,nm^{-1}$) of the Sun and Moon during clear-sky conditions and significantly different zenith angles. Note there is a discontinuity in both the x- and y-axes (denoted by the zigzags).

The results presented in Fig. 57 indicate the following with respect to the performance of EML sensors: a) the spectral dynamic range of the sensors is excellent; b) the detail (absorption lines) and consistency in the data suggest good intercalibration (the calibrations are presently based on a NIST FASCAL traceability with the OSPREy lamp library); c) the signal dynamic range (about eight decades) indicates the Sun and the Moon can be used to monitor sensor performance during clear-sky conditions; and d) the large lunar zenith angle data suggest Langley plots from lunar data are possible.

The performance of an EME sensor is presented in Fig. 58, wherein the recorded solar observations (red) are compared to a radiative transfer model (gray) based on the conditions encountered during the field measurements. In this case, the spectrograph data have been interpolated to higher resolution to better match the detail of the model. The agreement between the spectrograph and the microradiometers is on average to within 2.5%, and the agreement of both with respect to the model is similar over the 300–785 nm spectral range. Although at different scales, a comparison of the solar observations in Figs. 57 and 58 reveal the strength of the dyad (dual radiance and irradiance sensors) measurement suite, because one sensor can be compared to the other. The chance that two sensors would malfunction at exactly the same time or exactly in the same spectral domain is negligible, so aberrant performance is quantifiable, especially under circumstances

wherein modeling can also be included in the analysis (e.g., solar observations).
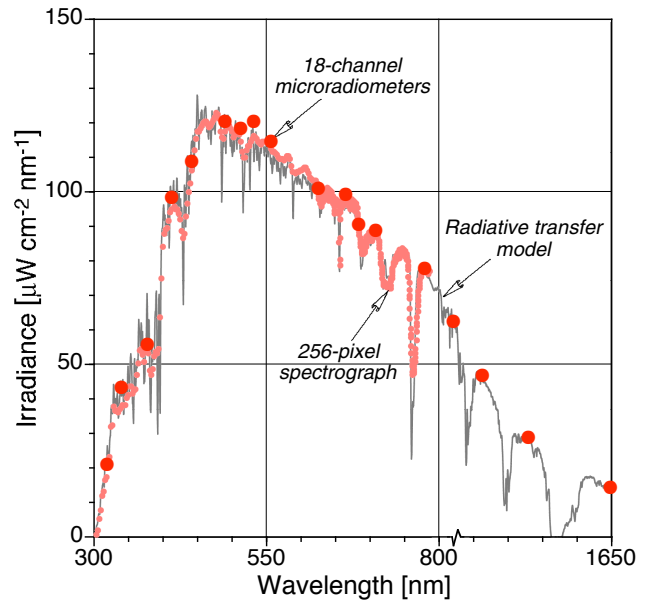
Fig. 58. Solar EME measurements (in units of $\mu W\,cm^{-2}\,nm^{-1}$) during clear-sky conditions (recalling that EME sensors have 18 microradiometers, because one is removed for the spectrograph fiber). Note there is a discontinuity in the x-axis after the spectrograph data ends (denoted by the zigzag).

S.B. Hooker, G. Bernhard, J.H. Morrow, C.R. Booth, T. Comer, R. Lind, and V. Quang

Acknowledgments

Conceived in 2004, the enabling technology for building new sensors for the OSPREy activity is the microradiometer—a small, integrated photodetector, preamplifier high resolution (24 bits) ADC, microprocessor, and an addressable digital port, all in one small circuit assembly. The microradiometer was developed as a joint activity between BSI and NASA under an SBIR program entitled "*In Situ* Radiometers: Smaller, Faster, and Scalable to Hyperspectral." The SBIR Phase I contract NNG05CA40C (2005) resulted in a functioning microradiometer prototype (not required), which served to illustrate the potential for success of the project. The SBIR Phase II contract NNG06CA03C (2005–2007) moved the prototype instrument through a complete development cycle, which concluded with the release of a field-tested device. It was also completed on time and on budget.

Having proven the design in 2007, the first true microradiometers were successfully machine-manufactured in one lot of quantity 100. NASA contract NNG08HZ17C (2008) for OSPREy is on schedule and under budget to build the prototype instruments and begin the development of an expandable radiometer system for deployment on above-water platforms. An ACE project office augmentation (2011) added a nine-position filter-wheel assembly in line with the spectrograph fiber optics and a digital camera to EML sensors.

The preparation of the manuscript and its final level of completeness benefitted significantly from the technical editing and computer graphics expertise of Elaine Firestone, whose attentiveness to detail, and her good cheer, are greatly appreciated.

Appendices

The appendices provide additional information on various aspects of the OSPREy activity. The inclusion of the appendices is to anticipate the need for clarification regarding some technical details that are not summarized in the individual chapters and to provide a broader perspective of the deployment of the sensors as it is presently envisioned.

A. Above- and In-Water Methods

B. Vicarious Calibration Protocols

C. The BSI Calibration Facility

D. Ancillary Measurements

E. The BioSHADE Accessory

F. Platform Power and Data Telemetry

G. Extended Test Deployments

H. Operational Deployment

I. Absolute Calibration

J. Uncertainty Analysis

K. Platform-Perturbation Mapping

L. The SABSOON Towers

M. BSI Quality Assurance Experience

The last appendix provides an example of a quality assurance program for a network with similar objectives as the OSPREy activity.

Appendix A:
Above- and In-Water Methods

The two methodologies for estimating $L_W(\lambda)$ require either above- or in-water sampling. Above-water methods use direct observations of the radiance emanating from the sea surface, which after correction for glint contamination, yields an estimate of $L_W(\lambda)$. In-water techniques, however, use vertical profiles of upwelled radiance, $L_u(z,\lambda)$, where z is the vertical coordinate, to establish a near-surface extrapolation interval from which $L_W(\lambda)$ is estimated after propagation through the sea surface.

Although above-water data are part of global bio-optical databases, the majority are in-water data (O'Reilly et al. 2000). Part of this disparity is because in-water measurements have a longer history, and part of it is the consequence of the frequently poor agreement between the two methods (Rhea and Davis 1997, Fougnie et al. 1999, Toole et al. 2000, and Hooker et al. 2002a), so in-water methods have dominated. In principle, there are no *a priori* reasons to select water-leaving radiances from an above-water method, $\hat{L}_W(\lambda)$, over an in-water method, $\tilde{L}_W(\lambda)$, when sampling the optically simplistic environment required for vicarious calibration exercises. Furthermore, satellite sensors themselves are above-water instruments.

Most in-water methods for estimating $L_W(\lambda)$ are based on the Smith and Baker (1984) technique for analyzing $L_u(z,\lambda)$ profiles. From a near-surface portion of the profile (or all available depths from a buoy), the attenuation coefficient is computed as the local slope of $\ln\left[L_u(z,\lambda)\right]$, and is used to extrapolate the upward radiance through the upper layer to determine $L_u(0^-,\lambda)$ at null depth $z = 0^-$. The water-leaving radiance is obtained using

$$\tilde{L}_W(\lambda) \;=\; 0.54\,L_u(0^-,\lambda), \qquad (A1)$$

where the constant 0.54 accurately accounts for the partial reflection and transmission of the upwelled radiance through the sea surface (Mobley 1999). The formulation in ($A1$) assumes there are no artificial perturbations to the L_u data (a similar assumption is made for an above-water method), and if they are (unavoidably) present, corrections are required. Routine corrections include instrument self shading (Gordon and Ding 1982, and Zibordi and Ferrari 1995) and platform shading (Doyle and Zibordi 2002, and Zibordi et al. 2002a).

Despite the advantages of time series measurements, buoys have some important deficiencies: a) the sensors are usually mounted close to the main body and can be negatively influenced by the buoy (mounting the sensors on standoffs can reduce this effect, but not completely eliminate it); b) to minimize the complexity and vulnerability of moving parts, multiple light sensors are deployed at a small number of fixed depths, so there is a spatial resolution problem; and c) because the sensors are mounted relatively close to the surface, they can be subjected to significant biofouling, surface effects, and damage, which can be being difficult to detect without divers.

Sampling problems are primarily engineering challenges, and if properly solved, good data can be collected. Examples of radiometric buoys that were successfully deployed are as follows:

- The Marine Optical Buoy (MOBY), developed in the US and funded mostly by NASA in support of the SeaWiFS and MODIS satellite missions (Clark et al. 1997);

- The UK Plymouth Marine Bio-optical Data Buoy (PlyMBODy), developed by the Plymouth Marine Laboratory (PML) as a part of the SeaWiFS Exploitation Initiative (Pinkerton and Aiken 1999); and

83

- The French *Bouée pour l'Acquisition de Séries Optiques à Long Terme* (BOUSSOLE), developed by the *Laboratoire d'Océanographie de Villefranche* (LOV) primarily to support the Medium Resolution Imaging Spectrometer (MERIS) mission (Antoine et al. 2006 and 2008).

Although these buoy designs differ—the last two were designed with COTS radiometers—they are sufficiently similar that any one can be used to summarize the basic aspects of an in-water mooring. MOBY is selected, because it is the most sophisticated and has the longest deployment record (since July 1997).

MOBY is instrumented with a solar irradiance reference plus identical pairs of downward irradiance (E_d) and upwelling radiance (L_u) sensors located at three shallow depths (2, 5, and 9 m). The light sensors are mounted on arms so the perturbative effects of the buoy superstructure are reduced. All of the light sensors collect data from 380–900 nm using custom-built hyperspectral sensors with high spectral resolution. Orientation sensors allow the exclusion of data degraded by excessive tilts or direct shading from the buoy superstructure. Biofouling is mitigated with an approximately monthly interval of diver visits to keep the optical apertures clean.

The biggest difference between MOBY and other buoy designs is the use of custom-built hyperspectral sensors. This means that MOBY data can be spectrally combined to match any remote sensor in the applicable spectral range. In addition, if the spectral response functions of the satellite channels are known, the summation process can include this information to provide a properly weighted *in situ* observation. The capabilities of an instrument system like MOBY is well established (McClain et al. 2004); the only question about such an enterprise is whether or not such a costly undertaking is required.

The use of offshore towers as an alternative to moored buoys for calibration and validation activities was investigated (Zibordi et al. 2002a). An in-water system was deployed close to a tower, but anchored with cables strung between the sea bottom and a protruding deck to provide a stable measurement geometry. The difficulty with this arrangement is the proximity of the tower can produce significant perturbations to the in-water light field under certain illumination conditions and solar geometries. The stability of the platform, however, permits an exact identification of the solar geometry needed to accurately remove shading effects (Zibordi et al. 1999).

Above-water methods are based on pointing a radiance sensor at the sea (at a prescribed nadir viewing angle, ϑ, of 40 or 45°), so the total radiance at the surface, $L_T(\lambda)$, is measured. The acquisition does not disturb the sea surface, so the net effect of the vertical complexity of the water column is precisely captured. Unwanted radiance contributions must be avoided, so all methods avoid the glint in the sun plane. This is accomplished by pointing the sensor an angle ϕ' away from the Sun (90° or 135°), while avoiding any platform perturbations.

The remaining difficulty in above-water methods is to remove the reflected sky light from the L_T measurement, and it is this procedure that distinguishes above-water methods from one another. For the method presented here, sky glint is removed by measuring the sky radiance, $L_i(\lambda)$, in the same plane as $L_T(\lambda)$, and at a zenith angle ϑ' equivalent to ϑ ($\vartheta' = 180-\vartheta$). These two measurements can then be used to derive the water-leaving radiance (omitting the angles for brevity):

$$\hat{L}_W^{S95}(\lambda) \;=\; L_T(\lambda) \;-\; \rho\,L_i(\lambda) \qquad (A2)$$

where the S95 notation denotes the SeaWiFS 1995 revision of the Ocean Optics Protocols (Mueller and Austin 1995), and ρ

is the surface reflectance, which is small (about 3%, so L_i is the important correction term). If the interface was level, ρ would be the Fresnel reflectance, but the sea surface is usually wind roughened, so ρ depends on the capillary wave slopes, and, thus, on wind speed, W (Austin 1974 and Mobley 1999). An updated version of the S95 method using a more accurate $\rho(W)$ value derived from the Mobley (1999) results is referred to as the S01 method (Hooker et al. 2003).

The anisotropy of the upwelled radiance field means above- and in-water determinations of $L_W(\lambda)$ cannot be intercompared directly—one observation must be transformed to the geometry of the other. The transformation equations (Morel and Gentili 1996 and Mobley 1999) are an established part of the Protocols and were successfully incorporated into above-water methods (Hooker and Morel 2003, Hooker et al. 2003, and Hooker and Zibordi 2005b), so only a brief summary is given. The radiance bidirectionality is parameterized by the so-called Q function, which takes a particular value, denoted Q_n, for nadir-viewing measurements. For Case-1 waters, the functional dependence of the variables can be simplified by assuming the IOPs are universally related to the chlorophyll a concentration, C_a (Morel and Prieur 1977). Because a nadir-transformed, above-water estimate of L_W is equivalent to the in-water value, a formulation can be produced (Morel and Mueller 2002) to improve the S01 method, and is hereafter referred to as the Q02 method:

$$\hat{L}_W^{Q02}(\lambda) \;=\; \frac{\hat{L}_W^{S01}(\lambda)\,\Re_0}{\Re(\theta',W)}\,\frac{Q(\lambda,\theta,\phi',\theta',C_a)}{Q_n(\lambda,\theta,C_a)}, \qquad (A3)$$

where the Q terms are evaluated at null depth, θ' is the above-water viewing angle (ϑ) refracted by the air–sea interface, and the $\Re$ merges all the effects of reflection and refraction ($\Re_0$ is evaluated at nadir). All the correction terms are computed from look-up tables (Morel et al. 2002).

The formulation in ($A3$) allows for a direct comparison between above- and in-water L_W values, but only if extraneous (platform) perturbations are absent. A set of experiments were conducted to map the above-water perturbation field associated with a tower (Hooker et al. 2003). Based on the height of the tower superstructure, H, the tower perturbation analyses were partitioned into near- and far-field sets ($x < H$ and $x > H$, respectively, where x is the perpendicular distance from the tower to the *surface spot* viewed by the sea-viewing sensor). The primary conclusions (Hooker and Zibordi 2005) were: a) the maximum perturbations occur very close to the tower ($x/H \ll 1$), and as $x/H \to 1$ (i.e., as the surface spot becomes as far away as the main superstructure height), the perturbations converge towards very small values; and b) within the far field ($x > H$), the perturbation is negligible, and a remote sensing 5% absolute accuracy objective can be satisfied (see Appendix K for more details).

The investigations into above-water measurements and the tower perturbations contributed to a complete inquiry into the uncertainty budgets for deriving water-leaving radiances from above- and in-water sensors. This information was needed to a) establish that the quality of the data from both measurement types was in keeping with calibration and validation requirements, and b) determine whether or not a convergence between the two methodologies to within the calibration uncertainties of the sensors is possible.

A summary of the total uncertainty budgets derived from a variety of coastal field campaigns and laboratory exercises is given in Table A1, with more complete spectral details available

in Hooker et al. (2004). Although the absolute calibration of the radiometers is important (Hooker et al. 2002b), other uncertainty sources contribute significantly. The *in situ* stability includes sensor decay over time and variations in the calibration coefficients caused by differences in the calibration conditions. The uncertainty for L_u immersion factors are estimated from the parameters used in the analytical model (Mueller and Austin 1995). The uncertainty in the proper characterization of E_d immersion factors is less than 0.5% (Zibordi et al. 2004a), and although this uncertainty can influence the selection of the near-surface extrapolation interval and, thus, the $L_W(\lambda)$ values, this is usually a minor effect (so it is omitted).

Table A1. An averaged summary of the major sources of uncertainties in the above- and in-water (AW and IW, respectively) computation of L_W for blue–green wavelengths. The last two rows give the net uncertainties assuming the indicated sources combine in quadrature (square root of the sum of the squares).

Uncertainty Source	IW	AW
1. Absolute calibration	2.1	2.5
2. *In situ* sensor stability	1.2	1.2
3. L_u immersion factor	1.0	
3. Surface reflectance†		0.6
4. Instrument self shading	0.8	
4. Bidirectional correction†		0.5
5. Platform perturbation ‡	1.2	0.2
6. Deployment stability	1.0	0.2
7. Environmental variability	3.0	2.2
1–6 Quadrature Sum	3.1	2.9
1–7 Quadrature Sum	4.3	3.6

† Representative of the uncertainty in $\hat{L}_W^{Q02}$ as a result of typical uncertainties in the input parameters used to calculate these quantities and not the intrinsic uncertainties in the look-up tables.

‡ Only the in-water observations are corrected for platform perturbations; the above-water measurements were made under circumstances significantly minimizing this uncertainty.

The uncertainties in computing self- and tower-shading corrections, as well as the surface reflectance and bidirectional correction, are estimated for the former from the magnitude of the parameters used to correct for their effects, whereas for the latter two, the net uncertainties are derived from a sensitivity analysis of the input variables. The in-water uncertainties due to the instability of the deployment platform were estimated by Hooker and Maritorena (2000) for an instrument deployed from a large ship. The corresponding above-water values are considerably less, because the tilt filtering of the above-water data retains only those data within 2° of the viewing angle.

The environmental variability is mostly uncontrollable, except it can be minimized by collecting all the *in situ* data under excellent conditions (which was done for the Table A1 analysis). The in-water component was estimated using successive casts under different measurement conditions (Zibordi et al. 2002a) and are assumed to be independent of the optical profiling system. For the above-water instruments, the environmental variability was estimated using successive acquisitions in two coastal campaigns and closely match previous estimates in the same study area (Hooker et al. 2002a). The quadrature sum of uncertainties, all assumed independent, for both systems gives

values lower than 4.5%. Assuming half of the remote sensing total uncertainty budget is apportioned to the satellite sensor, the allowed uncertainty in the *in situ* data is approximately 3.5% $(\sqrt{5^2/2})$. Although the net uncertainties exceed this level, this is primarily a consequence of environmental variability. If only the controllable sources of uncertainty are considered, the net uncertainties are (on average) to within 3.5%.

An intercomparison of above- and in-water techniques for estimating L_W, based on the aforementioned Hooker et al. (2004) study, is presented in Fig. A1. The comparison is based on the relative percent difference (RPD) between the nearly-simultaneous (within 3 min) deployments of the two types of instruments. Because in-water methods are the most prevalent, the in-water data were selected as the reference in the RPD† calculation.
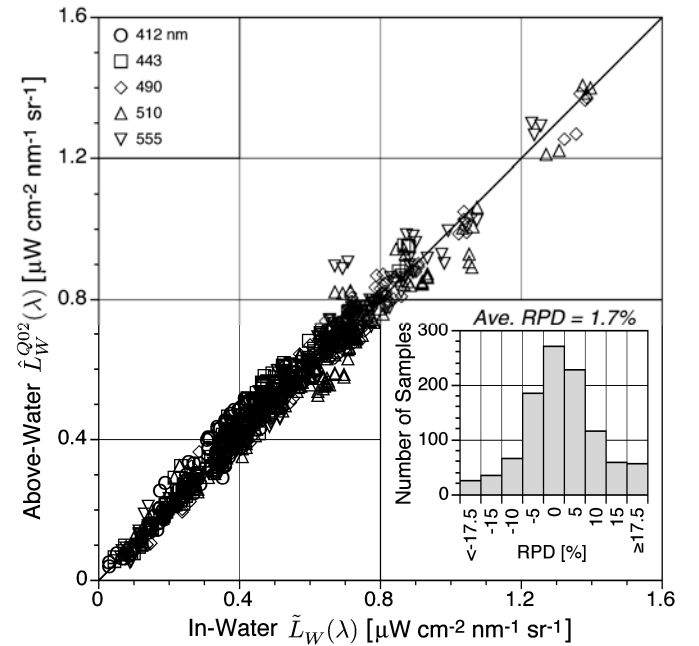
Fig. A1. A comparison of the above- and in-water determinations of water-leaving radiances, $\hat{L}_W^{Q02}(\lambda)$ and $\tilde{L}_W(\lambda)$, respectively.

The two types of data in Fig. A1 were collected under mostly excellent conditions: cloud cover less than 4/10, wind speed less than $5\,\mathrm{m\,s^{-1}}$, and wave height less than 0.5 m. At the same time, they were acquired over an appreciable range in seawater properties—in fact, most of the environmental variables spanned an order of magnitude change that is representative of the differences between clear and turbid waters (the data set is approximately 86% Case-1 and about 14% Case-2). The data show there is a significant convergence between above- and in-water methods over a wide range of conditions: they agree to within 1.7% on average, which is in keeping with the uncertainty in instrument intercalibrations (2–3%), as well as the intercomparisons derived from simultaneous in-water deployments (also 2–3%).

---

† The RPD is defined as $\psi = 100(X - Y)/Y$, where X is the above-water observation and Y is the corresponding in-water (reference) value.

Appendix B:
Vicarious Calibration Protocols

The fact that low-cost and easily-deployed COTS sensors can serve as a data source for vicarious calibration (Bailey et al. 2008) makes it compelling to revisit the tenets established for vicarious calibration in the Protocols and to discuss these within the capabilities of alternative sources of high-quality data. The three considered here are a) an ocean-surface reflectance model (ORM) based on Case-1 parameterizations (Werdell et al. 2007); b) the NASA Bio-Optical Marine Algorithm Data (NOMAD) archive (Werdell and Bailey 2005), which is a subset of high-quality *in situ* optical data from the SeaWiFS Bio-Optical Archive and Storage System (SeaBASS); and c) and the *Bouée pour l'acquisition de Séries Optiques à Long Terme* (BOUSSOLE) Project (Antoine et al. 2006 and 2008). The latter two constitute a variety of COTS instruments and different data processors.

Given the recent more expansive inquiry into vicarious calibration data sources, a review discussion of the vicarious calibration procedures currently being used seems warranted. An item-by-item presentation and subsequent discussion of the original vicarious calibration protocols (shown in slanted typeface) is as follows:

1. *The performance of a satellite sensor must be monitored at daily-to-weekly intervals by comparing derived normalized water-leaving radiances with contemporaneous sea-truth values (both made to within the established uncertainty criteria).*

   All vicarious calibration methods must comply with this requirement and about 30 quality-assured matchups are needed. To understand a new satellite sensor, and to have scientifically useful data as early in the mission as possible, the 30 good matchups are needed as quickly as possible. Multiple sites (SeaPRISM) or multiple investigators on ships (NOMAD) are a good way to accomplish this, although a modeling approach (ORM) will always provide the greatest number of data points in the shortest time.

2. *The most direct way of making the sea-truth measurements on a continuing daily basis over periods of several years is to utilize a specially-designed array of radiometers mounted on a moored buoy.*

   Off-shore structures are an alternative, and an above-water measurement is more direct than an in-water one. A large number of investigators equipped with suitable profilers (NOMAD) can also provide large amounts of data over extended time periods. A model approach represents a hybrid opportunity wherein a surrogate variable (e.g., the chlorophyll *a* concentration), which is much easier to measure, is used (ORM). For the in-water methods, the distinguishing aspect is the high vertical resolution of profilers versus the limited vertical resolution of a buoy (although profiling buoys are possible).

3. *The buoy must be designed to mount the optical collectors well away from platform shading and reflections; although, instrument self-shading corrections will be needed unless the sensors are very small.*

   Free-fall profilers (NOMAD) satisfy this requirement (assuming a self-shading correction is applied). In addition, it is rather easy to avoid platform shading and reflections with an above-water system, and no self-shading correction is needed. A modeling approach (ORM), by definition, will not have any of these problems as long as the

data used to initially build and validate the model are not contaminated.

4. *To minimize uncertainties arising from extrapolating the upwelling radiance to the sea surface, the buoy must be moored at a location with consistently transparent Case-1 waters and with negligible mesoscale to sub-mesoscale spatial variability.*

   The QA criteria of the match-up process forces compliance of this requirement for all vicarious calibration methods. The results from BOUSSOLE and NOMAD suggest some relaxation in the strictness of this language is appropriate (i.e., allowing the chlorophyll concentration to rise is not significantly detrimental). In addition, given the robustness of the Case-1 model, unequivocally clear waters are not such a strict requirement, which is reinforced by the ORM results.

5. *To ensure frequent occurrences of matched satellite and buoy measurements, the site must be cloud free throughout most of the year.*

   The QA criteria of the match-up process forces compliance of this requirement for all vicarious calibration methods, even though an easily replicated system that can be economically deployed could satisfy—and very likely exceed—this requirement by simply having multiple sites.

6. *The mooring must be located close to an island-based sun photometer and sky radiance sensor to allow concurrent determinations of aerosol optical thickness and sky radiance distribution.*

   An above-water system based on a modified sun photometer satisfies this automatically, as would a modeling approach (ORM).

7. *The atmospheric conditions at the mooring location must not be significantly subjected to land-induced (e.g., orographic) effects.*

   The QA criteria used in the match-up process forces compliance of this requirement for all vicarious calibration methods. Again, a model (ORM) can satisfy this most easily.

8. *Extraordinary calibration maintenance procedures are needed to ensure low uncertainties in the radiometric measurements.*

   Calibration is only one part of the uncertainty in a measurement. Bailey et al. (2008) showed that different approaches can have very similar uncertainties, because of their different strengths and weaknesses.

9. *Comparative shipboard measurements must be made near the buoy to check the radiometric stability of the buoy sensors, to determine spatial variability surrounding the buoy location, and to develop and validate bio-optical algorithms.*

   All vicarious calibration methods have to comply with this requirement, and no one method distinguishes itself with respect to the others, except an offshore structure is likely to be easier to access.

10. *The sea-truth radiometric measurements must reproduce the spectral response functions of the satellite sensor bands and this cannot be accomplished using COTS radiometers.*

The results from BOUSSOLE and NOMAD suggest this is not really true. Furthermore, the results summarized in App. J, Fig. J1 confirm that measurements with a 10 nm bandpass are suitable for accurately determining radiometric quantities for a 1 nm bandpass.

11. *The need for flexibility in the choice of spectral response weighting functions used to determine band-averaged measurements imposes a requirement for full-spectrum (i.e., hyperspectral) measurements with resolutions less than 1 nm.*

    The results from BOUSSOLE and NOMAD suggest this is not really true, and the emergence of multispectral sensors with many channels (13 and 14 channels were common with legacy sensors, and 19 is now common for current-generation designs) means a significant portion of the spectrum can be covered with reasonable resolution. It is important to remember that the ORM method is also hyperspectral and could be coupled to a fixed-wavelength approach for certain problems.

12. *Provisions to assure radiometric stability throughout the extended period of operations should include, as a minimum, pre- and post-deployment calibrations of all radiometers, combined with continuous monitoring of onboard light sources of known stability (if possible).*

    All vicarious calibration methods have to comply with this requirement. The advantage of an above-water system is it is rather easy to use natural targets (e.g., the Sun, and even the full Moon, when environmental conditions permit) as a calibration check or to measure a portable source (the latter can be more easily maintained, because it is not submerged). As has already been demonstrated (Hooker and Aiken 1998), profiling radiometers (NOMAD) can be very easily monitored on a daily basis using a portable source and are capable of calibration monitoring in the field at the 1% level.

13. *Instruments suspended in seawater for long periods of time experience fouling by biological organisms that, if not countered effectively using antifouling methods and frequent cleaning by divers, seriously degrade the performance of optical sensors.*

    Free-fall profilers (NOMAD) do not foul, although they must be properly cared for in the field. Above-water autonomous systems experience very little fouling, because the sensor is parked in a downward-viewing orientation when not in use (this could be almost completely eliminated with a movable housing guard).

Probably the most important point to make about vicarious calibration is:

  There is no absolute truth; truth is defined by the process or processes employed in the vicarious calibration methodology.

If there are any biases in the vicarious calibration approach, the biases will be transferred to the remote sensor and the data products derived from the satellite observations. Given that it is rather common for the space sensor to have unknown degradations in the prelaunch characterization that can only be determined after launch by using field data as a source of truth, it is imperative that the *in situ* observations used for vicarious calibration strictly adhere to the Protocols and all instruments are properly characterized, calibrated, sited (notably the solar reference), and maintained (both in the field and in the laboratory).

Appendix C:
The BSI Calibration Facility

The BSI Calibration Facility (Fig. C1) is equipped with dedicated optical benches for irradiance and radiance calibrations, an apparatus for the measurements of spectral responsivity functions, and test benches for angular response and linearity characterizations. The entire laboratory is painted in flat black and has additional curtains and baffles to ensure the proper minimization of stray light.
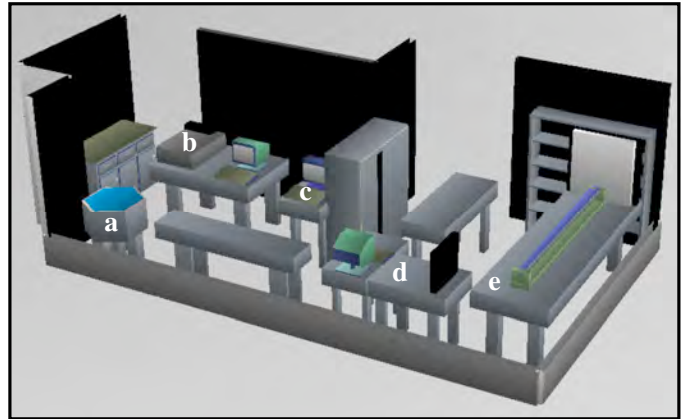
Fig. C1. The BSI calibration facility showing the following: **a)** test tank, **b)** spectral tester, **c)** directional tester, **d)** irradiance calibration, and **e)** radiance calibration.

The irradiance calibration facility is optimized for the operation of 1,000 W tungsten halogen FEL lamps and maintains precision power supplies, shunts, and voltmeters, which are regularly calibrated externally. Radiance calibrations are also based on FEL lamps and performed by pointing the test radiometer at an angle of 45° at a Lambertian plaque made of Spectralon, which is typically located about 2.9 m from the FEL light source. The bidirectional reflectance distribution function (BRDF) of the plaque is regularly calibrated by Labsphere, and the OSPREy project is taking the opportunity to examine plaque uncertainties in greater detail. The facility has been validated by several calibration intercomparisons sponsored by NASA (Meister et al. 2003). BSI maintains several FEL standards of spectral irradiance that have been calibrated by the NIST FASCAL. There are also several working standards that are regularly calibrated against the NIST FASCAL lamps.

Additional lamps from different sources and manufacturers were obtained and screened to establish a lamp library of 21 FELs for the OSPREy activity (Chap. 6). In addition, the calibration facility was upgraded to operate lamps at the highest level of accuracy achievable. Upgrades included a new system for powering the lamps, which allows regulation of the lamp current to within a precision of 50 μA (or 0.0006% for a target current of 8.2 A). Other facilities required for accurate lamp transfers were also upgraded to reduce uncertainties caused by stray light, misalignment, and temperature variations.

The device used for the characterization of spectral responsivity consists of a 1,000 W xenon arc lamp and a 0.5 m grating double monochromator with prism predisperser. This device was custom designed and built by BSI (Bernhard et al. 2005). The two single monochromators that make up the double monochromator are stacked vertically and share a common shaft to which the gratings are mounted. This design ensures

that the two single monochromators are always synchronized. Each of these is equipped with three gratings, machined with 2,400, 1,200, and 600 grooves per millimeter, for covering a wavelength range from 200–2,000 nm.

The angular response tester is equipped with a laser alignment apparatus and a computer-controlled rotary table. Linearity of detectors can be determined either via the inverse-square law using a 3 m rail with precision distance-measurement capability or an automated *lineator*, which compares the test radiometer with a reference radiometer with known linearity characteristics. This instrument was established as part of the development of microradiometers (Morrow et al. 2010a).

Other major equipment that is part of the BSI calibration facility includes the following:

- Several integrating spheres;
- An Aires FF250 imaging, 0.25 m flat-field spectrograph;
- A helium-neon (HeNe) lasser at 633 nm; and
- A helium-cadmium (HeCd) laser at 325 nm.

The latter is part of the equipment used for establishing the stray-light characteristics of the spectrographs integrated into EPIC radiometers.

As part of the UVSIMN project, BSI also maintains a solar calibration facility on the roof of the company's building. One of the UVSIMN SUV-100 radiometers is permanently located in a dedicated room below the roof and is available for intercalibration exercises with OSPREy sensors.

Several improvements to the present facility were undertaken to accommodate the development requirements for OSPREy radiometers:

- The stray light suppression within the laboratory was improved to accommodate calibrations in the SWIR domain. The wall paint was tested for reflectivity beyond 1,000 nm, and a new flat-black paint with the requisite performance in the SWIR was applied.
- Kinematic sensor mounts for reproducible fixation of EPIC radiometers in both the irradiance and radiance calibration facility were designed, fabricated, and installed. Identical mounts will also be used by the Sun-tracker system.
- The radiance calibration setup was modified to permit simultaneous viewing of the plaque with the OXR and standard EPIC radiometers.
- The apparatus for responsivity characterizations will be optimized for use in the SWIR domain. This will include improvements to the wavelength calibration and the reference detector. The software will be modified to allow rapid scanning over a large wavelength range.
- Screening and seasoning of a set of 12 FEL lamps to be used in calibration transfer exercises. These lamps are part of what is referred to as the OSPREy Lamp Library (Chap. 6).

The stability of the OXR and OSPREy technology likely accommodates measurements historically made with the Sea-WiFS Transfer Radiometer (SXR) and the second generation version called the SXR-II. The number of channels in these heritage instruments is significantly less than an EPIC sensor and they only cover the visible part of the spectrum. Nonetheless, they had well-established performance capabilities, particularly in terms of stability and absolute response (Johnson et al. 1998 and 2003), which can be contrasted to the performance metrics of the OXR.

Appendix D:
Ancillary Measurements

Environmental instruments are an important adjunct to the optical measurement systems, including meteorological observations and ocean wave height. Some of these measurements are crucial inputs to atmospheric models, some describe the state of the sea or sky being sampled, others warn of weather conditions that could compromise measurements or even the sensors themselves, and others provide enhanced remote viewing of the installed system.

While many platforms where OSPREy might be installed may already be equipped with meteorological instruments, this is not a certainty; furthermore, the sensors might not be calibrated and in working condition, and their data streams might not be accessible or compatible with the OSPREy data acquisition architecture. For this reason, a set of environmental sensors will be fully integrated into the OSPREy system and the resulting data products.

The required ancillary sensors include the following:

1. Barometric pressure, which is required for calculating relevant atmospheric properties and as a warning of impending severe weather;

2. Rain gauge, which is used as one of the indicators that sampling conditions are unfavorable for the radiance scanning systems (R.M. Young model 55202 heated tipping bucket);

3. Relative humidity and air temperature (R.M. Young model 41382V);

4. Wind speed and direction will be a part of the sea state characterization and will be used to determine if it is prudent to deploy the tracking and shadowband systems (R.M. Young marine wind monitor model 5106);

5. Global positioning system (GPS) with processing for total precipitable water;

6. Pyranometer for broadband radiation (Kipp & Zonen model CMP21 with ventilation);

Future revisions of ancillary sensors could also include imaging technologies, such as the following:

7. All-sky (fisheye) camera using either the Schreder model VIS-J10060CC2 camera from Austria or the Yankee model TSI440A (the Schreder camera seems to have advantages, but it is new to the market); and

8. Network pan-tilt-zoom camera (AXIS model 233D).

The outputs from the meteorological sensors are common signal sources and easily integrated: rain (pulse output), wind (pulse output), wind direction (variable resistor), humidity (voltage), temperature (voltage), barometer (voltage), and other ancillary voltage sensors are digitized by an Agilent U2300 USB data acquisition module connected to the PC. The wave height sensor has a digital output.

The wave height (radar-based) sensor, is useful for monitoring the sea state. A lidar system was considered, but rejected, because of the potential interference with the SWIR optical channels. A radar system is considered the most appropriate, and the plan is to use these data with the anemometer measurements to estimate when whitecaps are likely contaminants in the sea-viewing radiance data (O'Connor FMCW Radar). The high cost of radar systems necessitates that this component be added when the field deployments are more established.

Appendix E:
The BioSHADE Accessory

Shadowband radiometry is provided by the BioSHADE accessory, which is a device that attaches to the OSPREy irradiance sensors (Bernhard et al. 2010). The device uses a microprocessor for command and control, and is compatible with a GPS receiver option for use on ships. There are three modes of operation:

- The shadowband can be kept in the stowed (hidden) position below the plane of the irradiance cosine collector for a global irradiance measurement (Fig. E1a).

- The shadowband can be set to a particular hemispherical angle with a direct (Go to) command to occult the Sun, so the diffuse irradiance can be measured (Fig. E1b).

- The device can be commanded to move over a range of positions and at a programmed rate, for instance, a full hemispherical sweep over a range of $\pm 90°$ ($0°$, which is straight up towards the sky, is zenith).

BioSHADE appears as just another microradiometer-type device when it is used within the microradiometer architecture of sensors.
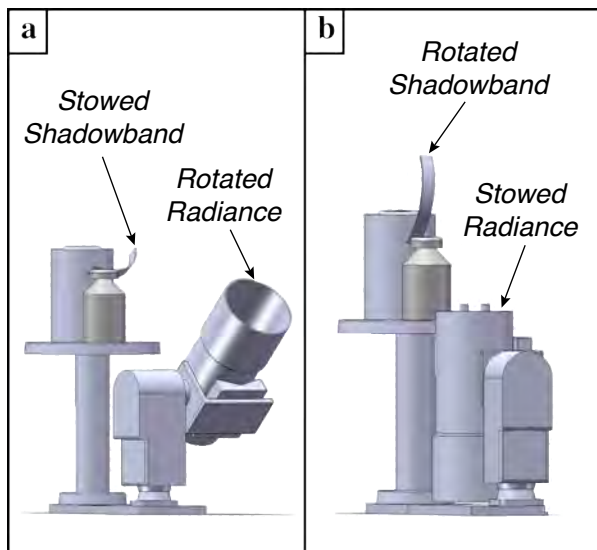

Fig. E1. The BioSHADE mechanism shown attached to an irradiance sensor and in two modes of data acquisition: **a)** global irradiance, for which the shadowband is in the stowed position below the irradiance cosine collector, and **b)** diffuse irradiance, for which the shadowband is rotated to occult the solar disk. In the same respective panels, the radiance sensor is shown rotated to view the sky, and stowed to protect the optical aperture.

BioSHADE is typically programmed to cycle through measurements of global and diffuse irradiance, plus special measurements, wherein the shadowband is positioned $10°$ on either side of the Sun, are also possible. The latter can be used to correct for the partial shading of the sky when the diffuse irradiance is measured with the solar disk occulted. The shadowbands of the two dyads operate asynchronously, so the global irradiance is always measured during a data acquisition scenario. The position of the shadowband is recorded in the data stream.

Appendix F:
Platform Power and Data Telemetry

Power and communications for the instrument suite may be available at some deployment structures, but it is expected in most cases that this infrastructure will be lacking. To design a complete system flexible enough to exploit any kind of physically suitable platform, power generation will have to be done onsite, and high-speed data transmission will have to be facilitated.

Even if a platform already equipped with power is identified and used to deploy an OSPREy system, some portion of a separate power generation capability will probably be needed to ensure a suitable backup capability. The latter is needed not only to safeguard the system, but also to aid in risk assessment by being able to point and receive data from the cameras that are part of the system. Consequently, certain aspects of what is presented here are expected to be a part of every OSPREy system.

Platform Power

Several power technologies have been considered, including diesel-electric, solar, wind, fuel cells, and wave power. For most anticipated platform locations, a hybrid system of solar and wind-charged battery power was selected as the best solution. A small (less than $5\,\text{kW}$) diesel generator would be used for battery charging during platform visit periods, because there will be a high load demand when people are on-platform and during radiometer calibrations.

Fuel cells are an emerging technology with few commercial products available. Given the viable alternatives, it was considered more cost effective and less hazardous if the transportation of compressed gasses (hydrogen) to the platform could be avoided. Wave power for the requirements of the OSPREy systems is too exotic in its current state; it is also costly and not well proven for autonomous systems.

The OSPREy system, during autonomous operation, is projected to use or require less than $1\,\text{kW}$ peak, $500\,\text{W}$ during normal daylight operation, and $300\,\text{W}$ in dormancy (nighttime and storms, but the radiometers are temperature controlled continuously). The OSPREy system will be battery powered, and all components will run off of a $24\,\text{VDC}$ bus. This voltage choice is convenient in a number of significant ways:

- It is relatively safe in contrast to operating at $120\,\text{VAC}$ ($60\,\text{Hz}$);

- It is more efficient for autonomous local-generation systems, because it avoids the substantial power losses from inverters to step up to $120\,\text{VAC}$ and then back down to the DC levels OSPREy uses; and

- It is a commonly used industrial control and automation power level, which provides cost savings, because commercial components are widely available at competitive pricing.

Battery capacity will be specified to support the system in its dormant state for $72\,\text{h}$ (long duration storm), depleting the batteries to 50% of their charge in this period. The batteries will be a lead-acid Absorbent Glass Matt (AGM) type specifically intended for wind and solar charging. They will be maintenance free, with a completely sealed valve-regulated construction. This type is classified as *nonspillable battery* for transport and complies with the US Department of Transportation (DOT) HMR49, as nonhazardous material.

To charge batteries, solar power has the greatest appeal and will probably be the primary power source. Photovoltaic (PV) is a clean, silent, and low maintenance solution that is readily available. Field solutions are well documented (e.g., `polarpower.org`), and easily scalable to address the requirements of different latitudes and climates. PV has limitations, because it is only effective when sunshine is available (no charging during rain or at night) and the panels take up space. For a design latitude of 40° (New York City) and maximum reserve capacity, about a $30\,\mathrm{m}^2$ array of PV panels (4 kW) would be needed to supply the daily requirements of OSPREy. Given this, supplemental power is necessary.

The secondary battery charging technology will probably be one or more small wind turbines designed for stationary marine and coastal applications. Two commercially available three-bladed turbines, approximately 2.7 m in swing diameter, can provide 400 W continuous charging in as little as $5.4\,\mathrm{m\,s}^{-1}$ (12 mph) wind. These same turbines can provide as much as 2 kW in $13.4\,\mathrm{m\,s}^{-1}$ wind conditions (30 mph storms). This potentially facilitates indefinite period charging during times when solar charging is ineffective (and OSPREy is operating in its dormant state).

Wind turbines have the added advantage that they can charge continuously during the day or night, again offsetting PV in a complementary manner. Because wind turbines have moving parts, they are generally higher maintenance than solar systems and this needs to be considered carefully for long-term deployment scenarios. They also provide no charging in low wind conditions (less than $3.1\,\mathrm{m\,s}^{-1}$), so reasonably complete wind histories for a planned location are needed. In many cases, offshore structures are already instrumented with meteorological sensors, so detailed wind information is frequently available. For design purposes, however, wind climatologies are usually sufficient.

The balance of PV and wind will be tailored to the climate conditions of the specific platform location. To optimize charging efficiency, the plan is to use Maximum Power Point Charge Tracking charge controllers, with remote monitoring features. Charging, battery charge state and health, and OSPREy loading of the power system will be monitored, in an attempt to prevent data loss from a power system problem. The solar and wind charging subsystems, as well as battery banks, will be configured in parallel to the 24 VDC power bus. In this configuration, should a power system component fail, the OSPREy system will not be completely crippled until the next servicing opportunity, which means emergency response scenarios (which might be expensive for some locations) can be kept to a minimum.

The OSPREy power requirements are a small fraction of the power typically available from diesel generators designed for continuous unattended operation. This power source is also a source of particulates with the potential to compromise the radiometer light collection (optical) surfaces and some of the atmospheric observations, although proper attention to siting the generator can greatly minimize this problem. It would also require supply and storage of fuel at the platform, and the engine would require periodic maintenance from a mechanic brought to the site.

It is expected, however, that during platform visits by personnel to service the equipment, particularly during the monthly maintenance activities, power demands could be on the order of 1.2 kW (continuous). Much of the needed power will be dedicated to radiometer calibrations and system service activities.

It is also possible that remote troubleshooting of a malfunctioning sensor could increase power requirements as other systems are reprogrammed or exercised to diagnosis the problematic equipment.

To address the occurrence of any occasional peak demands, a small diesel generator would be part of an OSPREy power system. The generator would be used for charging during platform maintenance visits in conjunction with solar PVs and wind, as well as providing 120 VAC directly from the generator's integral inverter. Its occasional use and compact size will require minimal maintenance, little fuel to be transported or stored, and will not be a continuous polluting source. Diesel is chosen not only for its efficiency, but also with fuel transportation safety in mind.

Data Telemetry

The volume of *in situ* data plus remote system management communications is expected to require a daily transfer of up to 1 GB of information. To achieve OSPREy objectives, including diagnostic images, a reliable high-speed data link and static Internet protocol (IP) addressing is needed. At offshore locations, it is unlikely that the estimated $500\,\mathrm{kB\,s}^{-1}$ (or faster) data link will be readily available for dedicated OSPREy use. To optimize costs and the amount of time in a 24 h period available for communications, commercial bandwidth options are considered the most appropriate.

It is anticipated that most platform locations will not be so convenient with respect to the common bandwidth and Internet access options, and cellular telephony cannot provide the required sustained bandwidth. At this time, the most cost-effective solutions for these locations are satellite-based, so this type of service will be used for OSPREy data communications. Of the available options, the most readily available and affordable is Very Small Aperture Terminal (VSAT) technology. Dedicated channel VSAT is high reliability (the bit error rate is 10^{-7} or better), small footprint (typical dish diameters are 0.8–1.8 m), and available with a variety of fixed bandwidth rate options from $300\,\mathrm{kB\,s}^{-1}$ to greater than 1 MBps (transmit rate from ground link to receive rates are generally higher). Static IP addresses are available, and bandwidth can be scaled up or down as OSPREy requirements change.

Available VSAT coverage includes the contiguous US coasts (up to 100 km offshore), the coasts of Alaska and Hawaii, the Gulf of Mexico, the Caribbean Sea, and the northwest coast of Mexico. VSAT has the potential to provide an affordable single-technology bandwidth solution for all currently envisioned OSPREy platform locations. Should OSPREy platforms be in other regions of the globe, VSAT services are available for Europe, most of South America, North Africa and the Middle East, and many coastal regions of East Asia.

If OSPREy systems are placed on platforms at high latitudes or far offshore, there are other satellite-based solutions with global, or near-global availability, including broad swath links more typically employed in the maritime industry (commercial vessels). These services will be substantially more expensive per bit than VSAT, however. There is also the NASA Tracking and Data Relay Satellite System (TDRSS). While TDRSS availability is not 24 h per day globally, channel bandwidth is substantial enough to achieve OSPREy data transfer objectives, at nearly any conceivable OSPREy platform site. Because of geosynchronous orbits, TDRSS is available at extreme latitudes (the poles).

90

S.B. Hooker, G. Bernhard, J.H. Morrow, C.R. Booth, T. Comer, R. Lind, and V. Quang

Appendix G:
Extended Test Deployments

The OSPREy suite of sensors is designed to operate autonomously in remote, sometimes harsh, environments. Service and maintenance opportunities are normally expected to be limited to monthly visits, but an emergency servicing capability is also anticipated (e.g., for unexpected equipment problems or a safeguard response to a severe weather forecast). Most likely, the system will be running on power and telecommunications links for which BSI is responsible. Fortunately, BSI has been designing and operating complex multisensor optical systems for over 20 years, some in even more hostile environments than anticipated for OSPREy systems (the center of the Greenland Ice Sheet, for example). BSI has typically achieved a greater than 95% acquisition of all possible data products in these circumstances.

In any newly designed system, a shakedown or commissioning period is required, and the first deployment of an OSPREy system will be no different. There will be two phases to this early testing of a new system: the first, will be on the rooftop optical platform at BSI, which will test all of the individual components as they are available and characterized; the second will be a two-week deployment at an offshore site to be selected early in the project. After the successful completion of these two tests, the system will be considered ready for operational deployment (App. H).

Component reliability is an issue, because all components eventually fail. With the BSI systems deployed in polar environments, this is dealt with first by designing for reliability, and then by stocking spare components onsite (in rare instances one of the facility technicians is asked to change a standard lamp or replace a fuse), and finally with annual visits to each site with a set of tools, calibration standards, and spares. For OSPREy, there is no capability of onsite assistance, so monthly visits will include the availability of a complete set of spare, fully calibrated radiometers in the event one shows degradation problems, or more simply, is scheduled to be rotated out of operation for refurbishment.

Part of the envisioned operational cycle will include sensor calibrations back at the BSI calibration facility (App. C). Although calibration monitoring at the platform will be done monthly using a portable source (App. H), the monthly maintenance plan involves bringing back one of the two radiometer sets on a regular rotation, perhaps quarterly (to be determined more exactly once experience with the system has been acquired). In this case, the spare set of radiometers would be installed and the system would spend a day running in a more intense intercomparison mode. The advantage of this approach is that it would periodically freshen the calibration of the full set of radiometers independently of using the portable calibration source. This provides an alternate operating mode in the case that the portable calibration source is not as successful as anticipated.

The BSI corporate facility is located 3.4 mi northeast of downtown San Diego, California. The facility has had a rooftop optical observation platform since BSI moved to the location in 1991. The rooftop platform has been host to a UV-Visible Scanning Spectroradiometer installation, which is part of the NSF Polar Programs UV Monitoring Network. A GUV-511 UV filter radiometer is also permanently installed, and other instruments are regularly deployed as various projects are initiated and concluded. After using the rooftop platform to develop and test the tracking systems, shadowband, and other components, the entire OSPREy system, including solar power generation and satellite data communications, will be deployed on the rooftop platform for several months with all components operating autonomously.

During rooftop testing, OSPREy global irradiance measurements will be compared with the Scanning Spectroradiometer (300–600 nm) permanently installed on the roof. Shadowband measurements, sky radiance, Sun tracking, solar principal plane, and almucantar sky radiance measurements will all be made. Although this arrangement does not allow for any sea-viewing observations, all of the other sensor systems and resulting data products can be completely tested. The sea-viewing sampling scenario will be simulated by using series of painted targets on the roof that can be designed to provide a relatively stable signal. Of course, these would not be calibration targets, but targets with reflectances similar to that of the ocean, the selection of which will be based on the Munsell Color Classification colors used in early remote sensing studies. The objective here is to subject the system to the most realistic dynamic range in variables possible.

While testing on the rooftop optical platform at BSI should provide a convincing demonstration of the ability to routinely obtain solar irradiance and atmospheric properties, and even the ability to accurately measure radiance from calibrated targets, it will not completely demonstrate the ability to provide sea-truth data for ocean color satellite missions. A two-week deployment of all components, except the ancillary meteorological instruments (App. D) and autonomous power generation, at a site with a good sea-viewing geometry is part of the first field commissioning exercise. This deployment will include simultaneous in-water AOP profiles to validate the above-water determination of water-leaving radiances and the production of higher order data products (e.g., the derived chlorophyll a concentration).

The platform to be used for the initial deployment has not been finalized. NASA has ongoing relationships that may allow access to a number of coastal observatories and other locations—all of which have scheduling and logistical advantages and disadvantages. Although each is different in terms of capability and access, the South Atlantic Bight (SAB) Synoptic Ocean Observing Network (SABSOON) observatory is documented as an exemplary facility for comparison purposes (App. L). In the past, BSI has installed solar tracking radiometric systems on the Scripps Institution of Oceanography pier, which extends far out into the ocean, and certain types of testing might be advantageous at this site. This location would also permit the deployment of an in-water profiling system for additional validation data. Recent advances in the use of a telescoping mast to mount solar sensors well clear of local obstructions (Hooker 2010) means deployment opportunities on previously awkward structures like piers are more tenable. When extended, the mast also safeguards the equipment from unwanted access by other personnel on the structure.

Another option is to charter a boat and deploy for several days of repeated observation sequences of both above- and in-water optical observations following the methods of Hooker et al. (2004). An advantage of this approach is that several water types could be accessed off San Diego, but the disadvantage is that a moving ship would make Sun tracking very difficult (but this is rigorously tested on the BSI rooftop facility). A final decision on the optimum location and deployment method will be researched during the first year of the project and finalized before the third year (when the deployment is scheduled to take place).

Appendix H:
Operational Deployment

After the extensive test phase and field commissioning deployment (App. G), an OSPREy system will be ready for operational deployment on an ocean platform. An engineer and optical scientist will be sent to inspect and survey candidate platforms for suitability. This survey will include meeting with the custodians of the platforms to preview suitable mounting locations (for all instruments and solar power panels), and to assess the availability of pre-existing logistical support. The latter includes power, communications, storage, and laboratory space, all of which are not required for successful OSPREy operations, but all of which would enhance the operational reliability of the system.

The possible methods for mounting devices will also be investigated to determine if welding will be necessary, and the type of tools that will be required for installation. Part of this assessment will include the mitigation of perturbations to the observational suite from unavoidable obstructions (some of which are inevitable). The site will be photographed at different times of the day to understand and document the solar geometry. When the various mounting locations are determined, cable lengths and disconnect points will be determined. The mode of deployment will be reviewed carefully, paying particular attention to vertical distances to be traversed, lifting assistance (hoists), types of ladders, and other logistical factors.

Approximately six weeks will be needed to fabricate the necessary mounting hardware and to procure and test all of the required cabling. Any needed services required for deployment (e.g., helicopter, boat, electrician, or welder) will be contracted and scheduled. Based on the deployment vehicles and their carrying capacity, plus the means of vertical transport on the platform, shipping containers will be fabricated and made ready for transport. When the installation opportunity arrives, the equipment will be shipped and the team will travel to the staging site for the installation. Installation time will range from 3–7 days, depending on weather conditions, as well as the conditions of the platform and the difficulty of working on it. As the sensors are brought online, data analysts back at BSI will exercise the communications links and start data collection. After all sensors are functioning nominally, a 24 h undisturbed period will allow the instruments to come to thermal equilibrium, and permit the data analysts at BSI to review system performance.

Finally, the engineers will revisit the platform and perform calibrations using a portable calibration source. After the field calibrations are performed, an in-water deployment of matching submersible AOP radiometers (in terms of the fixed wavelength microradiometers) will be used to characterize the optical properties of the water. Additional field measurements will be made for IOPs, as well as sampling for the analysis of HPLC pigments and biogeochemical parameters. At the end of the installation, the OSPREy system should be fully operational. Based on operational experience with other remote systems, shortly after midnight each day, all data and logs collected the previous day will be automatically transferred to BSI. An archived copy will remain on the data collection computer at the platform. A remote session will be initiated, to inspect all connected sensors and systems. The remote host software will also have the ability to generate electronic mail messages and corresponding alerts for any problems that might demand immediate attention. Finally, a remotely operated digital camera, sited on the platform to have unobstructed viewing of all important components, can be used for remote visual inspection and problem diagnosis.

Initially, measurements from the previous day will be processed and compared with historical and modeled data to detect outliers on a daily basis. The log files will be filtered for unusual events, and the results of this automated data review will be used to produce a daily report summarizing system operation. This review will focus on such factors as temperature regulation and dark offset stability, tracking of redundant sensors during sampling modes when pairs of radiometers are operating in the same mode and viewing the same target, monitoring battery power levels, and system power consumption. This type of functionality will run automatically and will be timed in keeping with personnel work schedules. For some deployment locations, time zone differences might increase the desired lag time between the end of an observational day for an OSPREy system and the start of a BSI work day.

A second level of monitoring will examine data quality from the aspect of agreement of various radiometric products derived from different paths (such as direct solar irradiance derived from the shadowband radiometer and the Sun-tracking radiometer). The results of this monitoring will be used to build data reports, including data quality estimates, which will be posted on the OSPREy Web site (typically with a one day lag). Initially, these reports will be semiautomatic as the formats are tuned to be the most useful. As the analysts involved become more accustomed to the data flow and quality, the reports will become fully automatic and delivered as a portable document format (PDF) file via e-mail. Unless directed otherwise, *the OSPREy Web site will be public, because this kind of visibility greatly increases the number of people looking at the data, which significantly increases the chance of detecting problems and improving the quality of the data products throughout the lifetime of the activity.* Synergistic activities with other customers of OSPREy sampling systems will be pursued where mutually advantageous and permissible.

Regular platform visits will be scheduled on a monthly basis. These visits will include calibrating each radiometer with a portable calibration source before and after cleaning the sensors. The latter provides the opportunity to detect any biases caused either by fouling or sensor drift. The solar panels will be cleaned and the meteorological sensor suite inspected, along with all computer and power systems. Water samples will be collected for HPLC pigment and biogeochemical analyses, and a C-OPS in-water profiling package will be deployed to collect contemporaneous measurements of the AOPs of seawater for subsequent comparison to the OSPREy AOP data products. In the event of a system component failure or degradation, a spare component will be available for installation at the monthly visit. If a major problem is encountered (e.g., responding to a significant power supply problem or the damage from a severe weather event), the time span of the work may require more than a one-day visit.

The various sampling systems will be designed such that the monthly maintenance and sampling visit can be completed in less than 8 h under normal circumstances. This makes it possible to accomplish the work by helicopter at all times of the year if the offshore structure has helicopter access. If the only access is by ship, the transit time will be longer, but more people can be taken to ensure the amount of work can still be done in the time anticipated. Regardless of helicopter access, a certain number of visits will always be done by ship to ensure the greatest flexibility in accommodating personnel and equipment. In particular, the transportation of heavy or bulky items will be staged for ship transportation (helicopters have restrictive cargo transport capabilities).

S.B. Hooker, G. Bernhard, J.H. Morrow, C.R. Booth, T. Comer, R. Lind, and V. Quang

Appendix I:
Absolute Calibration

This appendix summarizes the method presently being applied to convert field measurements made with radiometers built with microradiometers to geophysical units, such as spectral radiance and irradiance. This *standard* method is based on the NIST FASCAL scale of spectral irradiance, as detailed in the Protocols, and is straightforward to implement. This task is performed in the BSI calibration laboratory (Sect. 6.3.2 and App. C) using a NIST standard lamp for all calibrations, plus a reflectance standard for radiance.

The standard method does not provide radiometry at the 1% accuracy level, however, which is one of the goals of the OSPREy concept. A new, more advanced calibration method based on a NIST SIRCUS calibration is currently under development that will be published in a subsequent report. This new method will take several sources of uncertainty into account, which are absent from the standard method, and will address the calibration of the spectrograph component of OSPREy radiometers, with additional features.

Dark Measurements

Each microradiometer used in OSPREy instruments has three gain stages (Sect. 2). The ratios between the three gain values are accurately measured during the manufacturing process of each microradiometer and stored in the nonvolatile memory of each sensor. The outstanding linearity exhibited by all three gain stages (Sect. 2.3) ensures that a single-point calibration coefficient, determined at any one gain, satisfies the uncertainty requirements for obtaining calibrated reading at all gains. The use of high-quality gain resistors having temperature coefficients of less than 20 ppm ensure minimum drift over time. Each gain stage has a unique dark signal amplitude, or *offset*, that is somewhat temperature dependent and determined during calibration.

Dark measurements can be acquired using different procedures (Sect. 8.9) and are usually recorded to track the sensitivity of the dark signal to environmental forces (e.g., temperature). At BSI, the dark measurement for each microradiometer and gain setting is usually acquired over a 30 s time period at 5 Hz. BSI has three ways to measure the average *dark* signal amplitude (μ denotes an average signal amplitude and the accent establishes the way the dark measurement is made):

$\bar{\mu}^{\blacksquare}$ Covering the sensor aperture with an opaque cap that blocks all the light reaching the aperture (this measurement is the most common, because it directly establishes the dark offset, and it can be done in the field);

$\overleftarrow{\mu}^{\blacksquare}$ Closing a shutter between the compartment of the laboratory that contains the lamp (while it is operating) and the compartment where the radiometer is mounted, which allows only the *background* radiation scattered from the lamp compartment to reach the radiometer (this dark measurement is unique to calibration and establishes how good the baffling is for the compartment where the lamp is operated, although some background radiation that would pass through the aperture is not measured); and

$\overleftrightarrow{\mu}$ Placing an occulting device between the source of direct radiation (a lamp for irradiance and a reflectance plaque for radiance) and the radiometer such that the occulting device only blocks the direct radiation across the size of the aperture but nonetheless allows *ambient* radiation

scattered from the backside of the lamp compartment and the walls of the radiometer compartment to reach the radiometer (this dark measurement is also unique to calibration and establishes how good the baffling is for the entire calibration facility).

Because of the extensive baffling and reflection minimization procedures used at the BSI calibration facility to suppress stray light (Sect. 6.3.2 and App. C), the differences in the dark signal amplitudes determined with the three methods is less than 0.2% at SWIR wavelengths, and less than 0.1% in the UV, visible, and NIR domains. Consequently, the first two methods are used for routine calibrations, because they are the most expedient.

As noted above, the most common method involves covering the sensing aperture with an opaque cap to measure the average dark signal amplitude. When these data are obtained in the field close in time to the collection of light data, these dark measurements are referred to as *field darks*; if obtained in the laboratory as a necessary part of completing the calibration procedure, these dark measurements are referred to as *calibration darks* and are recorded in the calibration file. For sensors built with microradiometers, the dark offsets obtained by capping the sensor aperture are also stored in the radiometer's nonvolatile memory and used by the firmware to calculate the signal amplitude when exposed to radiation (these values can be updated in the field to provide the most accurate real-time geophysical values).

Responsivity

The next step in the calibration process involves determination of the spectral responsivity, $\gamma(\lambda)$, as it pertains to calibration for each microradiometer. The responsivity term converts a measured signal amplitude to calibrated geophysical units. For irradiance sensors (identified by the E subscript) built with microradiometers (identified by the M superscript), responsivity is defined as:

$$
\begin{aligned}
\gamma_E^M(\lambda) &= \frac{\left(\mu_E^M(\lambda) - \bar{\mu}_E^{\blacksquare M}(\lambda)\right) - \left(\overleftarrow{\mu}_E^{\blacksquare M}(\lambda) - \bar{\mu}_E^{\blacksquare M}(\lambda)\right)}{E_F(\lambda)} \\
&= \frac{\mu_E^M(\lambda) - \overleftarrow{\mu}_E^{\blacksquare M}(\lambda)}{E_F(\lambda)},
\end{aligned}
\tag{I1}
$$

where $\mu_E^M(\lambda)$ is the average light signal amplitude derived from repeated measurements of the spectral irradiance $E_F(\lambda)$ from the standard lamp at the calibration distance of 50 cm. The average is usually based on a sampling time of 30 s and a sampling rate of 5 Hz.

For radiance sensors (identified by the L subscript) built with microradiometers, responsivity is defined as:

$$
\gamma_L^M(\lambda) = \frac{\mu_L^M(\lambda) - \overleftarrow{\mu}_L^{\blacksquare M}(\lambda)}{L_P(\lambda)},
\tag{I2}
$$

where $L_P(\lambda)$ is the radiance of a standard (typically Spectralon) reflectance plaque illuminated by a standard FEL lamp, wherein the instrument to be calibrated is facing the center of the plaque at an angle of 45°, and $\mu_L^M(\lambda)$ and $\overleftarrow{\mu}_L^{\blacksquare M}(\lambda)$ are the light and dark average signal amplitudes, respectively, measured in a similar fashion as for irradiance radiometers. The $L_P(\lambda)$ term in (I2) is calculated using the following formulation:

$$
L_P(\lambda) = \frac{\rho_P(\lambda)}{\pi} E_F(\lambda) \left[\frac{\ell_r + \Delta\ell}{\ell_c + \Delta\ell}\right]^2
\tag{I3}
$$

where ℓ_r is the reference distance for the lamp (50 cm for a NIST standard lamp and measured from the front of the lamp posts); $\ell_c + \Delta\ell$ is the centerline distance between the surface of the plaque and the center of the lamp filament (in the same units as ℓ_r) for which $\Delta\ell$ is the offset distance between the center of the lamp filament and the front of the lamp posts; and $\rho_P(\lambda)$ is the spectral reflectance factor of the plaque for an incidence angle of $0°$ and a viewing angle of $45°$.

Measurement Equation

The formulation of the measurement equation follows from the definition established by the National Bureau of Standards (NBS†) in a series of monographs describing optical radiation measurements. As part of laying down the foundation for such measurements, Nicodemus et al. (1976) defined the following:

> The measurement equation is the mathematical expression that quantitatively relates the output of a measuring instrument to the radiometric quantity that is being measured, taking into account all of the pertinent factors contributing to the measurement result. The main part of that measurement equation relates the radiation input at the receiving aperture of the instrument to the resulting output in terms of the instrument responsivity (output "signal" per unit incident radiation input).

The explicit reference of responsivity being equal to output over input (I1 and I2) sets the form for the measurement equation, but there is an added requirement that Nicodemus et al. (1976) made clear:

> The complete equation also accounts, as needed, for the effects of interactions between matter and radiation at the source and along the optical path of the radiation beam as well as at the instrument.

From the generalized perspective of BSI calibrations, the majority of which are for in-water sensors, a principal interaction effect is the so-called *immersion factor*.

The immersion factor is a necessary part of the spectral characterization of an in-water sensor, because when the collector is immersed in water, its light transmissivity is less than it was in air. In-water sensors are calibrated in air, however, so a correction for this change in transmissivity must be applied when the in-water raw data are converted to physical units. The immersion factor for irradiance must be determined experimentally (Hooker and Zibordi 2005a), whereas for radiance it can be computed to an acceptable accuracy; by definition, the immersion factor is unity when the sensor is used in air.

There are other interaction effects that need to be included, but not all of these are handled explicitly as part of the measurement process, because some of the needed parameters are typically not available at the time the data are acquired. For example, a correction for the self-shading effect is frequently applied when the data products are derived from the observations. Nonetheless, it is useful to be able to consider an expanded multidimensional concept for responsivity wherein the complexity of the term is built up as the characterization of the instrument becomes more comprehensive.

The dimensionality of γ is denoted by including arguments to the responsivity term, wherein each added argument represents a new interaction effect. In other words, if e_i represents a particular interaction effect, then $\gamma(\lambda, e_1, e_2)$ indicates which two of those interaction effects are included in the definition of

responsivity that is being applied. Note that in the simplest representation of responsivity (I1 and I2), the term simply represents what is usually called the *calibration coefficient*.

Considering now the formulation to convert a measured signal amplitude $A(\lambda)$ to geophysical units as obtained for in-water irradiance (E subscript) and radiance (L subscript) sensors equipped with microradiometers (M superscript), the measurement equations are as follows:

$$E^M(\lambda) = \frac{A_E^M(\lambda) - \ddot{\mu}_E^M(\lambda)}{\gamma_E^M(\lambda, F)} \qquad (I4)$$

and

$$L^M(\lambda) = \frac{A_L^M(\lambda) - \ddot{\mu}_L^M(\lambda)}{\gamma_L^M(\lambda, F)} \qquad (I5)$$

where the F argument for responsivity accounts for immersion factor interaction effects. In this case,

$$\gamma_E^M(\lambda, F) = \frac{\gamma_E^M(\lambda)}{F_E^M(\lambda)} \qquad (I6)$$

and

$$\gamma_L^M(\lambda, F) = \frac{\gamma_L^M(\lambda)}{F_L^M(\lambda)}, \qquad (I7)$$

where the numerators in (I6) and (I7) are the aforementioned calibration coefficients and the denominators are the immersion factors (which for OSPREy sensors are unity).

Note that (I6) and (I7) do not specify the target. For example, the calibration procedure is independent of whether or not the shadowband of the irradiance unit is in use or whether the radiance radiometer measures the radiance of the sky, Sun, or Moon (by pointing up), or the sea surface (by pointing down). Furthermore, for remotely installed instruments, it is sometimes possible to utilize ambient darks measurements performed at night to provide a temporally more representative measure of the dark offsets.

OSPREy Considerations

The formulations presented above, (I1)–(I7), are not in agreement with the legacy approach documented in the Protocols. The differences are a result of the Protocols not adhering to the principles first established by the NBS, retained by NIST (Larason and Houston 2008), and adopted by the wider community (Boivin 2005). In the Protocols, responsivity is erroneously defined as the radiometric input quantity per unit output. This inversion is not necessarily a significant source of uncertainty for simplistic calibration scenarios (e.g., single-point calibrations).

The standard calibration procedure outlined above does not provide radiometry at the 1% accuracy level. The procedures, therefore, need to be amended to achieve this level of accuracy. OSPREy technology anticipates development of a new, more accurate and complete method to calibrate radiometers, which are presented in detail by Bernhard et al. (2012). The new method serves to minimize uncertainties in calibrated irradiance or radiance data arising from several sources of error that are not addressed by the standard method. It also deals with the special challenges involved in calibrating the spectrograph component of OSPREy radiometers and the new capabilities afforded by the filter wheel of the radiance unit.

---

† The NBS was the precursor agency of NIST.

OSPREy irradiance radiometers have a state-of-the-art cosine collector (Chap. 3). Although the cosine error of the collector is small, it is not zero, and a correction is required to minimize the impact of this error on calibrated spectral irradiance measurements. The correction method is based on measurements of the cosine error, which are performed for every OSPREy irradiance radiometer, the ratio of direct to global spectral irradiance measured with the instrument's shadowband, and assumptions on the distribution of sky radiance (Bernhard et al. 2010). The new calibration method will build on these earlier results. For example, rather than assuming that sky radiance is isotropic, measurements of the sky radiance distribution provided by the tracker-mounted radiance sensor can be used to further reduce the uncertainty of the current cosine error correction scheme.

Spectral Resolution

Microradiometer channels cover a spectral band of approximately 10 nm FWHM, while spectrographs have a bandwidth of 6–10 nm (Table 11). Largely due to absorption processes in the outer region of the Sun's atmosphere, the solar spectrum is not constant over these wavelength ranges, and varies greatly on a 0.001 nm scale. These absorption processes lead to the Fraunhofer lines in the extraterrestrial solar spectrum. These lines are not resolved by either the micrometer channels or the spectrograph, which cause uncertainties in the measurement when calibrations are applied.

Although ground-based OSPREy instruments do not measure the extraterrestrial spectrum (ETS) directly, spectral measurements including observations of the direct Sun, sky radiance, or the radiance emanating from the sea surface, can be considered as the product of the ETS and a transmission spectrum that takes into account absorption and scattering processes in the Earth's atmosphere. Even though OSPREy microradiometer channels occur at wavelengths where absorption by the Earth's atmosphere is minimal, the detailed Fraunhofer structure of the ETS cannot be neglected because it introduces calibration uncertainties arising from the finite bandwidth of the sensors. To determine the magnitude of the effect, a high-resolution ETS solar spectrum was compared with two simulated spectra: one from a moderate bandwidth (10 nm boxcar) radiometer and one from an idealized spectrometer that has a triangular slit function and a resolution of 1 nm FWHM. The maximum divergence of the simulated spectra and the ETS was a factor of 15. These differences can be explained by the smoothing of the high-resolution ETS by the finite bandwidth of the hypothetical sensors.

The new calibration method will take into account the relative spectral responsivity functions of OSPREy instruments, including bandwidth differences between two units and nuances such as manufacturing tolerances of interference filters and geometric factors such as filter detuning from acceptance cones. The method will result in a reporting of spectral irradiance or radiance identically to spectra measured by ideal spectrometers. For example, the 10 nm FWHM 380 nm channel of an OSPREy irradiance sensor will be calibrated such that the reported spectral irradiance would be identical to that of a hypothetical spectrometer with a triangular slit function and a bandwidth of 1 nm. With this approach, measurements of all OSPREy radiometers would be comparable and the quantities to be measured are unambiguously defined. The method requires accurate knowledge of the spectral responsivity functions

of all microradiometer channels. All instruments are therefore characterized using the BSI spectral tester (App. C).

Spectrograph measurements for OSPREy radiometers are calibrated using a similar procedure and gridded to a standard wavelength interval (e.g., 300, 301, 302 nm, etc.), resulting in spectra with a defined bandwidth and wavelength interval, regardless of the native bandwidth and pixel wavelength of the spectrographs. This standardization is particularly important because spectrographs installed in irradiance and radiance sensors have different bandwidths. By standardizing the calibrated data product, measurements of the two units become comparable. Standardization is also required for comparison of measurements of microradiometer and spectrograph components and radiometers that are not OSPREy instruments.

Spectrograph Considerations

Calibration of spectrograph data is subject to unique challenges because the units are affected by dark signal drifts, limited dynamical range, stray light, and nonlinearity. These four sources of uncertainty will be addressed in the new calibration method. Although the OSPREy spectrographs are temperature stabilized to better than $\pm 0.03°$C, data analysis indicates that the remaining variation in temperature leads to noticeable variation in the dark signal amplitude. For irradiance sensors, these variations are characterized and corrected by analyzing variations in spectrograph measurements spanning 245–285 nm. Because Earth's atmosphere is opaque to radiation in this wavelength range because of ozone absorption, variations in spectrograph data in this domain can be attributed to the combined effects of dark current drifts and stray light. Drifts of the dark signal amplitude of spectrographs used in radiance units are characterized by turning the filter wheel to the opaque position.

The dynamic range of the spectrograph is limited by the 15 bit ADC capability of the unit (Table 11). The dynamic range can be extended by two methods: a) measuring at a different integration time, and b) using the neutral density filters of the filter wheel (Figs. 49 and 55). The first option is addressed by considering that the spectrograph responsivity is proportional to the integration time, whereas the second option requires accurate knowledge of the spectral transmission of the two neutral density filters installed in the filter wheel. The transmission of each neutral density filter is determined in the BSI calibration laboratory.

The stray light correction for each spectrograph requires the measurement of the spectrograph's slit-scattering function over the entire wavelength range. The function is determined using measurements of laser lines (e.g., the measurement of the 632.816 nm line of a HeNe laser, as discussed in Sect. 7.4.2). From these measurements, a stray-light correction matrix is determined using a method similar to that suggested by Kreuter and Blumthaler (2009) and applied to spectra that have been corrected using the dark signal data. The resulting spectra are then corrected for nonlinearity. The associated correction factor is a function of the light signal amplitude and is determined in the laboratory.

The filter wheel installed in all OSPREy radiance sensors is equipped with three polarizers, oriented at $0°$, $45°$, and $90°$ (Figs. 49 and 55). From measurements taken at these three positions, the polarization state of radiance can be determined in terms of the Stokes vector. The calibration process requires characterization of the Mueller matrices for each of the three polarizers, which will be done in the BSI calibration laboratory using methods developed by Voss and Liu (1997) and Liu and Voss (1997).

95

Appendix J:
Uncertainty Analysis

Although microradiometers offer a step-function improvement in many practical aspects of design and deployment of field radiometers, the underlying photodetector technologies remain unchanged from PRR instruments. These legacy systems were capable of acquiring data over almost the entire performance envelope of the detectors, and remain an excellent proxy for the ultimate performance characterizations of the OSPREy EPIC instruments (Chap. 2). The following uncertainty analysis is offered to represent the uncertainty approach, and to a qualified extent, an excellent first approximation of what is expected from OSPREy.

The uncertainty of SIRCUS responsivity calibrations for the spectral range 406–920 nm is 0.2% (Brown et al. 2000). The uncertainty of the calibration transfer from an OXR to an OSPREy EPIC radiometer is mainly influenced by small changes (0.1%) in the lamp output within the time period needed to execute the calibration and small alignment uncertainties in the physical setup. The latter will be limited to less than 0.5 mm, because all OSPREy radiometers are equipped with a kinematic mount designed for high positioning accuracy.

Repeated lamp calibrations performed on PRR-800 radiometers over the time span of several years have indicated that the instruments are typically stable to within 1% during one year, although single channels may change at a somewhat larger rate. With daily intercomparisons of the various radiometers, uncertainties caused by changes in responsivity can be limited to approximately 1.0%. The primary source of daily intercomparisons with the OSPREy sensors are natural targets, although other targets are available at longer time periods (e.g., the portable source that will be used during monthly maintenance visits).

Changes in responsivity resulting from collector contamination (e.g., sea spray, air pollution, and birds) are hard to quantify, because they depend on the platform location, position of the sensors on the platform, and environmental conditions around the platform. Contamination of irradiance radiometers is minimized by using a diffuser made of polytetrafluoroethylene (PTFE), an inert material that is easily cleaned by rain and wind. Fouling of the radiance optics are reduced by stowing the radiometers with the glass apertures protected. Should this prove to be ineffective, addition of a (distilled) water-spray system will be considered and has been conceptualized. Contamination may be a problem during significant dust events, but these periods can be identified by regular intercomparison of the radiometers. Data with discrepancies larger than 2% will be flagged as abnormal and will be subjected to additional scrutiny.

The uncertainty, due to the deviation from an ideal cosine response of the UV-VIS EPIC irradiance radiometers, will be similar to the PRR-810 radiometers, which is to within 2% for zenith angles spanning 0–65° and to within 10% for 65–85°. Correction procedures developed for the spectroradiometers in the UVSIMN activity (Bernhard et al. 2004) will be applied to OSPREy EPIC instruments. The associated uncertainty of 1% is based on a sensitivity analysis using UVSIMN data (Bernhard et al. 2004). Accurate knowledge of the ratio of the direct-to-global irradiance from shadowband measurements will reduce the uncertainty further. The cosine error for the VIS-SWIR EPIC irradiance radiometers is larger because of the difficulty of designing diffusers for the SWIR domain. Global irradiance in the SWIR during clear skies, however, is mostly from the direct component, which considerably reduces correction uncertainties.

The uncertainties related to the transfer of an instrument from the laboratory environment to field measurements arise from the very different shapes of a standard lamp and the solar spectra: a solar spectrum provided at a 1 nm resolution may change by up to a factor of 2.5 within the 10 nm bandpass of an OSPREy EPIC channel, whereas a lamp spectrum is almost constant. OSPREy EPIC measurements will be normalized to a standard bandpass of either 1 nm, or 10 nm using radiative transfer modeling introduced in Apps. I and M, and which is expanded in detail in Bernhard et al. (2012). The associated uncertainty stems from the fact that the shape of the solar spectrum changes as a function of solar zenith angle (θ_s) and environmental factors. This problem is addressed during data processing by multiplying conversion factors—used to convert measurements from 10 nm to 1 nm bandpass—with correction factors.

The magnitude of the correction factors and the resulting uncertainty were estimated by comparing conversion factors calculated for different radiometric quantities (E_s, L_i, and L_W), solar zenith angles ($\theta_s = 40°$ and $80°$), cloud conditions (clear sky and overcast), and chlorophyll concentrations. The latter is determined using a Case-1 model with [Chl a]$= 0.045$ mg m^{-3} as described by Morel and Maritorena (2001). The results of these calculations are shown in Fig. J1, which depicts the ratios of the conversion factors determined for various parameter settings to the factor calculated for $E_s(\lambda)$, $\theta_s = 40°$, and clear sky.
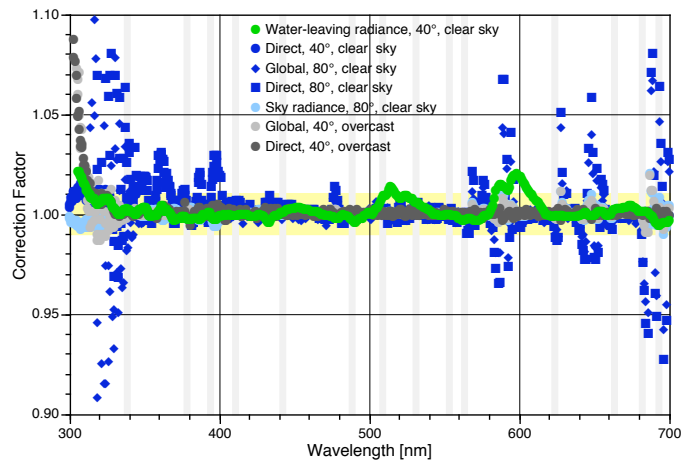
Fig. J1. Correction factors for the conversion of OSPREy EPIC measurements from 10 nm to 1 nm bandpass. The results are shown for widely diverse set of situations (shown with separate symbols as listed at the top of the plot). OSPREy wavebands are indicated by the gray vertical lines; the horizontal yellow band denotes a $\pm 1\%$ variation with respect to a correction factor of 1.00.

The correction factors in Fig. J1 are usually smaller than 0.5% for most channels, confirming that measurements with 10 nm bandpass are suitable for accurately determining radiometric quantities for a 1 nm bandpass. Exceptions include wavelengths below 340 nm, where absorption by ozone has to be considered, and in the vicinity of strong water absorption (e.g., between 590–600 nm). The latter is of minor importance, because OSPREy wavelengths were chosen such that interference

S.B. Hooker, G. Bernhard, J.H. Morrow, C.R. Booth, T. Comer, R. Lind, and V. Quang

with water absorption is minimal. Differences for $L_W(\lambda)$ (green circles in Fig. J1) are typically smaller than 0.5%, except at 510 and 589 nm, where the total value of the correction factor is as high as 1.015, because of the large spectral change of $L_W(\lambda)$ at these wavelengths. Because the parameters controlling the total value of correction factors are well known, the uncertainty of a correction factor is assumed to be 10% of the total value, which equates to less than 0.5% at all wavelengths under consideration.

Nonlinearity is mostly a consequence of gain changes (OS-PREy EPIC sensors have three gain stages) combined with offset drifts. Uncertainties caused by offset drifts are minimized in the OSPREy radiometers through the use of temperature stabilization and automated nighttime offset measurements—so-called *dark* measurements (which are usually taken with the caps on the radiometers, but were taken here with the radiometers in their stowed position, so the influence of ambient light is minimized to the greatest extent possible).

The successful use of *nighttime* darks has already been demonstrated (Hooker 2010), and the only extra work involves some additional quality assessment of the data to ensure no contamination from natural and artificial light sources (e.g., the Moon and navigational lights, respectively). The PRR-810 radiometers are linear to within 1% over their usable dynamic range. The linearity of OSPREy EPIC radiometers was further improved to within approximately 0.5% using test equipment developed as part of the NASA SBIR project titled, "*In Situ* Microradiometers: Smaller, Faster, and Scalable to Hyperspectral" (Contract Number NNG06CA03C).

The uncertainties unique to deriving the principal data product, $L_W(\lambda)$, are independent of the specifications for the radiometers, and the values in Table 2 are adopted from Appendix A. The uncertainty in computing the surface reflectance and anisotropy correction were derived from a sensitivity analysis of the input variables used by the correction methods. Uncertainties due to perturbation from the observation platform, such as tower shading, were assumed to be 25% of the associated correction factor. The influence of wave effects and similar environmental factors was estimated from a statistical analysis of nearly simultaneous above- and in-water measurements of $L_W(\lambda)$.

One source of uncertainty in the calculation of surface reflectance that has not been considered here is polarization. Sky radiance is polarized and the reflectance of radiation from the water surface depends on the polarization state of the incoming radiation. The $L_T(\lambda)$ values will, therefore, depend on the degree of polarization of the sky. The polarization of sky radiance depends in turn on various factors such as aerosol loading, the presence of clouds, and the scattering angle between the Sun and the direction of sky viewing.

While the effect of polarization can be partially corrected using a radiative-transfer modeling approach, an accurate determination is not possible because of the many factors involved. A sensible solution consists of measuring the degree of polarization of skylight directly. The EPIC radiance sensors have a nine-position filter-wheel assembly permitting polarization measurements with the spectrograph. The filter wheel has nine positions (Sect. 8.2), so three components of polarization will be measured.

Appendix K:
Platform-Perturbation Mapping

Hooker and Zibordi (2005b) quantified how significant platform perturbations can be when using an above-water method on an offshore structure, and also showed they are avoidable (or can be minimized) using some simple metrics associated with the sampling protocol. Regardless of the environmental variability, the primary avoidance principle for a sea-viewing sensor mounted on the illuminated side of a platform is that it must be pointed to a spot on the sea surface that is at least as far away (perpendicular to the structure, x), because the platform is high (H). If this rule is followed, the platform perturbation will be negligible, that is, less than the repeatability of so-called *far-field measurements* (defined as those measurements for which $x/H > 1$); whereas, *near-field measurements* ($x/H < 1$) will be contaminated. Although this rule is sufficient for many purposes, such as test deployments, the uncertainty requirements for calibration and validation activities require a detailed platform perturbation mapping.

The principal objective of a platform perturbation study is to determine at what viewing angles and solar geometries will the *surface spot* (sampled by a sea-viewing sensor) not be contaminated with platform perturbations. The surface spot is the cross-sectional area on the sea surface intersected by the FOV of the radiometer pointed at the sea surface. The sea surface is usually perturbed by wind, so the roughness of the surface is a source of oblique wave facets that can reflect light from a variety of directions into the view of the radiometer. The platform can also block light that would normally reach the surface spot. In either case, the farther the surface spot is from the platform, the less likely unwanted perturbations caused by the platform can contaminate the natural light field.

The perturbation analysis is based on the spatial characteristics of a diagnostic variable, r:

$$r(x, \lambda_r) = \frac{L_T(x, \lambda_r)/L_i(\lambda_r)}{\rho(W)}, \tag{K1}$$

where λ_r is a reference wavelength in the NIR domain (e.g., 865 nm). Under *natural* circumstances (i.e., in the absence of platform perturbations) and in Case-1 water conditions, $\rho(W) = L_T(\lambda_r)/L_i(\lambda_r)$, within the accepted variance and provided $\rho(W)$ is given a correct value, and $r(x, \lambda_r) = 1$. Any other reflected radiation added to the sky-reflected radiation leads to an increase in $L_T(x, \lambda_r)$, and $r(x, \lambda_r) > 1$.

The most important aspects of $r(\lambda_r)$ as an analytical variable are as follows:

1. It intrinsically includes the effects of changing solar illumination, because the sea-viewing observations are normalized by the sky radiance; and

2. It is a *severity index*, in the sense that the stronger the artificial increase in $L_T(x, \lambda_r)$, the larger the increase in $r(x, \lambda_r)$, and the magnitude of the departure from unity (or an appropriate reference value) is an estimate of the severity of the contamination.

3. It is completely insensitive to bottom perturbations, because of the high attenuation of NIR wavelengths.

In Case-2 water conditions, or if the water type is close to the threshold of Case-1 and Case-2 conditions, $r(x, \lambda_r)$ is not expected to be unity even at far-field distances, so the last point requires some qualification. The time needed to make a sequence of horizontal displacement system (HDS) measurements

is less than 1 h (on average) and covers 1–20 m or more in sampling distance from the platform. This is with using a movable boom with the sensors at one end from the near field to the far field at a particular solar geometry. In the absence of a source of artificial reflections, $r(x, \lambda_r)$ is expected to remain essentially constant over this time. In other words, if the tower were not present, $r(\lambda_r)$ might not be unity, but it would remain constant over the short time period of a single experiment. Multiple experiments over a variety of solar geometries are needed to map out the perturbation field.

An example platform-perturbation mapping (Hooker et al. 2003) is presented in Fig. K1. The data show far-field observations are not significantly influenced by platform reflections, which lead to positive RPD values, but the near-field data are (shading produces negative RPD values). Near-field reflection contamination was confirmed by a) comparing $L_W(\lambda)$ values from above-water data from the near and far field with an independent set of simultaneous (to within 5 min) in-water observations, and b) above-water normalized water-leaving radiances spanning all of the near field and part of the far field, with one observation in the latter used as the reference in the perturbation analysis. The inset panel in Fig. K1 shows a schematic of the localized (x,y) coordinate system, along with the geometry for the pointing angles with respect to the Sun (β) and the surface spot viewed by the sea-viewing sensor (α). The a–d arc shows the transit of the Sun from early morning to late afternoon, respectively (the concomitant change in the solar zenith angle is not depicted and is also important to reflection contamination). Note the origin of the localized coordinate system (denoted by the intersection of the $+x$ and $+y$ axes) is a point at the northwest corner of the tower within the area associated with a squared-off extension to the platform.
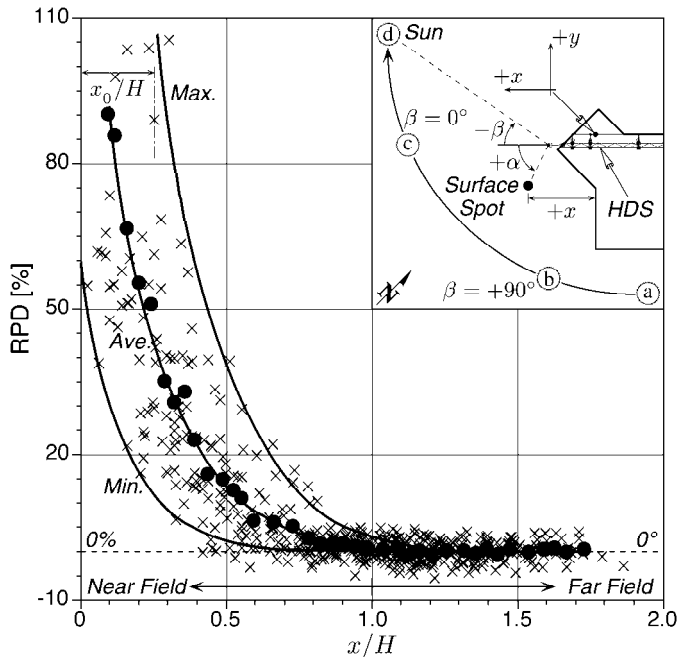

Fig. K1. An example perturbation mapping experiment based on $r(865)$ RPD values (crosses), with their maximum and minimum extents also shown. The bin-averaged values (solid circles and associated curve) as a function of x/H give the principal characterization of the perturbation field.

Appendix L:
The SABSOON Towers

The South Atlantic Bight (SAB) Synoptic Ocean Observing Network (SABSOON) is a good example of the level of sophistication available at some offshore towers, as well as the extent of available partners for enhancing scientific activities. SABSOON was a prototype ocean observatory based on an array of offshore fixed structures that operated from the spring of 1999 to the fall of 2009. During operation, the platforms are part of a U.S. Navy combat flight training range managed by the Naval Surface Warfare Center, Marine Corps Air Station (MCAS), Beaufort Detachment (Beaufort, South Carolina). Through the cooperation of the Beaufort Range Manager, the Skidaway Institute of Oceanography (SkIO) provided access to the towers to make year-round atmospheric and oceanographic observations.

The SABSOON tower array is located about 60–110 km off the Georgia coast (Fig. L1a). The three central towers (M1R1, R2, and M2R6) have onsite power generation from solar panels, wind turbines, and backup diesel generators, with a climate-controlled enclosure. The outer five towers are somewhat smaller, with only solar panels for power generation, and without climate control for the instrumentation enclosure, which is smaller. Additional power generating capability has been added to R8 to ensure sufficient power for SABSOON research.

In the eight-tower array, there are four- and three-legged designs (Fig. L1b). The former (R2, M2R6, M1R1) are larger and equipped with higher-capacity power systems. All towers have a helicopter landing pad (Fig. L1b), a ship docking area (Fig. L1c), and an antenna truss platform for communications antennas, which was made available for scientific instruments (Fig. L1d). The water depth across the range varies from about 25 m (R5 and R7) to 43 m or more (R3 and R8, respectively).

The network supported continuous time series and near-real time data delivery from a variety of sensors. Developmental funds were provided by the National Oceanographic Partnership Program (NOPP) in 1998 (Seim 2000). Scientific investigations operated on a *not-to-interfere* basis with respect to Navy activities, with all installations submitted to the Range Manager for approval. Three towers had meteorological and oceanographic sensors (R2, M2R6, and R8), and a fourth (R4) had only a meteorological package. The ocean sensors included conductivity, temperature, and depth (CTD) sensors, chlorophyll fluorometers, bottom-mounted acoustic doppler current profilers (ADCPs), plus above- and in-water photosynthetically available radiation (PAR) sensors. At the larger R2 and M2R6 platforms, SABSOON was allocated 360 W (48 VDC) from the Navy power system (solar and wind power generation, with diesel generator backup). At R8, the Navy power capacity was considerably lower, and SkIO installed a separate power system (solar panels, wind turbine, liquid propane gas backup generator, batteries, controller) providing 250 W (24 VDC) of power.

Data telemetry bandwidth within the Navy microwave communications system was equivalent to a T1 line, which together with a T1 land line connecting to SkIO provided two-way, real-time communications at 1.472 Mbps. The SABSOON data system operated as a wireless local area network (LAN) with offshore computers being nodes on the SkIO network. For routine operation, most data were logged to offshore computers at 6 min intervals and retrieved hourly. Offshore data logging was used to avoid data loss during microwave communication downtimes. Transportation for servicing the SABSOON tower systems was by helicopter, the SkIO research vessel (R/V *Savannah*), and by smaller vessels operated by GRNMS. The GRNMS program provided considerable logistic support for SABSOON through an agreement with SkIO.

S.B. Hooker, G. Bernhard, J.H. Morrow, C.R. Booth, T. Comer, R. Lind, and V. Quang
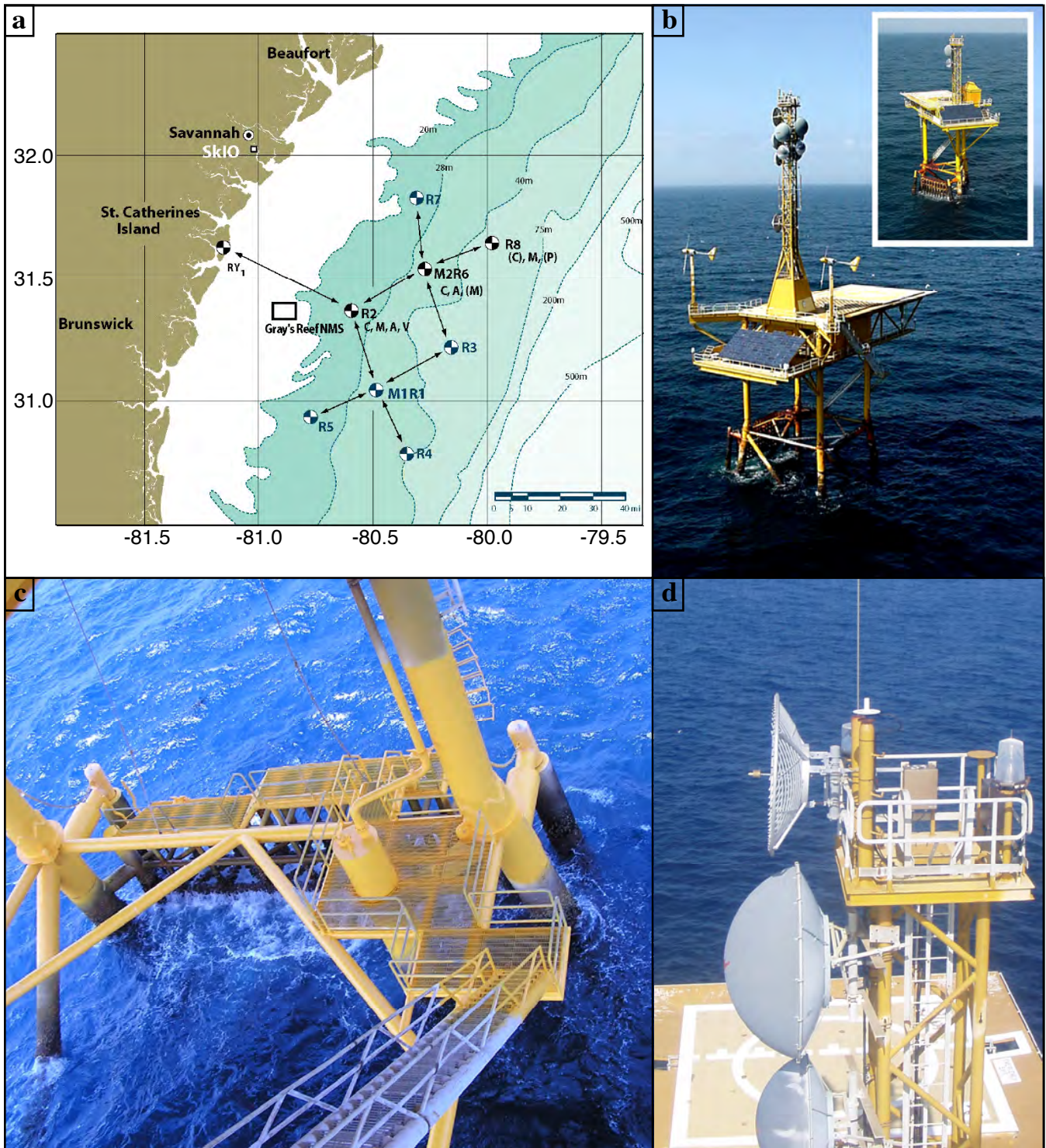
Fig. L1. The SABSOON offshore tower array: **a)** the location of the tower network superimposed on the local bathymetry and with respect to the National Oceanic and Atmospheric Administration (NOAA) Gray's Reef National Marine Sanctuary (GRNMS) site, **b)** the large and small (inset panel) tower designs, **c)** the ship docking facilities at M2R6 (after refurbishment), and **d)** the antenna truss deck at R8 (with the helicopter pad below).

Appendix M:
BSI Quality Assurance Experience

BSI has been operating the UV Spectral Irradiance Monitoring Network (UVSIMN) for the National Science Foundation (NSF) since 1988†. The network was established in 1987 by the NSF Division of Polar Programs in response to serious ozone depletion reported in Antarctica. Seven sites are involved and the instrumentation provides global irradiance measurements between 280–600 nm, and secondary data products, such as, total column ozone, effective albedo, and cloud optical depth. The tasks BSI has undertaken include hardware and software development, oversight of daily operations, data processing, QA and QC of data products, data distribution, documentation, and publication in peer-reviewed journals. The complexity of the instrumentation and the level of QA and QC BSI has developed are good indicators that BSI has the relevant experience for designing, building, and managing the OSPREy system.

Network data are routinely used by the research community for the validation of satellite observations, the verification of models describing radiative transfer through the atmosphere, and the preparation of assessment reports, such as the Scientific Assessments of Ozone Depletion published by the World Meteorological Organization (WMO 2007). Experience gained during almost 20 years of operation will be highly beneficial for OSPREy. This includes familiarity in handling large data volumes, management of automated procedures for data screening, quality control implementation of radiative transfer codes for data correction and interpretation, and data distribution.

One of the more important accomplishments of the UVSIMN activity that BSI is directly responsible for, in terms of the requirements of the OSPREy project, is the quality control plan. The plan consists of a wide diversity of elements executed over significantly different time scales—spanning daily checks to annual activities—which require a large variety of skills and expertise:

- *Automatic quality checks* (every few seconds) in which all spectroradiometers sample ancillary data (such as system temperatures at high frequency) and if these measurements deviate from control limits, remedial action is initiated.

- *Daily checks* wherein the proper functioning of the system is checked by research associates (who also clean the instrument collectors), and measurements of irradiance and wavelength standards are used to determine instrument stability or uncover instrument problems.

- *Weekly data processing and QC* for which raw data are processed, preliminary data are posted, and the following steps are executed: a) review of weekly briefs from the research associates, b) application of preliminary wavelength and irradiance calibration to raw data, c) generation of a quality report and review, d) posting of new data, and e) initiation of remedial action(s) if needed. As an example of the weekly quality review, Fig. M1 shows an automatically generated report comparing instrument parameters measured within the previous seven days with pre-established control limits. Out-of-limit parameters are highlighted in red to facilitate inspection. Further

analysis may initiate corrective action such as adjustment of instrument settings or followup with instrument operators.

- *Biweekly calibrations* wherein the spectroradiometers are calibrated by research associates with standards traceable to the NIST spectral irradiance scale, the calibration data are reviewed during the weekly data processing, and during the austral spring, a UV Bulletin is posted on the aforementioned BSI Web site for the UVSIMN activity.

- *Radiometric intercomparisons* for which data from multi-channel radiometers are compared with data from collocated spectroradiometers several times during the year.

- *Annual activities* wherein the following tasks are conducted: a) training of research associates at BSI; b) visits of network sites by BSI personnel (for end-of-season calibrations; comparison of onsite standards with traveling standards; inspection, maintenance, repair, and upgrade of instruments; and start-of-season calibrations); and c) preparation of final *Version 0* data.

Following a review of the data obtained during the site visit, all solar data recorded between two annual site visits are reprocessed and published using the following procedures: a) review of all calibration scans performed during the last year; b) application of the final wavelength correction to solar data; c) calculation of calibration factors for ancillary sensors; d) QC of final data, which involves a comparison of measured data with target values, comparison of new data with data from previous years, and external (remote sensing) data; e) dissemination of final Version 0 data; f) documentation of QC results in reports; and g) publication of final data on compact disk–read only memory (CD-ROM).

There are also a number of activities that fall into a variety of longer-term accomplishments, which are detailed as follows:

- *Comparison of standards of spectral irradiance* wherein the lamp standards of spectral irradiance used in the UVSIMN, which are traceable to the NIST irradiance scale, are sent out for recalibration at regular intervals. In addition, calibration lamps are compared with standards of the NIST/NOAA Central UV Calibration Facility (CUCF).

- *Participation in intercomparisons* wherein UVSIMN spectroradiometers regularly participate in national and international intercomparisons. Results have been published in peer-reviewed journals and have been used to improve instrumentation, measurement protocols, and data analysis procedures. Figure M2 shows some of the instrument types (installed in the field) involved in the radiometric intercomparisons.

- *Comparison with radiative transfer models* wherein spectral data of the UVSIMN are compared in regular intervals with results of radiative transfer models.

- *Publication of results in scientific journals* wherein data from the UVSIMN are regularly published by either BSI personnel or researchers not associated with BSI.

- *Re-evaluation of network data*, because Version 0 data of the UVSIMN exhibits some known and well-documented systematic errors, a new data version (denoted *Version 2*), is being produced.

---

† Detailed information regarding UVSIMN and the type of work BSI does for this activity is available at the following Web site: `www.biospherical.com/nsf/`.

S.B. Hooker, G. Bernhard, J.H. Morrow, C.R. Booth, T. Comer, R. Lind, and V. Quang

	PALMER		SOUTH POLE		USHUAIA		SAN DIEGO		BARROW	
DB1: Max PMT	427.75	< 950	612.32	< 950	608.71	< 950	778.74	< 950	519.48	< 950
DB5: Max PMT	269.54	< 950	400.04	< 950	524.04	< 950	790.31	< 950	510.86	< 950
DB1: Min Dark current	.38184	> 0.03	.17628	> 0.03	.53803	> 0.03	.21771	> 0.03	.23559	> 0.03
DB1: Lowest λ-offset	-.0645	> -3	-.2119	> -3	-.0132	> -3	-.0877	> -3	-.2908	> -3
DB1: Highest λ-offset	-.0502	< 3	-.1981	< 3	-.0045	< 3	-.0635	< 3	-.2600	< 3
DB1: Max λ-offset change	.01138	-0.2<X<0.2	.00522	-0.2<X<0.2	.008	-0.2<X<0.2	.00637	-0.2<X<0.2	.02185	-0.2<X<0.2
DB1: Max-Min λ-pot	.88040	< 0.3	103.70	< 0.3	.19229	< 0.3	.13259	< 0.3	.19979	< 0.3
DB1: Lowest bandwidth	.74535	> 0.71	.70698	> 0.71	.75977	> 0.75	.91153	> 0.9	.77687	> 0.73
DB1: Highest bandwidth	.75536	< 0.75	.72690	< 0.75	.76608	< 0.785	.93530	< 0.94	.78890	< 0.76
DB2: StDev Noise @285	.00055	< 0.002	.00039	< 0.002	.00084	< 0.002	.00061	< 0.003	.00049	< 0.002
DB5: Lowest DMM	.06513	> 0.065	.06496	> 0.0649	.06503	> 0.0649	.06503	> 0.0649	.06498	> 0.0649
DB5: Highest DMM	.06515	< 0.0652	.06496	< 0.0651	.06506	< 0.0651	.06503	< 0.0651	.06501	< 0.0651
DB1: Max-Min Ground	.00011	< 0.0003	.00007	< 0.0003	.0001	< 0.0003	.00003	< 0.0003	.00005	< 0.0003
DB1: Change HV?	-		-		-		-		-	
DB1: Avg MonoT	32.716	31.5<X<33.5	32.848	31<X<33.5	33.250	32.5<X<34.5	32.522	32.5<X<34	33.407	32.5<X<34.5
DB1: Max-Min Mono T	.36621	< 0.8	.66583	< 0.8	.27002	< 0.8	.34771	< 1.2	.28482	< 0.8
DB5: Avg MonoT	32.768	31.5<X<33.5	32.835	31<X<33.5	33.383	32.5<X<34.5	32.465	32.5<X<34	33.469	32.5<X<34.5
DB5: Max-Min Mono T	.15906	< 0.8	.01109	< 0.8	.14056	< 0.8	.19976	< 0.8	.17755	< 0.8
DB1: Avg UpperBox T	27.995	26.5<X<31	24.908	23<X<31	29.738	26.5<X<31	28.109	26.5<X<31.5	28.348	26.5<X<31
DB1: Max-Min UpperBox	2.0566	< 2	5.1010	< 2	1.6904	< 2	2.4118	< 3.5	1.6830	< 3.5
DB5: Avg UpperBox T	28.853	26.5<X<31	24.954	23<X<31	30.488	26.5<X<31	29.825	26.5<X<31.5	30.378	26.5<X<31
DB5: Max-Min UpperBox	.13095	< 2	2.8464	< 2	.25006	< 2	.25708	< 2	1.1220	< 2
DB1: Avg LowerBox T	30.596	26<X<32	29.012	23<X<30	28.939	26<X<32	28.233	26.5<X<31.5	26.743	26<X<32
DB1: Max-Min LowerBox	2.5708	< 3	3.3772	< 3	5.2268	< 3	1.4981	< 3	2.4783	< 4.5
DB5: Avg LowerBox T	31.556	25<X<32	29.002	23<X<30	27.618	25<X<32	28.467	25<X<32	26.787	25<X<32
DB5: Max-Min LowerBox	.82859	< 3	.11837	< 3	1.2206	< 3	.58446	< 3	2.0715	< 3

Fig. M1. Weekly quality control chart of NSF UVSIMN. Measured instrument parameters from five network sites are compared with pre-set control limits to identify instrument and data problems. Out-of-limit parameters are highlighted in red.
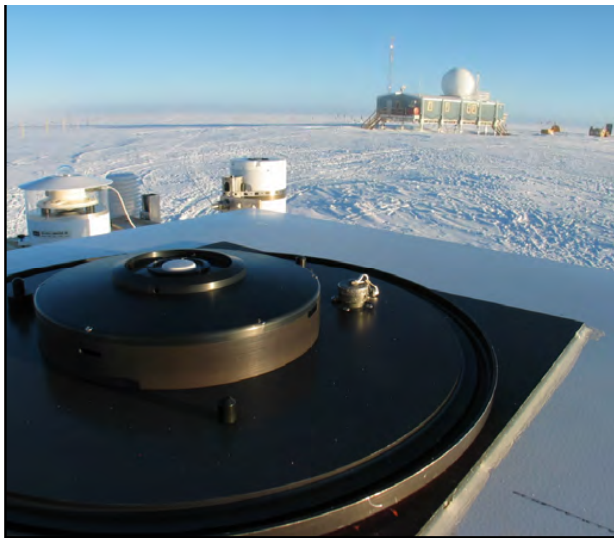

Fig. M2. The NSF UVSIMN network site at *Summit Station*, located in the center of the Greenland ice sheet. Shown in the foreground is the collector of a BSI SUV-150B scanning spectroradiometer. Farther back are a GUV-511 UV filter radiometer and a PSP pyranometer. The system was installed in 2004 and is remotely controlled by BSI.

Since 1988, BSI has collaborated with the Los Angeles Department of Water and Power (LADWP) to design and deploy a series of water-quality monitoring systems in five reservoirs (Morrow et al. 2000). These systems represent the earliest industrial application of the bio-optical instruments that were originally designed for oceanographic and remote sensing applications. Matched pairs of sensors located on a minimal-shadow mooring provide *in situ* measurements of spectral downward irradiance and upwelling radiance at six SeaWiFS satellite bands. A radiometrically matching reference provides incident irradiance at the outlet tower of each reservoir. Multiple algorithms using derived reflectance, diffuse attenuation, and solar-stimulated fluorescence allows for calculation of Chl_a concentration over a range of 0.02–$40.0\,mg\,m^{-3}$, and a nephelometric turbidity equivalent based on PAR. Uncontrolled algal growth can quickly compromise the taste, odor, and appearance of impounded water.

The monitoring systems were designed to provide reservoir managers with the daily data needed to recognize and react to incipient algal blooms before water quality is degraded. In particular, water operators can control the delivery of disinfection agents to the water system, minimizing disinfection by-products, and potential taste and odor, at minimal expense. The near-real time (30 min averages) reporting of data supports early intervention of nuisance algal blooms and complements grab sample data acquired during manned reservoir surveys. High temporal resolution data also provides useful information on short time scale processes such as algal blooms, thermal destratification, and rain runoff events.

1. *What are the basic differences between OXR and EMR sensors?*

   An OXR is designed and built to be a transfer radiometer that is used exclusively in the laboratory and not in the field, whereas EMR sensors are designed and built for field work (Sect. 1.3). Consequently, an OXL (radiance) sensor does not have a filter-wheel assembly, because it does not need to view bright targets, and it does not have an integrated camera, because it does not need to track a target or be autonomously pointed. If there were an application wherein an OXL needed to track a target, it is compatible with the tracker used in the OSPREy activity (FAQ 24).

   In addition, the spectrograph fiber in an OXL (radiance) radiometer is not placed outside the microradiometer cluster as it is in an EML (radiance) sensor. Instead, one microradiometer is removed and the spectrograph fiber in an OXL sensor is fed through the missing microradiometer position, which is the same as is done with all OXE and EME sensors. This means that the interior design of OXE and OXL sensors are more similar than the interior design of EME and EML sensors. Both OXE and OXL sensors have a maximum of 18 microradiometers, whereas EML sensors have a maximum of 19 microradiometers and EME sensors have a maximum of 18 microradiometers (like the OXR sensors).

   In summary, OXL and EML sensors are rather different (and have different wavelength configurations as shown in Table 13), whereas OXE and EME sensors are more similar. The basic difference between the two types of irradiance instruments is the color: the OXE sensor is black for darkroom use and the EME sensor is white for outdoor use.

2. *Why is the so-called "operational" OSPREy system (Fig. 44d), which has redundant radiance and irradiance instruments (i.e., two dyads), an advantage?*

   The presence of duplicate (or redundant) sensors in an operational system (Sects. 1.2 and 8.6) allows for synchronous and asynchronous sampling with those sensors, which has several advantages:

   - With two radiance sensors, both the sea surface and sky can be measured simultaneously. This synchronous sampling eliminates any temporal evolution in one or the other, which can occur if measured sequentially.

   - With two irradiance sensors fitted with shadowband accessories, one can be measuring the global solar irradiance while the other measures the sky irradiance. This asynchronous sampling allows the global irradiance to be available for normalizing measurements subjected to small (linear) changes in atmospheric conditions.

   - Each pair of instruments can be used to measure the same source simultaneously. This synchronous sampling provides the opportunity to detect calibration drift and other factors that degrade the measurements.

   - The independence of two systems—including data acquisition computer, GPS, and tracker—provides increased resistance to hardware failure. This is particularly important because the system is designed to be operated in harsh environments with minimal support personnel.

   - Two independent systems allows one to be removed for calibration, while the other maintains the measurement time series. When the first instrument is returned, its calibration can be compared with the instrument that remained on station. This is particularly important when the remoteness of the location means extended shipping times for calibration.

3. *What kind of maintenance is required for an OSPREy system?*

   Ideal radiometric measurements depend on invariance in the properties of the radiometer. The least constant component is normally the optical aperture with the external environment, which in an OSPREy system is the quartz window on the radiance sensor and the cosine collector on the irradiance sensor. The shadowband accessory, if run on a regular cycle, is a bird deterrent. The outer layer of the cosine collector is made from PTFE (Teflon), which greatly resists the adherence of deposits, and the surrounding surfaces are designed to shed particles when washed by rainwater (Fig. 14). The radiance aperture is also subject to the deposition of contaminants, which can increase scattering at this surface, thereby degrading solar tracking-dependent measurements. Unlike an irradiance sensor, a radiance sensor is mounted on a tracker and can be stowed in a downward-pointing orientation to minimize the opportunities for deposition.

   In all cases, dust, grime, and salt spray deposits gradually build up and degrade the signal at the affected aperture. The rate of this reduction depends on the environment in which the OSPREy system is installed, and the impact differs depending on the data product being generated. Although an OSPREy system is designed to be continuously operated remotely, periodic manual cleanings of the radiance windows and irradiance collectors is required.

   The interval between cleaning is highly dependent on the deployment site; ideally, daily cleaning is advised. Much less frequent cleaning, i.e., weekly or even monthly, may be acceptable in some conditions or for some science objectives. A cleaning cycle requires approximately 10 min time per sensor, and should be done

only by someone who is properly trained. As an aid to determining the need for cleaning, a remote camera system can be deployed to allow inspection of the sensor windows and collectors. Current testing of such a system indicates it is helpful in examining radiance windows when the radiometer is pointed at the remote camera.

If the remote camera can be mounted above the plane of the irradiance radiometers, the collectors can be inspected using the camera. In particular, large contamination events from animals (specifically birds) are also easily detected. The remote camera is very helpful in verifying operation of other OSPREy system components, and can be used to diagnosis other mechanical issues or can function as an aid to allow a remotely located engineer to assist personnel servicing the installation.

4. *What are the types and recommended frequencies of radiometer calibrations for an OSPREy system?*

The types and frequencies of calibrations for an OSPREy system depend on the sampling and research objectives established for the system. For example, if the system is used for algorithm validation, research applications, or water-mass monitoring, a *standard* calibration is advised annually or every six months, depending on the desired quality level for the measurements. This recommendation is based on a weekly-to-monthly cleaning regimen.

For vicarious calibration systems, the recommendation is a combination of standard and a so-called *characterization* calibration. If the vicarious calibration work involves significant sun photometry components, a *solar* (Langley) calibration is available and is anticipated in combination with the standard and characterization calibrations. The frequency of the combination of calibration types is expected to be discerned from monitoring with a portable source, e.g., PURLS (Sect. 1.5.4), plus daily sensor intracomparisons using the spectrograph and the microradiometers in each EMR sensor and intercomparisons using at least a Minimal System (Fig. 44).

All calibrations include a thorough inspection of the instrument, cleaning, and any required software updates. Longer servicing intervals are also anticipated. The specific concern here is that the risk associated with intrusive maintenance may outweigh the reward when it comes to disassembling and reassembling the seals on a properly functioning and stable unit. For example, the replacement of most O-rings is presently scheduled for a 3–5 yr interval, but only experience with how EMR sensors age, which is presently unknown, will determine if that interval is appropriate.

A standard calibration for irradiance instruments is performed on the irradiance bench and a radiance calibration is done on the radiance bench (Chap. 6). These calibrations should be done at least annually, and more frequently if intercomparisons with other instruments (if applicable) indicate a problem. It is not necessary to perform the more elaborate irradiance calibration of radiance radiometers annually, so this calibration is not considered part of the standard calibration. For example, if the responsivity of a particular detector changed by 2%, both the signal obtained from the radiance and irradiance calibration of that instrument should change by 2%. Consequently, the irradiance calibration could be tied to the radiance calibration, which is much easier to perform.

A solar calibration is performed following the Langley method, and is part of the protocol to track instrument stability. The advantage of this method is that the instruments can stay in place at the deployment site and do not have to be brought back to the BSI calibration laboratory. The problem is that the uncertainty of Langley calibrations at a marine site with marine aerosols is comparatively large. Consequently, changes in the calibration at the 1% level is hard to detect. Significant problems (e.g., a defective channel) can be readily discovered, however.

A comprehensive calibration involves the following:

- Determination of spectral responsivity functions of filter channels;

- Radiance optical bench calibration of EML (radiance) sensors;

- Irradiance calibration of EML (radiance) sensors using an x–z stage and determination of filter transmission function;

- Spectrograph slit function, including determination of stray light correction matrix;

- Determination of the Mueller matrix for polarimetry;

- Irradiance optical bench calibration of EME (irradiance) sensors;

- Angular response characterization (FVA of radiance optics or cosine response of irradiance collector);

- Linearity characterization of spectrograph component;

- Wavelength-to-pixel mapping of spectrograph component; and

- Assembly and QC of all calibration files and parameters.

Changes in many of these instrument parameters, e.g., the angular response and the slit function, are less

likely. Consequently, all characterizations that are part of the characterization calibration are anticipated to be done every 2–3 yr. More complete details about BSI calibrations are available in Bernhard et al. (2012).

5. *How can the broad sampling capability of an OSPREy system—that is the pointing and tracking associated with viewing the sea surface, the sky, the Sun, and the Moon—be achieved with a less costly configuration?*

There are several ways to reduce the cost of an OS-PREy system, but still exploit the unique capabilities of autonomous sampling that OSPREy systems offer. Some possibilities are only applicable to systems with redundant sampling opportunities, so not all options are available for all system configurations. From that larger perspective, cost savings are available as follows:

- The number of microradiometers in each sensor can be reduced to the minimum required.

- With respect to a maximal perspective wherein two irradiance sensors are used to cover the full spectral range that OSPREy is capable of (Fig. 44c), the number of irradiance sensors can be reduced to one, while maintaining a broad UV-SWIR spectral coverage, as long as the compromise in accuracy is acceptable.

- Redundant sensors in the system can be removed, as long as the resulting increase in risk is acceptable.

- If hyperspectral observations are not required, a custom instrument patterned after the EMR can be built without the spectrograph or filter wheel (which also removes the present implementation of polarimetric measurements). Alternatively, XTRA sensors (Morrow et al. 2010c) can be used rather than EMR sensors (which removes thermal regulation as well as spectrograph components).

- If the data products associated with the shadow-band accessory are not needed, the shadowband can be eliminated.

The important point to remember is an OSPREy system can be custom configured in terms of the instrument suite (the number of sensors) and the sensor capabilities (the individual specifications of each sensor).

6. *Why is the spectral range of an EME (irradiance) sensor different from an EML (radiance) sensor?*

EMR sensors are designed and built to function autonomously in the field. Unlike the OXR instruments, which are used in the laboratory, EMR sensors can generally not be capped for the measurement of the dark offsets of both the microradiometers and the spectrograph. Of the two types of dark measurements, the spectrograph dark offsets are the most important, because the spectrograph is more temperature sensitive (Sect. 7.4.5), which is a principal reason why EMR and OXR sensors are thermally regulated.

To solve the dark measurement problem, and to provide other functionalities (e.g., polarization, improved stray-light correction, and bright target viewing), EML (radiance) sensors have a nine-position filter wheel (Figs. 49 and 56) with an opaque disk in one position. The opaque disk position permits the measurement of dark offsets for the spectrograph, although the entire filter-wheel assembly is sufficiently light tight that dark offsets can be measured in the half interval between any two filter positions. The microradiometer darks are acquired during the night when conditions are optimal (e.g., overcast sky), which has been shown to provide sufficient quality measurements over extended periods of time (Hooker 2010). With the tracker, an EML sensor is *stowed* by pointing it towards nadir, which further improves the night darks acquired for radiance sensors.

EME sensors do not have a filter-wheel assembly, so the spectrograph darks must be established using a different technique. Because the atmosphere is opaque below 290 nm, spectrograph measurements spanning 245–290 nm can be used to monitor variations in dark current and correct the data accordingly. This correction is possible because spectrograph testing showed that changes in dark current are nearly independent of the spectrograph pixel, which means that information from the 245–290 nm range can be used to correct measurements in the other UV and visible wavelengths. Consequently, EME sensors have to have a spectrograph with a spectral range below 290 nm (Sect. 8.2.2).

7. *Because OXR sensors are laboratory devices, which can be capped, why were they not equipped with a spectrograph that covered a larger spectral range like their EMR counterparts?*

The shorter wavelength range used in OXR sensors is advantageous to their role as transfer radiometers, because it allows more accurate measurements in the UV where lamp standards have the largest variability and may suffer from emission lines (Sect. 6.7.2). In contrast, the lamp-to-lamp difference at SWIR wavelengths can be approximated with a second-order fit function, so high spectral resolution data are not necessary in this part of the spectral range of OXR sensors.

8. *How do the design (theoretical) wavelength ranges established for EMR and OXR sensors compare with the typical performance values observed during commissioning the new sensors for the OSPREy activity?*

The design specifications for the wavelength ranges used with the four types of radiometers in the OSPREy activity are as follows:

EME 290–1,670 nm;
EML 300–1,670 nm;
OXE 244–1,670 nm; and
OXL 300–1,670 nm.

These end-member values are based on the *combined* specifications of the microradiometer and spectrograph components. For an OSPREy system configuration wherein two irradiance sensors are used to establish a sensor triad (rather than a dyad), e.g., the spectral or maximum systems (Fig. 44c and 44e, respectively), the two wavelength ranges for the irradiance sensors are 290–1,100 nm and 1,000–1,670 nm. The standard diffuser for EME and OXE sensors cover the 244–1,670 nm wavelength range.

The typical performance specifications for the wavelength ranges used with the four types of radiometers in the OSPREy activity are as follows:

    EME 305–1,640 nm;
    EML 320–1,640 nm;
    OXE 305–1,640 nm; and
    OXL 320–1,640 nm.

These end-member values are based on the *typical* specifications of the microradiometer and spectrograph components as experienced in commissioning the first *operational* system in support of ACE and PACE.

The individual microradiometer specifications for the wavelength ranges used with the four types of radiometers in the OSPREy activity are as follows:

    EME 340–1,640 nm;
    EML 340–1,640 nm;
    OXE 340–1,640 nm; and
    OXL 320–875 nm.

These end-member values are based on the *manufacturer's* specifications and all the individual microradiometer wavebands are presented in Table 13.

The individual spectrograph specifications for the wavelength ranges used with the four types of radiometers in the OSPREy activity are as follows:

    EME 245–785 nm (Zeiss/Tec5 MMS UV-VIS II;
    EML 300–1,150 nm (Zeiss/Tec5 MMS1);
    OXE 244–785 nm (Zeiss/Tec5 MMS UV-VIS II; and
    OXL 325–792 nm (Hamamatsu C9407MA).

These end-member values are based on the *manufacturer's* specifications. The OXL was the first sensor built for the OSPREy activity. The Hamamatsu spectrograph was used in the OXL, because at the time the OXL was built alternatives were either not available or were still undergoing testing.

9. *What are the advantages and disadvantages of the microradiometer component of EMR and OXR sensors compared to their spectrograph component?*

Microradiometers offer a larger dynamic range, better SNR, and higher sampling rates than the spectrograph component. The main advantage of the spectrograph is its higher spectral resolution. For EMR sensors, the spectrograph filter-wheel assembly provides the additional advantages of polarization measurements and improved stray-light correction. Spectrograph measurements, however, must be corrected for dark offset drifts, stray light, and nonlinearity. Uncertainties of these corrections make measurements of the spectrograph component in general, less accurate than those of the microradiometer component, particularly nearing the lower and upper ends of the spectral range. By combining the superiorities of microradiometer measurements with the added spectral information obtained from spectrograph measurements, a superior sensor combination is attained compared to either of the individual components alone (Chap. 8). For example, the spectrograph measurements can be vicariously calibrated against the microradiometer measurements (making the former as accurate as the latter), while also providing spectral information in regions of the solar spectrum where absorption by trace gases occurs.

10. *How is the temperature of OXR and EMR sensors maintained?*

There are two heating elements and temperature controllers in OXR and EMR sensors, which are designated "primary" and "secondary." The primary temperature regulation is for the entire housing, so all components benefit, and the secondary regulation is just for the spectrograph. The instrument housing temperature is maintained with a primary heater strip attached to the inner microradiometer sleeve in the main housing (Fig. 3). The secondary heater element is integrated with the spectrograph.

The primary temperature control uses an ultra-low-noise 15 VDC switching power source located in the PCS; the internal electronics and spectrograph secondary temperature control uses a separate 12 VDC power (Fig. 50). Rapidly switching power on and off using a customary PID approach with the heater strip can couple electrical noise into the optical measurements. To preclude any adverse effects, the OXR and EMR primary instrument housing temperature is stabilized using a precision temperature controller operating in an analog PI mode. This approach smoothly adjusts the current to the heater strip without switching, ensuring temperature regulation of the main housing to within 40°C ±0.1°C.

A similar arrangement for a secondary heater element integrated with the spectrograph supports stable temperatures to better than ±0.03 °C. Gradients across the spectrograph component are minimized by thermal insulation, but cannot be completely avoided and have an effect on the dark offset for the spectrograph. Consequently, for the most accurate measurements, it is necessary to measure the spectrograph dark offset several times throughout the day.

11. *Are the spectral characteristics of OXR and EMR sensors fixed or predetermined?*

No, the spectral characteristics of all OXR and EMR sensors are neither fixed nor predetermined. There are, however, size and communications protocol limitations in choosing alternative spectrographs. Zeiss/Tec5 spectrographs are presently being used, although a Hamamatsu spectrograph was selected for the very first instrument that was built, which was the OXL. Consequently, these manufacturers and models that were selected are the easiest to consider for alternatives.

The microradiometer component of OXR and EMR sensors can be populated with whatever filters the researcher desires (recalling that there are cosine response specifications as a function of wavelength), but the cost of the filters are less if they are selected from the existing BSI inventory (the current inventory of filters is available at `http://www.biospherical.com`).

12. *Why do all OXR sensors (OXE and OXL) and the EME sensors have a maximum of 18 microradiometers, whereas EML sensors can have 19 microradiometers?*

OXR sensors are a class of laboratory irradiance (OXE) and radiance (OXL) instruments designed in parallel with the EMR field instruments. The OXR class shares many of the same features and components with their EMR equivalents. The OXE laboratory instrument is functionally identical to the EME field instrument (Chap. 8). The OXE and EME both replace one microradiometer position with the entrance optics of the spectrograph, reducing the microradiometer complement to 18.

An important distinction between an OXL and EML sensor is that the OXL lacks the spectrograph filter-wheel assembly and integrated video camera that are installed in the EML. The OXL replaces one microradiometer position with the entrance optics for the spectrograph, again reducing the microradiometer component to 18. For the EML, the spectrograph is external to the microradiometer cluster, and the maximum number of microradiometers is 19 (Sect. 6.4.2).

13. *What is the advantage of two irradiance sensors (Fig. 44c) with two different cosine responses rather than one covering the combined range of the two (and vice versa)?*

The standard EME (irradiance) radiometer has a cosine response spanning 290–1,670 nm. This allows the wide spectral range needed for next-generation missions (e.g., ACE and PACE) to be satisfied in a single sensor. Although this is a state-of-the-art accomplishment, the cosine error is elevated in the SWIR domain, which might not be acceptable for certain applications. To make sure a highest-quality option is nonetheless available, two optimized cosine collectors can be used, but this requires two sensors (Sect. 8.5).

14. *What are the advantages of using an EML (radiance) sensor as a sun photometer compared to other commercial alternatives?*

An EML sensor has a large dynamic range of 10 decades, a wide spectral range of 290–1,670 nm, and a high data rate for the microradiometers (15 Hz). The large dynamic range allows sky, solar, and lunar measurements across an unprecedented diversity of wavelengths. For the spectrograph, the large dynamic range is achieved by combining the ADC 15 bit dynamic range with the option to change the integration time and use one of two ND filters installed in the filter-wheel assembly, which is in front of the spectrograph fiber. The AOD can also be measured at night using the Moon.

The built-in (or added as a second device on a tracker) video camera allows accurate Sun (Moon) tracking (to better than $\pm 0.1°$) and detection of clouds passing in front of the solar (lunar) disk. The cloud detection can also be accomplished using an EME (irradiance) sensor, if it is part of the OSPREy system configuration, which it is except for the starter system (Fig. 44a).

Commercially available sun photometers are typically less capable by having one or more deficiencies with respect to the following (Table 3):

a) Less than 10 fixed-wavelength channels, whereas EML sensors have 19 fixed-wavelength channels;

b) No hyperspectral capability, whereas EML sensors have a 256-pixel spectrograph;

c) No thermal regulation, whereas EML sensors are thermally regulated;

d) No integrated camera, whereas EML sensors have an integrated camera and can be used in conjunction with other camera configurations;

e) No easily accommodated polarization measurements across a wide spectral range, whereas EML sensors use a filter-wheel assembly to provide hyperspectral polarization observations for three axes of polarization; and

f) No sensor networking (i.e., the instruments are standalone units), whereas EML sensors can be part of a network or system configuration (Fig. 44) and the tracker allows a second device to be pointed with the EML instrument.

15. *From the perspective of using an EML (radiance) sensor as a sun photometer, why is the FVA 2.5° with a 0.7° slope angle?*

An EML radiometer is designed for multiple purposes, one of which is to function as a sun photometer. When viewing the Sun, the instrument should ideally only see the solar disk, and not any scattered radiation originating from points close to the Sun, i.e., the aureole. From

this perspective alone, the FOV should be as small as possible, but this must be considered with respect to the angular size of the Sun when viewed from Earth (0.527–0.545°, over the course of the year), compensation for the pointing accuracies of the sun tracker, and compliance with the recommendations and specifications for sun photometers as issued by cognizant authorities (e.g., the WMO). The FVA of an EML radiometer must also be large enough to allow accurate measurements of all sources considered by the OS-PREy activity, including low-light applications (e.g., the Moon, which has a size when viewed from Earth that is similar to the Sun).

Given these considerations, the specifications of most COTS sun photometers (Table 3), and the multipurpose measurement objectives of EML (radiance) sensors (sea, sky, Sun, and Moon), the FOV for an EML sensor was set to 2.5° FVA (Sect. 4.2). One advantage regarding this specification is there are many sun photometers that use this specification (Table 3), although the CE-318 sun photometer used with AERONET has a 1.2° FVA.

As part of the work the OSPREy team did in selecting the FVA for EMR and OXR sensors, a careful investigation of the resulting increases in uncertainty in using a 2.5° versus 1.2° FVA was undertaken and the following conclusions were obtained:

- For a 1.2° FVA, the measurement uncertainty is smaller than 0.005 optical depth units for an AOD value of up to 4.4.

- For a 2.5° FVA, the measurement uncertainty is smaller than 0.005 optical depth units for an AOD value of up to 2.2.

- In most environments, the AOD is not larger than 1.0, thus a 2.5° FVA is sufficiently small to calculate AOD with good accuracy for all but the most extreme environments (e.g., Mexico City).

- The effect of wavelength on the AOD uncertainty is small.

- Because the systematic error resulting from the finite FOV can be calculated, direct measurements with the EML (radiance) sensor can be corrected for this error before the AOD is retrieved. Such a correction would increase the complexity of the AOD retrieval, but it is a tractable calculation.

16. *What data products are supported by EMR (radiance and irradiance) sensors, and why is it advantageous to derive one data product with more than one instrument?*

Data products that can be retrieved by EMR sensors are summarized in Table 17. Some data products can

be derived from measurements of more than one sensor, providing redundancy in case of equipment failure and options for intercalibration. The latter is effective in detecting sensor drift and mechanical problems in the tracking mechanisms. The ability to derive one data product from two different methods (e.g., AOD can be retrieved from measurements of the EML (radiance) sensor pointing at the Sun and from an EME (irradiance) sensor equipped with a shadowband accessory) provides intercomparison opportunities, thereby establishing additional confidence in the results and an opportunity to detect problems as they occur, rather than long after (the chance that two sensors would malfunction or degrade in exactly the same manner simultaneously is remote).

17. *What OSPREy configuration can be used to replace a SeaPRISM unit?*

The simplest OSPREy configuration is the so-called *Starter System* (Sect. 8.3), which uses a single radiance sensor to provide a starting point for automated above-water radiometry or an advanced replacement for a SeaPRISM unit (Fig. 44a). With respect to the latter, a SeaPRISM unit is not hyperspectral, has many fewer fixed-wavelength channels (eight), does not have a video camera, and cannot measure channels simultaneously. In addition, any polarization capability reduces the number of unpolarized channels, and the tracking ability of a SeaPRISM unit does not support two devices at once.

The starter system is envisioned as a low-cost entry system, which can be incrementally improved as resources or science objectives evolve. For example, a single radiance sensor can be used as an algorithm validation system or a monitoring device, for atmospheric, terrestrial, and oceanic applications. An even lower cost, and functionally more equivalent, SeaPRISM replacement can be constructed using an XTRA sensor and a tracker.

18. *Are radiance polarization measurements restricted to the EML (radiance) spectrograph?*

No, individual microradiometers can be fitted with glass polarization filters. The disadvantage of this approach is if multiple axes of polarization need to be measured, then the number of microradiometers needed to accomplish the task is rather high, leaving fewer and fewer unpolarized channels for those measurements. Because Moxtek filters are too large and cannot be cut to fit microradiometer fore optics, the most efficient way to obtain high-quality polarized data is with the combination of using the spectrograph and filter-wheel assembly.

A SeaPRISM replacement using an XTRA sensor with some polarization capabilities can be built by assigning 10 microradiometers for unpolarized observations

(SeaPRISM units have 8 wavelengths), and then having three wavelengths with three polarization axes each (for a subtotal of 9 microradiometers used for polarization measurements, plus 10 making unpolarized observations, for a grand total of 19 microradiometers).

19. *Can an OXR instrument be used in the field?*

Yes, but there are limitations in what measurements can be made with an OXL (radiance) sensor. Because an OXL instrument does not have a filter-wheel assembly, there are no ND filters for the spectrograph, so it saturates if pointed at a very bright target (e.g., the Sun). OXL sensors do not have an integrated camera, which compromises the built-in capability to track, but a camera can be mounted on a tracker to provide this missing capability.

There are, however, almost no limitations for OXE (irradiance) sensors. The only problem is that an OXE is black and may overheat in direct sunlight. If it is necessary to use an OXE outside, this problem can be mitigated by wrapping the instrument housing with reflective material (e.g., aluminum foil), which has been demonstrated to be effective.

20. *Can an OSPREy system be used for terrestrial applications?*

Yes, an OSPREy system appropriately mounted (e.g., perhaps on a tower) to view terrestrial targets can be autonomously pointed to make appropriate radiance and irradiance measurements to produce a reflectance for terrestrial applications (Chap. 5). The advantage of the OSPREy system is the excellent pointing accuracy permits measurements at multiple nadir and azimuth angles, thereby providing the opportunity for a more complete description of the BRDF of the target.

21. *Can an EMR (radiance or irradiance) sensor be used as a transfer radiometer?*

Yes, because for lamp transfers, the radiometer only has to be stable over the period of the experiment (typically hours to days) and EMR sensors are stable over a longer time period. The capabilities of an EMR sensor as a transfer radiometer are best retained over time if the radiometer is used exclusively in the laboratory and not subjected to the additional stresses of repeated transportation, more extreme environmental cycling, harsh weather, etc. In fact, there is no reason why an OXR sensor should be more stable than an EMR sensor, if both are kept in the laboratory.

One difficulty with an EML (radiance) sensor is the physical separation of the spectrograph outside the cluster of microradiometers, so the spectrograph cannot view the same spot on the target as the microradiometers. This problem requires two separate measurement activities whereby the instrument has to be moved in one measurement sequence, so the same target registration is achieved in both measurements. The OXL sensor does not have this difficulty.

22. *Can the wavelength filters used with the microradiometers in OXR and EMR sensors be changed?*

Yes, the microradiometers in both OXR and EMR sensors can have the filters in the fore optics changed (Fig. 4). One of the advantages of instruments built with microradiometers is this procedure is greatly simplified in comparison to legacy radiometers.

23. *Can OXR and EMR sensors be built with microradiometer clusters that are not fully populated (i.e., less than 18 or 19 microradiometers, depending on the sensor type), and then be upgraded later?*

Yes, both OXR and EMR sensors can be cost effectively built with as few as eight microradiometers; a fewer number of microradiometers would be a custom configuration. Figure 6 (right) shows a full complement of 19 microradiometers, which plug in as whole subunits, so reducing the number installed is trivial at the construction stage. The number of microradiometers can be increased at any time up to the allowed maximum for the radiance or irradiance sensor type (FAQ 1). One of the advantages of sensors built with microradiometers is they are rather modular and this procedure is comparatively easy to accomplish (especially with respect to legacy sensors).

24. *Can an OXL (radiance) instrument be used on a tracker even though it does not have an integrated camera?*

Yes, as long as an appropriate camera is available. The tracker used in the OSPREy activity (the PTU-D300) supports the mounting of devices on both sides of the pedestal (Chap. 5). This means an OXL radiometer can be mounted on one side and an appropriate camera on the other. The OSPREy data acquisition and control software supports this configuration for having the instrument track a target.

25. *What is the advantage of the video camera when using the tracker?*

The angular variation when tracking with the video camera is about $\pm 0.03°$, although refinements to the algorithm could theoretically improve this to $\pm 0.02°$. When using the ephemeris algorithm alone (no video camera, and no adjustments as described in Chap. 5 and Fig. 22) an accuracy of $\pm 0.2°$ is achievable, as long as the tracker is perfectly level and the zenith and azimuth offsets are applied without error. In practice, $\pm 0.3°$ is more realistic. So the camera that is currently integrated into EML sensors improves the tracking accuracy by about an order of magnitude.

26. *What are the advantages of being able to mount two devices on a tracker?*

One advantage is unique to the application of viewing the sky and sea surface to derive the water-leaving radiance. For this measurement, the sky- and sea-viewing radiometers use fixed-angle offsets with respect to zenith and nadir (e.g., 40°). This means a single tracker can be used to point the two fixed-angle radiometers azimuthally with respect to the Sun (usually 90° or 135° away from the Sun plane).

Another opportunity is to mount a camera in the second position and point it in accordance with how a radiometer mounted in the first position is pointed. This is an advantage if the radiometer does not have an integral camera or if the integrated camera is configured for viewing an alternative target. For example, the integrated camera in EML sensors are configured for viewing the Sun and have an ND filter. This makes the camera difficult to use when viewing the Moon, so a second camera mounted on the tracker can facilitate this problem.

27. *Why does an EML (radiance) sensor have a shroud?*

As noted in Sect. 4.2 (and FAQ 15), when viewing the Sun, an EML sensor should ideally only see the solar disk, and not any scattered radiation originating from points close to the Sun, i.e., the aureole. The CE-318 sun photometer used by AERONET has a 1.2° FVA, so the effect of the aureole is necessarily smaller than for an EML sensor (2.5° FVA). In the direct viewing of the Sun, there is no mitigation that can be applied to overcome the larger FVA of an EML sensor, which was a compromise value selected to satisfy the multipurpose sampling objectives of OSPREy systems. There is another aspect to the aureole problem, however, that can be mitigated.

The other issue is the effect of direct sunlight when looking at the sky. Any contamination on the front window scatters direct sunlight on the detector when pointing at the sky, and this is an important source of uncertainty. The problem is greater for an EML (radiance) sensor than a CE-318, because the front window of the former is close to the top of the instrument. In contrast, the Gershun tube of the CE-318 extends well beyond the front window. Consequently, a shroud is mounted at the front of the EML (radiance) sensor to shade the window from this contamination when viewing the sky (Sect. 4.5).

28. *What is the advantage of the BioSHADE (shadowband) accessory?*

The shadowband accessory (App. E) allows the measurement of the diffuse (sky) irradiance, which complements the measurement of global irradiance provided by the EME (irradiance) radiometer (Fig. 45). From the two components, the direct irradiance can be calculated, which in turn allows the retrieval of AOD, aerosol size distribution, and calibration of the sensor from the Langley technique. Direct irradiance measurements and related data products can be compared with similar data products obtained when the EML (radiance) sensor views the Sun.

29. *What is a NEMA 4X rating and why is it used in an OSPREy system?*

NEMA 4 enclosures are specified for use in applications where an occasional wash down of the enclosure occurs or where exposure to pressurized water is possible. NEMA 4 enclosures have doors with gasket seals, and the door is clamped for maximum sealing. The 4X rating specifies the use of stainless steel or plastic (noncorrosive materials) for all exterior enclosure components, and are typically used in harsh environments (e.g., the marine environment). NEMA 4X enclosures are used with the OSPREy system, specifically the PCS unit, to ensure proper protection of PCS components against the harsh marine environment (Sect. 8.2.4).

GLOSSARY

AC	Alternate Current
ACE	Aerosol-Cloud-Ecosystems
ACM	Archive and Communications Master
ADC	Analog-to-Digital Converter
ADCP	Acoustic Doppler Current Profiler
AERONET	Aerosol Robotic Network
AGM	Absorbent Glass Matt
AOD	Aerosol Optical Depth
AOPs	Apparent Optical Properties
ASCII	American Standard Code for Information Interchange
BioSHADE	Biospherical Shadowband Accessory for Diffuse Irradiance
BioSORS	Biospherical Surface Ocean Reflectance System
BOUSSOLE	*Bouée pour l'acquisition de Séries Optiques à Long Terme*
BRDF	Bidirectional Reflectance Distribution Function
BSI	Biospherical Instruments Inc.
CALIPSO	Cloud-Aerosol Lidar and Infrared Pathfinder Satellite Observations
CCA	Climate-Centric Architecture
CCD	Charge-Coupled Device
CDOM	Colored Dissolved Organic Matter
CDR	Climate-quality Data Records
CD-ROM	Compact Disc-Read Only Memory
CMOS	Complementary Metal Oxide Semiconductor
C-OPS	Compact Optical Profiling System
COTS	Commercial-Off-The-Shelf
CTD	Conductivity, Temperature, And Depth
CUCF	Central UV Calibration Facility
CZCS	Coastal Zone Color Scanner

DC   Direct Current

DIN   *Deutsches Institut für Normung* (German Institute for Standardization)

DOT   Department of Transportation (US)

DXW   Not an acronym, but a lamp code.

ENVISAT   Environmental Satellite

EME   EPIC Multitarget Irradiance (radiometer)

EML   EPIC Multitarget Radiance (radiometer)

EMR   EPIC Multitarget Radiometer

EOS   Earth Observing System

EPIC   Enhanced Performance Instrument Class

ESA   European Space Agency

ESRL   Earth System Research Laboratory

ETS   Extraterrestrial Spectrum

FAD   Fish Attraction Device

FAQ   Frequently Asked Question

FASCAL   Facility For Spectroradiometric Calibrations

FEL   Not an acronym, but a lamp code.

FLIR   Not an acronym, but part of the name of FLIR Motion Control Systems, Inc.

FMCW   Frequency Modulated Continuous Wave

FOV   Field of View

FVA   Full View Angle

FWHM   Full Width at Half Maximum

GAW   Global Atmosphere Watch

GEO-CAPE   Geostationary Coastal and Air Pollution Events

GMD   Global Monitoring Division

GPS   Global Positioning System

GRNMS   Gray's Reef National Marine Sanctuary

GSFC   Goddard Space Flight Center

GUV   Ground-based Ultraviolet

HDS   Horizontal Displacement System

HEC   Hoffman Engineering Corporation

HPLC   High Performance Liquid Chromatography

HyspIRI   Hyperspectral Infrared Imager

InGaAs   Indium Gallium Arsenide

IOPs   Inherent Optical Properties

IP   Internet Protocol or Ingress Protection if appearing with a numeric value (e.g., IP67)

JGOFS   Joint Global Ocean Flux Study

LADWP   Los Angeles Department of Water and Power

LAN   Local Area Network

LED   Light-Emitting Diode

LOV   *Laboratoire d'Océanographie de Villefranche*

MCAS   Marine Corps Air Station

MERIS   Medium Resolution Imaging Spectrometer

MFRSR   Multi-Filter Rotating Shadowband Radiometers

MMS   Multiple Microradiometer System (from BSI), or Monolithic Miniature-Spectrometer (from Zeiss/Tec5), depending on usage.

MOBY   Marine Optical Buoy

MODIS   Moderate Resolution Imaging Spectroradiometer

MODIS-A   MODIS Aqua platform

MODIS-T   MODIS Terra platform

NAS   National Academy of Sciences

NASA   National Aeronautics and Space Administration

NBS   National Bureau of Standards

ND   Neutral Density

NDS   NRC Decadal Survey

NEI   Noise Equivalent Irradiance

NEMA   National Electrical Manufacturers Association

NER   Noise Equivalent Radiance

NIR   Near Infrared

NIST   National Institute of Standards and Technology

NMOS   Negative Metal Oxide Semiconductor

NOAA   National Oceanic and Atmospheric Administration

NOMAD   NASA Bio-Optical Marine Algorithm Data

NOPP   National Oceanographic Partnership Program

NPOESS   National Polar Orbiting Environmental Satellite System

NPP   NPOESS Preparatory Project

NRC   National Research Council

NSF   National Science Foundation

OBB   Ocean Biology and Biogeochemistry

OD   Optical Depth

OEM   Original Equipment Manufacturer

ORM   Ocean-Surface Reflectance Model

OSPREy   Optical Sensors for Planetary Radiant Energy

OXE   OSPREy Transfer Irradiance (radiometer)

OXL   OSPREy Transfer Radiance (radiometer)

OXR   OSPREy Transfer Radiometer

PACE   Pre-Aerosol, Clouds, and Ocean Ecosystem

PAR   Photosynthetically Available Radiation

PARASOL   Polarization and Anisotropy of Reflectances for Atmospheric Sciences Coupled with Observations from Lidar

PC   Personal Computer

PCS   Power and Component Scheduler

PDA   Photo-Diode Array

PDF   Portable Document Format

PI   Proportional-Integral

PID   Proportional-Integral-Derivative

PlyMBODy   Plymouth Marine Bio-optical Data Buoy

PML   Plymouth Marine Laboratory

PMOD   *Physikalisch-Meteorologisches Observatorium Davos*

pPTFE   Porous PTFE

PRR   Profiling Reflectance Radiometer

PTFE   Polytetrafluoroethylene

PTU   Pan Tilt Unit

PURLS   Portable Universal Radiometer Light Source

PV   Photovoltaic

PWV   Precipitable Water Vapor

Q02   An above-water method formulated using the Morel and Mueller (2002) bidirectional correction.

QA   Quality Assurance

QC   Quality Control

RAID   Redundant Array Of Independent Drives

RAM   Random Access Memory

RPD   Relative Percent Difference

RS   Recommended Standard

RT   Radiative Transfer

R/V   Research Vessel

S01   An above-water method formulated using the Mobley (1999) determination of ρ and including wind effects (Hooker et al. 2003).

S95 An above-water method formulated using the SeaWiFS 1995 revision of the Ocean Optics Protocols.

SAB South Atlantic Bight

SABSOON South Atlantic Bight (SAB) Synoptic Ocean Observing Network

SBIR Small Business Innovation Research

SeaBASS SeaWiFS Bio-Optical Archive and Storage System

SeaPRISM SeaWiFS Photometer Revision for Incident Surface Measurements

SeaWiFS Sea-viewing Wide Field-of-View Sensor

SHALLO Submersible Hydro-optical Applications for Light-Limited Oceanography

SIRCUS Spectral Irradiance and Radiance Responsivity Calibrations using Uniform Sources

SkIO Skidaway Institute of Oceanography

SNR Signal-to-Noise Ratio

SQL Structured Query Language

SQM SeaWiFS Quality Monitor

SSA Single Scattering Albedo

SSD Solid-State Disk

SuBOPS Submersible Biospherical Optical Profiling System

SWIR Short-Wave Infrared

SXR SeaWiFS Transfer Radiometer

TDRSS Tracking and Data Relay Satellite System

TE Thermoelectric

UPS Uninterruptible Power Supply

USB Universal Serial Bus

USDA United States Department of Agriculture

UV Ultraviolet

UV-B Ultraviolet-B

UVSIMN Ultraviolet Spectral Irradiance Monitoring Network

VIIRS Visible and Infrared Imaging Radiometer Suite

VIS Visible

VSAT Very Small Aperture Terminal

WMO World Meteorological Organization

WRC World Radiation Center

XGUV GUV-based Transfer Radiometer

YES Yankee Environmental Systems

Symbols

A The signal amplitude.

$\overleftarrow{A}$ A calibration value signal amplitude.

$\overset{\bullet}{A}$ The night (dark) signal amplitude.

$\overset{\bullet\bullet}{A}$ The ambient or occluded calibration (dark) signal amplitude.

$\overleftarrow{A}$ The background or shutter (dark) signal amplitude.

$\overset{\square}{A}$ The dark signal amplitude that is obtained with a capped sensor.

$\overset{\bullet}{\hat{A}}$ The shadowband night (dark) signal amplitude.

$\overset{\shortparallel}{A}$ An ideal value signal amplitude.

$\overset{=}{A}$ A true value signal amplitude.

$\overset{\bullet\bullet}{\underline{A}}$ The two-gain stage sensor dark signal amplitude.

$\overset{\bullet\bullet\bullet}{\underline{A}}$ The three-gain stage sensor dark signal amplitude.

$\overset{\bullet}{{}_{\circ}A}$ The high gain of a two-gain sensor signal amplitude.

$\overset{}{{}_{\circ}{}^{\bullet}A}$ The low gain of a two-gain sensor signal amplitude.

$\overset{\bullet\circ\circ}{A}$ The high gain of a three-gain sensor signal amplitude.

$\overset{\circ\bullet\circ}{A}$ The medium gain of a three-gain sensor signal amplitude.

$\overset{\circ\circ\bullet}{A}$ The low gain of a three-gain sensor signal amplitude.

$\overset{\square}{\underset{\circ\circ\bullet}{A}}$ The low gain (of a three-gain sensor) signal amplitude obtained with a capped sensor.

$\tilde{A}$ The sky signal amplitude.

$\breve{A}$ The sea signal amplitude.

$\overset{*}{A}$ The solar signal amplitude.

$\overset{\circ}{A}$ The lunar signal amplitude.

$\overset{\overline{\cdot\cdot}}{A}$ The direct-Sun signal amplitude.

$\overset{\overline{\odot}}{A}$ The direct-Moon signal amplitude.

$\hat{A}$ The shadowband sky signal amplitude.

$\overset{*}{\hat{A}}$ The shadowband solar global irradiance (Sun and sky) signal amplitude.

$\overset{\circ}{\hat{A}}$ The shadowband lunar (Moon and sky) signal amplitude.

$\overset{\overleftarrow{}}{A}$ The FEL lamp calibration signal amplitude.

$\overset{*\overleftarrow{}}{A}$ The solar calibration signal amplitude.

$\overset{\circ\overleftarrow{}}{A}$ The lunar calibration signal amplitude.

$\overset{\square\overleftarrow{}}{A}$ The plaque calibration signal amplitude.

C_a The chlorophyll a concentration.

d_p The distance between the aperture and the photodetector.

e_i An indexed term to establish a particular interaction effect.

e_1 The first interaction effect.

e_2 The second interaction effect.

E Irradiance.

$E(\lambda, t_i)$ Net irradiance detected by the radiometer while exposed to light.

$E_0(\lambda)$ The irradiance at the top of the atmosphere.

$E_d(\lambda)$ In-water spectral downward irradiance.

$E_d(0^+)$ The downward irradiance above the water surface (the global solar irradiance).

$E_d(0^-)$ The downward irradiance at null depth).

E_F The spectral irradiance from an FEL lamp.

$E_i(\lambda)$ The diffuse irradiance.

$E_l(\lambda)$ The (unknown) spectral irradiance of a lamp.

$E_n(\lambda)$ The solar direct irradiance at the surface of the Earth for an overhead Sun.

$E_s(\lambda)$ The spectral global irradiance from the Sun.

$E_s(\lambda_i)$ The spectral global irradiance at λ_i referenced to a bandpass of 1 nm.

$E_u(0^-)$ The upward irradiance at null depth.

$E_u(\lambda)$ The in-water spectral upward irradiance.

F The measurements of an FEL lamp.

$f(\lambda)$ The fit function.

H The height of the tower superstructure.

k The coverage factor.

L Radiance.

ℓ_c The centerline distance between the surface of the plaque and the front of the lamp posts.

$L_i(\lambda)$ The sky radiance.

$L_P(\lambda)$ The radiance of the plaque.

ℓ_r The reference distance for a standard lamp measured from the front of the lamp posts (50 cm for a NIST standard lamp).

$L_T(\lambda)$ The total radiance emanating from the sea surface.

$L_u(0^-)$ The upwelling radiance.

$L_u(z,\lambda)$ The vertical profiles of upwelled radiance.

$L_W(\lambda)$ The water-leaving radiance.

$\hat{L}_W(\lambda)$ The water-leaving radiances from an above-water method.

$\tilde{L}_W(\lambda)$ The water-leaving radiances from an in-water method.

$\left[L_W(\lambda)\right]_{\mathrm{N}}$ The normalized water-leaving radiance.

$\boldsymbol{\mathcal{L}}_T^j(\lambda)$ The total sea radiance from a hybridspectral instrument, wherein $\boldsymbol{\mathcal{L}}_T^M(\lambda)$ denotes the microradiometer data and $\boldsymbol{\mathcal{L}}_T^S(\lambda)$ denotes the hyperspectral spectrograph data.

M A superscript to indicate the microradiometer data.

$\boldsymbol{\mathcal{M}}$ The maximum level of signal saturation.

N_s The number of samples.

$\boldsymbol{\mathcal{N}}$ The noise equivalent signal.

$\boldsymbol{\mathcal{N}}_E(\lambda)$ The NEI of the spectrograph.

$\boldsymbol{\mathcal{N}}_L(\lambda)$ The NER of the spectrograph.

$\boldsymbol{\mathcal{N}}_E^M(\lambda)$ The NEI computed for the microradiometers.

$\overline{\boldsymbol{\mathcal{N}}}_E^M(\lambda)$ The mean NEI computed for the microradiometers.

$\boldsymbol{\mathcal{N}}_E^S(\lambda)$ The NEI computed for the spectrograph.

$\overline{\boldsymbol{\mathcal{N}}}_E^S(\lambda)$ The mean NEI computed for the spectrograph.

P The measurements of a Spectralon plaque.

$P(\lambda)$ The Planck functions.

$\boldsymbol{\mathfrak{P}}$ A radiometric parameter of interest.

$\boldsymbol{\mathcal{P}}$ A radiometric parameter of interest for a hybridspectral sensor.

Q The bidirectional function for the radiance field, which is expressed as an irradiance-to-radiance ratio.

Q_n The Q function for nadir-viewing measurements.

$R(0^-)$ The irradiance reflectance, $E_u(0^-)/E_d(0^-)$.

$r(x,\lambda_r)$ A diagnostic variable expressing departures in the spatial distribution of the radiance field, specifically departures caused by platform perturbations.

r_a The radius of the front aperture.

r_p The radius of the circular opening of a photodetector mount.

R_{rs} The remote sensing reflectance.

$\Re$ The merged effects of reflection and refraction.

$\Re_0$ $\Re$ evaluated at nadir.

S A superscript to indicate the spectroradiometer data.

$\boldsymbol{\mathsf{S}}$ The signal noise.

$\overline{\boldsymbol{\mathsf{S}}}$ The mean signal noise.

t_i The integration time.

$u'(\lambda)$ The relative uncertainty.

W Wind speed.

X The above-water observation.

x The generalized horizontal direction.

x_a The horizontal position of the Sun converted to angular variation.

x_o The observation.

x_p The horizontal position of the center pixel.

Y The in-water (reference) value.

x The generalized meridional direction.

y_a The vertical position of the Sun converted to angular variation.

y_p The vertical position of the center pixel.

y_r The reference value.

z The vertical (depth) coordinate, where the depth is the height of water above the cosine collectors.

$z = 0^-$ A depth immediately below the sea surface (the null depth).

$z = 0^+$ A height immediately above the sea surface.

α The surface spot viewed by the sea-viewing sensor.

β The pointing angle with respect to the Sun.

γ The responsivity.

$\gamma(\lambda)$ The responsivity defined with the calibration coefficient.

$\gamma(\lambda, F)$ The responsivity defined with the calibration coefficient and the immersion factor.

$\gamma_i(\lambda)$ The spectral response function of channel i.

$\Gamma_l(\lambda_i)$ The lamp comparison ratio at channel λ_i.

$F(\lambda)$ The immersion factor interaction effect.

δ Difference.

$\Delta\ell$ The offset distance between the center of the lamp filament and the front of the lamp posts.

ΔL The simulated radiance.

$\delta\lambda$ The wavelength resolution.

η_i A fit coefficient (for $i = 1, 2, \ldots, 8$).

θ_s The solar zenith angle.

θ' The above-water viewing angle (ϑ) refracted by the air–sea interface.

ϑ The nadir viewing angle.

ϑ' A zenith angle.

$\kappa(\lambda)$ The maximum (or saturation) signal level.

λ Wavelength.

λ_i A particular wavelength (or channel).

λ^c The centroid wavelength.

λ_i^c The centroid wavelength of channel i.

λ_R The spectral range.

λ_r A reference (NIR) wavelength.

μ A mean value.

$\mu(\lambda)$ The mean value of light data.

$\bar{\bar{\mu}}(\lambda)$ The mean value of (capped) dark data.

$\widehat{\mu}(\lambda)$ The mean value of dark data.

$\mu_E^M(\lambda)$ The average light signal amplitude.

$\mu_l(\lambda_i)$ The 1 min mean of light data for the transfer radiometer when measuring lamp l with channel λ_i.

$\mu_L^M(\lambda)$ The light average signal amplitude.

$\mu_r(\lambda_i)$ The 1 min mean of light data for the transfer radiometer when measuring reference lamp r (F-616) with channel λ_i.

$\widehat{\mu}_l(\lambda_i)$ The 1 min mean of dark data for the transfer radiometer when measuring lamp l with channel λ_i.

$\widehat{\mu}_r(\lambda_i)$ The 1 min mean of dark data for the transfer radiometer when measuring reference lamp r (F-616) with channel λ_i.

$\widehat{\mu}_L^S(\lambda)$ The mean value of dark data for the spectrograph data of a hybridspectral radiance sensor.

ρ The surface reflectance.

$\rho(W)$ The surface reflectance when dependent on wind speed.

$\rho_P(\lambda)$ The spectral reflectance factor of the plaque (for an incidence angle of $0°$ and a viewing angle of $45°$).

σ A standard deviation.

$\sigma(\lambda)$ The standard deviation for light data.

$\bar{\bar{\sigma}}(\lambda)$ The standard deviation of the (capped) dark data.

$\widehat{\sigma}(\lambda)$ The standard deviation of the dark data.

Υ The ratio of the signals when comparing lamps.

Υ' The simplified lamp ratio.

ϕ The azimuth angle.

ϕ' The sensor pointing angle away from the Sun ($90°$ or $135°$).

$\Phi(\lambda)$ The analytical fit function.

$\Phi_l(\lambda_i^c)$ The value of the fit function of lamp l at the centroid wavelength that is associated with channel i.

$\Phi_r(\lambda_i^c)$ The value of the fit function of reference lamp r (F-616) at the centroid wavelength that is associated with channel i.

ψ The RPD.

Ω A solid angle.

References

Antoine, D., M. Chami, H. Claustre, A. Morel, G. Bécu, B. Gentili, F. Louis, J. Ras, E. Roussier, A.J. Scott, D. Tailliez, S.B. Hooker, P. Guevel, J-F. Desté, C. Dempsey, and D. Adams, 2006: BOUSSOLE: A Joint ESA, CNES, CNRS, and NASA Ocean Color Calibration and Validation Activity. *NASA Tech. Memo. 2006–214147,* NASA Goddard Space Flight Center, Greenbelt, Maryland, 59 pp.

——, F. d'Ortenzio, S.B. Hooker, G. Bécu, B. Gentili, D. Tailliez, and A.J. Scott, 2008: Assessment of uncertainty in the ocean reflectance determined by three satellite ocean color sensors (MERIS, SeaWiFS and MODIS-A) at an offshore site in the Mediterranean Sea (BOUSSOLE project). *J. Geophys. Res.,* **113,** C07013, doi:10.1029/2007JC004472, 23 pp.

Austin, R.W., 1974: "The Remote Sensing of Spectral Radiance from Below the Ocean Surface." In: *Optical Aspects of Oceanography,* N.G. Jerlov and E.S. Nielsen, Eds., Academic Press, London, 317–344.

Bailey, S.W., and P.J. Werdell, 2006: A multi-sensor approach for the on-orbit validation of ocean color satellite data products. *Remote Sens. Environ.,* **102,** 12–23.

——, S.B. Hooker, D. Antoine, B.A. Franz, and P.J. Werdell, 2008: Sources and assumptions for the vicarious calibration of ocean color satellite observations. *Appl. Opt.,* **47,**(12), 2,035–2,045.

Ballard, D.H., 1981: Generalizing the Hough Transform to Detect Arbitrary Shapes, *Pattern Recognition,* **13,** 111–122.

Bernhard, G., and G. Seckmeyer, 1997: New entrance optics for solar spectral UV measurements. *Photochem. Photobiol.,* **65**(6), 923–930.

——, C.R. Booth, and J.C. Ehramjian, 2004: Version 2 data of the National Science Foundation's Ultraviolet Radiation Monitoring Network: South Pole. *J. Geophys. Res.,* bf109, D21207, doi:10.1029/2004, JD004937.

——, ——, and ——, 2005: Real-time ultraviolet and column ozone from multichannel ultraviolet radiometers deployed in the National Science Foundation's ultraviolet monitoring network. *Opt. Eng.,* **44,** 041011-1–041011-12.

——, C.R. Booth, J.H. Morrow, R.N. Lind, and S.B. Hooker, 2010: "Biospherical Shadowband Accessory for Diffuse Irradiance (BioSHADE): A Marine Shadowband and GPS Accessory." In: Morrow, J.H., S.B. Hooker, C.R. Booth, G. Bernhard, R.N. Lind, and J.W. Brown, Advances in Measuring the Apparent Optical Properties (AOPs) of Optically Complex Waters. *NASA Tech. Memo. 2010–215856,* NASA Goddard Space Flight Center, Greenbelt, Maryland, 51–59.

——, T. Comer, V. Quang, C.R. Booth, R.N. Lind, J.H. Morrow, and S.B. Hooker, 2012: OSPREy Transfer Radiometers and Absolute Calibrations. *NASA Tech. Memo.,* NASA Goddard Space Flight Center, Greenbelt, Maryland, (in prep.).

Bigelow, D.S., and J.R. Slusser, 2000: Establishing the stability of multi-filter UV rotating shadowband radiometers. *J. Geophys. Res.,* **105,** 4,833–4,840.

Boivin, L.P., 2005: Realization of Spectral Responsivity Scales. In: *Optical Radiometry,* A.C. Parr, R.U. Datla, and J.L. Gardner, Eds., Academic Press, Waltham, Massachusetts, **41**(05), 97–154.

Booth, C.R., T.B. Lucas, J.H. Morrow, C.S. Weiler, and P.A. Penhale, 1994: The United States National Science Foundation's Polar Network for Monitoring Ultraviolet Radiation. *Antarctic Research Series,* C.S. Weiler and P.A. Penhale, Eds., American Geophysical Union, Washington, D.C., **62,** 17–37.

——, J.H. Morrow, and S.B. Hooker, 2010: "Development of the Microradiometer." In: Morrow, J.H., S.B. Hooker, C.R. Booth, G. Bernhard, R.N. Lind, and J.W. Brown, Advances in Measuring the Apparent Optical Properties (AOPs) of Optically Complex Waters. *NASA Tech. Memo. 2010–215856,* NASA Goddard Space Flight Center, Greenbelt, Maryland, 27–41.

Brown, S.W., G.P. Eppeldauer, and K.R. Lykke, 2000: NIST facility for Spectral Irradiance and Radiance Responsivity Calibrations with Uniform Sources. *Metrologia, 37,* 579–582.

Clark, D., H.R. Gordon, K.J. Voss, Y. Ge, W. Broenkow, and C. Trees, 1997: Validation of atmospheric correction over the oceans. *J. Geophys. Res., 102,* 17,209-17,217.

Dahlback, A., 1996: Measurements of biologically effective UV doses, total ozone abundances, and cloud effects with multichannel, moderate bandwidth filter instruments. *Appl. Opt., 35,* 6,514–6,521.

Disterhoft, P., 2005: Stability characteristics of 1,000 W FEL-type QTH lamps during the seasoningand screening process. *Proc. SPIE, Inter. Soc. Opt. Eng., Ultraviolet Ground and Space-based Measurements Models, and Effects V,* San Diego, California, **5886,** 58860G, doi:10.1117/ 12.614584.

Doyle, J.P., and G. Zibordi, 2002: Optical propagation within a three-dimensional shadowed atmosphere-ocean field: Application to large deployment structures. *Appl. Opt., 41,* 4,283–4,306.

Dubovik, O., and M.D. King, 2000: A flexible inversion algorithm for retrieval of aerosol optical properties from Sun and sky radiance measurements. *J. Geophys. Res., 105,* 20,673–20,696.

Eppeldauer, G.P., S.W. Brown, T.C. Larason, M. Racz, and K.R. Lykke, 2000: Realization of a spectral radiance responsivity scale with a laser-based source and Si radiance meters. *Metrologia, 37,* 531–534.

Fougnie, B., R. Frouin, P. Lecomte, and P-Y. Deschamp, 1999: Reduction of skylight reflection effects in the above-water measurement of diffuse marine reflectance. *Appl. Opt., 38,* 3,844–3,856.

Gordon, H.R., 1998: In-orbit calibration strategy for ocean color sensors. *Remote Sens. Environ., 63,* 265–278.

——, and K. Ding, 1992: Self shading of in-water optical instruments. *Limnol. Oceanogr., 37,* 491–500.

Harrison, L., J. Michalsky, and J. Berndt, 1994: Automated multifilter rotating shadow-band radiometer: An instrument for optical depth and radiation measurements. *Appl. Opt., 33,* 5,118–5,125.

Herman, J., A. Cede, N. Abuhassan, and M. Tzortziou, 2006: "DS-DOAS: An Accurate Direct-Sun Method for Measuring NO_2 Total Column Content Using a Brewer Monochromator and a Small Spectrometer." Poster presented at *Aura Science and Validation Team Meeting,* NCAR Center Green Facility, Boulder, Colorado, 11–15.

Holben, B.N., T.F. Eck, I. Slutsker, D. Tanré, J.P. Buis, A. Setzer, E. Vermote, J.A. Reagan, Y.I. Kaufman, T. Nakajima, F. Lavenu, I. Jankowiak, and A. Smirnov, 1998: AERONET—A federated instrument network and data archive for aerosol characterization. *Remote Sens. Environ., 66,* 1–16.

Hooker, S.B., 2010: "The Telescoping Mount for Advanced Solar Technologies (T-MAST)." In: Morrow, J.H., S.B. Hooker, C.R. Booth, G. Bernhard, R.N. Lind, and J.W. Brown, Advances in Measuring the Apparent Optical Properties (AOPs) of Optically Complex Waters. *NASA Tech. Memo. 2010–215856,* NASA Goddard Space Flight Center, Greenbelt, Maryland, 66–71.

——, and W.E. Esaias, 1993: An overview of the SeaWiFS project. *Eos, Trans., Amer. Geophys. Union, 74,* 241–246.

——, and J. Aiken, 1998: Calibration evaluation and radiometric testing of field radiometers with the SeaWiFS Quality Monitor (SQM). *J. Atmos. Oceanic Technol., 15,* 995–1,007.

——, and S. Maritorena, 2000: An evaluation of oceanographic radiometers and deployment methodologies. *J. Atmos. Ocean. Technol., 17,* 811–830.

——, and C.R. McClain, 2000: The calibration and validation of SeaWiFS data. *Prog. Oceanogr., 45,* 427–465.

——, G. Zibordi, J-F. Berthon, S.W. Bailey, and C.M. Pietras, 2000: The SeaWiFS Photometer Revision for Incident Surface Measurement (SeaPRISM) Field Commissioning. *NASA Tech. Memo. 2000–206892, Vol. 13,* S.B. Hooker and E.R. Firestone, Eds., NASA Goddard Space Flight Center, Greenbelt, Maryland, 24 pp.

——, G. Lazin, G. Zibordi, and S. McLean. 2002a. An evaluation of above- and in-water methods for determining water-leaving radiances. *J. Atmos. Oceanic Technol., 19,* 486–515.

——, S. McLean, J. Sherman, M. Small, G. Lazin, G. Zibordi, and J.W. Brown, 2002b: The Seventh SeaWiFS Intercalibration Round-Robin Experiment (SIRREX-7), March 1999. *NASA Tech. Memo. 2002–206892, Vol. 17,* S.B. Hooker and E.R. Firestone, Eds., NASA Goddard Space Flight Center, Greenbelt, Maryland, 69 pp.

——, and A. Morel, 2003: Platform and environmental effects on above- and in-water determinations of water-leaving radiances. *J. Atmos. Ocean. Technol., 20,* 187–205.

——, G. Zibordi, J-F. Berthon, D. D'Alimonte, D. van der Linde, and J.W. Brown, 2003: Tower-Perturbation Measurements in Above-Water Radiometry. *NASA Tech. Memo. 2003–206892, Vol. 23,* S.B. Hooker and E.R. Firestone, Eds., NASA Goddard Space Flight Center, Greenbelt, Maryland, 35 pp.

——, ——, ——, and J.W. Brown, 2004: Above-water radiometry in shallow, coastal waters. *Appl. Opt., 43,* 4,254–4,268.

——, and ——, 2005a: Advanced methods for characterizing the immersion factor of irradiance sensors. *J. Atmos. Oceanic Technol.,* **22,** 757–770.

——, and ——, 2005b: Platform perturbations in above-water radiometry. *Appl. Opt.,* **44,** 553–567.

——, C.R. McClain, and A. Mannino, 2007: NASA Strategic Planning Document: A Comprehensive Plan for the Long-Term Calibration and Validation of Oceanic Biogeochemical Satellite Data. *NASA Special Pub. 2007–214152,* NASA Goddard Space Flight Center, Greenbelt, Maryland, 31 pp.

——, J.H. Morrow, and J.W. Brown, 2010a: "The Biospherical Surface Ocean Reflectance System (BioSORS)." In: Morrow, J.H., S.B. Hooker, C.R. Booth, G. Bernhard, R.N. Lind, and J.W. Brown, Advances in Measuring the Apparent Optical Properties (AOPs) of Optically Complex Waters. *NASA Tech. Memo. 2010–215856,* NASA Goddard Space Flight Center, Greenbelt, Maryland, 8–16.

——, R.N. Lind, J.H. Morrow, and J.W. Brown, 2010b: "The Submersible Biospherical Optical Profiling System (SuBOPS)." In: Morrow, J.H., S.B. Hooker, C.R. Booth, G. Bernhard, R.N. Lind, and J.W. Brown, Advances in Measuring the Apparent Optical Properties (AOPs) of Optically Complex Waters. *NASA Tech. Memo. 2010–215856,* NASA Goddard Space Flight Center, Greenbelt, Maryland, 17–26.

Johnson, B.C., J.B. Fowler, and C.L. Cromer, 1998: The SeaWiFS Transfer Radiometer (SXR). *NASA Tech. Memo. 1998–206892, Vol. 1,* S.B. Hooker and E.R. Firestone, Eds., NASA Goddard Space Flight Center, Greenbelt, Maryland, 58 pp.

——, S.W. Brown, K.R. Lykke, C.E. Gibson, G. Fargion, G. Meister, S.B. Hooker, B. Markham, and J.J. Butler, 2003: Comparison of cryogenic radiometry and thermal radiometry calibrations at NIST using multichannel filter radiometers. *Metrologia,* **40,** S216–S219.

Joint Global Ocean Flux Study, 1991: JGOFS Core Measurements Protocols. *JGOFS Report No. 6,* Scientific Committee on Oceanic Research, 40 pp.

Kostkowski, H.J., 1997: *Reliable Spectroradiometry,* Spectrometry Consulting, La Plata, Maryland, 609 pp.

Kouremeti, N., A. Bais, S. Kazadzis, M. Blumthaler, and R. Schmitt, 2008: Charge-coupled device spectrograph for direct solar irradiance and sky radiance measurements. *Appl. Opt.,* **47,** 1,594–1,607.

Kreuter, A., and M. Blumthaler, 2009: Stray light correction for solar measurements using array spectrometers. *Rev. Sci. Instrum.,* **80,** 096108-1–3.

Larason, T.C., and J.M. Houston, 2008: Spectroradiometric detector measurements: ultraviolet, visible, and near-infrared detectors for spectral power. *NIST Special Pub. 250–41 (2008),* National Institute of Standards and Technology, Gaithersburg, Maryland, 99 pp., plus appendices.

Laurion, I., F. Blouin, and S. Roy, 2003: The quantitative filter technique for measuring phytoplankton absorption: Interference by MAAs in the UV waveband. *Limnol. Oceanogr. Meth.,* **1,** 1–9.

Liu, Y., and K.J. Voss, 1997: Polarized radiance distribution measurement of skylight. II. Experiment and data. *Appl. Opt.,* **36,** 8,753–8,764.

Mayer, B., and A. Kylling, 2005: Technical note: The libRadtran software package for radiative transfer calculations—description and examples of use. *Atmos. Chem. Phys.,* **5,** 1,855–1,877.

McClain, C.R., G.C. Feldman, and S.B. Hooker, 2004: An overview of the SeaWiFS project and strategies for producing a climate research quality global ocean bio-optical time series. *Deep Sea Res. II,* **51,** 5–42.

——, S. Hooker, G. Feldman, and P. Bontempi, 2006: Satellite data for ocean biology, biogeochemistry, and climate research. *Eos, Trans. Amer. Geophys. Union,* **87,** 337, 343.

Meister, G., P. Abel, K. Carder, A. Chaplin, D. Clark, H. Cooper, C. Davis, D. English, G. Fargion, M. Feinholz, R. Frouin, F. Hoge, D. Korwan, G. Lazin, C.R. McClain, S. McLean, D. Menzies, A. Poteau, J. Robertson, J. Sherman, K. Voss, and J. Yungel, 2003: The Second SIMBIOS Radiometric Intercomparision (SIMRIC-2), March–November 2002. *NASA Tech. Memo. 2003–210006, Vol. 2,* NASA Goddard Space Flight Center, Greenbelt, Maryland, 71 pp.

Mobley, C.D., 1999: Estimation of the remote-sensing reflectance from above-surface measurements. *Appl. Opt.,* **38,** 7,442–7,455.

Morel, A., and L. Prieur, 1977: Analysis of variations in ocean color. *Limnol. Oceanogr.,* **22,** 709–722.

——, and B. Gentili, 1996: Diffuse reflectance of oceanic waters, III. Implication of bidirectionality for the remote sensing problem. *Appl. Opt.,* **35,** 4,850–4,862.

——, and S. Maritorena, 2001: Bio-optical properties of oceanic waters: a reappraisal. *J. Geophys. Res.,* **106,** 7,163–7,180.

——, and J.L. Mueller, 2002: "Normalized Water-Leaving Radiance and Remote Sensing Reflectance: Bidirectional Reflectance and Other Factors." In: Mueller, J.L., and G.S. Fargion, Ocean Optics Protocols for Satellite Ocean Color Sensor Validation, Revision 3, Volume 2. *NASA Tech. Memo. 2002–210004/Rev3–Vol2,* NASA Goddard Space Flight Center, Greenbelt, Maryland, 183–210.

——, D. Antoine, and B. Gentilli, 2002: Bidirectional reflectance of oceanic waters: Accounting for Raman emission and varying particle scattering phase function. *Appl. Opt.,* **41,** 6,289–6,306.

Morrow, J.H., M.S. Duhig, and C.R. Booth, 1994: Design and evaluation of a cosine collector for a SeaWiFS-compatible marine reflectance radiometer. *SPIE Ocean Optics XII,* **2,258,** 879–886.

——, B.N. White, M. Chimiente, and S. Hubler, 2000: A bio-optical approach to reservoir monitoring in Los Angeles, California. *Arch. Hydrobiol. Spec. Issues Advanc. Limnol.,* **55,** 179–191.

——, S.B. Hooker, C.R. Booth, G. Bernhard, R.N. Lind, and J.W. Brown, 2010a: Advances in Measuring the Apparent Optical Properties (AOPs) of Optically Complex Waters, *NASA Tech. Memo. 2010–215856,* NASA Goddard Space Flight Center, Greenbelt, Maryland, 80 pp.

——, C.R. Booth, R.N. Lind, and S.B. Hooker, 2010b: "The Compact-Optical Profiling System (C-OPS)." In: Morrow, J.H., S.B. Hooker, C.R. Booth, G. Bernhard, R.N. Lind, and J.W. Brown, Advances in Measuring the Apparent Optical Properties (AOPs) of Optically Complex Waters. *NASA Tech. Memo. 2010–215856,* NASA Goddard Space Flight Center, Greenbelt, Maryland, 42–50.

——, S.B. Hooker, G. Bernhard, and R.N. Lind, 2010c: "Scalable Hydro-optical Applications for Light-Limited Oceanography (SHALLO)." In: Morrow, J.H., S.B. Hooker, C.R. Booth, G. Bernhard, R.N. Lind, and J.W. Brown, Advances in Measuring the Apparent Optical Properties (AOPs) of Optically Complex Waters. *NASA Tech. Memo. 2010–215856,* NASA Goddard Space Flight Center, Greenbelt, Maryland, 60–65.

Mueller, J.L., 2000: "Overview of Measurement and Data Analysis Protocols." In: Fargion, G.S., and J.L. Mueller, Ocean Optics Protocols for Satellite Ocean Color Sensor Validation, Revision 2. *NASA Tech. Memo. 2000–209966,* NASA Goddard Space Flight Center, Greenbelt, Maryland, 87–97.

——, 2002: "Overview of Measurement and Data Analysis Protocols." In: Mueller, J.L., and G.S. Fargion, Ocean Optics Protocols for Satellite Ocean Color Sensor Validation, Revision 3, Volume 1. *NASA Tech. Memo. 2002–210004/Rev3–Vol1,* NASA Goddard Space Flight Center, Greenbelt, Maryland, 123–137.

——, 2003: "Overview of Measurement and Data Analysis Methods." In: Mueller, J.L., and 17 Coauthors, Ocean Optics Protocols for Satellite Ocean Color Sensor Validation, Revision 4, Volume III: Radiometric Measurements and Data Analysis Protocols. *NASA Tech. Memo. 2003–211621/Rev4–Vol.III,* NASA Goddard Space Flight Center, Greenbelt, Maryland, 1–20.

——, and R.W. Austin, 1992: Ocean Optics Protocols for SeaWiFS Validation. *NASA Tech. Memo. 104566, Vol. 5,* S.B. Hooker and E.R. Firestone, Eds., NASA Goddard Space Flight Center, Greenbelt, Maryland, 43 pp.

——, and ——, 1995: Ocean Optics Protocols for SeaWiFS Validation, Revision 1. *NASA Tech. Memo. 104566, Vol. 25,* S.B. Hooker, E.R. Firestone, and J.G. Acker, Eds., NASA Goddard Space Flight Center, Greenbelt, Maryland, 66 pp.

National Aeronautics and Space Administration, 2010: *Responding to the Challenge of Climate and Environmental Change: NASA's Plan for a Climate-Centric Architecture for Earth Observations and Applications from Space.* National Aeronautics and Space Administration, Washington, DC, 48 pp.

NRC, 2007: *Earth Science and Applications from Space: National Imperatives for the Next Decade and Beyond.* The National Academies, Washington, DC, 456 pp.

Nicodemus, F.E., H.J. Kostkowski, and A.T. Hattenburg, 1976: "Introduction." In: Nicodemus, F.E., Ed., Self-Study Manual on Optical Radiation Measurements: Part 1—Concepts, Chapters 1 to 3. U.S. Govt. Printing Off., *C 13 46 910-1,* Washington, D.C., 82 pp.

Ohno, Y., 1997: Improved photometric standards and calibration procedures at NIST. *J. Res. Natl. Inst. Stand. Technol.,* **102,** 323–331.

O'Reilly, J.E., S. Maritorena, B.G. Mitchell, D.A. Siegel, K.L. Carder, S.A. Garver, M. Kahru, and C. McClain, 1998: Ocean Color chlorophyll algorithms for SeaWiFS. *J. Geophys. Res.,* **103,** 24,937–24,953.

——, and 24 Coauthors, 2000: SeaWiFS Postlaunch Calibration and Validation Analyses, Part 3. *NASA Tech. Memo. 2000–206892, Vol. 11,* S.B. Hooker and E.R. Firestone, Eds., NASA Goddard Space Flight Center, 49 pp.

Pinkerton, M.H., and J. Aiken, 1999: Calibration and validation of remotely-sensed observations of ocean colour from a moored data buoy, *J. Atmos. Oceanic Technol.,* **16,** 915–923.

Rhea, W.J., and C.O. Davis, 1997: A comparison of the SeaWiFS chlorophyll and CZCS pigment algorithms using optical data from the 1992 JGOFS Equatorial Pacific Time Series. *Deep Sea Res. II,* **44,** 1,907–1,925.

Sanders, C.L., 1962: A photocell linearity tester. *Appl. Opt.,* **1,** 207–212.

Schmid, B., and C. Wehrli, 1995: Comparison of Sun photometer calibration by use of the Langley technique and the standard lamp. *Appl. Opt.,* **34,** 4,500–4,512.

——, J. Michalsky, R. Halthore, M. Beauharnois, L. Harrison, J. Livingston, P. Russell, B. Holben, T. Eck, and A. Smirnov, 1999: Comparison of aerosol optical depth from four solar radiometers during the fall 1997 ARM intensive observation period. *Geophys. Res. Lett.,* **26,** 2,725–2,728.

Seim, H.E., 2000: Implementation of the South Atlantic Bight Synoptic Offshore Observational Network, *Oceanogr.,* **13,** 18–23.

Siegel, D.A., S. Maritorena, N.B. Nelson, and M.J. Behrenfeld, 2005: Independence and interdependencies among global ocean color properties: Reassessing the bio-optical assumption. *J. Geophys. Res.,* **110,** C07011, doi:10.1029/2004JC002527.

Slusser, J., J. Gibson, D. Bigelow, D. Kolinski, P. Disterhoft, K. Lantz, and A. Beaubien, 2000: Langley method of calibrating UV filter radiometers. *J. Geophys. Res.,* **105,** 4,841–4,849.

Smith, R.C., and K.S. Baker, 1984: The analysis of ocean optical data. *Ocean Optics VII,* M. Blizard, Ed., *SPIE,* **478,** 119–126.

Space Studies Board, 2000: *Ensuring the Climate Record from the NPP and NPOESS Meteorological Satellites.* National Academy Press, Washington, DC, 51 pp.

Toole, D.A., D.A. Siegel, D.W. Menzies, M.J. Neumann, and R.C. Smith, 2000: Remote sensing reflectance determinations in the coastal ocean environment—impact of instrumental characteristics and environmental variability. *Appl. Opt.,* **39,** 456–469.

Voss, K.J., and Y. Liu, 1997: Polarized radiance distribution measurements of skylight. I. System description and characterization. *Appl. Opt.,* **36,** 6,083–6,094.

Walker, J.H., R.D. Saunders, J.K. Jackson, and D.A. McSparron, 1987: Spectral Irradiance Calibrations. *NBS Special Publication 250–20,* U.S. Dept. of Commerce, National Bureau of Standards, Washington, DC, 37 pp., plus appendices.

Wehrli, C., 1989: World optical depth research and calibration center. PDF available via downloadable FTP: `ftp://ftp.pmodwrc.ch/pub/worcc/gaweth98.pdf`

Werdell, P., and S. Bailey, 2005: An improved in-situ bio-optical data set for ocean color algorithm development and satellite data product validation. *Remote Sens. Environ.,* **98,** 122–140.

——, ——, B.A. Franz, A. Morel, and C.R. McClain, 2007: On-orbit vicarious calibration of ocean color sensors using an ocean surface reflectance model. *Appl. Opt.,* **46,** 5,649–5,666.

Wesely, M.L., 1982: Simplified techniques to study components of solar radiation under haze and clouds. *J. Appl. Meteorol.,* **21,** 373–383.

Wilson, W.H., 1980: Solar Ephemeris Algorithm. *SIO Ref. 80-13,* Scripps Institution Of Oceanography Visibility Laboratory, La Jolla, California, 72 pp.

World Meteorological Organization, 2003: WMO/GAW aerosol measurement procedures: Guidelines and recommendations. *Global Atmospheric Watch Report, No. 153,* Geneva, Switzerland, 67 pp.

——, 2007: Scientific Assessments of Ozone Depletion: 2006. *Global Ozone Research and Monitoring Project, Report No. 50,* World Meteorological Organization, Geneva, Switzerland, 572 pp.

——, 2008: Guide to Meteorological Instruments and Methods of Observations, Seventh Edition, *WMO, No. 8,* Secretary of the World Meteorological Organization, Geneva, Switzerland. Downloadable PDF available at `http://www.wmo.int/pages/prog/gcos/tdocuments/gruanmanuals/CIMO/CIMO_Guide-7th_Edition-2008.pdf`.

Yoon H.W., C.E. Gibson, and P.Y. Barnes, 2002: Realization of the National Institute of Standards and Technology detector-based spectral irradiance scale. *Appl. Opt.,* **41,** 5,879–5,890.

——, and ——, 2011: Spectral Irradiance Calibrations, *NIST Special Publication 250-89,* National Institute of Standards and Technology, Gaithersburg, Maryland, 25 pp.

Zalewski, E.F., A.R. Schaefer, K. Mohan, and D.A. McSparron, 1972: Optical Radiation Measurements: Photometric Instrumentation and Research (1970 to 1971). *Tech. Note 594–2,* National Bureau of Standards, Gaithersburg, Maryland, 44 pp.

Zibordi, G., and M. Ferrari, 1995: Instrument self-shading in underwater optical measurements: Experimental data. *Appl. Opt.,* **34,** 2,750–2,754.

——, J.P. Doyle, and S.B. Hooker, 1999: Offshore tower shading effects on in-water optical measurements. *J. Atmos. Ocean. Tech.,* **16,** 1,767–1,779.

——, J-F. Berthon, J.P. Doyle, S. Grossi, D. van der Linde, C. Targa, and L. Alberotanza 2002a: Coastal Atmosphere and Sea Time Series (CoASTS), Part 1: A Tower-Based Long-Term Measurement Program. *NASA Tech. Memo. 2002–206892, Vol. 19,* S.B. Hooker and E.R. Firestone, Eds., NASA Goddard Space Flight Center, Greenbelt, Maryland, 29 pp.

——, S.B. Hooker, J-F. Berthon, and D. D'Alimonte, 2002b: Autonomous above-water radiance measurements from an offshore platform: A field assessment experiment. *J. Atmos. Oceanic Technol.,* **19,** 808–819.

——, S.B. Hooker, J. Mueller, G. Lazin, 2004a: Characterization of the immersion factor for a series of underwater optical radiometers. *J. Atmos. Oceanic Technol.,* **21,** 501–514.

——, F. Mélin, S.B. Hooker, D. D'Alimonte, and B. Holben, 2004b: An autonomous above-water system for the validation of ocean color radiance data. *Trans. IEEE Trans. Geosci. Remote Sens.,* **42,** 401–415.

REPORT DOCUMENTATION PAGE

The public reporting burden for this collection of information is estimated to average 1 hour per response, including the time for reviewing instructions, searching existing data sources, gathering and maintaining the data needed, and completing and reviewing the collection of information. Send comments regarding this burden estimate or any other aspect of this collection of information, including suggestions for reducing this burden, to Department of Defense, Washington Headquarters Services, Directorate for Information Operations and Reports (0704-0188), 1215 Jefferson Davis Highway, Suite 1204, Arlington, VA 22202-4302. Respondents should be aware that notwithstanding any other provision of law, no person shall be subject to any penalty for failing to comply with a collection of information if it does not display a currently valid OMB control number.
PLEASE DO NOT RETURN YOUR FORM TO THE ABOVE ADDRESS.

1. REPORT DATE *(DD-MM-YYYY)*	2. REPORT TYPE	3. DATES COVERED *(From - To)*

4. TITLE AND SUBTITLE

5a. CONTRACT NUMBER

5b. GRANT NUMBER

5c. PROGRAM ELEMENT NUMBER

6. AUTHOR(S)

5d. PROJECT NUMBER

5e. TASK NUMBER

5f. WORK UNIT NUMBER

7. PERFORMING ORGANIZATION NAME(S) AND ADDRESS(ES)

8. PERFORMING ORGANIZATION REPORT NUMBER

9. SPONSORING/MONITORING AGENCY NAME(S) AND ADDRESS(ES)

10. SPONSORING/MONITOR'S ACRONYM(S)

11. SPONSORING/MONITORING REPORT NUMBER

12. DISTRIBUTION/AVAILABILITY STATEMENT

13. SUPPLEMENTARY NOTES

14. ABSTRACT

15. SUBJECT TERMS

16. SECURITY CLASSIFICATION OF:			17. LIMITATION OF ABSTRACT	18. NUMBER OF PAGES	19b. NAME OF RESPONSIBLE PERSON
a. REPORT	b. ABSTRACT	c. THIS PAGE			19b. TELEPHONE NUMBER *(Include area code)*